CRANFIELD UNIVERSITY

SUNGTAEK LIM

THE IMPROVEMENT OF METER PERFORMANCE OF EM SENSING FLOWMETERS, USING SOFTWARE MODELLING

SCHOOL OF ENGINEERING

PhD Thesis

CRANFIELD UNIVERSITY
SCHOOL OF ENGINEERING

PhD THESIS

Academic Year 2004-2008

SUNGTAEK LIM

THE IMPROVEMENT OF METER PERFORMANCE OF EM SENSING FLOWMETERS, USING SOFTWARE MODELLING

Supervisor: Prof M.L.Sanderson

NOVEMBER 2008

This thesis is submitted in partial fulfilment of the requirements
for the degree of PhD

Abstract

This thesis is focused on the improvement of the meter performance and power consumption of non-mechanical flowmeters such as the conventional electromagnetic flowmeter and the fluidic oscillator. Each flowmeter is studied using Finite Element Modelling for the magnetic field, the virtual current and the fluid dynamics in order to simulate flow signal.

The meter design of the conventional electromagnetic flowmeter is modified to provide a better signal level by optimising the geometry of the flow channel and the magnetic field. The signal level increase can be used to reduce power consumption. This improvement provides a 1.96 times greater signal or 51% less power consumption for the conventional electromagnetic flowmeter.

An alternative coil-less electromagnetic flowmeter is proposed to reduce the energy consumption. A laminated magnetostrictive material/PZT piezoelectric material is used to control the magnetic field from a permanent magnet. Modelling is carried out to optimise the meter and the magnetic field control device. The device can provide a further reduction of 54.7% of energy usage over the improved conventional electromagnetic flowmeter.

The modelling of the fluidic oscillator is undertaken not only with the fluidic dynamics but also the flow signal by using the electromagnetic sensing technique. Using these approaches, recommendations for a better signal level are proposed.

Acknowledgements

I would like to give great thank to my supervisor, Prof Mike Sanderson for his unchanging support and excellent advice. Thanks also to Prof. Chris Thompson for his support.

I would like to thank Mr Philip Crowther and Mr Thomas Doyle from Elster Metering Ltd. for giving me an opportunity to work with the fluidic oscillator team and supporting me.

I thank my parents for their everlasting love and support.

To my kids, Chaewhi, Chaeyoon and little princess Lynnah, I have not forgotten what you have given to me during the past four years.

Finally, my wife, wonderful friend of mine and the best mum of three kids, this moment could not come to me without you, Ji-Young.

Table of Contents

Table of Figures

Table of Tables

Nomenclature

English Letter Symbols

A	cross-section area of flow channel
B	magnetic flux density
B_r	remanent flux density of permanent magnet
$\mathbf{B}$	magnetic field
C	velocity of sound in the liquid
C_{TX}	capacity of the piezoelectric material
D	pipe diameter
d	thickness of piezoelectric material
$\mathbf{E}$	electric field
E	Young's modulus ratio
e	electromotive force
e_m	piezoelectric coefficient of magnetostrictive material
f	frequency of oscillation
$\mathbf{F}$	force
F_b	blocking force
h	height of flow channel
H	magnetic field strength
i,I	current
$\mathbf{j}$	virtual current
$\mathbf{J}$	current density
k	meter factor
l	distance between electrodes for electromagnetic flowmeters
L	distance between transducers for ultrasonic flowmeters
N	number of turn of coil
N_T	total retarding torque
P	permeance of magnetic circuit

q	flowrate in m^3/s
Q	flowrate in m^3/hr
Q	charge on piezoelectric material
$Q1$	minimum flowrate
$Q2$	transitional flowrate
$Q3$	permanent flowrate
$Q4$	overloaded flowrate
R	Resistance for electric circuit
R	Reluctance for magnetic circuit
S	sensitivity of flowmeter
S_m	strain in the x-direction
S_r	Strouhal number
t_{ud}	transit time from downstream transducer to upstream transducer
t_{du}	transit time from upstream transducer to downstream transducer
T	temperature
U	electric potential of flow signal
v	velocity
V	voltage
w	jet width
W	weight function

Greek letter symbols

α	blade pitch angel
δ	deflection of cantilever actuator
ε	permiativity of material
θ	angle between acoustic path and meter axis
λ	coefficient of geometrical structure of Tefernol-D
μ	permeability
ρ	fluid density
r	root-mean-square of the inner and outer blade radii

σ fluid conductivity

ω rotor angular velocity

Φ magnetic flux

σ conductivity

Chapter 1. Introduction

This thesis is focused on the investigation of improvements to different domestic water meter designs using an electromagnetic sensing technique, one of which is the conventional electromagnetic water meter using coils and the other is the fluidic oscillator employing an electromagnetic sensing technique.

The conventional electromagnetic domestic water meter has a rectangular flow channel with line electrodes and a C-shape transformer core with coil, of which the cross section is 10mm wide and 5mm high. This water meter design is optimised, being modified both in the cross section of the flow channel and the design of the magnetic field to increase the flow signal by changing the dimensions of the flow channel and using soft iron plates between the flow channel and both ends of transformer core to improve the uniformity and extent of the magnetic field.

Power consumption is also considered for the conventional electromagnetic water meter, because the coil not only takes up space within the flowmeter device but is also a power consuming device; therefore an alternative device which is able to change the magnetic flux without using a coil is investigated. The investigation introduces two novel devices: one employing magnetostrictive material which changes magnetic properties under an external stress, and the other is the mechanical device using a piezoelectric actuator which changes the air gap of the magnetic circuit. Both devices use a permanent magnet as the magnetic flux source.

The fluidic oscillator uses permanent magnets to sense the hydro-dynamically induced oscillation within the flowmeter body to measure the flowrate. Thus the power consumption is not a major concern in terms of the sensing technique, but the improvement of the flow signal at low flow and meter factor performance over the

flow range are investigated. The improvement of the flow signal is obtained by finding the most suitable location of electrodes and magnets, and modifications to the geometric structure.

The investigations for all the water meters are undertaken by software modelling, comparing the modelling with experimental results and providing an analysis of the comparative results obtained using computational and experimental methods. The software modelling of CFD (Computational Fluid Dynamics) and electromagnetic simulations are provided using COMSOL Multiphysics software package and MatLab programming tools. The experimental results for the response from the various meters have been obtained using the Class-D flow rig in PASE Lab.

In this chapter, an overview of flow metering and types of water meter is provided. The types of water meter are classified according to which measuring mechanism is used in the water meter and categorised as either a mechanical or non-mechanical water meter. The mechanical water meter category includes any meter having moving parts such as a turbine, a piston or an impeller. The non-mechanical water meter does not contain any moving part to measure the flow. As a summary of the overview, a comparison table is given at the end of this chapter.

An overview of the recommendations for water meters from OIML (The International Organization of Legal Metrology) is given for understanding and specifying the target performance of improved water meters. Power consumption and running time are also important issues for the electronic water meter, so the battery capacitance and minimum power consumption to run the water meter for the long time regulated in the recommendation is described.

1.1 Flow meter types

Flow measurement was started over 4,000 years ago by the Romans who measured water flow from their aqueducts to each house to control allocation. Since that time flow measurement techniques have been developed in response to demands to measure new fluids, to measure old fluids under new conditions of flow and to measure with accuracy the value of the increased fluid.

Figure 1-1 shows types of flowmeter which are classified by the flow metering techniques commonly in current use, although it is not possible to list all types of flowmeter. The list is restricted to technologies used for water metering. In a mechanical flowmeter the meter has a moving part or obstacle to measure flow and for the non-mechanical flowmeter there are no moving parts. From the chart, only some of the mechanical and non-mechanical meters are used mostly for measuring domestic water, in particular for billing households.

1.2 Mechanical meters

A mechanical meter has moving parts to measure the flow. A moving part can be a rotary piston, an impeller or a turbine. Mechanical meters are very widely used as domestic water meters because they are simpler, cheaper and operate without an internal or external power source. In this section, four representative mechanical water meters are explained: rotary piston, single jet, multi-jet and turbine.

1.2.1 Rotary piston meters

Rotary piston meters are one type of positive displacement meter used widely for the domestic water industry. Figure 1-2 shows the major types of the displacement meters used for liquid flow measurement. This meter is the most popular positive

displacement meter used as a water meter, which uses the rotation of the moving parts to transport water through the meter in isolated compartments. The flow is formed by means of rotors which keep contact as they rotate and cause a certain metered volume to be passed through the meter from inlet to outlet. The volume passed is proportional to the number of rotations of the piston and the volume transferred in each rotation. The volumetric flowrate, q_v, is proportional to the speed of the rotation.

Figure 1-3 shows an exploded view of the rotary piston water meter. Part 14 in this figure rotates as the flow goes through the meter. The accuracy of the meter depends on the adjustments between the chamber and the piston because the errors originate in the leaks in that area. Consequently the tolerances in the dimensions of these two elements are very important because excessive wear may create negative errors and a reduction in the inner volume of the chamber due to limescale will prevent the piston rotation.

The rotary piston meter has been used for some considerable time because it is a very reliable technology unaffected by the flow profile and installation position and has excellent performance at low flowrates. The installation of this meter is simple and more compact than other types of meter. However, the rotary piston meter is affected by solids or particles in water, which degrade the low flow performance and generate noise at high flowrates.

1.2.2 Single jet meters

The single jet meter is a well known mechanical water meter, widely used in many countries especially in Asia and America due to its low cost and reliability. The single jet meter is based on the tangential incidence of a single jet over a radial-vaned impeller placed inside the body of the meter. The rotation velocity of the impeller is proportional to the impact velocity of the water. Figure 1-4 shows a top view of the

impeller of the single jet meter. The single jet meter usually consists of an impeller, a brass housing and a totaliser. The accuracy of the meter is dependent on the internal housing and impeller dimension so the manufacturing cost will increase because of strict tolerance in the manufacturing process when higher accuracy is demanded. For this reason, the single jet meter is mostly used in smaller diameter pipework such as 20mm or less. For larger diameter pipework, a multi-jet meter is more economical.

The advantages of single jet meters are that they are resistant to suspended solids or particles. The cost of small bore size meters, i.e. 13mm, 15mm and 20mm, is low and their length probably the most compact and capable of being to installed in a small space. But the moving parts such as the impeller and its bearing will be worn by aging and hence degrade meter performance.

1.2.3 Multi-jet meters

The operating principle of multi-jet meters is very similar to the single jet meter but the water impacts on the impeller at multiple points around its perimeter instead of at a single point. This method achieves better performance at low flowrates and lowers the starting flowrate. Figure 1-5 shows the exploded view of a multi-jet meter. The measuring chamber with multiple ports is placed inside the meter housing so the dimension of the meter housing does not affect the accuracy. Although the manufacturing process allows lower tolerance of the meter body, the added measuring chamber makes the multi-jet meters larger and heavier than the single jet meter with the same bore size. The multi-jet meters are therefore suitable for a bore size of 25mm to 40mm.

Multi-jet meters can give a more reliable performance than other mechanical water meters because the multiple jets make the impeller rotate in a more balanced condition and no upstream straight pipework is needed. These meters have good resistance to solids or particles and great variety of models, constructions and prices. Meters ranging from 20mm to 40mm are very competitive in price compared to other

measuring technologies. But the size of these meters is larger then single jet meters and they are also affected by installation conditions. A lower starting flow has been demanded recently to detect leakage, but the multi-jet meter does not have enough performance to satisfy this requirement.

1.2.4 Turbine meters

Modern turbine meters are the product of considerable development based on the original axial vaned flowmeter principle first credited to Woltman in 1790 for water metering. Figure 1-6 is a schematic cross-section through the axis of symmetry depicting the key component of a typical meter. The meter in the figure is a single rotor turbine meter, concentrically mounted on a shaft within a cylindrical housing. The shaft and shaft bearings are located by end supports inside a suspended diffuser. Thus the flow passes through an annular region occupied by the rotor blades. The blades are inclined at an angle to the incident flow velocity and generate a torque which drives the rotor.

Figure 1-7 shows the vector diagram for a flat bladed rotor with a blade pitch angle α. By assuming that the rotor blades are flat, the velocity is everywhere uniform and parallel to the rotor axis, the rotor angular velocity ω is written as

$$\omega = \frac{v \tan \alpha}{r} \tag{1-1}$$

then the total flowrate becomes

$$\frac{\omega}{Q} = \frac{\tan \alpha}{\bar{r} A} \tag{1-2}$$

where Q is the volumetric flowrate, A is the area of the annular flow cross-section and r is the root-mean-square of the inner and outer blade radii. In the ideal equation

the meter response is linear and determined only by the geometry of the rotor. In practice, there is instead a number of rotor retarding torques of varying relative magnitudes and therefore equation (1-2) is re-written as:

$$\frac{\omega}{Q} = \frac{\tan\alpha}{\bar{r}A} - \frac{N_T}{\bar{r}^2 \rho Q^2} \tag{1-3}$$

where ρ is the fluid density and N_T is the total retarding torque, but in liquid the rotor blade surfaces' fluid drag torque is considerable. Therefore equation (1-3) expresses the meter characteristic of turbine meter poorly at very low flows.

The performance of turbine meters especially at the very low flowrates is improved by changing the shape of the blades' rotor or increasing the number of rotors. The shape of the rotor is changed from flat blades to helical blades as shown in Figure 1-8. The first design of helical blades was used for measuring fuel consumption and fuel transfer within an aircraft in 1953 (Frey).

Turbine meters give good accuracy over a wider range but have pressure and temperature limitations. The cost of this meter is mid range compared to other non-mechanical meters. Turbine meters are affected by the viscosity of liquid so a different meter factor may be required for different viscosities. Also, accuracy may be poorer when the flow has swirl.

1.2.5 Limitations of mechanical meters

Although mechanical meters provide adequate performance and low cost, the limitations arising from the principles of the mechanical meter can be considerable. The major problem with this meter is that accuracy is not maintained with age. A report on multi-jet meters which were used for seven years after installation showed an accuracy of -39.21% at the lowest flowrate and 21% of the tested meters could not measure the flow at the minimum flowrate at all (Chang *et al.*, 2005).

Arregui and his working group tested the performance shift of 13mm single jet meters and the charts are shown in Figure 1-9. According to the figure, three out of four samples under-estimated at the lowest flow and one sample under-estimated by as much as 23% after flowing a total volume of 1,500 m^3 (Arregui *et al.*, 2005). This meter performance deteriorated with age as a consequence of the wear of the impeller or the bearing of the moving part.

Moving parts can also cause jamming or clogging when water contains particles, limescale or sands. Some solids such as limescale may deposit on the inside of the flow chamber of the mechanical water meter which may cause over-registration at mid-hi flowrates and under-registration at low flowrates (Arregui *et al.*, 2005). Figure 1-10 shows deposits of limescale inside the flow chamber. The deposits can grow so large that they prevent the impeller from rotating.

In the particular operating conditions of the domestic water meter, the water supply is not always serviced continuously. When the water supply is smaller than the demand the water supply may cut off. After cutting off, air fills the supply pipe instead of water. Mechanical meters will continue to rotate when the water supply returns to the pipe, pushing the trapped air flows though the water meter. Mechanical meters will therefore over-read the quantity of water supplied. From equation (1-3), the angular velocity of a turbine meter at the same volumetric flowrate only depends on the density of liquid which means the impeller of a turbine rotates much faster when air flows then when water does.

These limitations of mechanical water meters translate into an increased cost of ownership and lost revenue for the utility, which can be equivalent to many times the original cost of the meter over a long period. By appropriating solid-state and non-mechanical water meters with electronic registering, it is possible to overcome the limitations of a mechanical water meter because the non-mechanical meter has no moving parts to cause jamming, clogging or wearing.

1.3 Non mechanical meters

The expression ‘non-mechanical meter’ is frequently used as the opposite of mechanical meter, i.e. the meter does not have any moving parts to measure flow. Although meters such as the vortex and differential pressure flowmeters do not have moving parts inside the flow tube, these meters are not generally used as domestic water meters because the flow tubes need more installation space and additional instruments such as a differential pressure transmitter require an external power supply. For this reason, the non-mechanical meters considered in this thesis are the electromagnetic flowmeter, the ultrasonic flowmeter and the fluidic oscillator only.

1.3.1 Electromagnetic meters

Figure 1-11 is a diagram of electromagnetic flowmeters. These flowmeters operate by measuring an electromotive force generated between the electrodes which are at right angles to the flow direction when a magnetic field applied is orthogonal to both the flow direction and the electrodes. The electromotive force measured is proportional to the mean velocity of liquid, which is then converted to the flowrate as:

$$e = Blv \tag{1-4}$$

where e is electromotive force, B is the magnetic flux density, l is distance between electrodes ,v is the mean velocity and k is meter factor so that the flowrate of pipe of which the diameter is D can be calculated as:

$$Q = (\frac{\pi}{4}D^2)\cdot v = (\frac{\pi D}{4B})e \tag{1-5}$$

because the electrodes distance, l, is the same as the pipe diameter, D.

Equation (1-5) shows the measuring principle of the electromagnetic flowmeter is not affected by the temperature, pressure or density of the liquid. The flowmeter can use the full-bore of the pipe which means no head loss is incurred. This type of flowmeter can measure both directions of flow.

The electromagnetic flowmeter normally uses coils to generate the magnetic field but these coils consume the most power required to operate the flowmeter in order to measure the flow and this makes the flowmeter bulkier and more expensive than the mechanical meter. For these reasons, the electromagnetic water meter is used for large bore water meters especially for the distribution network or on industrial sites rather than for the small bore domestic water meter. Figure 1-11 shows the battery powered water meter for a large bore pipe from Siemens which has sizes from 25mm to 600mm and is able to operate for 6 years with an internal battery pack according to its specification.

The development of small bore domestic water meters using the electromagnetic technique operated by internal battery was presented by Kent Meters Limited in 1997 under UK patent GB2324606A. An exploded drawing of the meter is shown in Figure 1-12. This meter is specifically designed as a domestic water meter and has a more compact size than the common electromagnetic water meter which uses external power. A further literature review of the electromagnetic sensing technique is described in the next chapter.

1.3.2 Ultrasonic meters

There are two primary types of ultrasonic meter, the Doppler flowmeter which measures the flow of liquids by Doppler-shifted reflections off particles or bubbles in the liquid, and the transit time flowmeter which measures the time of pulses of ultrasound being transmitted across the pipe at an angle and being received at the opposite transducer. In water metering, only the transit time ultrasonic method is used since the level of particles is low and indeterminate. It would therefore be

difficult for the meter to continue to operate with the required accuracy over the required flow range.

Figure 1-14 shows the principle of the transit time ultrasonic flowmeter. If two transducers are facing across a flow tube with axial distance x, the distance between transducers L and the angle between acoustic path and meter axis θ, then transit time from upstream transducer to downstream is:

$$t_{ud} = \frac{L}{C + v\cos\theta} \tag{1-6}$$

The transit time from downstream transducer to upstream is described as:

$$t_{du} = \frac{L}{C - v\cos\theta} \tag{1-7}$$

where C is the velocity of sound in the liquid and v is the velocity of the liquid. From equations (1-6) and(1-7), the velocity is described as:

$$v = \frac{L}{2\cos\theta}\left(\frac{t_{du} - t_{ud}}{t_{du}t_{ud}}\right) \tag{1-8}$$

Equation (1-8) can be rewritten in simple form because $v^2cos^2\theta$ is much smaller than C^2 as:

$$v = \frac{C^2}{2L\cos\theta}\left(t_{du} - t_{ud}\right) \tag{1-9}$$

Figure 1-15 shows different locations of ultrasonic transducers and blocks (Baker, 2002). At low flowrates in a small bore flow tube, the transit time differences

become difficult to measure so that multiple reflection or axial configuration are more commonly used. The lower picture in Figure 1-15 presents the axial configuration of the ultrasonic water meter which is for the small bore pipe. Although the axial configuration is very efficient to secure a long acoustic path to measure low flowrates, bends at the inlet and outlet can disturb flow profile and generate measuring errors when the flowrate changes as a consequence of the effective length of flowmeter, as opposed to the geometric distance between the transducers, which changes with flowrate.

Ultrasonic meters are currently not commonly used as domestic water meters because the manufacturing cost is still high so that the ultrasonic water metering technique is used for domestic heat metering as the sale price is higher than for the water meter. Figure 1-16 shows the domestic heat meter using the ultrasonic method from Hydrometer, Germany. This meter has ultrasonic transducers in the middle of the flow tube. The configuration of this meter can cause flow disturbance around transducers and a greater pressure drop than the common ultrasonic flow meter configuration.

To resolve this geometry issue, the axial ultrasonic flowmeter was presented by Sanderson in 2005 under UK patent, GB 2423363A. Sanderson's meter has ring type transducers at the inlet and outlet and does not disturb any flow profile. Figure 1-17 shows Sanderson's flowmeter configuration. This configuration provides averaging of the velocity profile irrespective of the flow profile and thus shows no change in sensitivity as the flow profile changes from laminar to turbulent (Sanderson, 2005). It achieves this performance by being a long wave acoustic flowmeter in which the wavelength of the ultrasound is greater than the pipe diameter, thus producing a plane wave which provides accurate velocity profile averaging as long as the profile remains axi-symmetric.

1.3.3 Fluidic oscillator

Figure 1-18 shows a typical feedback type fluidic oscillator with three possible locations of sensing (Sanderson, 1994). This fluidic oscillator can pick up the signal near the splitter post, feedback channels or exit channel. The flow within the fluidic oscillator enters the diffusing section through a jet region. The jet attaches itself to one of the walls of the diffuser because of the Coanda effect as described by Kadosch (1967). If it attaches itself to the upper wall of the diffuser, flow is entrained in the upper feedback channel.

The flow at the outlet of the feedback channel is entrained in the separation bubble between the jet and the diffuser wall, causing the jet to move away from wall. When the jet meets the splitter post, the separation bubble bursts and then switching across to the lower diffuser wall is speeded up. This operation of fluidic oscillator is shown in Figure 1-19.

This oscillation between diffuser walls continues while flow is present and its frequency is proportional to the rate of flow through the chamber and given by

$$f = S_r \frac{v}{w} \tag{1-10}$$

where f is the frequency of oscillation, S_r is the Strouhal number, v is the jet velocity and w is the jet width. If the Strouhal number is a constant over a flow range then the flowrate is proportional to the frequency of oscillation.

Sensing of the oscillation frequency is carried out using the electromagnetic technique as described by Sanderson and Heritage (1989) and Furmidge and Sanderson (1993). The fluidic oscillator water meter has permanent magnets but the oscillation switches the flow to enable a constant magnet field to be used The signal processing of the flow signal is implemented using a low power microprocessor and an integrated circuit which can be used for up to 10 years without maintenance.

Figure 1-20 shows the water meter using the fluidic oscillator technique manufacturing by Severn Trent Metering Services, Chesterfield, UK. The fluidic oscillator does not have any moving parts to measure the flow but the structure of the flow chamber is complicated in order to generate the jet and the oscillation so that it may drop in line pressure. Only a small proportion of power is needed to amplify and process the signal generated by the oscillation and to display the totalised flow. With a fluidic oscillator it is possible to maintain accuracy to ensure the performance of the meter for life-long application.

1.4 Performance requirements for water meters

The performance of water meters and testing methods are regulated by the government of each country. If the regulations of each country are different then water meter manufacturers manufacturing for international markets have to manufacture different water meters to different specifications to satisfy those regulations. For that reason, an international standardisation of regulations of water meter has been developed.

In this section, the recommendation of water meters by the international organisation of legal metrology (Organisation Internationale de Métrologie Légale, OIML) is reviewed and summarised from OIML R49-1 for the metering of cold potable water and hot water.

1.4.1 OIML Recommendation

The International Organization of Legal Metrology (OIML) is an intergovernmental treaty organisation whose membership includes Member States, countries which participate actively in technical activities, and Corresponding Members, countries which join the OIML as observers. It was established in 1955 in order to promote the global harmonisation of legal metrology procedures. Since that time, the OIML has

developed a worldwide technical structure that provides its Members with metrological guidelines for the elaboration of national and regional requirements concerning the manufacture and use of measuring instruments for legal metrology applications.

The OIML develops model regulations, International Recommendations, which provide Members with an internationally agreed upon basis for the establishment of national legislation on various categories of measuring instruments. Given the increasing national implementation of OIML guidelines, more and more manufacturers are referring to OIML International Recommendations to ensure that their products meet international specifications for metrological performance and testing.

The recommendation for the water meters intended for the metering of cold potable water and hot water is specified to R49-1 (Metrological and technical requirements) and R49-2 (Test methods).

1.4.2 Definition of characteristics of water meters

According to the recommendations from OIML, the flow characteristic of the water meter is defined by the values of Q1, Q2, Q3 and Q4. Minimum flowrate, Q1 is the lowest flowrate at which the water meter is required to operate within the maximum permissible error. Transitional flowrate, Q2 the flowrate which occurs between the permanent flowrate Q3, and the minimum flowrate Q1, that divides the flowrate range into two zones, the upper flowrate zone and the lower flowrate zone, each characterised by its own maximum permissible error. Permanent flowrate, Q3 is the highest flowrate within the rated operating conditions, at which the water meter is required to operate in a satisfactory manner within the maximum permissible error. Flowrate is expressed in m3/h in the OIML recommendation. Overload flowrate, Q4 is the highest flowrate at which a water meter is required to operate, for a short period of time, within its maximum permissible error, whilst maintaining its

metrological performance when it is subsequently operated within its rated operating conditions.

A water meter can be designated by a numerical value of Q3 and the ratio of Q3 to Q1. Q3 must be selected one of the specified list shown in Table 1-1 and expressed in m3/h. The value of Q3/Q1 must be one of numbers in Table 1-2. The ratio Q2/Q1 must be 1.6 and the value of Q4/Q3 must be 1.25 (OIML R49-1 Edition 2006).

Table 1-1 List of value of Q3 in m^3/h (OIML R49-1, 2006)

1	1.6	2.5	4	6.3
10	16	25	40	63
100	160	250	400	630
1000	1600	2500	4000	6300

Table 1-2 List of value of Q3/Q1 (OIML R49-1, 2006)

10	12.5	16	20	25
31.5	40	50	63	80
100	125	160	200	250
315	400	500	630	800

Water meters also must be designated as accuracy class 1 or accuracy class 2. Accuracy class 1 specifies the maximum possible error for the upper flow zone ($Q2 \leq Q \leq Q4$) is $\pm$ 1% for temperatures from 0.3˚C to 30˚C, and $\pm$ 3% for

temperatures greater than 30˚C. The maximum permissible error for the lower flowrate zone (Q1 ≤ Q ≤ Q2) is ± 3%. Accuracy class 1 is applied only to water meters with Q3 is equal or greater than 100 m^3/h.

The maximum permissible error for the upper flow zone (Q2 ≤ Q ≤ Q4) is ± 2% for accuracy class 2, when temperatures are between 0.3˚C to 30˚C, and ± 3% for temperatures greater than 30˚C. The maximum permissible error for the lower flow zone (Q1 ≤ Q ≤ Q2) is ± 5%. Accuracy class 2 can be applied to all water meters with Q3 is less than 100 m^3/h and may be applied to water meters with Q3 is equal to or greater than 100m^3/h.

1.5 Target Performance

In this thesis, the flowmeters are only concerned with Q3 is less than 3 m3/h so that the water meter is to be tested under the specification for accuracy class 2. The meter performance of the mechanical water meter, for example, Class D V100 (PSM-T) rotary piston meter from Elster Metering the size of which is 15 mm, is Q1 = 11.25 l/hr, Q2 = 17.25 l/hr and Q3 = 1.5 m^3/hr and Q1 = 10 l/hr, Q2 = 18 l/hr and Q3 = 1.5 m^3/hr for M100, i.e. the multi-jet water meter. The ratio of Q3 and Q1 is 133 and 150 for these meters (adapted from product specifications).

Based on the meter performance of mechanical water meters, the target performance of the meters studied in this thesis is defined as Q3 is 1.6 m^3/hr and the ratio of Q3 and Q1 is 200. Implementing OIML R49 recommendations, Q1 is 8 l/hr, Q2 is 12.8 l/hr and Q4 is 2 m^3/hr. This target performance is better than the class D mechanical meter performance which was used to classify water meter performance in previous regulations. The comparison of meter performance of mechanical meters and target performance is shown in Table 1-3 and the chart in Figure 1-21.

Table 1-3 Meter performance comparison

	Rotary piston meter	*Multi-jet meter*	*Target performance*
Q_1	11.25 l/hr	10 l/hr	8 l/hr
Q_2	17.25 l/hr	18 l/hr	12.8 l/hr
Q_3	1.5 m^3/hr	1.5 m^3/hr	1.6 m^3/hr
Q_4	3 m^3/hr	3 m^3/hr	2 m^3/hr
Q_3/Q_1	133	150	200
Q_2/Q_1	1.53	1.8	1.6

1.6 Power Consumption and Running Time

Another important issue of the performance of the non-mechanical water meter is that the meter has to have a power source so that power consumption and running time without changing the battery are issues of concern. There are two possible approaches to solve these problems, one is to use a higher capacity battery, the other to reduce power consumption.

Among all the different kinds of battery, the Lithium Thionyl Chloride battery ($Li/SOCl_2$) is commonly used for this application. Lithium-thionyl chloride cells have an anode in metallic lithium (the lightest of the metals) and a liquid cathode comprising a porous carbon current collector filled with thionyl chloride ($SOCl_2$). They deliver a voltage of 3.6V and are cylindrical in shape, in 1/2AA to D format, with spiral electrodes for power applications and bobbin construction for prolonged discharge.

Lithium-thionyl chloride cells have a high energy density, partly because of their high nominal voltage of 3.6V. Bobbin versions can reach 1220 W·hour/L and 760 W·hour/kg, for a capacity of 18.5 Ah at 3.6 V in D format. Because self-discharge is extremely low (less than 1% per year), this kind of cell can support long storage periods and achieve a very long service life

For different applications, the cells can be fitted with various types of connectors and assembled in various battery arrays, including a number of standardised versions.

This battery can operate down to -55˚C but the capacity is reduced then by 50% of that at normal temperature. The battery is classified by its nominal size as AAA, AA, C, D type. AA type Lithium Thionyl Chloride battery has 2.4 Ah capacity, C type cell has 8.5Ah capacity and D type battery has 19.0 Ah capacity (adapted from Tardiran products specifications).

To run the electromagnetic meter for 10 years, which is required by UK regulations, the power consumption must be lower than 27 μW with a 3.6V battery but this power limitation can be increased to 216 μW when the meter uses a D type battery having 19.0Ah capacity,

1.7 Layout of this thesis

Water meters, especially those used for domestic water metering, have been described in this chapter; additionally, the recommendation of water meters has also been reviewed in order to define the performance of target meters.
To achieve the target performance, modelling of the various flowmeters using the electromagnetic sensing technique is to be undertaken as described below.

Chapter 2 provides a literature review of the electromagnetic flow meter, the alternative method for a coil-less electromagnetic flowmeter, and fluidic oscillator.

Chapter 3 describes the test rig in PASE lab, Cranfield University and instrumentation for the experiments used in this work.

Chapter 4 covers the conventional electromagnetic flowmeter, which uses a coil for a magnetic source. The modelling of this flowmeter is used to simulate the flow signal at a given flowrate. This chapter also covers the improvement of the meter performance in terms of energy consumption and meter characteristics by changing the meter design.

Chapter 5 describes the alternative electromagnetic flowmeter using permanent magnets as its magnetic source. The coil-less electromagnetic flowmeter proposed uses a magnetostrictive material named Terfenol-D. The simulation of Terfenol-D is undertaken in this chapter. Changing the magnetic field by means of a mechanical actuator is also studied. This operates by changing the length of air gap.

In chapter 6, the modelling of the fluidic oscillator is carried out. The modelling is used to improve the quality of flow signal as well as the quantity. The electrodes' position and number of permanent magnets are changed for the improvements.

Finally, the results of this work and the further works are discussed in chapter 7.

Table 1-4 Comparision of major functional specification for flow measurement techniques, (Sanderson and Spendal, 1987)

Measurement Technique	Meet Accuracy Spec.	Power Requirement	Head Loss	Moving Part	No Obstacle	Velocity Profile Sensitivity	Cost
Turbine Meter	N	<96mW		N	N	Swirl Sensitive	Average
Fluidic Oscillator	N/A	<96mW	3 velocity heads	Y	N	Medium	Low
Electromagnetic Flowmeter	N/A	>480mW	0	Y	Y	Low	High
Ultrasonic Flowmeter	N	200-300mW	0	Y	Y	Medium	High

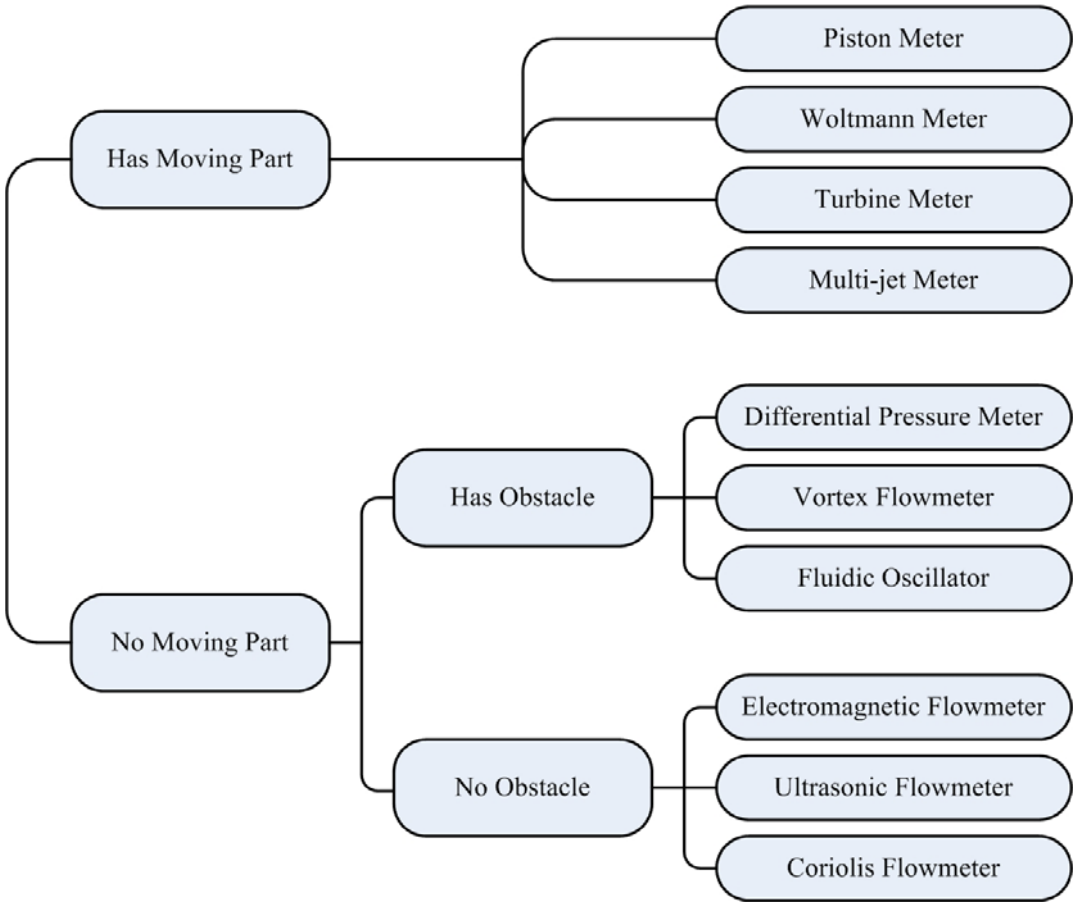

Figure 1-1 Type of flowmeters

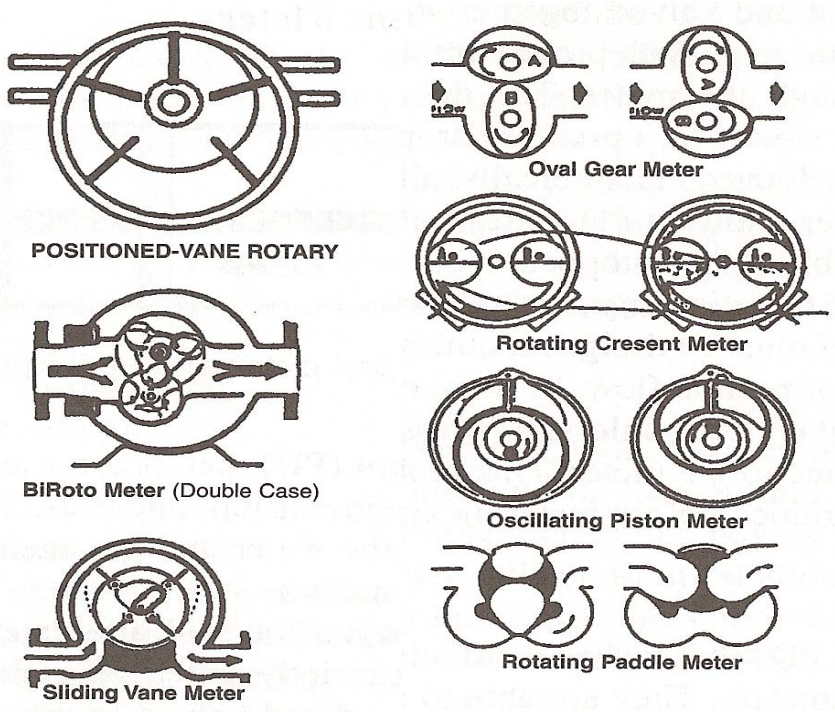

Figure 1-2 Major types of positive displacement meters (Upp and LaNasa, 2002)

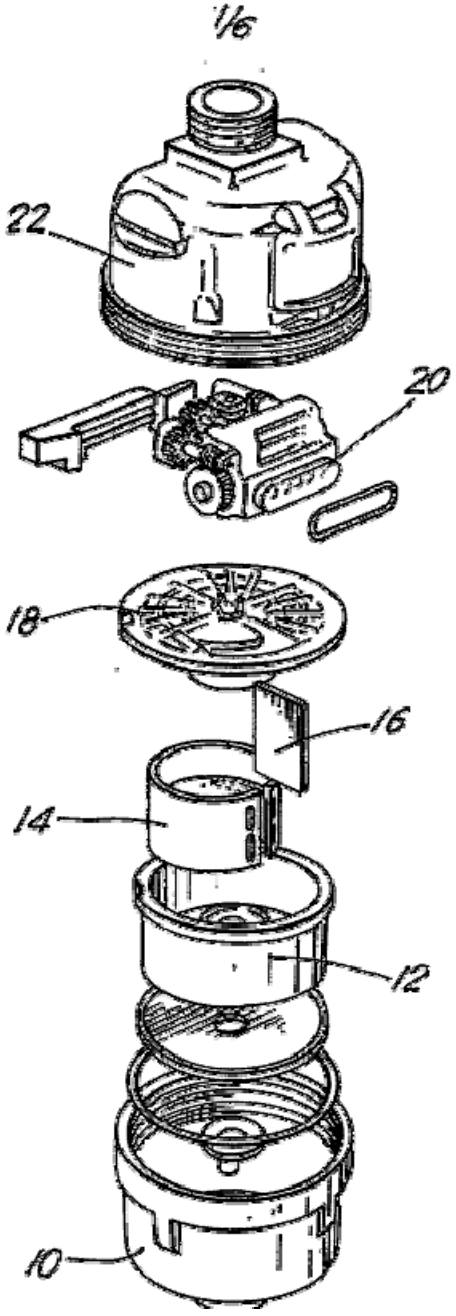

Figure 1-3 An exploded view of a known volumetric piston water meter (Barros *at el*, 1993)

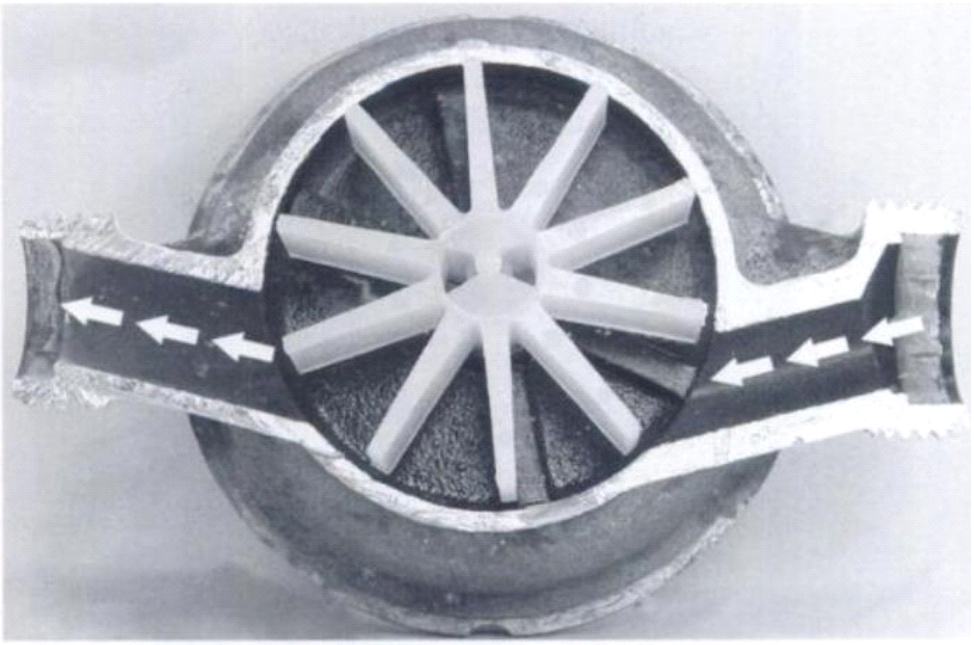

Figure 1-4 Operating principle of a single jet meter (Arregui *et al.*, 2007)

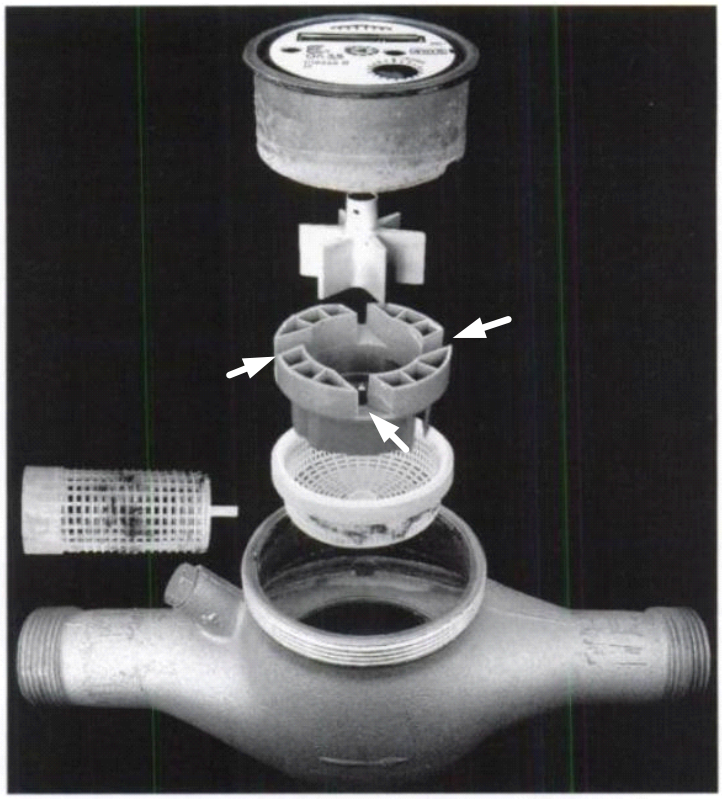

Figure 1-5 Exploded view of a multi-jet meter (Arregui *et al.*, 2007)

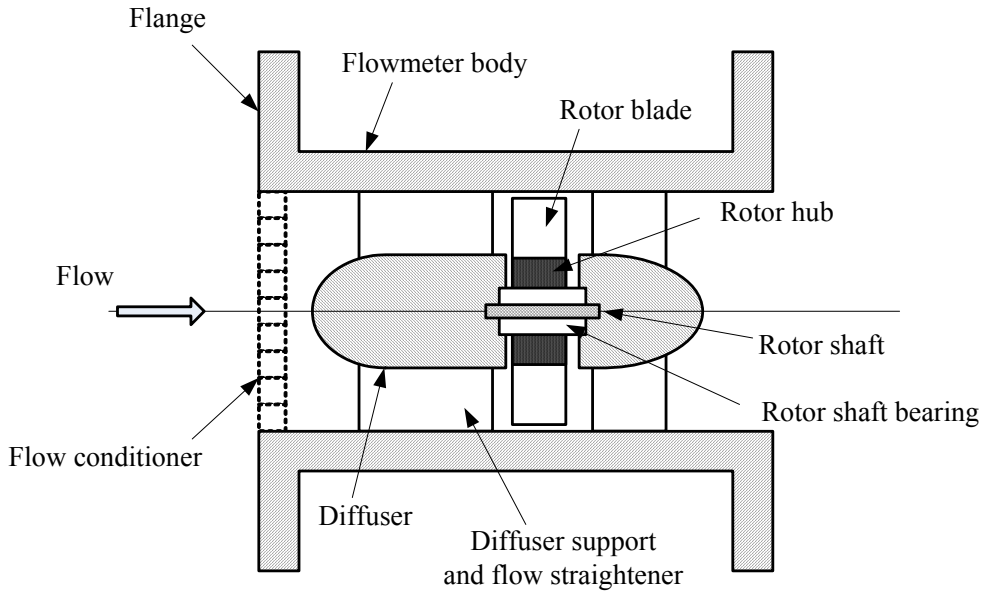

Figure 1-6 A cross-sectional view of a turbine meter depicting the key component

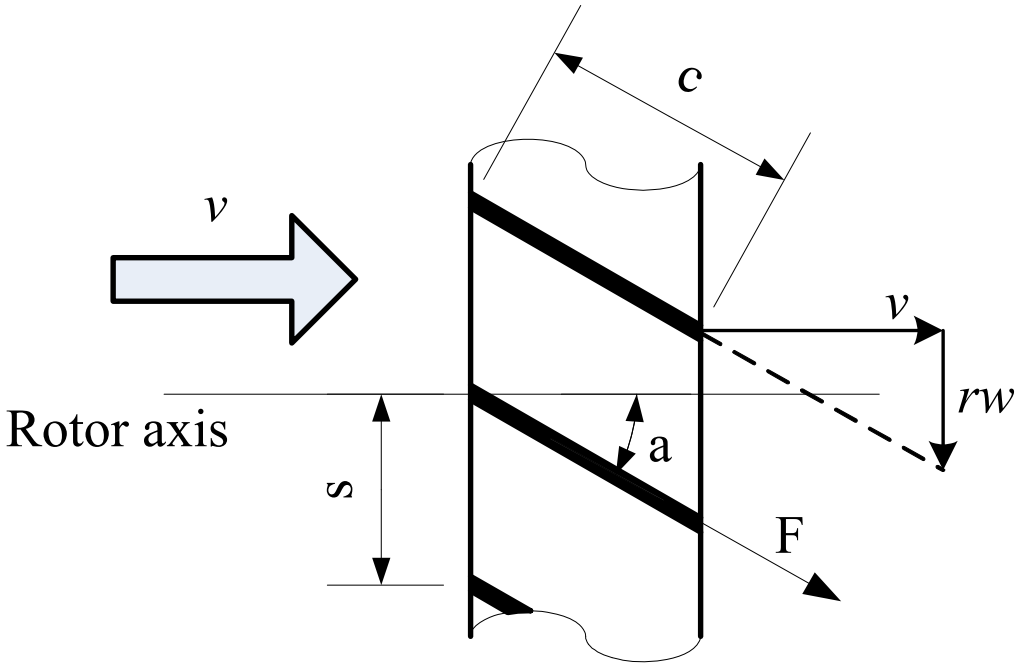

Figure 1-7 Vector diagram for a flat-bladed turbine rotor

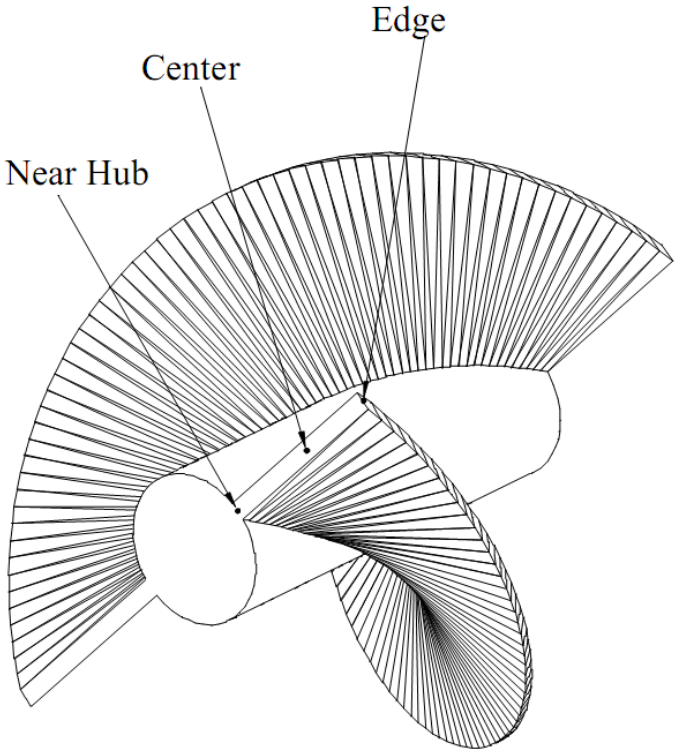

Figure 1-8 A helical blade (adapted from web source from Faure Herman Meter Inc.)

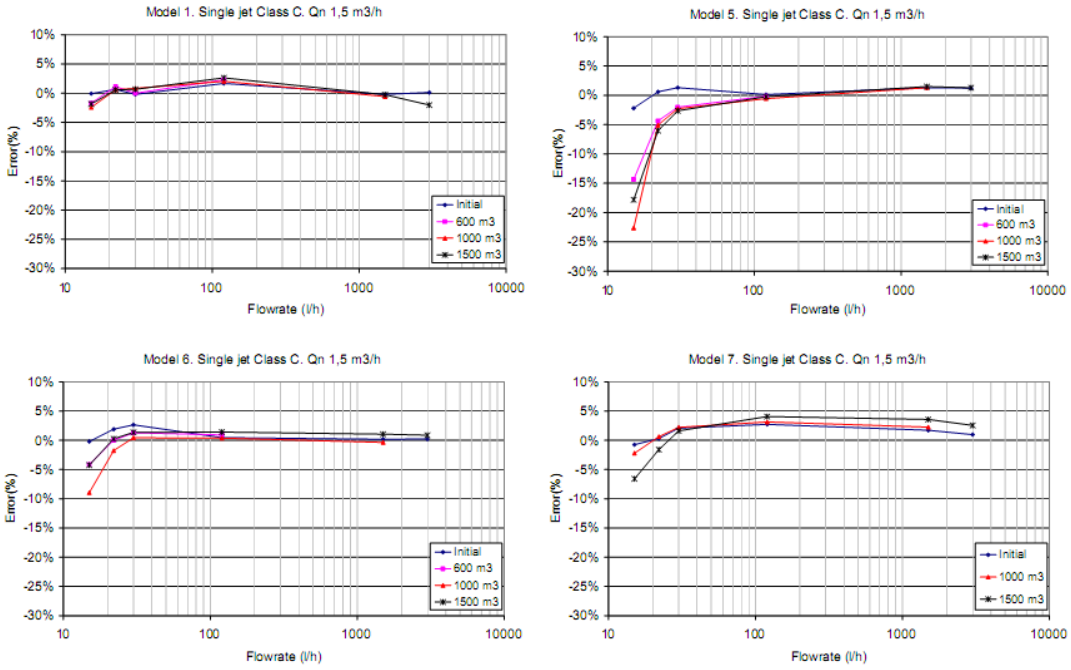

Figure 1-9 Fatigue tests performed for single jet water meters (Arregui *et al.*, 2005)

Figure 1-10 Limescale build-up in the inside of a single jet meter (Arregui *et al.*, 2005).

Figure 1-11 The battery powered electromagnetic flowmeter from Siemens (adapted from SITRANS F MAG 8000 Manual)

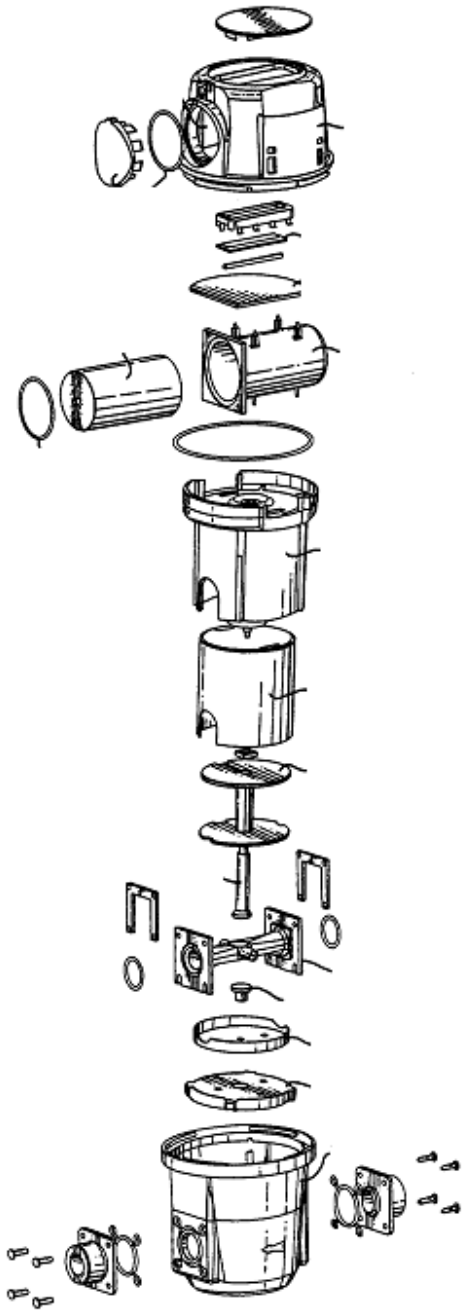

Figure 1-12 The exploded view of battery powered electromagnetic water meter for domestic meter (ABB, 1997)

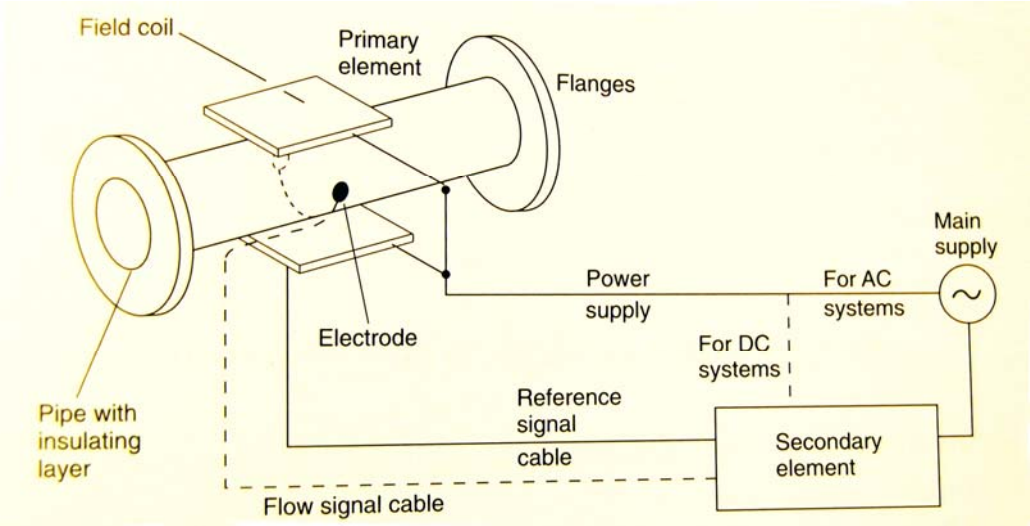

Figure 1-13 Diagram of an electromagnetic with the primary and the secondary element (Baker, 2002)

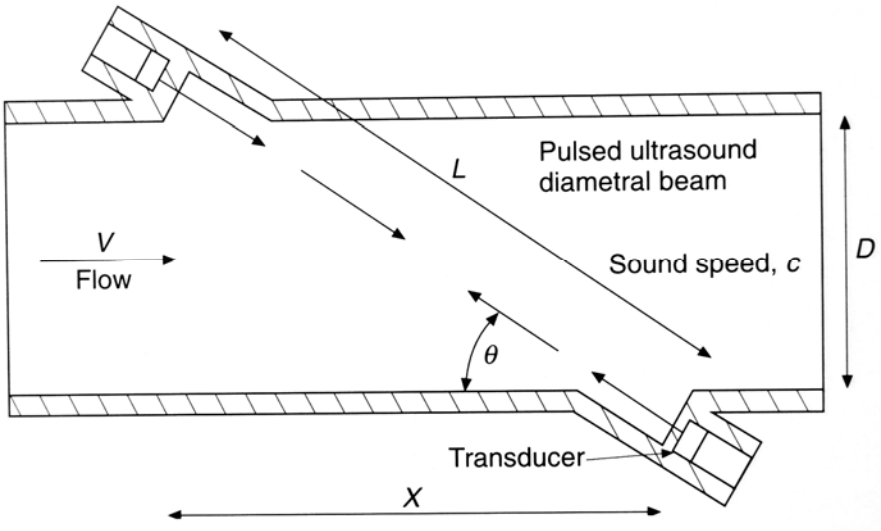

Figure 1-14 Ultrasonic transit time flowmeter (Baker, 2002)

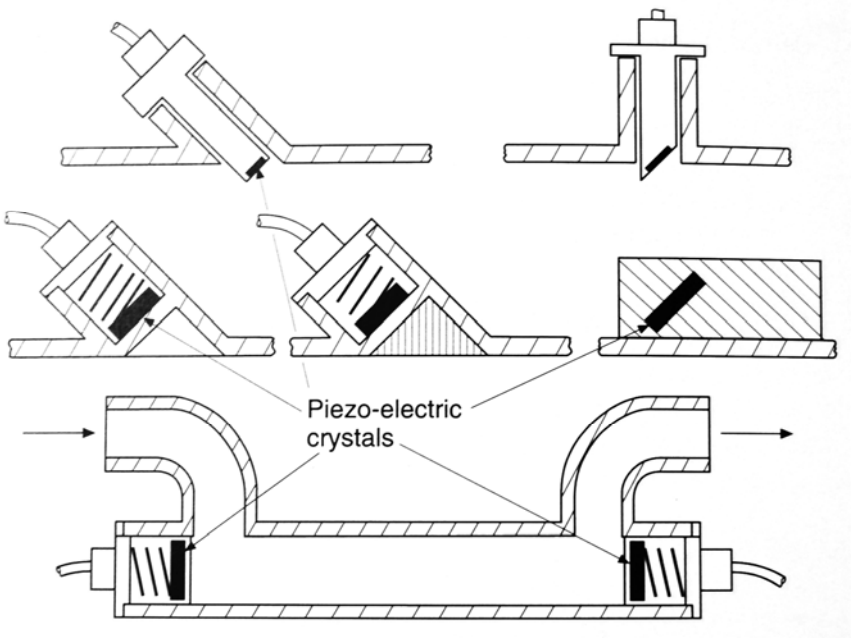

Figure 1-15 Different locations of ultrasonic transducers (Baker, 2002)

Figure 1-16 Ultrasonic heat meter (adapted from Hydrometer product catalogue)

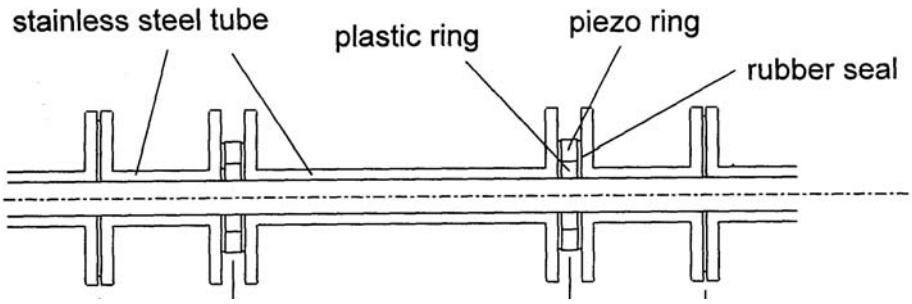

Figure 1-17 The configuration of Sanderson's axial ultrasonic flowmeter (Sanderson, 2005)

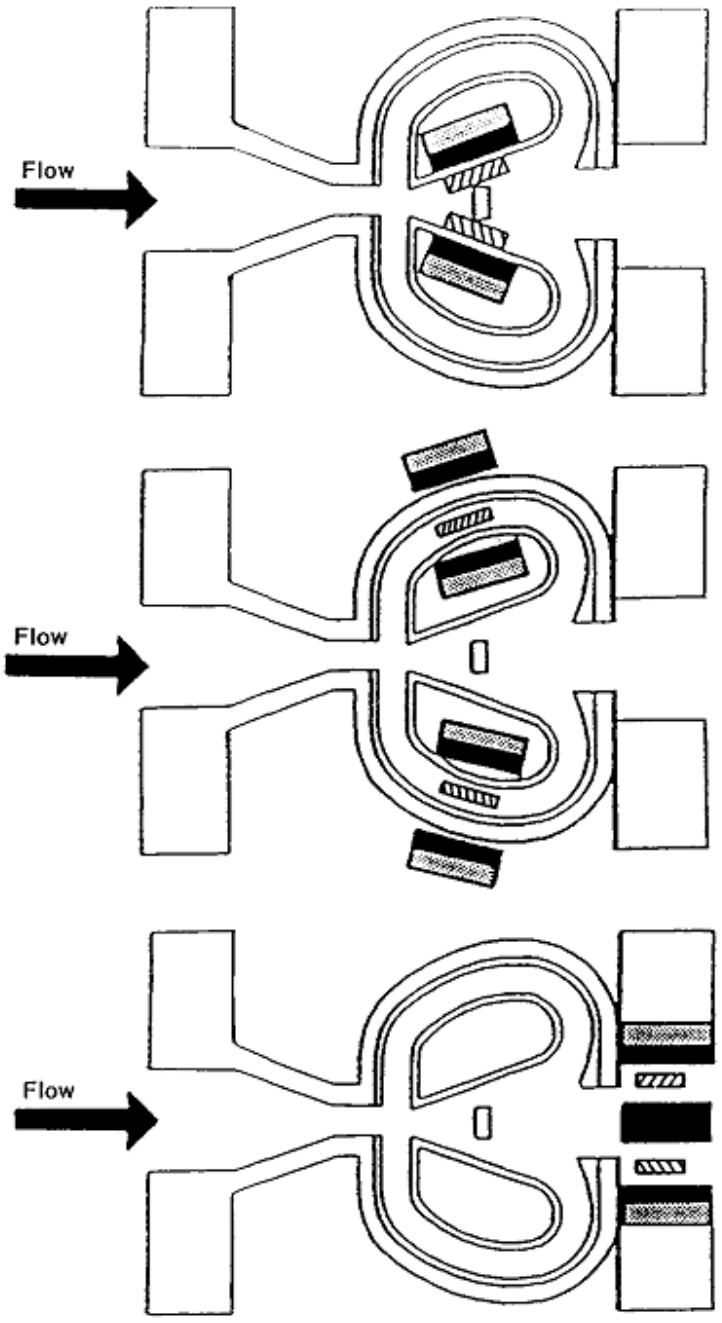

Figure 1-18 The configuration of fluidic oscillator with different location of sensing (Sanderson, 1994).

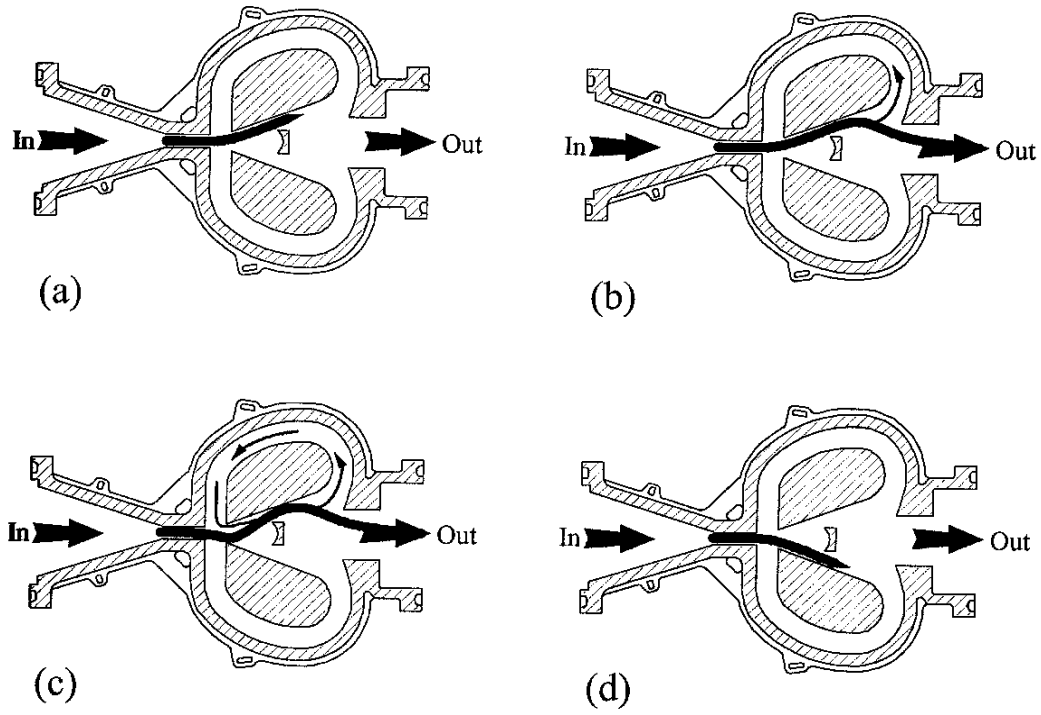

Figure 1-19 Operation of the fluidic oscillator water meter (Sanderson 1994)

Figure 1-20 The water meter using the fluidic oscillator technique
(adapted from the product catalogue of Severn Trent Metering Service)

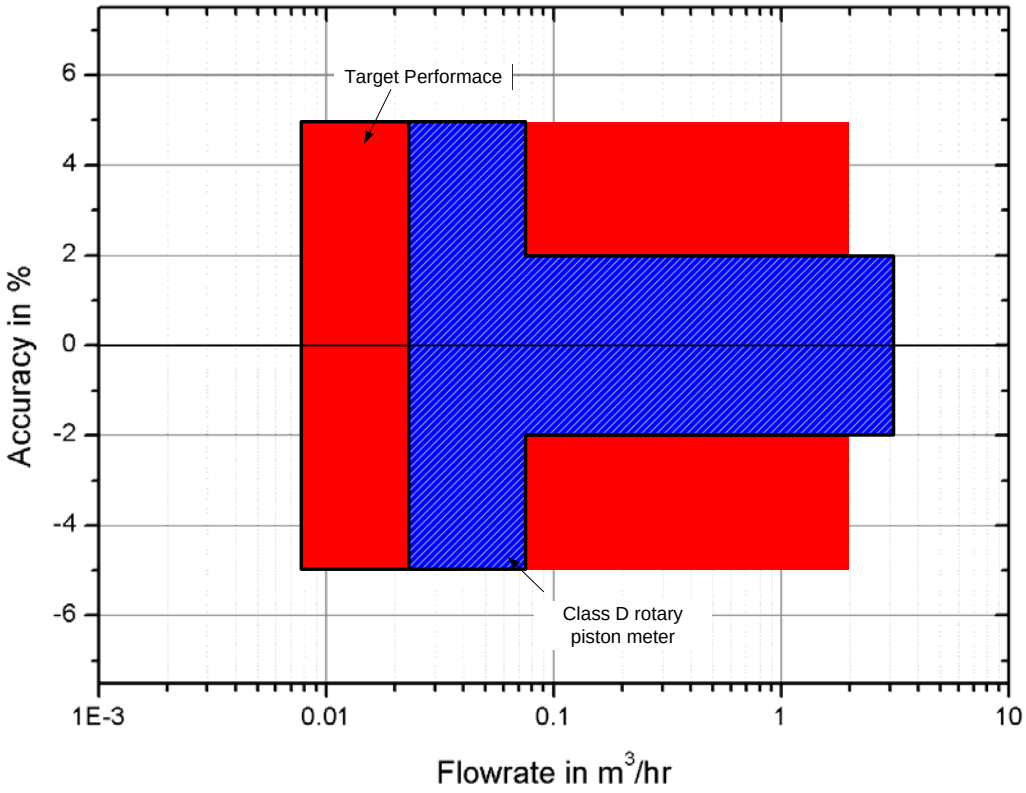

Figure 1-21 Comparison of meter performance of target water meter and the Class D rotary piston mechanical water meter

Chapter 2. Literature review

2.1 Introduction

This chapter provides the literature reviews for three electromagnetic sensing techniques for the conventional electromagnetic flowmeter, the coil-less flowmeter and fluidic oscillator.

In the conventional electromagnetic flowmeter section, the historical review of the electromagnetic flowmetering and the principle of electromagnetic flowmeter are considered. In the following section, the alternative methods for measuring the flow using the electromagnetic technique but not using coils are reviewed. The methods have permanent magnets as a constant magnetic source so a mechanical actuator or a magnetostrictive material is considered to control the magnetic field. A piezoelectric actuator is reviewed as a suitable actuator in terms of low power operation.

The fluidic oscillator is another major part of this thesis so the historical review and its theory are reviewed in the last section of this chapter. The fluidic oscillator is the most power-efficient flowmeter because it does not have any moving parts or electrical devices to measure the flow.

2.2 Conventional electromagnetic flowmeter

2.2.1 History of electromagnetic theory

This section is mainly summarised from Shercliff's book published in 1962 and a literature review by Amare (1995).

The flowmeter using the electromagnetic sensing technique is one of the most commonly used flowmeters in many industries, which has been successfully and accurately used to measure a liquid mean velocity. It has no pressure drop and a fast response time to the change of flow.

The principle of the electromagnetic flowmeter is based on the fact that a voltage is induced between the ends of a conducting material such as a wire when it moves through a magnetic field in a direction right-normal to the magnetic field direction. This effect was revealed by Michael Faraday in 1832 and is known as 'Faraday's Law' to explain the relationship between the electromotive force, the change of magnetic flux density and movement of material in a magnetic field.

Faraday's attempt to measure the flow velocity of the river Thames at Waterloo Bridge by detecting the voltage across the river which occurred by the earth's magnetic field failed because the river bed would short-circuit and the signals which Faraday had detected were flow induced signals plus spurious ones due to electrochemical and thermoelectric signals. These were all picked up together and thus it was not possible to separate the flow induced signals from the non-flow induced signals. Almost 20 years passed before Wollaston measured the induced voltage in the English Channel in 1851.

Wilson proved in 1904 that Faraday's law was equally applicable to dielectric materials by experimental measurements of the induced current in an ebonite cylinder rotating in a magnetic field. Wilson found this current was predicted correctly by Faraday's law of induction.

By patenting a scheme for finding the speed of ships using the electromagnetic method by Smith and Slepian in 1917, the measuring method using an emf in a magnetic field started to be used practically. Smith and Slepian installed two electrodes on the hull and placed a magnet on the bottom of the ship then measured the induced voltage by relative speed between ship and sea water. They tried an alternating magnetic field to remove signal losses from the polarisation of electrodes.

Williams applied the electromagnetic technique to measure the flow of copper sulphate solution through a circular glass pipe under the uniform transverse magnetic field in 1930. This is the first work of the electromagnetic flowmeter design similar to the industrial instruments used more recently. Figure 2-1 shows an electromagnetic flowmeter having a transverse magnetic field. A dc signal was measured between the two electrodes and the signal was proportional to the flow. Williams derived the equation for magnitude of voltage between electrodes in the case of a pipe in a uniform magnetic field and the induced voltage was independent of the flow distribution when the distribution was axially symmetric.

Fabre was the first scientist to develop many ideas for the electromagnetic flowmeter. He made it capable of being used in the medicine field to measure the flow of arterial blood because the electromagnetic sensing technique gave very fast response times which allowed accurate measurement of the pulsating flow, and a non-invasive design of the flowmeter ensured no obstruction structure. The blood flow could be measured in two ways: either by cutting a blood vessel and connecting it to the ends of a flow tube (a cannulated flowmeter), or by placing a whole blood vessel between the poles of a magnet with electrodes on the outside (a cuff flowmeter). Fabre noted that a cuff-type flowmeter was possible in 1932.

Kolin described a similar apparatus using non-polarisable electrodes in a steady magnetic field in 1936 and, with Katz, used ac sinusoidal excitation for the magnetic field to avoid polarisation problems in 1938 firstly because non-polarisable electrodes were inconvenient and secondly because of the problems occurring in amplifying small constant potentials. This technique generated an alternating flow signal produced by flow and the alternating sinusoidal magnetic field, and it was able to be amplified and rectified producing a dc signal proportional to the flow rate with an accuracy and stability better than before.

However, one of the difficulties in the design of an electromagnetic flowmeter is that the magnitude of the flow signal is small compared with those of various other noises. The main sources of noise are a transformer electromotive force and a power leakage caused by capacitive and resistive coupling between the power and signal circuits. To avoid error from the transformer, Kolin used a coil with a few turns to compensate the transformer electromotive force and this is still being used by some meter manufacturers. The electrochemical voltage potential between the electrodes and the liquid is another source of noise for the electromagnetic sensing technique, or if the liquid contains solids as slurry then the solids may hit the electrode surface. This hit can break the oxidation layer on the surface of the electrode which then induces spiky voltage potential on the electrode surface.

As an alternative, Denison and Spencer devised a way to solve the problems by changing the excitation wave-form by supplying square-wave current to coils in 1955 and Yanog and Salz used a trapezoidal wave in 1960 for the same reason.

In 1954, Shercliff presented ‘weight function, W’ to express the degree of the contribution of the fluid velocity to the signal in the cross-section of a conduit and used the technique for the flow measurement of liquid metal in nuclear power stations.

The concept of the weight function was extended by Bevir. Bevir extended the weight function to the weight vector $W = B \times j$ in three dimensions using the concept of virtual

current j in 1970. The virtual current was defined as the current set up in the liquid when the unit current went through between electrodes. Using the virtual current, Wyatt and O'Sullivan presented the rectilinear weight functions for different shape, size and number of electrodes for rectilinear flow profile in 1983.

Vincent Cushing presented the theory of the dielectric liquid flow measurement using the electromagnetic sensing technique in 1961 and went on to design the meter which could measure the flow of conducting and insulating liquids using wide area electrodes in a capacitive pickup configuration in 1965. In order to reduce the effect of eddy current on his design, he used created electrodes with fine wires. Hence Cushing's design only operated under conditions of axisymmetric flow and uniform magnetic field. The electromagnetic flowmeter with point electrodes may be very sensitive to change of the non-axisymmetric flow profile therefore the improvement had been focused on resolving the meter characteristics.

Since Cushing's research, the electromagnetic sensing technique and design of the flowmeter has been improved rapidly. Hemp (1975) reported the improvement of the design of coils with point electrodes and provided a numerical calculation with an axisymmetric flow profile. The flowmeter design improved the meter characteristics significantly but the signal level also reduced and the coils had to be supplied with more power to obtain the same level of flow signal with the conventional design.

The capacitive coupled electromagnetic flowmeter was reported by Hofmann (1978), in which electrodes were insulated and designed not to make contact with liquid to avoid changing meter characteristics by fouling and rust on the electrodes. Cox and Wyatt (1984) improved the insulated large electrode flowmeter which was independent of the flow profile. Amare (1999) also improved the capacitive coupled electromagnetic flowmeter with specially designed electrodes to reduce the effect from eddy currents.

2.2.2 The principle of electromagnetic flowmeter

Figure 2-2 shows an electromagnetic flowmeter with a circular flow channel and point electrodes. The z axis coincides with the axis of the flowmeter channel and the x axis passes through the centre of the electrodes. Flow is regarded as positive when it occurs in the positive z direction. With respect to cylindrical coordinates, (r, θ, z), the tube wall is located at $r = b$.

When the conductive fluid moves in a magnetic field at right angles to the direction of motion an electromotive force will be generated in a perpendicular direction both to the flow and the magnetic field and in proportion to flow velocity and magnetic flux density. The voltage between electrodes is given by:

$$e = B \cdot l \cdot v \tag{2-1}$$

where, B is magnetic flux density in Tesla, l is the distance between a pair of electrodes in m and v is flow velocity of m/s. If the flow channel has cross-section area A in m^2 and q is flowrate in m^3/s then equation (2-1) is written as:

$$e = \frac{B \cdot l \cdot q}{A} \tag{2-2}$$

In the case of a rectangular channel with the height of h and width of l, equation (2-2) is given by

$$e = \frac{B \cdot q}{h} \tag{2-3}$$

This is the basic equation for the electromagnetic flowmeter and it is valid when the magnetic field is uniform However, there are several limitations to this simple theory and

Shercliff (1962) provided a complete theory of electromagnetically induced flow signals. He assumed that the fluid would obey Ohm's Law as well as being non-magnetic and have the same permeability μ as a vacuum and a reasonably low conductivity so that the current flow is proportional and parallel to the electric field referred to axes moving with the fluid motion and given by:

$$\boldsymbol{J} = \sigma(\boldsymbol{E} + \boldsymbol{v} \times \boldsymbol{B}) \tag{2-4}$$

where $\boldsymbol{J}$ is the current density vector, σ is the fluid conductivity and $(\boldsymbol{E}+\boldsymbol{v}\times\boldsymbol{B})$ is the electric field that is relative to the velocity, where $\boldsymbol{E}$ is the electric field in the stationary co-ordinate system, $\boldsymbol{v}$ is the fluid velocity and $\boldsymbol{B}$ is the magnetic flux density. The term $\mathbf{v}\times\mathbf{B}$ represents the emf induced by the fluid motion and **E** is due to charges distributed in and around the fluid and to any variation of the magnetic field in time.

If we can assume steady conditions then

$$\nabla \times \boldsymbol{E} = 0 \tag{2-5}$$

$$\nabla \times \boldsymbol{B} = \mu \boldsymbol{J} \tag{2-6}$$

are given by Maxwell's equations by excluding the self-inductance terms $\partial B/\partial t$ and the displacement current $\partial D/\partial t$. Hence, the electric field can be written as the gradient of a scalar potential U as:

$$\boldsymbol{E} = -\nabla U \tag{2-7}$$

Consequently, equation (2-4) may be rewritten as:

$$\boldsymbol{J} = \sigma(-\nabla U + \boldsymbol{v} \times \boldsymbol{B}) \tag{2-8}$$

and taking the divergence of this equation (2-8) and noting the divergence of $\boldsymbol{J}$ is zero, we obtain:

$$\nabla^2 U = \nabla \cdot (\mathrm{v} \times \boldsymbol{B}) \tag{2-9}$$

The right hand side of equation (2-9) may be expanded by vector identity:

$$\nabla^2 U = \boldsymbol{B} \cdot \nabla \times \boldsymbol{v} - \boldsymbol{v} \cdot \nabla \times \boldsymbol{B} \tag{2-10}$$

in which the last term may be neglected if the magnetic field is not seriously affected by induced current in the fluid and curl $\boldsymbol{B}$ is zero. Hence the non-zero part of equation (2-10) will be due to currents induced in the fluid by the motion, so equation (2-9) may be rewritten as:

$$\nabla^2 U = \boldsymbol{B} \cdot \nabla \times \boldsymbol{v} \tag{2-11}$$

which is known as the flowmeter equation.

2.2.3 Weight function

Shercliff (1962) suggested a means of predicting the effect of distorted profiles using what he called a weight function. Figure 2-3 shows Shercliff's weight function for the flowmeter having a uniform magnetic field and point-electrodes. The weight function of an electromagnetic flowmeter determines how the induced electromotive forces within the flowmeter channel contribute to the meter output signal.

Consider an ideal flowmeter in which the output signal is caused by an electrically conducting fluid flowing with velocity v through a magnetic field B. The flow velocity is directed along the channel axis and there are no transverse components. The magnetic field

is perpendicular to the channel axis. All field lines are parallel and uniform. The signal electrodes lie in a line perpendicular to both the fluid velocity and the magnetic field and uniform magnetic field.

The output signal of the ideal electromagnetic flowmeter is given by the general integral

$$U = \int_{\tau} \mathbf{v} \times \mathbf{W} d\tau \qquad (2\text{-}12)$$

in which

$$\mathbf{W} = \mathbf{B} \times \mathbf{j} \qquad (2\text{-}13)$$

where $\boldsymbol{v}$ is the flow velocity at any point, $\boldsymbol{B}$ is the magnetic field and $\boldsymbol{j}$ is the virtual current which describes the current distribution set-up when a unit current is passed between the electrodes. The integration in equation (2-12) must be carried out over the entire volume of the liquid. $\boldsymbol{W}$ is called the weight function for the flow channel configuration.

The weight function is determined by the flowmeter geometry including the size and shape of the electrodes. Equation (2-13) is valuable since it gives a clear indication of the relative importance of flow in each region of the cross-section to the total signal. When $\boldsymbol{B}$ and $\boldsymbol{j}$ are defined, U can be calculated from equation (2-12) only if assumptions are made regarding the flow velocity $\boldsymbol{v}$.

Shercliff showed that the response to a point-electrode uniform magnetic field electromagnetic flowmeter, when subjected to an arbitrary rectilinear flow profile, could be represented by a weighing function W given by

$$W = \frac{a^4 + a^2(x^2 - y^2)}{a^4 + 2a^2(x^2 - y^2) + (x^2 + y^2)^2} \qquad (2\text{-}14)$$

where a is height of rectangular flow channel in 2-D and x, y is location from the Cartesian co-ordinate system. Bevir then showed that the necessary and sufficient conditions for an ideal flowmeter, i.e. one which measured the mean flow regardless of flow profile, was:

$$\nabla \times \boldsymbol{W} = 0 \qquad (2\text{-}15)$$

Equations (2-12) and (2-14) possess a generality beyond electromagnetic flow measurement. Bevir proposed a rectangular section flowmeter that satisfied equation (2-14) , and he carried out extreme tests to demonstrate its performance. The implication of equation (2-15) is that the ideal flowmeter should respond only to the mean flow and not to any variation in the velocity over the cross-section of the meter.

This requires the meter to have a uniform magnetic field which must be infinitely long, the flow tube should be a rectangular chamber and the electrodes should be either side of the rectangular chamber facing each other. The ideal flowmeter is shown in Figure 2-4

2.2.4 Sensitivity of flowmeter

A dimensionless quantity S can be defined to measure the performance or the calibration of an electromagnetic flowmeter in which the potential different U_{XY} induced between two electrodes X and Y is shown as:

$$S = U_{XY} / LBv_m \qquad (2\text{-}16)$$

where L is the distance between X and Y, B is scalar of magnetic flux density and v_m is a mean velocity (Shercliff, 1962).

If the magnetic field and the direction of velocity are all mutually perpendicular, where both B and the velocity v are rectilinear and uniform, and the walls of the flow channel are non-conducting, then U_{xy} is the same as LBv_m and then S is 1.0 (Shercliff, 1962).

However, in the case of an actual flowmeter, the magnetic field is finite and has edge regions where the field falls off gradually. Each fringe region will extend in the z-direction for a distance of the same order of magnitude as the magnetic gap.

Hartmann (1937) realised that where the field falls off, the induced emf in the fluid will also decrease, allowing short-circuit currents to flow at the edges of the field. Unless the electrodes X and Y are remote from the edges of the field, a significant fall in U_{XY} for a given flow rate will be produced by this process of 'end-shorting'. This was described by Sutton (1959) and Fishman (1959) as:

$$S = 1 - \frac{8}{\pi^2} \sum \frac{1}{n^2} \exp\left(- \frac{n \pi c}{L} \right) \qquad (2\text{-}17)$$

The summation is taken over all odd positive integral values of n and the length of coil is $\pm c$. In equation 2-17, abrupt edges of the field occur at $z = \pm c$ and the electrodes X and Y were at the middle of the length of flowmeter, where $z = 0$, as shown as Figure 2-5. The relationship between S and c/b (coil length/channel width) for a rectangular channel electromagnetic flowmeter is presented in Figure 2-6. The sensitivity S equal to 0.99 is reached for the ratio c/b=2.8. Thus, for c/b > 2.8 the influence of the side effects is negligible (Shercliff, 1962).

2.3 Electromagnetic flowmeter without coil

The conventional electromagnetic flowmeter uses coils to generate the magnetic field and control it by supplying an ac or pulsed dc waveform to the coils. The magnetic field is modulated to distinguish the flow signal from background chemical potential noise present on the electrodes.

If a constant magnetic field is applied on a flow tube, the flow signal is difficult to distinguish from an electrochemical signal. The electrochemical signal can appear as a result of a chemical reaction at the interface of liquid and electrode. The size difference or electrical difference between two electrodes generates the electrochemical signal so that the electrochemical signal problem may be solved by making two electrodes, ideally having the exactly same size and shape, but they cannot be made having exactly the same electrochemical properties (Cushing Associates, 1999).

The power consumption of the electromagnetic flowmeter using coils is not a serious problem in the case of using an external power source for the most industrial applications. But if an electromagnetic flowmeter is to be operated by an internal battery as with domestic water meters, the coil wastes most of the power in generating the magnetic field and maintaining that field during picking up the flow signal. As part of this thesis it is proposed to investigate the use of switched permanent magnetic fields.

For this reason, magnetic field controlling devices using a constant magnetic source as a permanent magnet are proposed and reviewed in this section, showing two ways of achieving the changing field. One of these is to control the magnetic field by a mechanical actuator to change the distance of an air gap in the magnetic circuit and the use of a magnetostrictive material which can change its magnetic properties by an external force.

2.3.1 Magnetic equivalent circuit

Before describing the devices, the magnetic equivalent circuit of the magnetic circuit in the flowmeter is to be developed first. The prediction of performance of electromagnetic devices is possible by analysing the magnetic field system using an exact solution. Numerical analysis of such fields is very difficult in that Maxwell's equation has to be applied and solved for the complex structures of practical devices. A simpler method of magnetic circuit analysis based on an analogy to dc electrical circuits is described in this section. This provides sufficient accuracy to enable it to be used for the design of magnetic circuits.

Consider a simple structure consisting of a coil of N number of turns and a magnetic core of mean length l_c and a cross-sectional area A_c as shown in Figure 2-7, where the permeability of the core material is μ_c. Assume that the displacement current in Maxwell's equation from the size of the device and the operation frequency is negligible, and that the permeability of the core material is very high so that all magnetic flux will be confined within the core. By Ampere's Law,

$$\oint_C \mathbf{H} \cdot d\mathbf{l} = \oint_S \mathbf{J} \cdot d\mathbf{a} \qquad (2\text{-}18)$$

where **H** is magnetic field, **J** is current density, $d\mathbf{a}$ is the vector area of on infinitesimal element of surface S and $d\mathbf{l}$ is an infinitesimal element of the curve C. Then equation (2-18) can be rewritten as;

$$H_c l_c = Ni \qquad (2\text{-}19)$$

where H_c is the magnetic field strength in the core, l_c is the mean length of core and Ni is the magnetomotive force. The magnetic flux through the cross-section of the core can expressed as

$$\Phi_c = B_c A_c \tag{2-20}$$

where Φ_c is the flux in the core, A_c is the cross-sectional area of the core and B_c is the flux density in the core. The constitutive equation of the core material is

$$B_c = \mu H_c \tag{2-21}$$

Therefore, the magnetic flux can be given as

$$\Phi_c = \frac{Ni}{l_c \big/ (\mu_c A_c)} = \frac{F}{R_c} \tag{2-22}$$

where the reluctance is given by $R_c = \dfrac{l_c}{\mu_c A_c}$ and $F=Ni$ is magnetomotive force.

If we take the magnetic flux Φ_c as the current, the magnetomotive force as the voltage source and the magnetic reluctance as the resistance, then we have an analogue of Ohm's Law in electrical circuit theory. Figure 2-8 shows the comparison of magnetic circuit and its equivalent circuit, and Table 2-1 shows traditional analogues for magnetic circuit and electrical circuit.

Table 2-1 Traditional analogues

Magnetic Circuit		*Electrical Circuit*	
mmf	F	Voltage	*V*
Flux	Φ	Current	*I*
Reluctance	R	Resistance	R
Permeability	M	Conductivity	Σ

The magnetic circuit with an air gap of length l_g can also be considered. Figure 2-9 shows a simple magnetic circuit with an air gap, which is cut in the middle of the right transformer core. In the case of having an air gap, magnetic flux lines come off outwards at the edge of the air gap which increases the effective cross-sectional area A_g of the air gap as shown in Figure 2-10. The Ampere's law for the magnetic circuit is given as

$$F = Ni = H_c i_c + H_g i_g \tag{2-23}$$

where, $H_c i_c$ and $H_g i_g$ can be rewritten by equation (2-20) and (2-21) as

$$H_c i_c = \frac{B_c}{\mu_c} l_c = \frac{\Phi_c}{\mu_c A_c} l_c = \Phi_c R_c \tag{2-24}$$

$$H_g i_g = \frac{B_g}{\mu_g} l_g = \frac{\Phi_g}{\mu_g A_g} l_g = \Phi_g R_g \tag{2-25}$$

The magnetic flux is the same at any cross-section of transformer core and the air gap, the magnetic flux is

$$\Phi_c = \Phi_g = \Phi \tag{2-26}$$

Therefore, the magnetic motive force F from equation (2-23) and (2-26) gives

$$F = (R_c + R_g)\Phi \tag{2-27}$$

The above equation means the magnetic circuit with air gap is equivalent to a serial electric circuit.

A magnetic circuit having more than one air gap is derived from an equivalent serial electric circuit and Kirchhoff's law as

$$\sum R_k \Phi_k = \sum F_k \tag{2-28}$$

Equation (2-28) is capable of solving a complex magnetics circuit by applying these simplified laws. All electrical dc circuit analysis techniques such as mesh analysis and nodal analysis can be applied in the magnetic circuit analysis.

The alternative design in this thesis is to use a permanent magnet as a constant magnetic source. In the case of using the permanent magnet to generate a magnetic field, the characteristics of permanent magnets and the demagnetisation curve, which is the part of hysteresis loop in the second quadrant, are to be considered. Demagnetisation curves of commonly used magnet materials are shown in Figure 2-11. The magnetic properties of each magnetic material are listed in Table 2-2.

NdFeB and SmCo are known as Rare Earth magnets because they are both composed of material from the rare earth group of elements. In the table, remanence B_r is a measure of magnetic attraction, and coercivity H_c measures the resistance to an opposing magnetic field. The magnet quality factor $(BH)_{max}$ is the product of the remanence and coercivity and indicates the maximum work which a magnet can produce. T_c is Curie temperature.

Table 2-2 Magnetic material comparisons (Trout and Wooten)

Material	B_r *(T)*	H_s *(kOe)*	H_{ci} *(kOe)*	$(BH)_{max}$ *(MGOe)*	T_c *(˚C)*
NdFeB	1.34	35	15	43	310
SmCo	1.04	30	25	26	825
Alnico	1.25	3	0.64	5.5	890
Ceramic	0.40	10	3.3	3.8	460

Consider a piece of magnet which has a uniform cross-sectional area of A_m and a length l_m. The demagnetization curve of the magnet is a straight line with a coercive force of H_c and a remanent flux density of B_r. The demagnetisation curve can be expressed analytically as

$$B_m = \frac{B_r}{H_c}(H_m + H_c) = \mu_m(H_m + H_c) \qquad (2\text{-}29)$$

where $\mu_m = B_r/H_c$ is the permeability of the permanent magnet, which is very close to μ_0. Therefore equation (2-29) can be rewritten for the permanent magnet

$$H_m l_m = (\frac{B_m}{\mu_m} - H_c) l_m = \frac{l_m}{\mu_m A_m} \Phi_m - H_c l_c = R_m \Phi_m - F_m \qquad (2\text{-}30)$$

where $R_m = l_m/(\mu_m A_m)$ is the reluctance and F_m is the magnetomotive force which is equivalent to the voltage source of the electric circuit.

2.3.2 Mechanical actuator

The alternative magnetic field control circuit is modified from the basic magnetic circuit with one air gap for the flow channel as shown in Figure 2-9. The alternative circuit has one additional air gap, which is to change its length. The alternative magnetic circuit is shown in Figure 2-12.

The length of air gap for measurement is fixed but the length of the air gap for control is changeable. If the length of the air gap for control is changed then more magnetic flux is to be diverted to the air gap for measurement because the reluctance of the air gap for control is to be increased.

To change the length of the air gap for control, a movable yoke is placed at the end of the fixed yokes in Figure 2-13. The movable yoke in Figure 2-13 can be moved using a mechanical actuator. In this section a piezoelectric actuator is considered. When the length of the air gap for controlling is changed, the permeance $P_{gc} = \mu_0 A_{pg}/L_{pg}$ of the air gap for control is also changed so that the magnetic flux passing through the air gap is changed.

2.3.3 Piezoelectric actuator

Piezoelectric materials have been in use since 1815 when Coulomb presented a theory that an electric field was produced when a pressure was applied on a crystal or material. In 1820, Hauy and Becquerel also reported their experimental results that any change of its shape due to compression on a material might cause electricity.

According to a historical review by Ballato (1995 and 1996), Coulomb (1815) firstly theorised that electricity might be produced by pressure application. Later, Hauy and Becquerel (1820) experiments suggested that any charges which were produced due to compression might have been caused by simple friction or contact electricity. Becquerel did suggest that such potential charge production could occur by stretching rubber. By correlation, he suggested that experiments using crystalline minerals might also show similar effects.

The piezoelectric phenomenon which was defined as being those crystals having one or more axes whose ends are unalike, that is to say, hemihedral crystals with oblique faces, have the special physical property of giving rise to two electrical poles of opposite signs at the extremities of these axes when they are subjected to a change in temperature. This is the phenomenon known under the name of pyro-electricity which was discovered by P. and J. Curie (1880).

Again in 1881, Lippmann suggested that the reverse effect should also exist, i.e. the reimposition of surface charges would induce mechanical deformation. A year later, the Curie brothers (1882), verified experimentally this assumption by showing that the coefficients for both the direct and reverse effects were identical, (Ballato, 1996).

It was not until Neumann's experiments in 1890 that the existence of three basic principles which appear to govern the physical behaviour of all crystalline materials was established. Neumann (1890) suggested that the symmetry elements for any physical property of a crystal must include all symmetry elements of the point group of that crystal, every physical property of a crystal must possess at least the symmetry of the point group of that crystal and any kind of symmetry that is possessed by the crystallographic form of a material is also possessed by the material in respect of every physical property it possesses.

Kelvin (1893) provided the real groundwork for understanding the piezoelectric concept when he developed models which explained and expanded the concept earlier suggested that compression of a crystal produced a piezoelectric generated deformation and that the reverse or reimposition of a surface charge onto that crystal would induce mechanical crystal deformation.

In 1894, Voigt revealed that equations governing the linear behaviour of piezoelectric crystals were described as tensors. This tensor concept suggested that stress (T) is proportional to strain (S) which is proportional to electric field. Therefore, the piezoelectric coefficient which couples both mechanical and electrical tensor variables is the same. Voigt now converts his calculated second rank three-dimensional tensor equations so they could be represented in two-dimensional form.

In the 19th century, Langevin began to make practical applications of piezoelectric transducers, especially in use of submarine detection under water. Born published his studies in 1920 which provided the first theoretical lattice calculations for the piezoelectric coefficient as B-ZnS. In 1921, Cady showed that piezoelectric effect presence was identified in quartz crystal and later developed crystal resonators which were used for the stabilisation of oscillators.

More recently, the piezoelectric material most commonly used is PZT (Pb-Zr-Ti, lead-zirconate-titanate). PZT was developed in the 1940s and 1950s. This material exhibited very high dielectric and piezoelectric properties (Jordan and Ounaies, 2001).

Figure 2-14 shows the principle of transduction in a simplied way in 2D (Harvey, 2004). The relaxed state is shown in Figure 2-14(A) and the activated state in Figure 2-14(B). The piezoelectric material consists of negatively charged and positively charged atoms as shown. In the activated state, the piezoelectric is pushed together by an external force. This force deforms the crystal structure and then the location of the atoms in the structure becomes closer. This deformation changes the surface charge and produces an electric potential as

$$V = \frac{Q}{C_{Tx}} \tag{2-31}$$

where V is the electric potential across the piezoelectric material, Q is the generated charge and C_{Tx} is the capacity of the piezoelectric material, which is known as the direct piezoelectric effect (Harvey, 2004). The generated charge Q can be calculated as

$$Q = d \cdot F \tag{2-32}$$

where d is the piezoelectric charge coefficient d and F is the force. The capacity of the piezoelectric material is:

$$C_{Tx} = \frac{K \varepsilon_0 A}{d} \tag{2-33}$$

where ε_0 is the permeability of free space(=8.85x10^{-12} C/V-m), A is the area of the piezoelectric material, d is the thickness and K is the relative permeabilityof the piezoelectric material. K is also defined by:

$$K = \frac{\varepsilon_r}{\varepsilon_0} \tag{2-34}$$

where ε_r is the permeability of the piezoelectric material.

The unimorph cantilever has a piece of mild steel at the tip as a movable yoke. When the electric voltage is supplied to the piezoelectric unimorph cantilever, the tip of the cantilever starts bending and it moves the movable yoke outwards from the fixed yoke and the gap length is changed.

Figure 2-15 shows the structure of a unimorph cantilever actuator. A standard rectangular shape unimorph actuator under activation is illustrated in the figure. The actuator consists of a single piezoelectric layer bonded to a purely elastic layer. Steel or titanium is usually chosen for the elastic layer.

When a voltage is applied across the thickness of the piezoelectric layer, longitudinal and transverse strains develop. The elastic layer opposes the transverse strain which leads to a bending deformation (Sitti *et al*., 2001). The unimorph actuator is used in a wide range of applications as converters of electric input to mechanical motion or vice versa. For example, it is used for loudspeakers, microphones, precise machining, relays, force sensors, etc.

The invention and use of piezoelectric unimorph actuators was undertaken by Saywer in 1931. Since then, many researches have been conducted to detail the operation and application of these devices.

Steel *et al.* derived the tip deflection and stretching of unimorph actuator as functions of applied electric voltage by making a one-dimensional assumption in 1978. Later, Smith *et al.* derived the constituent equations of unimorph to explain its response under different loading conditions using 4 by 4 matrix equations.

When considering the unimorph cantilever with length L much larger than width w, which is also much greater than the total thickness t, if an electrical field E is applied across ceramic plate thickness, the expansion or contraction in length direction will produce a mechanical bending deformation and extensional deformation because it has asymmetric structure.

The tip deflection can be obtained by Sitti *et al.* (2001) as

$$\delta = \frac{3l^2}{2h_p} \cdot \frac{2AB(1+B)}{A^2B^4 + 2A(2B+3B^2+2B^3)+1} \cdot d_{31}V \qquad (2\text{-}35)$$

where, l is the length of the unimorph cantilever, h_p is the thickness of the piezoelectric layer, $A = s_p/s_s = E_s/E_p$ is the ratio of the electric field on the metal layer and the piezoelectric layer, $B = h_m/h_p$ is the ratio of the thicknesses of the piezoelectric layer and the metal layer, d_{31} is the piezoelectric coefficients which represent piezoelectric coupling between the electrical and mechanical variables, and V is the electrical field on the cantilever (Sitti *et al.*, 2001).

Sitti *et al.* (2001) derive the blocking force as

$$F_b = \frac{3wh_p}{4s_p l} \frac{AB(B+1)}{AB+1} d_{31}V \qquad (2\text{-}36)$$

The piezoelectric can be one of PZT-5H or PZN-PT, their properties and coefficients are shown in table 2-3. The parameters for steel layer properties are also included.

Table 2-3 PZT-5H, PZN-PT and steel layer properties (Sitti *et al.*, 2001)

	PZT-5H	*PZN-PT*	*STEEL*
E(GPa)	61	15	193
P (kg/m3)	7500	8000	7872
d_{31}*(C/N)*	320×10^{-12}	950×10^{-12}	-
k_{31}	0.44	0.5	-
K_3^T	3800	5000	-
E_3*(V/m)*	1.5×10^{6}	10×10^{6}	-

For the unimorph cantilever actuator, a maximum tip reflection point can be obtained by choosing a suitable thickness ratio, which is determined by the Young's modulus ratio of the metal layer and the piezoelectric layer. The mechanical hysteresis curve of PZT-5H unimorph actuator which has 16x3x0.21 mm^3 dimension for different voltages is shown in Figure 2-16. The thickness of steel, h_s is 76 μm. The mechanical hysteresis, i.e. the structural damping, increases by the higher voltages (Sitti *et al*., 2001).

2.3.4 Magnetostrictive material

The magnetostriction is a phenomenon in which a material undergoes mechanical compression under a magnetic field. The fact that a ferromagnetic substance changes its

length when magnetised was first established by Joule in 1842. He used an iron bar with a mechanical lever and was able to show that iron expands along the direction of magnetisation in small fields, the expansion being reduced as the field strength is increased. In addition to this effect, he was able to show that although the length of an iron bar changes when magnetised, the change in volume is very much smaller in comparison. Finally, he investigated the effects of external stresses on the magnetostriction of iron and showed that it is a contraction for all field strengths when under tension. However, the effect was very small – in the order of 10^{-5} corresponding to a strain. Joule's original measurement of the magnetostriction of iron is given in Figure 2-17.

Later studies were concerned with various subsidiary and reciprocal effects which are related to the ordinary longitudinal effect. In 1846, Guillemin observed how a bended ferromagnetic bar was straightened when it was magnetised. In addition he also found that if a rod or wire was twisted then the amount of twist decreased when it was magnetised.

Another key effect was reported by Wiedemann in 1883: if a ferromagnetic rod, which is clamped at one end, was circularly magnetised by the passage of an electric current along its axis and was at the same time subjected to a longitudinal magnetic field, a twist of the free end occurred. The twist was measured by detecting the deflection of a beam of light deflected from a small mirror fixed at the end of the free end. The resultant of the two fields was a helix and the effect merely a special case of the longitudinal magnetostrictive effect which provided the simplest means of magnetostrictive for the twist. The reverse Wiedemann effect, also known as the Matteuci effect, was used for magnetoelastic torque sensors (Lee 1955 and Lacheisserie 1993).

The associated inverse effect also exists for every magnetostrictive effect. The longitudinal magnetostriction has its inverse in the Villari effect revealed in 1865 which is the change of magnetisation produced by an external tension. These inverse effects followed from le

Chatelier's principle and the Joule and Villari effects are related by the thermodynamic identity

$$\left(\frac{d\lambda}{dH}\right)_{\sigma} = \left(\frac{dB}{d\sigma}\right)_{H} \tag{2-37}$$

where $(d\lambda/dH)_{\sigma}$ is the rate of change of magnetostriction with magnetic field at constant stress and $(dB/d\sigma)_H$ is the change of magnetic induction with stress at constant field, applied magnetic field strength H and magnetic flux density B within the magnetostrictive material. The source of this equation is the linearisation of the differential response of the λ and B to change in only two factors, the applied magnetic field H and stress σ.

Since $B = \mu_0(H+M)$, and H is not a function of stress, the right hand side term of equation (2-37) is rewritten as $\mu_0(dM/d\sigma)_H$, which is a derivation of interest in the magnetomechanical effect. Equation (2-37) merely shows that a large magnetomechanical effect $(dB/d\sigma)_H$ will be observed in materials with a large magnetostrictive strain derivative $(d\lambda/dH)_{\sigma}$.

The early application of the magnetostrictive effect with nickel, iron and permalloy was particularly focused on sensors, actuators and telephone receivers tested by Philipp Reis in 1861 and in scanning sonar, the bulk strains are up to 10×10^{-5}.

The magnetostrictive effect and its reverse effect, magnetomechanical effect, have been studied by other researchers. Craik and Wood in 1971 obtained experimental results of these effects by applying stress to polycrystalline magnetic materials in the presence of a small constant magnetic field. In 1995, Jiles proposed a consistent theory to explain the magnetomechanical effect of ferromagnetic materials.

Terfenol-D is one of the magnetostrictive materials which has very large bulk strains. It is an alloy of rare earths Dysprosium and Terbium with 3d transitions of metal iron, and is capable of bulk saturation strains in excess of 20 x 10^{-4} at moderate magnetisation levels at room temperature. The name Terfenol came from the composition of the alloy $TbFe_2$ and its place of origin, the Naval Ordnance Laboratory (NOL) now known as the Naval Surface Warfare Centre (NSWC). Terfenol-D is used as basic material for actuators and sensors. Its physical properties are shown in Table 2-4. Terfenol-D can be produced in a variety of forms, monolithic solid as a rod or bar, powder and thin film. A picture of a Terfenol-D bar taken from Theodoregray.com is shown in Figure 2-18. The applications of Terfenol-D are broadband shakers, surgical instruments, ultrasonic transducers, high power speakers and many others which require large displacement at both high and low frequencies.

Figure 2-19 provides diagrams to help understand the relationship between the strain and magnetic induction. In these diagrams, the essence of a magnetostrictive device is lumped into discrete mechanical and magnetic attributes that are coupled in their effect on the magnetostrictive core strain and magnetic induction. As shown, the external stress is set to a constant compressive value provided by the mass resting on a stiff spring on top of the magnetostrictive core.

First of all, in the case of any field applied ($H=0$), the magnetostrictive material has an initial length l_s for which the change of the length, Δl_s is 0 and no net axial magnetic induction ($B=0$) as shown in Figure 2-19 (a). When an external force is applied to the magnetostrictive material, the elliptical magnet components are rotated and the magnetisation of the magnetostrictive material is changed, as shown in Figure 2-19 (b) and (c). When the magnitude of the applied field H_c increases to its saturation limits ($H_c=H_s$) the elliptical magnet elements rotate to align with the applied field and the axial strain increases to Δl_s and magnetisation of the element in the axial direction is increased to $+ B_s$, as shown in Figure 2-19 (d) and (e).

Dapino *et al.* (2000) improved the theory of the magnetomechanical effect on ferromagnetic material to explain the same effect on Terfenol-D monolithic material. The magnetostrictive sensing using monolithic Terfenol-D was characterised by Calkins *et al.* (1997). The application of Terfenol-D for such actuators and sensors was described by Butler in 1988.

In 2005, Ueno and Higuchi described the design of the magnetic sensor using magnetostrictive/piezoelectric laminate composite for high sensitivity and heat-resistant application with a permanent magnet. In this chapter, the further investigation of the usage of magnetostrictive and piezoelectric laminated composite is undertaken in terms of the controlling magnetic flux density with a permanent magnet.

A diagram of a flowmeter using the magnetostrictive device for controlling the magnetic field is shown Figure 2-20. The magnetic circuit consists of a fixed yoke with an air gap, permanent magnets, and a magnetostrictive material (Terfenol-D). Neglecting leakage flux, the equivalent magnetic circuit consists of two parallel loops, one of which is passing through the magnetostrictive material and the other through the air gap. The magnet is used to generate the bias magnetic field at the air gap and to magnetise the magnetostrictive material and induce bias magnetostriction.

As shown in Figure 2-20 (b), application of a compressive load on the magnetostrictive material leads to a decrease of magnetisation inside the material due to the inverse magnetostrictive effect (magnetomechanical effect). This reduction of magnetisation yields an increase of the flux in the loop of the air gap. That means the stress to magnetostrictive material is able to be converted directly into the change of the magnetic flux at the air gap where the rectangular flow channel is located.

To provide compression of the magnetostrictive material, a laminate composite of magnetostrictive and piezoelectric materials is proposed. This control device has the

advantages of a simple configuration and ease of manufacture compared with conventional devices. The laminate composite is the magnetostrictive material plate bonding two piezoelectric layers on the top and bottom sides as shown in Figure 2-21. The flux in the air gap is varied according to the magnetisation of the magnetostrictive material. For example, if the magnetostrictive material is compressed with a shrinking of the piezoelectric material caused by a supply voltage to the control device, the magnetisation is decreased by the inverse magnetostrictive effect.

The magnetic flux change is capable of being calculated by solving an equivalent magnetic circuit as shown in Figure 2-22, following Ueno's calculation (2005). The cross-sectional area A, length L of the air gap, Terfenol, and the permanent magnet with the subscripts g,m, and p are shown in Figure 2-22. The magnetic field, magnetic flux, and magnetic flux density are denoted by H, B, and Φ with the subscripts g, m, p, and l for leakage flux. The magnetic flux density of the magnetostrictive material, B_m varies with H_m and S_m as

$$B_m = \mu_m H_{m0} + e_m S_m \tag{2-38}$$

where μ_m is the permeability of the magnetostrictive material, S_m is the strain in the x direction which is x_m/L_m and e_m is the coefficient of variation of B_m with S_m.

The first term in equation (2-38) is the bias magnetic flux density and the second is variation with the strain. Taking the integral of equation (2-38) gives

$$\int_0^{L_m} B_m dx = \int_0^{L_m} (\mu_m H_{m0} + e_m S_m) dx \tag{2-39}$$

Therefore equation (2-38) can be rewritten as

$$B_m = \frac{\mu_m}{L_m}(H_{m0} \cdot L_m) + \frac{e_m}{L_m}\int_0^{L_m} S_m dx \tag{2-40}$$

The magnetic flux of the magnetostrictive material can be calculated by taking integration of B_m over the area A_m as

$$\Phi_m = \int_{A_m} B_m dA = \frac{\mu_m A_m}{L_m}(H_{m0} \cdot L_m) + \frac{e_m}{L_m}\int_{V_m} S_m dx \tag{2-41}$$

The fluxes of the air gap Φ_g, and leakage Φ_l are given by

$$\Phi_g = A_g B_g = -\mu_0 A_g / 2l_g \times H_p L_p = -P_g H_p L_p \tag{2-42}$$

$$\Phi_l = -P_l H_p L_p \tag{2-43}$$

where μ_0 is the permeability of a vacuum. The permeance of leakage P_l is dependent on the air gap length L_g. Here, P and U with appropriate subscriptions denote the permeance and magnetomotive force. Kirchhoff's law regarding the paths of the air gap and the leakage derive the relation between the magnetomotive forces and are described as

$$U_p = -U_g = -U_l \tag{2-44}$$

and the permeance of the permanent magnet P_p, the permeance of the air gap P_g and the permeance of the leakage P_l can be defined as

$$P_p = \mu \frac{A_p}{L_p}, \tag{2-45}$$

Table 2-4 Physical Properties of Terfenol – D (adapted from Erema Product Inc.)

Nominal Composition	$Td_{0.3}Dy_{0.7}Fe_{2.0}$
Mechanical Properties	
Young's Modulus	25-35 GPA
Sound Speed	1640-1940 m/s
Tensile Strength	28Mpa
Compressive Strength	700Mpa
Thermal Properties	
Coefficient of Thermal Expansion	12ppm/°C
Specific Heat	0.35kJ/kg-K
Thermal Conductivity	13.5W/m-k
Electrical Properties	
Resistivity	58×10^{-8} O-m
Curie Temperature	380 ºC
Magnetostrictive Properties	
Strain(estimated linear)	800-1200 ppm
Energy Density	14-25 kJ/m^3
Magnetomechanical Properties	
Relative Permeability	3-10
Coupling Factor	0.75

$$P_g = \mu \frac{A_g}{L_g},$$

$$P_l = \mu \frac{A_l}{L_l}$$

The sum of Φ_g, Φ_m, and Φ_l, must be equal to Φ_p that is

$$\Phi_p = \Phi_g + \Phi_l + \Phi_m \tag{2-46}$$

Using a demagnetising curve of the magnet, $B_p = B_r + \mu_r H_p$ and $B_g = \mu_0 H_g$, where μ_r is the recoil permeability, B_r is the remanent induction, equations(2-45) and (2-46) can be written as

$$\Phi_p = A_p B_p = A_p \mu_r H_p + A_p B_r = \frac{A_p \mu_r}{L_p} L_p H_p + A_p B_r = P_p U_p + A_p B_r \tag{2-47}$$

$$\Phi_g = A_g B_g = -\mu_0 A_g H_g = -\frac{\mu_0 A_g}{L_g} H_p L_p = P_g U_g \tag{2-48}$$

$$\Phi_l = -P_l H_g L_g = P_l U_l \tag{2-49}$$

The relationship between Φ_g and Φ_m can be yielded from equation (2-43) by substituting equation(2-47), (2-48) and (2-49) as

$$\Phi_g = \lambda (A_p B_r - \Phi_m) \tag{2-50}$$

where

$$\lambda = \frac{P_g}{P_p + P_g + P_l} \tag{2-51}$$

Equation (2-50) indicates that the magnetic flux at the air gap, Φ_g is a linear function of the magnetic flux at the magnetostrictive material, Φ_m with slope $-\lambda$ which is determined by the components of the magnetic circuit excluding the magnetostrictive material because B_r and A_p are constant for the given design.

The value of $\Delta\Phi_g$ is obtained from equations (2-42) and (2-50) as

$$\Delta\Phi_g = \lambda \frac{e_m}{L_m} \int_{V_m} S_m dx \tag{2-52}$$

where e_m is the piezomagnetic coefficient of the magnetostrictive material and V_m is the volume of the magnetostrictive material. Therefore, $\Delta\Phi_g$ can be calculated from the total strain variation, the coefficient λ from the geometrical structure and the piezomagnetic coefficient e_m.

2.4 Fluidic oscillator

The standard geometry of the fluidic oscillator which is studied in this thesis is shown in Figure 2-23. The fluidic oscillator consists of a nozzle, a splitter, two diffuser walls for attracting jets, two feedback channels and an exit. The fluidic oscillator having a feedback channel is called a feedback type fluidic oscillator. The flow enters the flowmeter by means of the nozzle and passes though the oscillator to the exit.

When fluid enters the fluidic oscillator, a jet is formed by the nozzle then the diffuser walls provide two opposing forces on the jet though the action of the Coanda effect (Kadosh,

1967). The jet moves along the diffuser wall passing to one side of the splitter and exits while some of the main flow enters the feedback channel and flows back to the nozzle outlet normal to the jet. The feedback flow is entrained in the separation bubble between the jet and the diffuser wall. As the separation bubble becomes larger the jet moves away from the diffuser wall and separates to attach to the opposite diffuser wall and the feedback process is repeated (Furmidge, 1996).

The fluidic oscillator arose from a development of the Coanda switch which is shown in Figure 2-24. The Coanda switch is a fluidic device used in hydraulic computing. A nozzle is placed upstream of two diverging walls and forms a jet. The jet attaches to one of the diverging walls through the Coanda effect which means a jet flow attaches itself to a nearby surface and remains attached even when the surface curves away from the initial jet direction (Reba, 1966). In the Coanda switch, a small flow can be injected into one of control ports near the nozzle to deflect the jet from the wall to the opposite wall.

Figure 2-25 shows an early stage of the feedback channel fluidic oscillator which was carried out by Wilson *et al.* (1970), referring to the Coanda switch as seen in Figure 2-24. The feedback channels maintain the oscillation of the jet. The oscillation was detected using pressure transducers mounted in the receivers. The oscillation frequency is shown to be proportional to flowrate and not dependent on density and viscosity. Wilson *et al.* changed density from 0.76 to 1.019 and viscosity from 0.862 to 2.26 centipose of fluid as well as changing the aspect ratio, splitter distance, setback distance and feedback inlet location as shown in Figure 2-26.

In 1974, Beale and Lawler developed a semi empirical model of a fluidic oscillator for volume flow metering using thermal probes in the feedback channels to detect the oscillation, as shown in Figure 2-27. They tried to develop a device with maximum oscillation frequency, accuracy and linearity whilst minimising pressure loss and dependence on flow profile. They revealed the oscillation frequency is a function of fluid

velocity and geometrical parameters only by using analytical modelling. Using their analytical model a meter with a flow range of 10:1 with maximum pressure loss of 3 psi was developed.

Adams (1973) also reported the commercial version of the fluidic oscillator, in which the oscillation frequency depends only on the velocity of jet, and the meter calibration should be the same for all fluids.

Honda and Yamasaki (1985) proposed a target oscillator, as shown in Figure 2-28, using the complementary relationship between jets and wakes to explain the operation and achieved a minimum Reynolds number of 27. The target flowmeter consists of a target and a pair of edges at the meter exit. A diagram showing the complementary relationship of wakes and jets is included as Figure 2-29. They stated that circulations around a body can be replaced by a vortex, to remove the diffuser walls from a feedback fluidic oscillator meter whilst maintaining feedback flow which was generated by vortices shed from a bluff target. The oscillation is sensitively effected by the dimension of the target, distance from the nozzle and the target, and the dimension of flow duct.

Yamasaki *et al.* (1988) suggested a simplified version of the target meter using experimental flow visualisation and numerical modelling, as shown in Figure 2-30. The experimental work was carried out using air as the test fluid and a finite-difference programme was used to solve the two dimensional Navier-Stokes equations. Their simplified fluidic oscillator has no control port or downstream contraction. The meter has only the inlet nozzle and rectangular target, which made the numerical modelling easier.

Boucher and Mazharoglu (1988) used a variable geometry target meter to look at changes in geometry on minimum oscillation Reynolds number, and variation of the Strouhal number with the Reynolds number, using a meter which had two moving knives and a movable nozzle. They moved the edges of the knives to the centre line, the distance from

the jet throat to the target and the width of target. The results of their study showed the linearity characteristic of the meter depends only on the variation of the Strouhal number with the Reynolds number. They also developed the fluidic scaling equation to determine the dimension of the nozzle for the minimum pressure drop at the maximum flow. This equation showed the minimum flowrate, the meter factor depending on the Euler number, Strouhal number and minimum Reynolds number for any geometry of fluidic oscillator. The optimum aspect ratio of channel height to nozzle width from their experiment is 6.0, which produce the meter factor as around 50.

Kalsi *et al.* (1988) developed equations which are able to explain that the range of a meter of a given class is proportional to its physical size by employing the pressure drop at maximum and minimum flow. They also investigated the effect of upstream disturbances on the fluidic oscillator and showed that the fluidic oscillator is not affected by upstream disturbances. The fluidic oscillator flowmeter produced by Kalsi and his collaborators is shown in Figure 2-31. Their optimum aspect ratio was 3.9 and working range was linear to within 0.24% of maximum flowrate.

In 1997, Glynn and Kasli undertook computational fluid dynamics to optimise the design of the EMI flowmeter to predict the changes in meter performance by modifying the geometry of fluidic oscillator using PHOENICS software in two dimensional computations. The initial velocity at inlet was set at 5 m/s.

Sanderson (1994) developed the fluidic oscillator for the domestic water meter using the electromagnetic sensing technology for satisfying British Standard BS5728 Class D specification. He suggested three possible configurations of magnets and electrode position, and analysed flow signal strength for laminar and turbulent flow. After analysis, the best position for the magnet and electrodes was concluded to be behind the diverging walls for the magnets and behind the splitter post for the electrodes. His fluidic oscillator is described in the first chapter of this thesis. The meter performance was improved by putting a flow

conditioner at the inlet by Furmidge (1996), which reduced the uncertainty and improved repeatability. By changing the face of the splitter post into a concave shape, the meter had a better performance with a minimum flow of Reynolds number 82. The flow conditioner generated turbulence into the jet flow and improved the repeatability especially of the turbulent to laminar flow transition region. Figure 2-32 shows the fluidic oscillator chamber of the domestic water meter from Severn Trent Metering Service which uses two magnets in the diffuser wall and a line electrode situated between splitter and diffuser wall and the top side of the flow chamber (Harvey, 2004).

Boucher (1995) developed a fluidic oscillator operating at lower flow with a Reynolds number around 130 as shown in Figure 2-33. Boucher's difference of geometry from his previous design was having a flat front face of the splitter. However, the meter did not satisfy Class D specification.

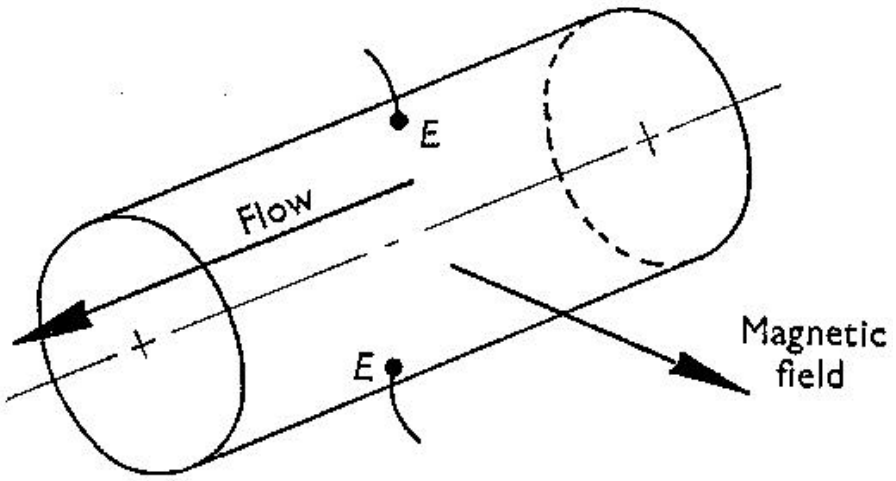

Figure 2-1 A transverse-field electromagnetic flowmeter (Shercliff, 1962)

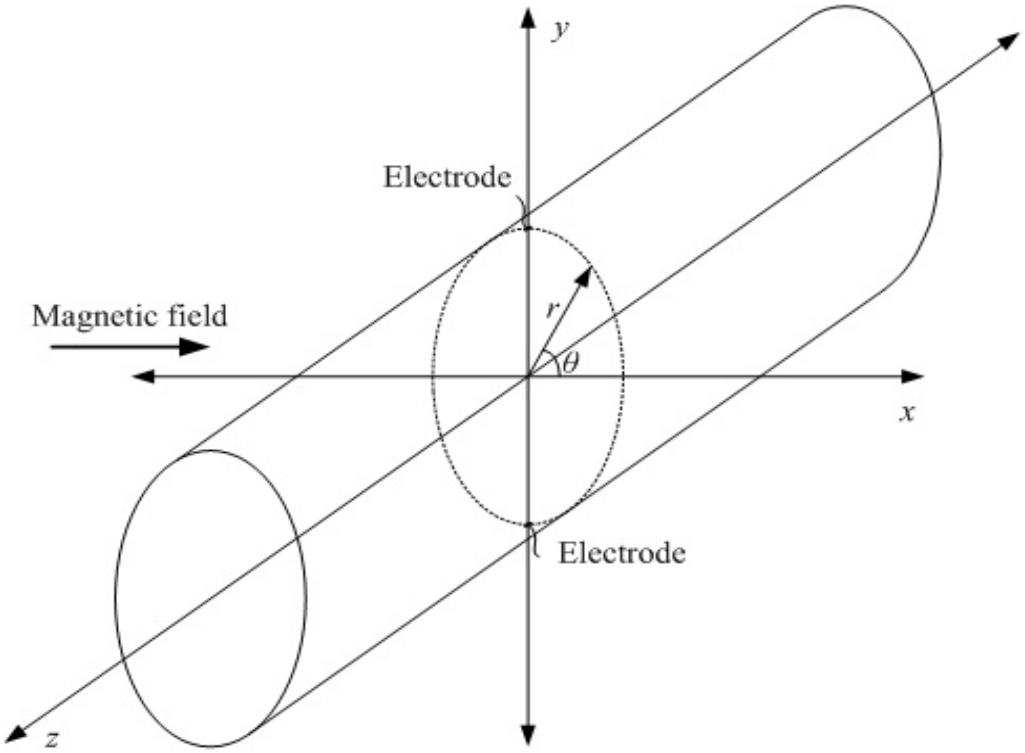

Figure 2-2 A electromagnetic flowmeter with a circular flow channel

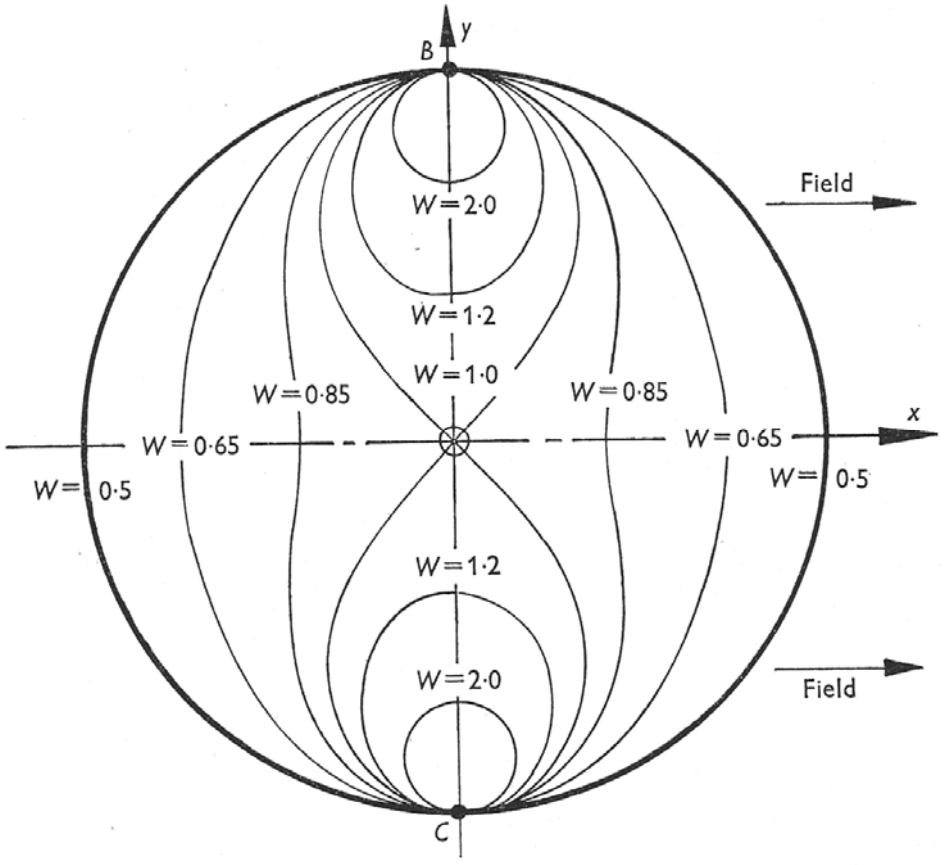

Figure 2-3 Weight function in circular pipe with small electrodes (Shercliff, 1962)

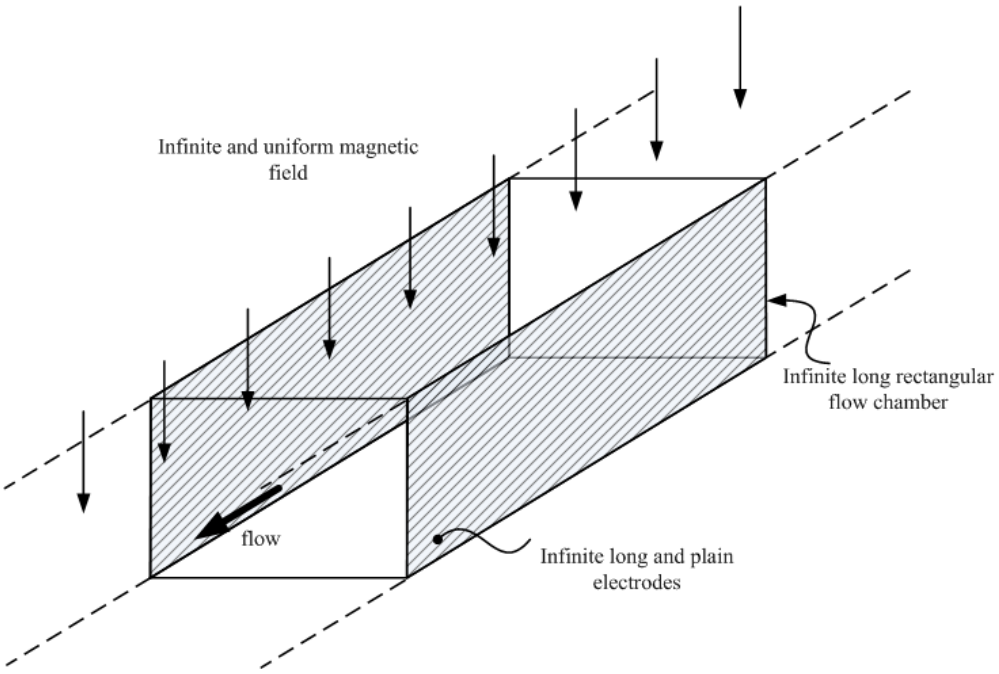

Figure 2-4 Ideal electromagnetic flowmeter

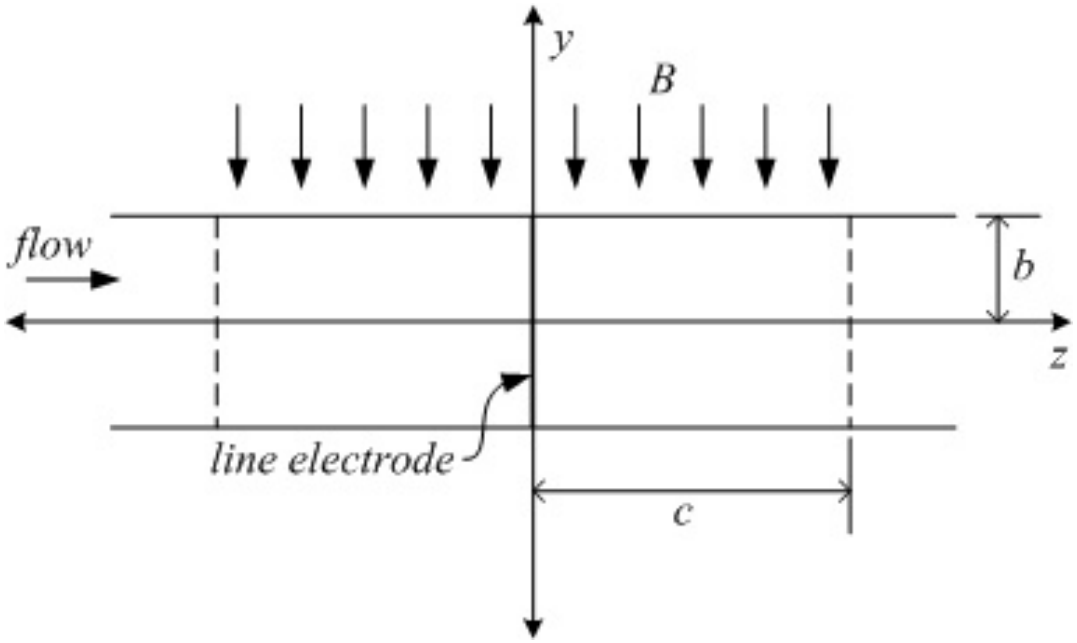

Figure 2-5 A electromagnetic flowmeter which has a finite uniform magnetic field in z≤ c area

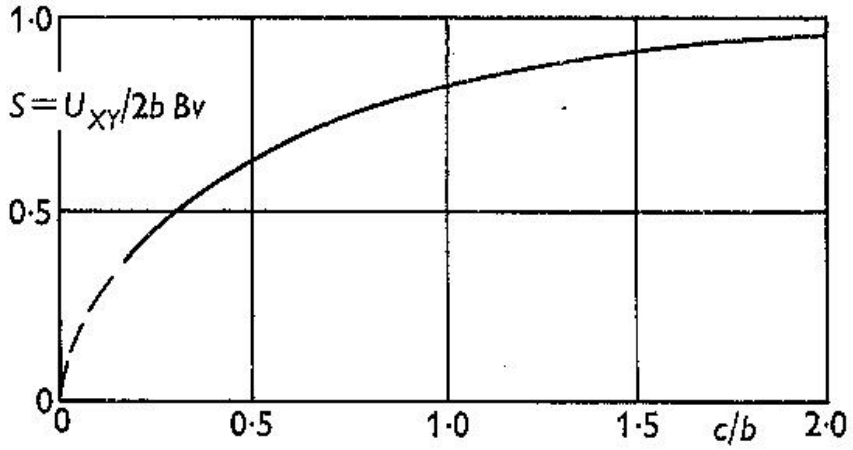

Figure 2-6 Fall in sensitivity due to end-shorting (Shercliff, 1962)

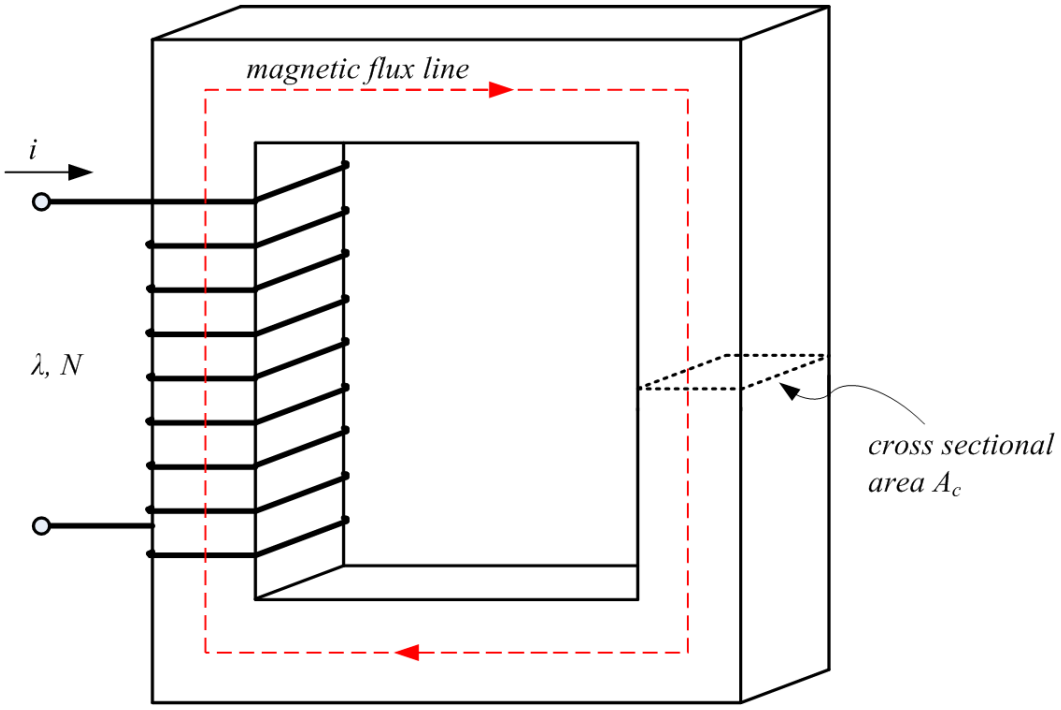

Figure 2-7 A simple magnetic circuit

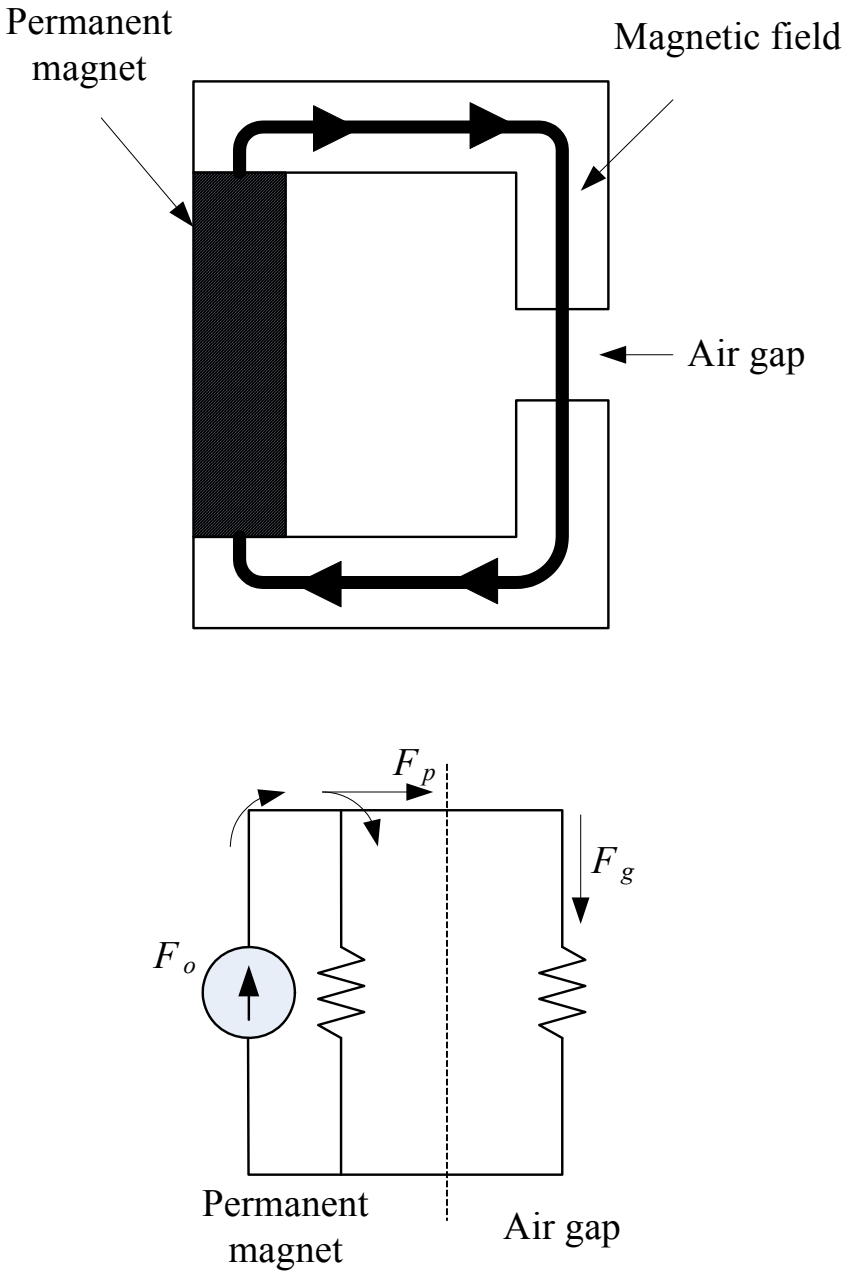

Figure 2-8 Magnetic circuit and its equivalent circuit in forms of electric circuit

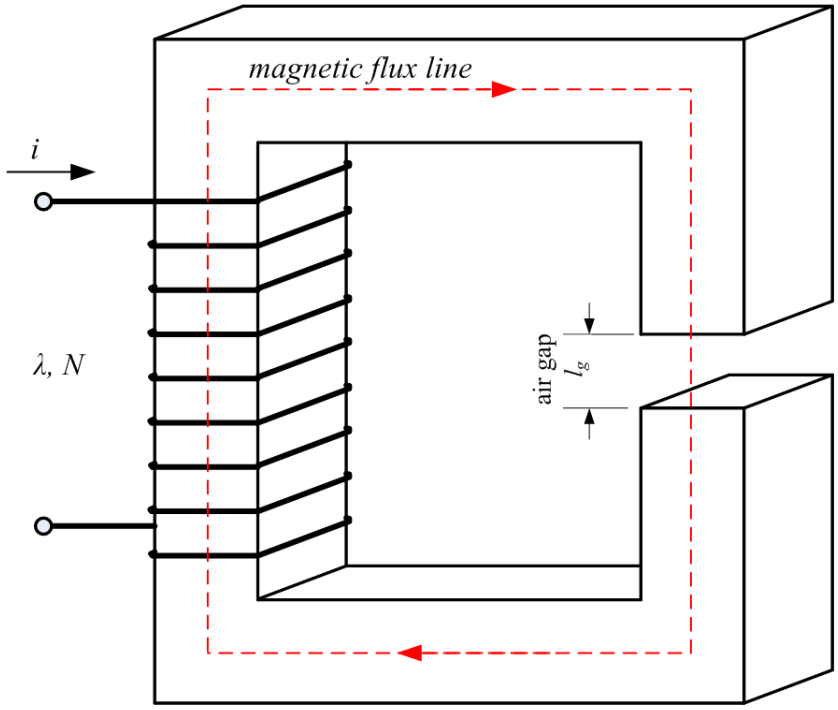

Figure 2-9 A simple magnetic circuit with an air gap

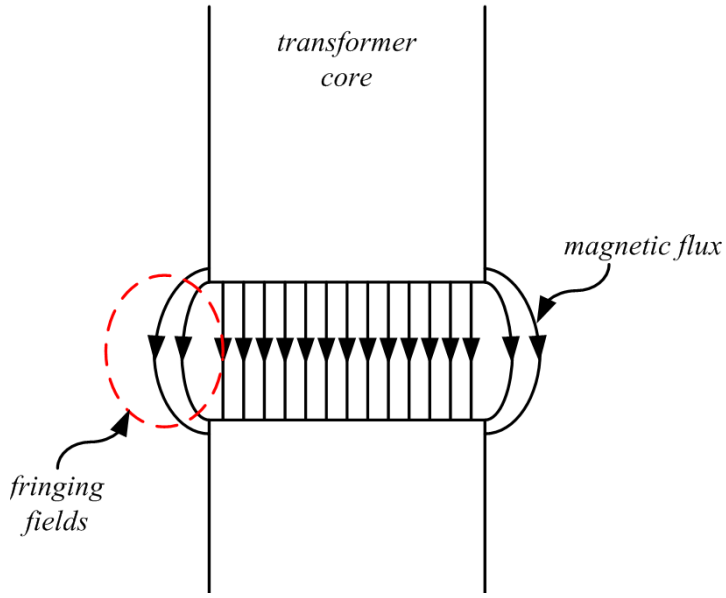

Figure 2-10 Fringing field at an air gap

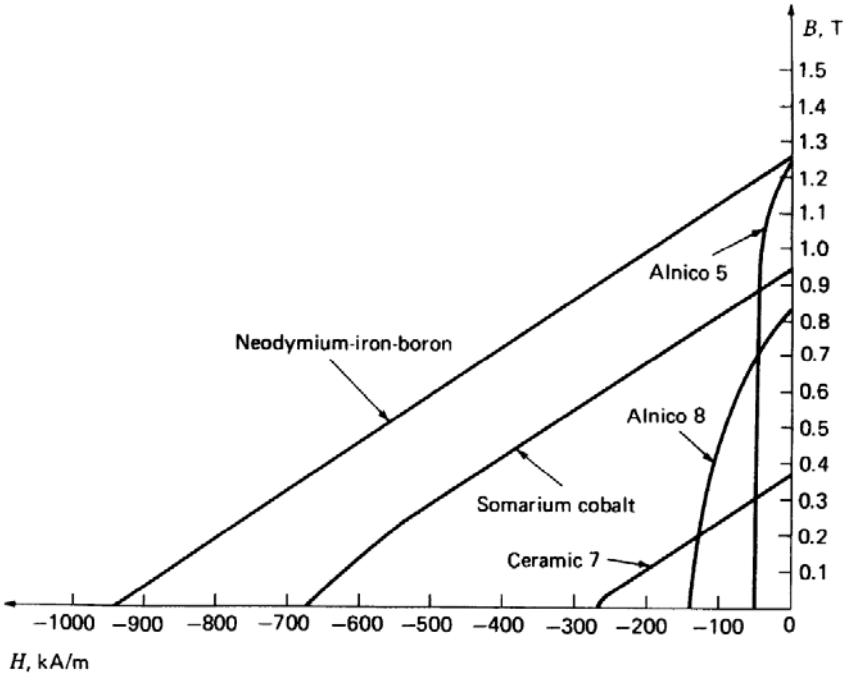

Figure 2-11 B/H curve of permanent magnets

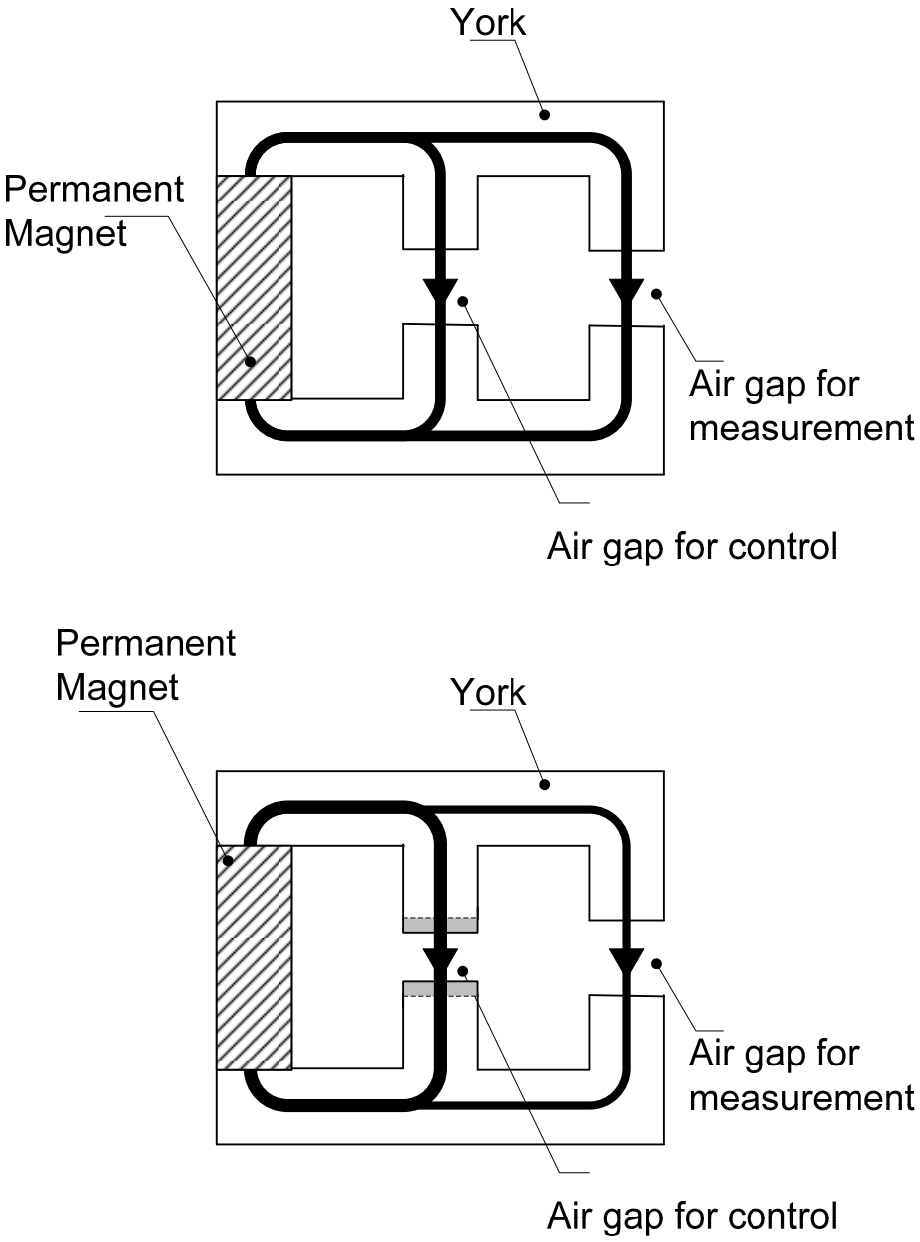

Figure 2-12 A magnetic circuit has two air gaps and change of magnetic field

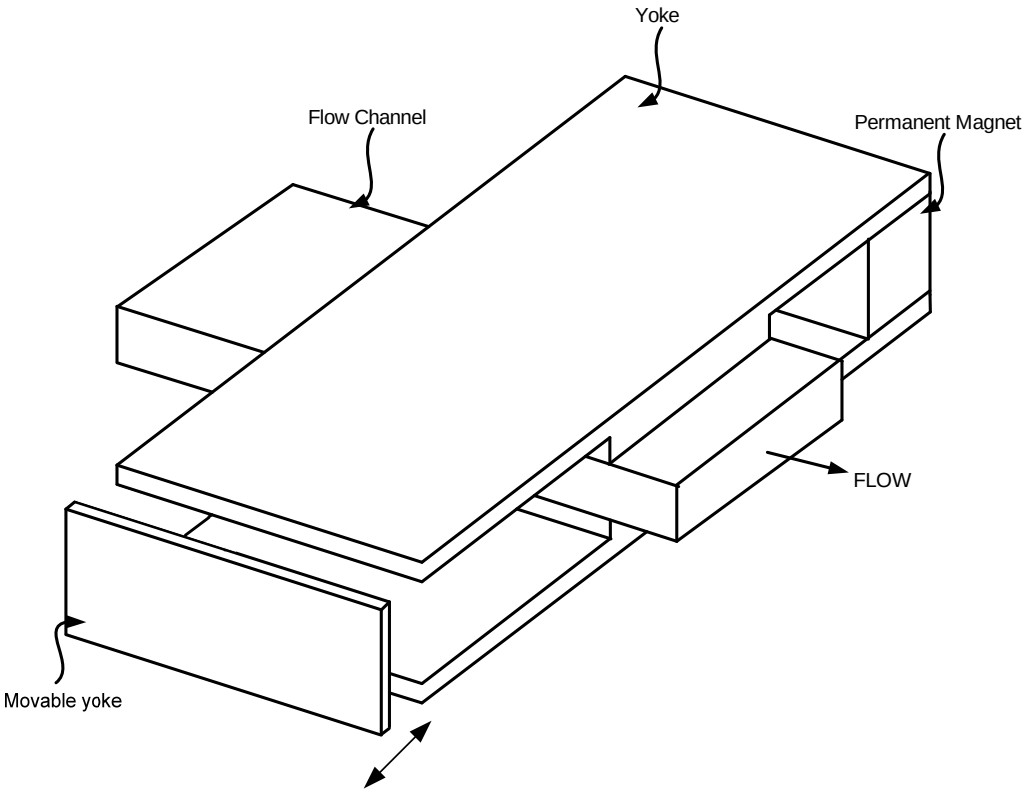

Figure 2-13 Concept drawing for the alternative electromagnetic flowmeter

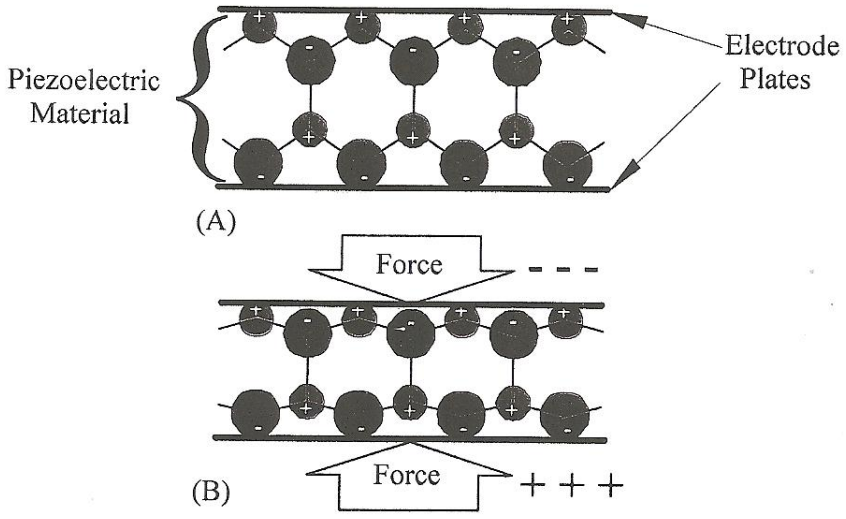

Figure 2-14 Principles of piezoelectric crystal structure (Harvey, 2004)

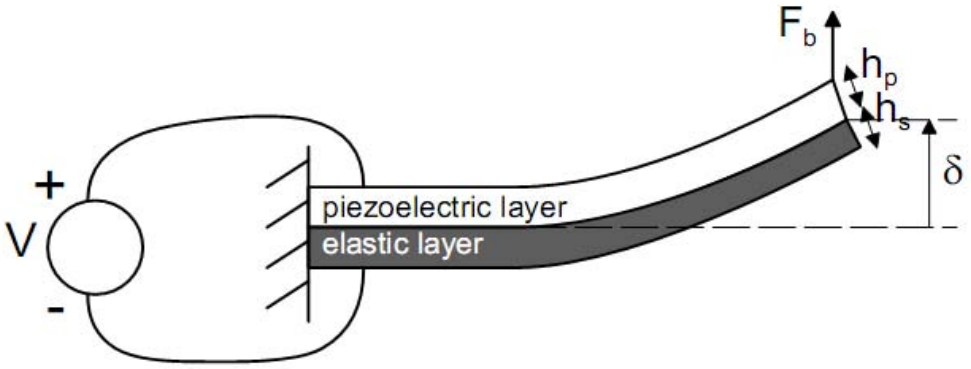

Figure 2-15 Basic cantilevered rectangular shape unimorph actuator (Sitti *et al.*, 2001)

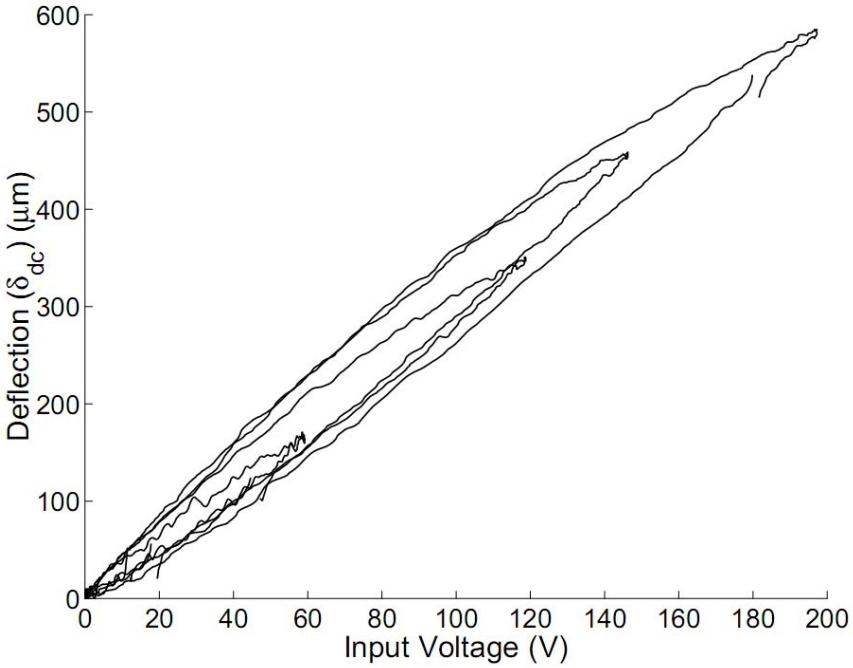

Figure 2-16 Mechanical hysteresis curve of the PZT-5H unimorph cantilever at 1Hz operation mode for different voltages (Sitti *et al.*, 2001)

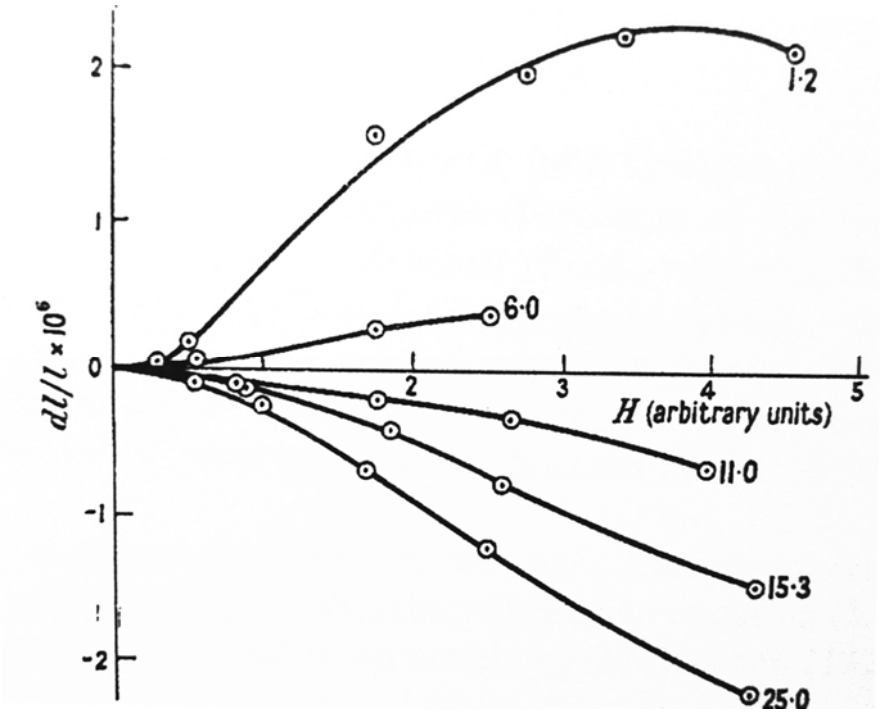

Figure 2-17 Joule's original measurements of the magnetostriction of iron(1842). The figures give the applied tension in kg/mm^2 (adapted from Lee 1955)

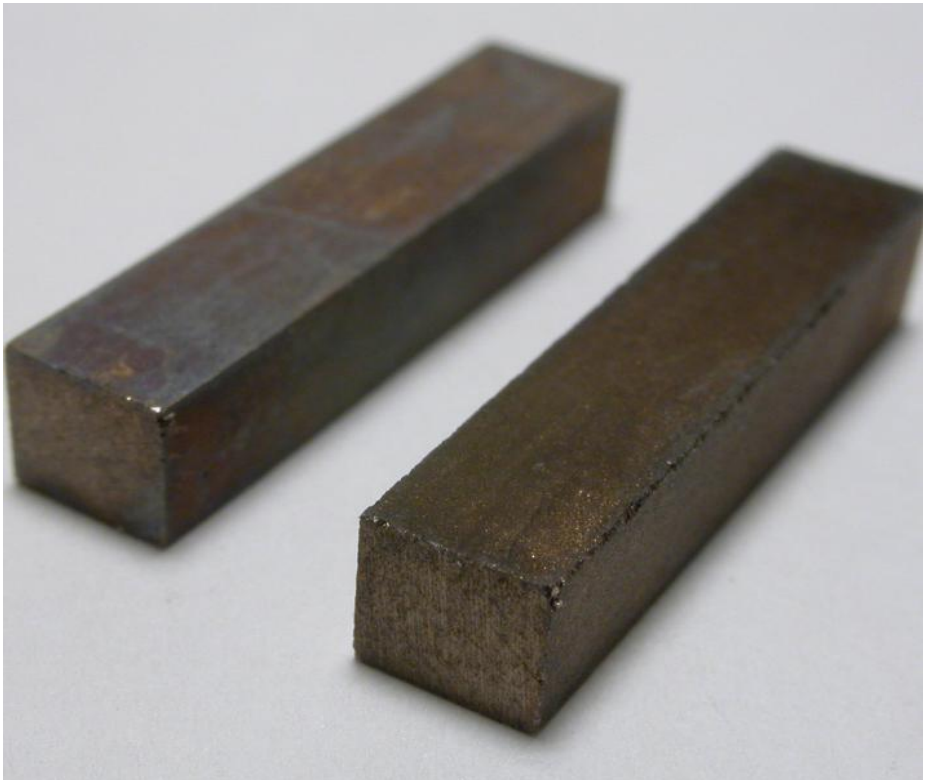

Figure 2-18 Picture of Terfenol-D rod (taken from Theodoregray.com)

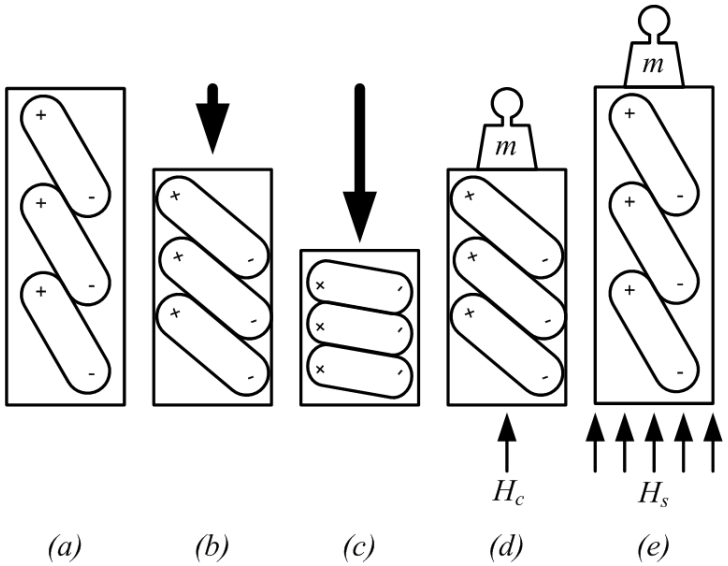

Figure 2-19 Diagrams of changing stain in magnetostrictive material

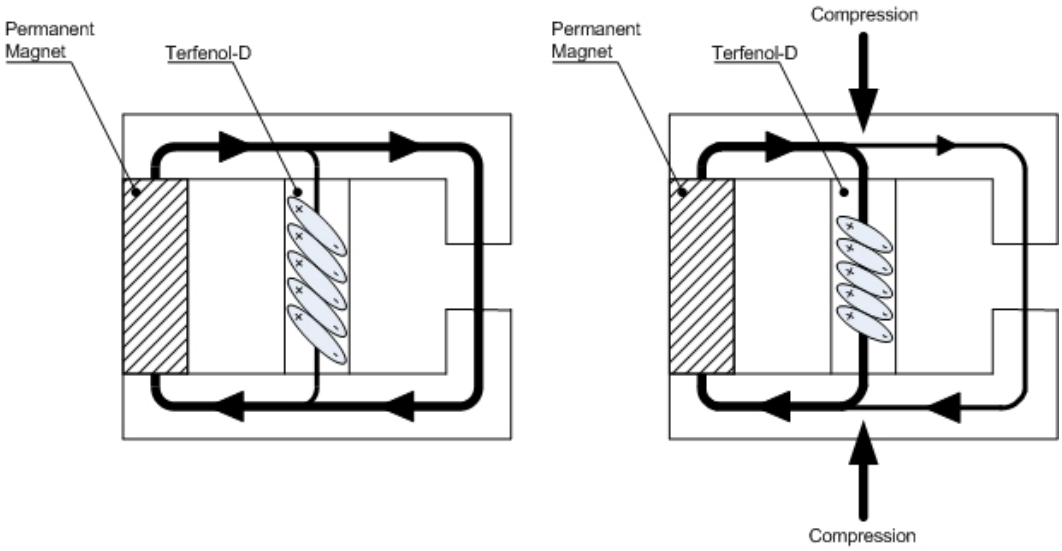

(a) without strain (b) with strain

Figure 2-20 The magnetic circuit using Terfenol-D material

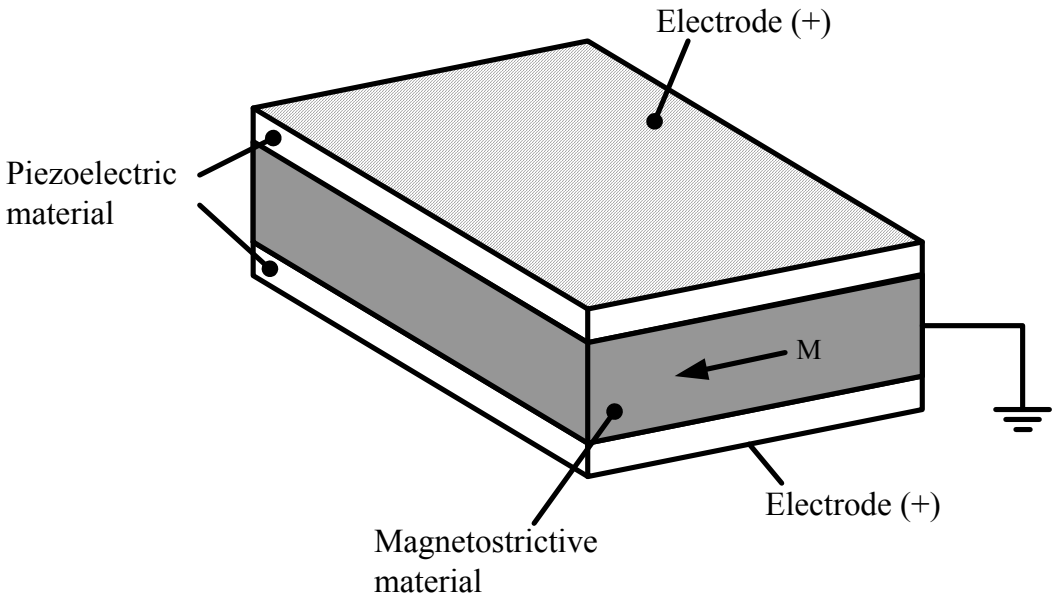

Figure 2-21 The laminated magnetostrictive and piezoelectric device

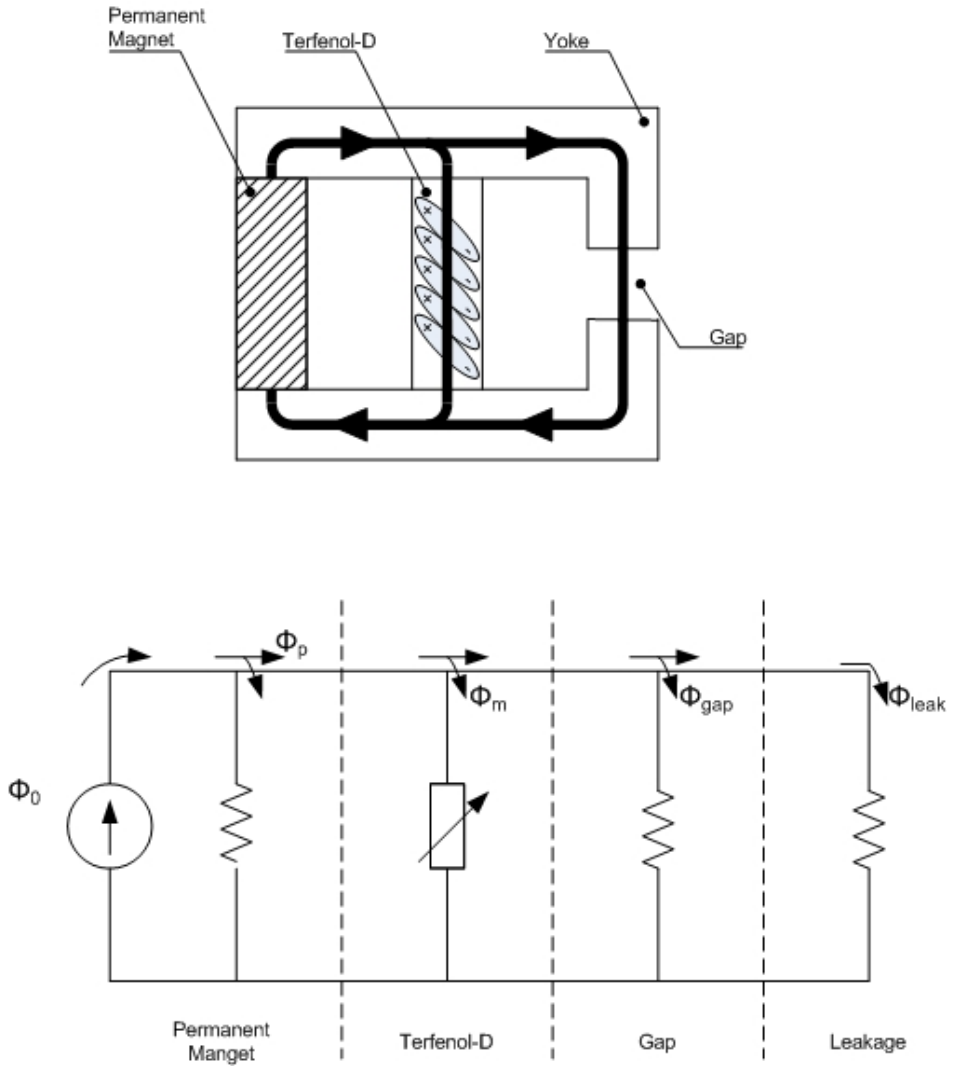

Figure 2-22 The magnetic equivalent circuit for flowmeter using Terfenol-D device

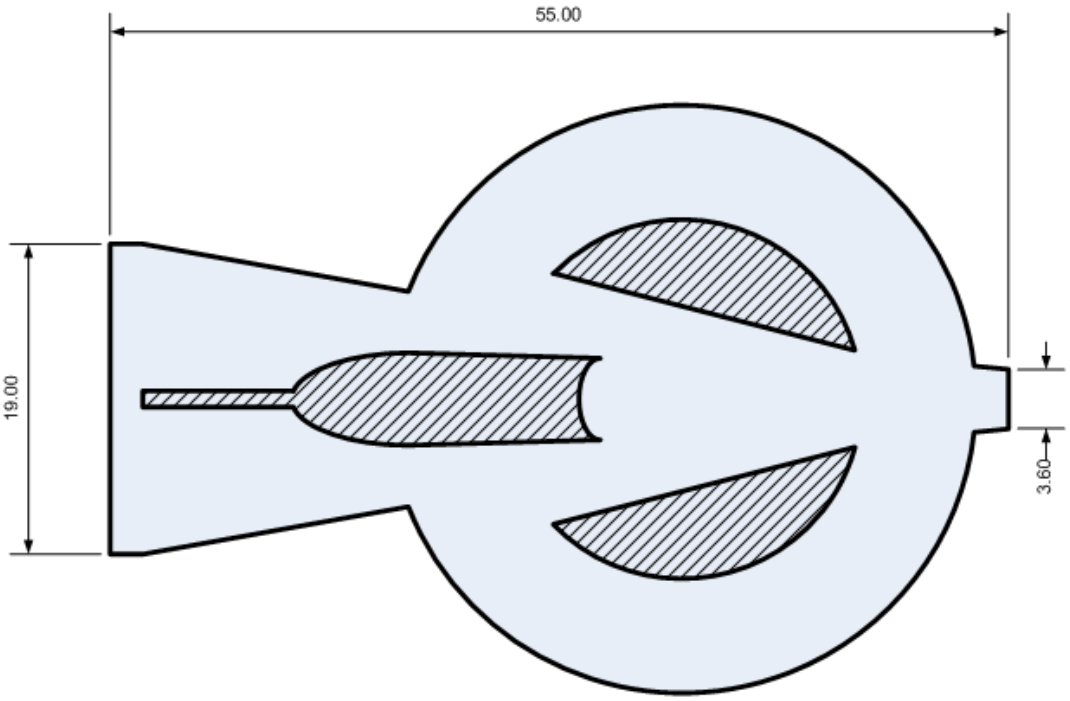

Figure 2-23 Geometry of fluidic oscillator

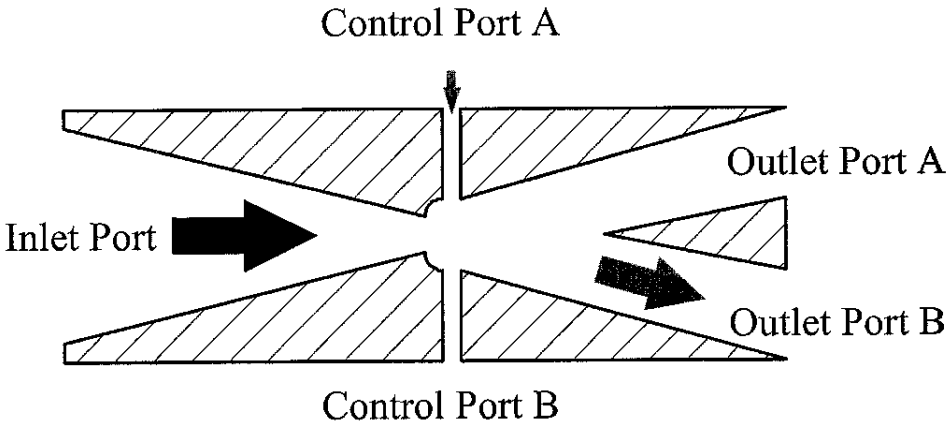

Figure 2-24 Coanada swtich

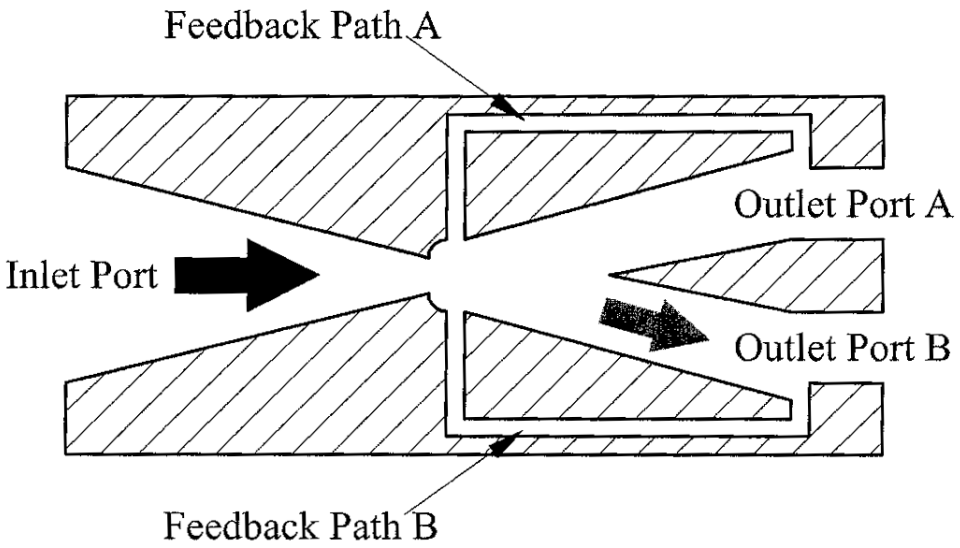

Figure 2-25 Feedback Oscillator (Wilson, 1970)

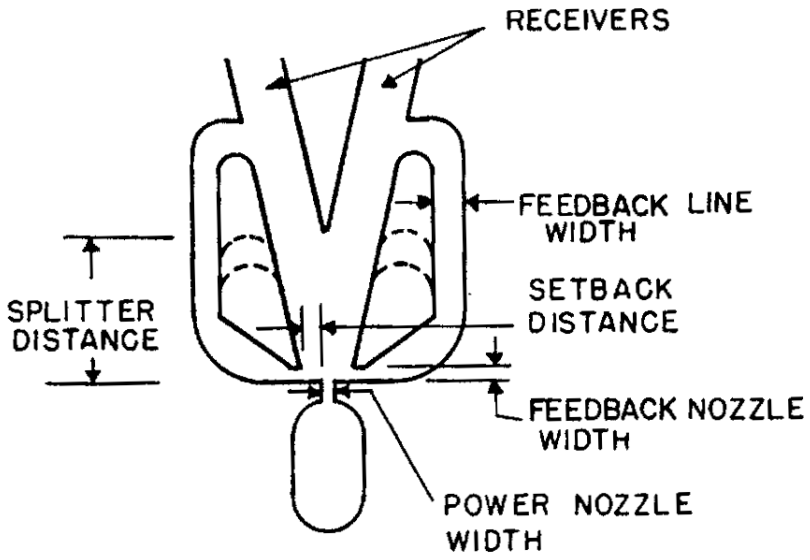

Figure 2-26 Fluidic oscillator by Wilson *et al.* (1970)

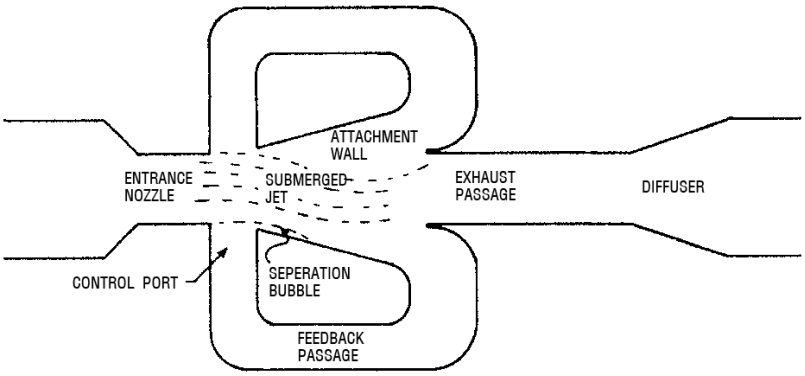

Figure 2-27 Fluidic oscillator by Beale and Lawler (1974)

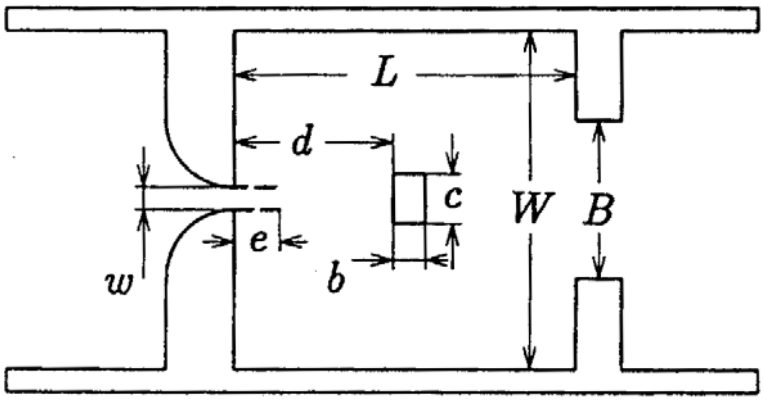

Figure 2-28 Target fluidic oscillator by Honda and Yamasaki (1985)

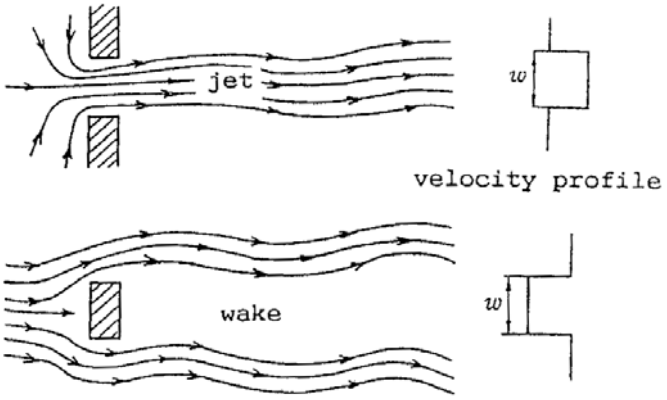

Figure 2-29 The relationship of jets and wakes (Honda and Yamasaki, 1985)

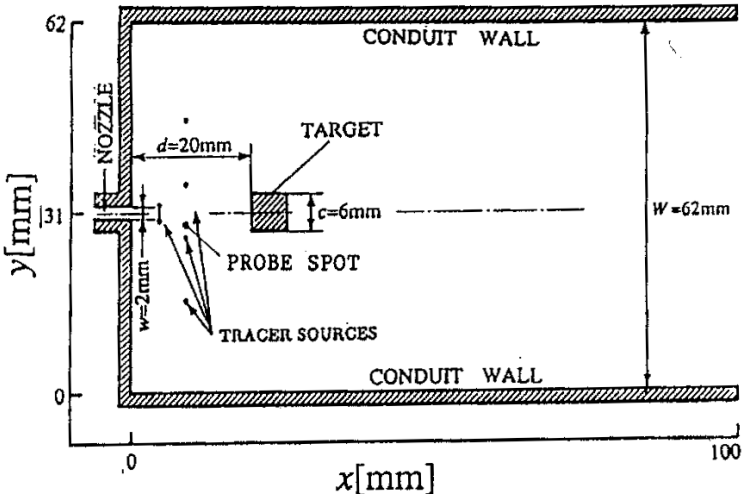

Figure 2-30 Simple target meter by Yamasaki *et al.* (1988)

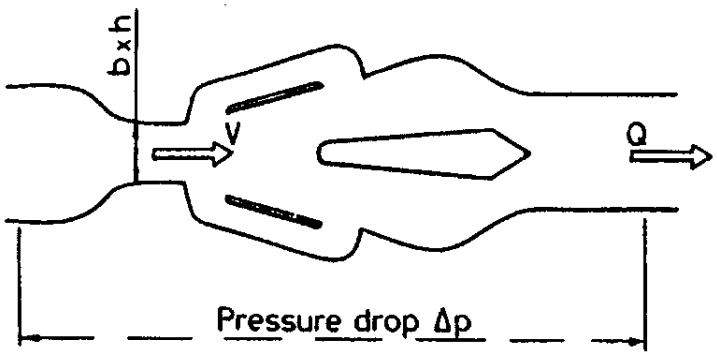

Figure 2-31 U100 fluidic oscillator by Kalsi *et al.* (1988)

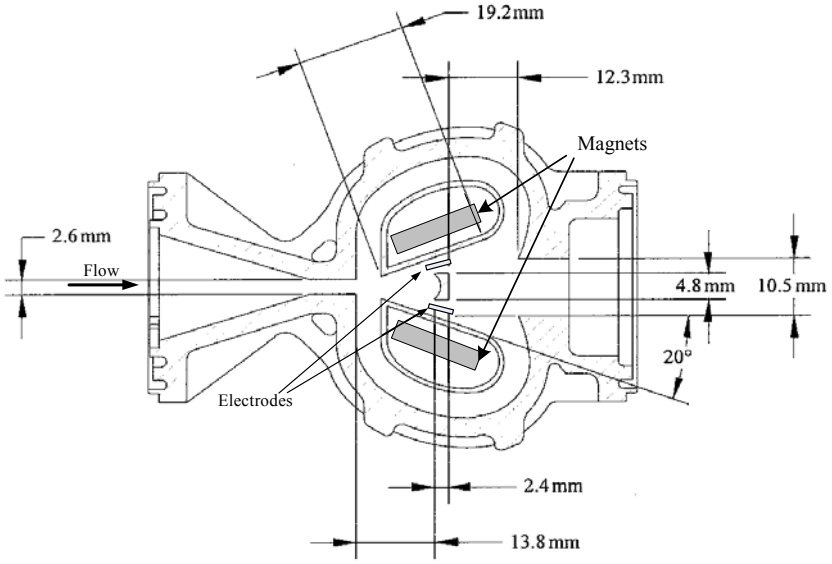

Figure 2-32 Drawing for the fluidic oscillator currently using for the domestic water metering (Harvey, 2004)

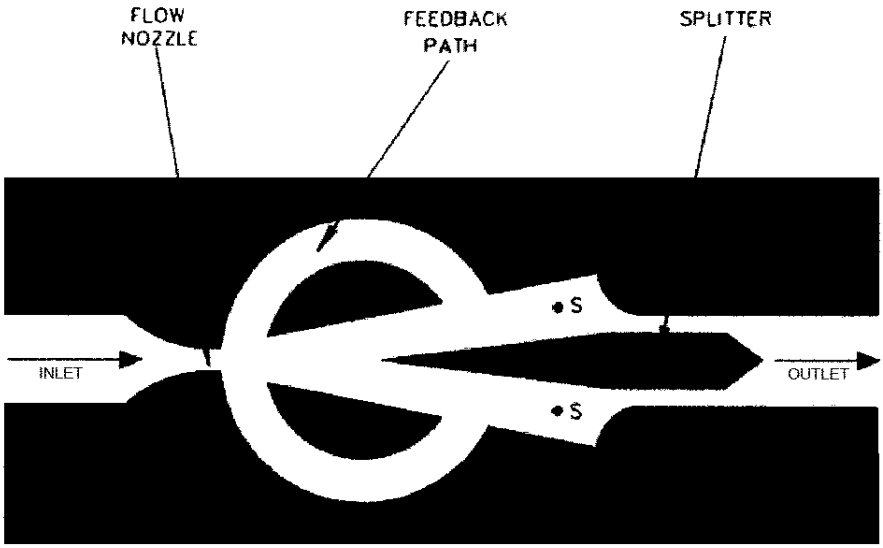

Figure 2-33 The schematic of fluidic oscillator by Boucher *et al.* (1991)

Chapter 3. Simulation tool and flow test rig

3.1 Simulation procedure

In this chapter the flow signal simulation procedure is described as shown in Figure 3-1. To design A flowmeter, the shape of flow channel, the magnetic field source as either coils or a permanent magnet and the shape and location of electrodes and geometry have to be understood. In this work, COMSOL Multiphysics software is used to simulate the design of flowmeter to understand those key factors.

The electromagnetic flow signal is calculated by computing the magnetic field, the virtual current and the velocity profile for the given design. The magnetic field and the virtual current can be simulated using the AC/DC module of COMSOL multiphysics software and then converted into 3-dimentional matrices covering the volume of the flow channel for use by MATLAB. The results file of COMSOL is exported to MATLAB for this conversion, then the weight function is calculated using MATLAB.

In this thesis, the computational fluid dynamics (CFD) modelling for the velocity field is undertaken in simplified 2D geometry instead of using 3D geometry. The fluidic oscillator has a rectangular cross-section so this simplification is possible. Further discussion about using 2D geometry is described in chapter five.

The velocity field is expanded to 3D by stacking the 2D layer up using the MATLAB program. For the fluidic oscillator, where the velocities are time varying, this modelling is

simulated in transient mode so the velocity field at each time-step is saved for computing the signals generated by the interaction of the flow with the magnetic fields.

Finally, the flow signal is calculated from the weight function and the velocity field for a particular time period. The flow signal is then plotted for evaluation. The results are considered for improvements to the meter performance and the results fed back to change the design or configuration of the flowmeter.

This procedure is looped until the target performance is achieved and the effects of changing design parameters and the flowmeter configuration are understood.

3.2 COMSOL Multiphysics

In this thesis, the research is undertaken using modelling software and the numerical data processing language package to simulate the flow signal from the proposed flowmeter design in this study.

The software simulation is undertaken to calculate the flow signal which can be calculated by the simulation of the flow behaviour on a flow chamber design, the magnetic field distribution with the magnetic material configuration as a permanent magnet or coils, and the virtual current which depends on the design of the flow chamber and the shape of the electrodes. COMSOL Multiphysics software is mainly used for the above simulation and MATLAB tools are used for further calculation. A screen capture for COMSOL is shown in Figure 3-2.

COMSOL Multiphysics is a unique modelling package in an interactive environment for the simulation of a single or coupled physical process and can be described with partial

differential equations (PDEs). The software has solvers that address complex problems, while its intuitive structure is designed to provide ease of use and flexibility. COMSOL Multiphysics has a built-in drawing tool, mesh generator, solvers and post-processing tools. The modelling results can be translated into MATLAB for continuous works.

COMSOL Multiphysics consists of several modules such as: AC/DC, Acoustics, Chemical Engineering, Earth Science, Heat Transfer, MEMS, RF, Structural Mechanics and CAD Import. Figure 3-3 is a diagram of COMSOL multiphysics and modules.

In this thesis, the AC/DC and Chemical Engineering modules are used to simulate the virtual current and magnetic field modelling in the particular geometry, and the fluid behaviour for the fluidic oscillator.

The AC/DC module is used for modelling the performance of capacitors, inductors, motors and microsensors. Although these devices are principally characterised by electromagnetics, they are also affected by other types of physics. The AC/DC module is used for the magnetic field simulation and the virtual current simulation in this thesis. The magnetic field simulation is also made with coils and a permanent magnet material.

The Chemical Engineering Module is the tool for process-related modelling. It is specifically designed to easily couple transport phenomena – computational fluid dynamics (CFD) or mass and energy transport – to chemical reaction kinetics. The Chemical Engineering Module is used for CFD modelling for a flow chamber and performed in 2D.

MATLAB is the high-level technical computing language created by Mathworks, which can handle all kinds of data including numbers and strings, interactive environment for algorithm development, data visualisation, data analysis and numeric computation. It also solves computing problems faster and even simpler than traditional programing languages, such as C, C++ and FORTRAN. MATLAB allows easy matrix manipulation, plotting of

functions and data, implementation of algorithms and interfacing with programs in other languages. The applications of MATLAB are wide including signal and image processing, communications, control design, test and measurement, financial modelling and analysis, and computational biology.

In this thesis, several data processing programs are coded based on MATLAB programing language to calculate and analyse the flow signals and plot them. Further descriptions about how to adapt these software packages into this research will be explained later.

3.3 Flow test rig

The experiments were undertaken using a Class D test rig in the PASE Lab at Cranfield University. The test rig consists of a water tank, pump, pipe works, diverter and weighing system. The water flowrate can be calculated by measuring the weight of water diverted into the weighing tank in the time interval measured during the diversion. This method is one of the most accurate methods for calibrating flowmeters and is used widely by flowmeter manufacturers and calibration laboratories.

The schematic for the Class D test rig in the PASE Lab is shown in Figure 3-5. A three cubic meter size water tank supplies water to the test rig, taken from a water tap controlled via a float ball valve. The main pump takes water from the tank and delivers the supply to the main pipe line. The flowrate through the pipe line can be set from 0 m^3/h up to 6 m^3/h and the flowrate is set by changing the pump speed and the flow control valve.

The bypass line from the main flow line diverts flow back into the water tank to help the pump to operate at a constant rate and reduce any pulsation which may cause instability of flow, especially at low flowrates. A picture of the Class D test rig is shown in Figure 3-4 and Figure 3-5.

The supply flow to the main line takes two different flow paths using loop control valves. When the lower loop control valve is opened, the flow path is about 20 metres long. If the lower loop control valve is closed and lets water flow through the shortest loop, then the flow path will be 7.55 metres from the pump to the testing section. There is a straight upstream pipe run of at least 1.65m from the last bend of the loop to the front of the flowmeter test bed and this ensures that the straight upstream pipework is 75 times the pipe diameter to stabilise the flow.

Once the flow has gone through the flowmeter on the test bed, the flow will travel though the swan neck, the control valve and into the nozzle which is the end of the pipework. The nozzle is shaped like a fish tail which is the flattened triangle with flat end to produce a thin jet which can be diverted into the weighing system or the water tank. The fish tail jet nozzle has a 60mm by 2mm cross-section at its exit. The optical sensor located at the diverter measures the time interval of the diverting.

Figure 3-6 shows the fish tail jet nozzle and the diverter. The diverter rotates around an axis which is located at the bottom and left corner of the diverter and can cut across the jet stream from the nozzle to divert water into the weighing tank. The shape of the diverter is designed to make a perfect diversion without any loss of water. The optical switch located on the frame of the diverter triggers the electrical timer on and off to measure time of diversion, t.

Figure 3-7 shows the weighing system of the test rig. The weighing system consists of the weighing tank, the weighing scale and the electrical timer. The trigger signal from the optical switch of the diverter activates the timer. When the bar is moved off the optical switch, the timer runs and the bar is moved back into the optical switch, and the timer stops. The timer has a highly accurate oscillating crystal and can measure 0.0001 of a second. The water passing through the diverter is caught in the weighing tank which is

located on the weighing scale. The weighing scale can measure up to 50kg at 0.0001 kg resolution. The flowrate is calculated by dividing the weight by diverted time.

The signal from the water meter is taken on the Ono Sokki FFT spectrum analyser which is shown in Figure 3-8. The analyser has two input channel having 10MOhm input impedance. The Fast Fourier Transform (FFT) spectrum analyser stores the input signal waveform which is time-domain, as sampled discretely, determines the Fourier coefficients using FFT and displays the results of this analysis in frequency-domain.

For the experiments in this thesis, the analyser was used to pick up the flow signal directly from electrodes to analyse on screen in real time. This instrument was used to understand the relationship between the oscillation frequencies and flowrates for the fluidic oscillator as well as the conventional dc pulsed electromagnetic flowmeter.

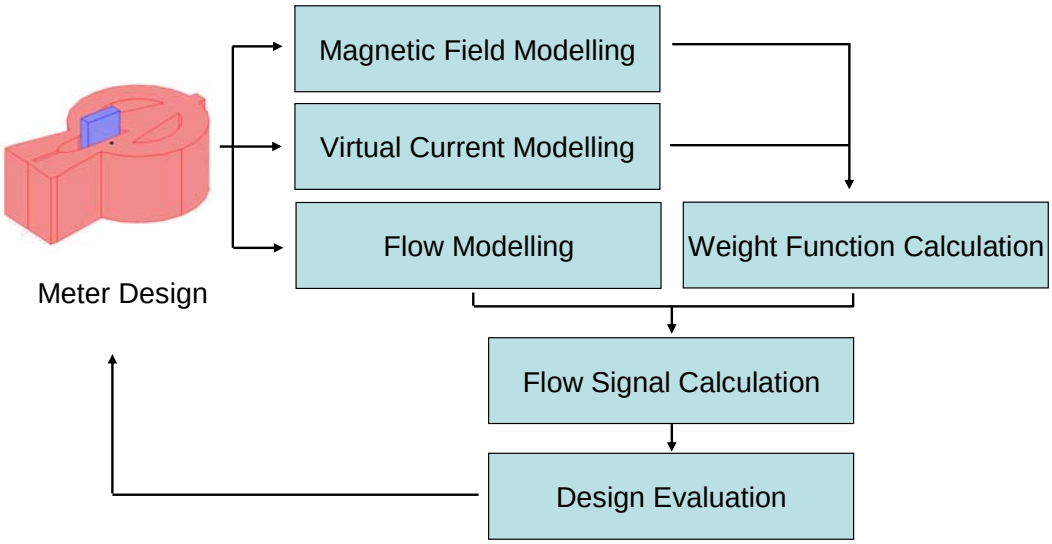

Figure 3-1 Simulation procedure

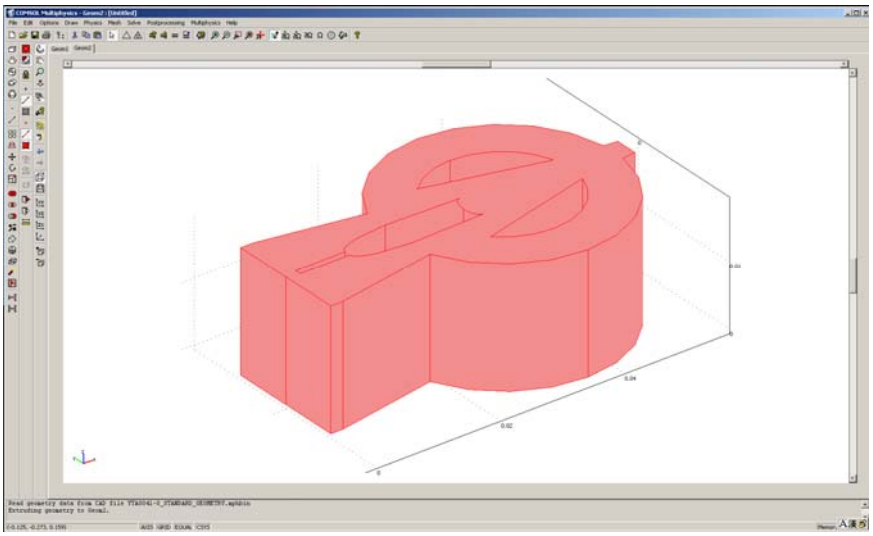

Figure 3-2 Screen capture of COMSOL Multiphysics

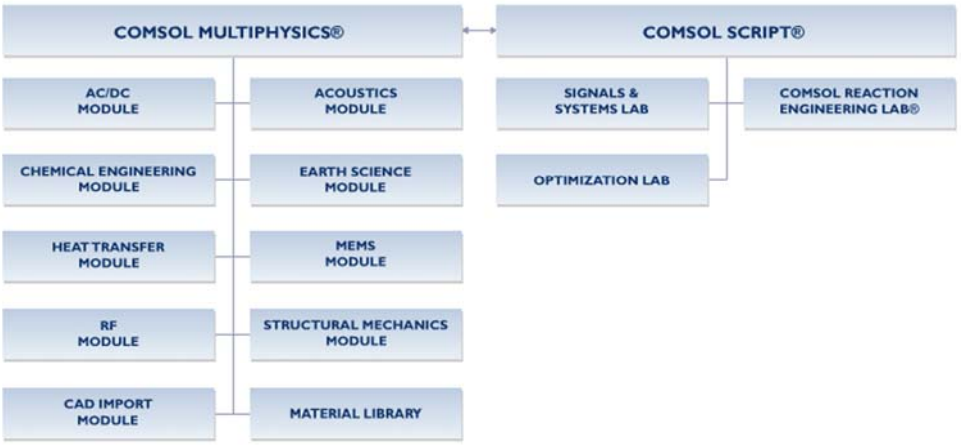

Figure 3-3 Diagram of COMSOL Multiphysics and modules

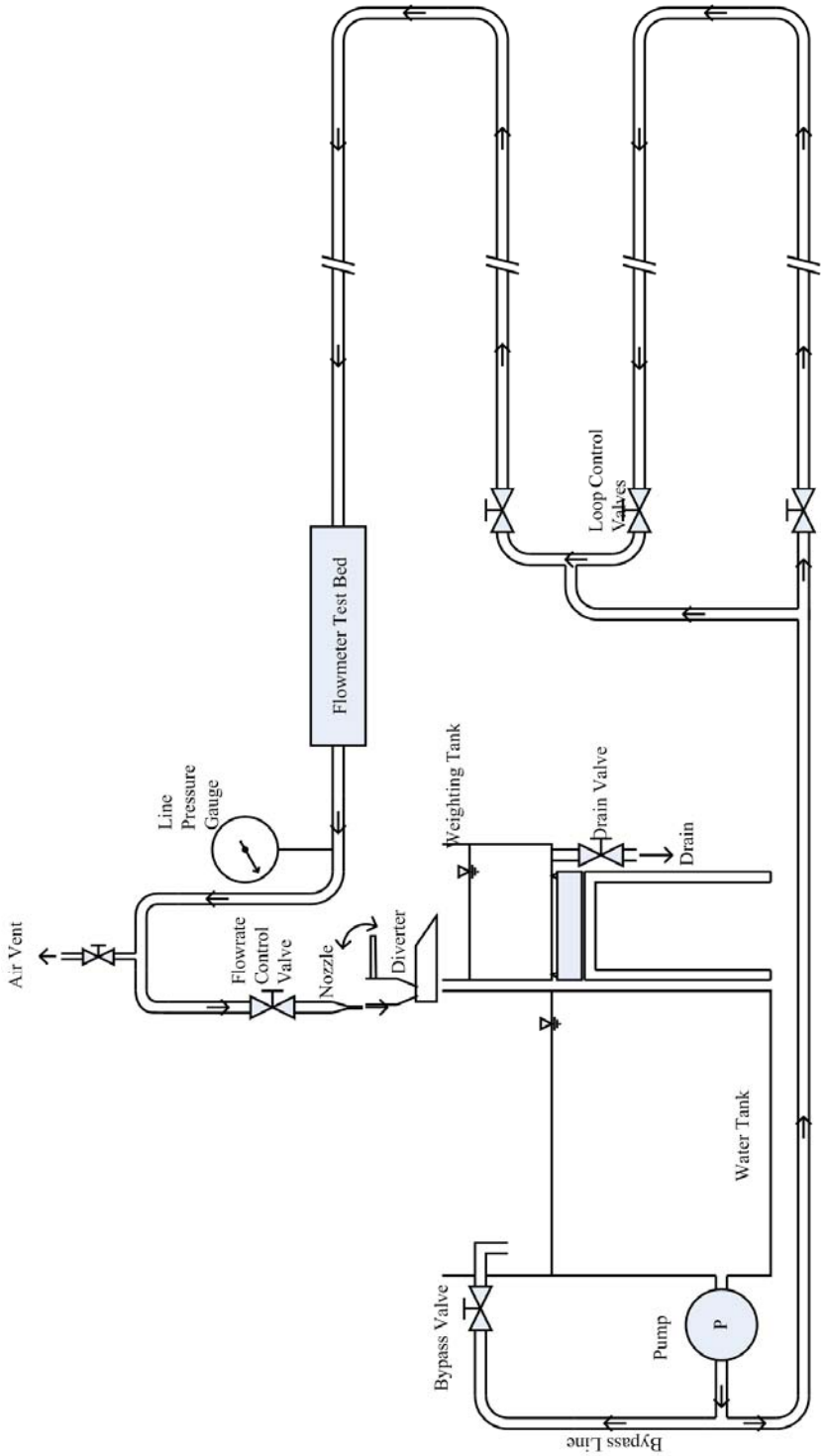

Figure 3-4. The schematic of Class D test rig in PASE Lab, Cranfield University

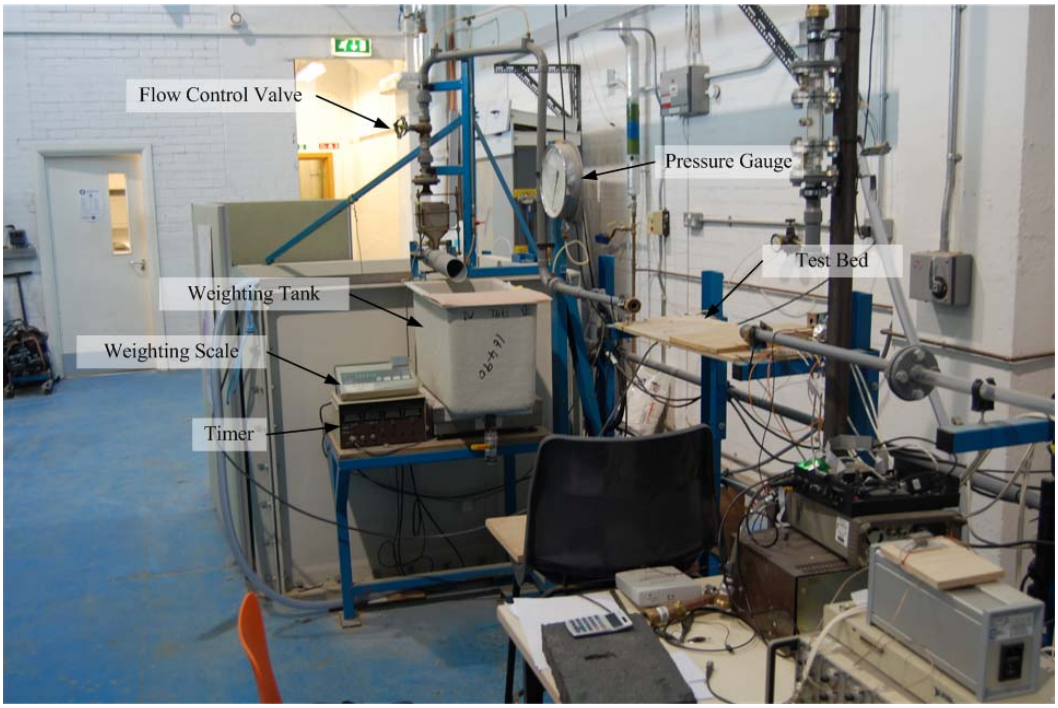

Figure 3-5 Picture of Class D test rig in PASE Lab

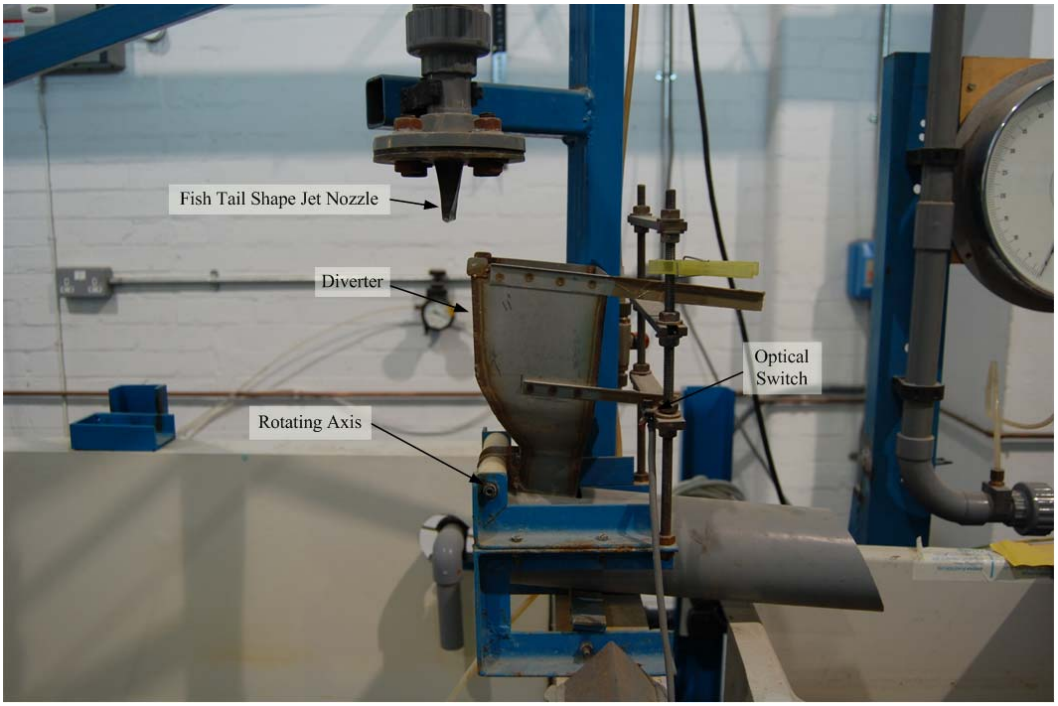

Figure 3-6 Fish tail shape jet nozzle and diverter of the test rig

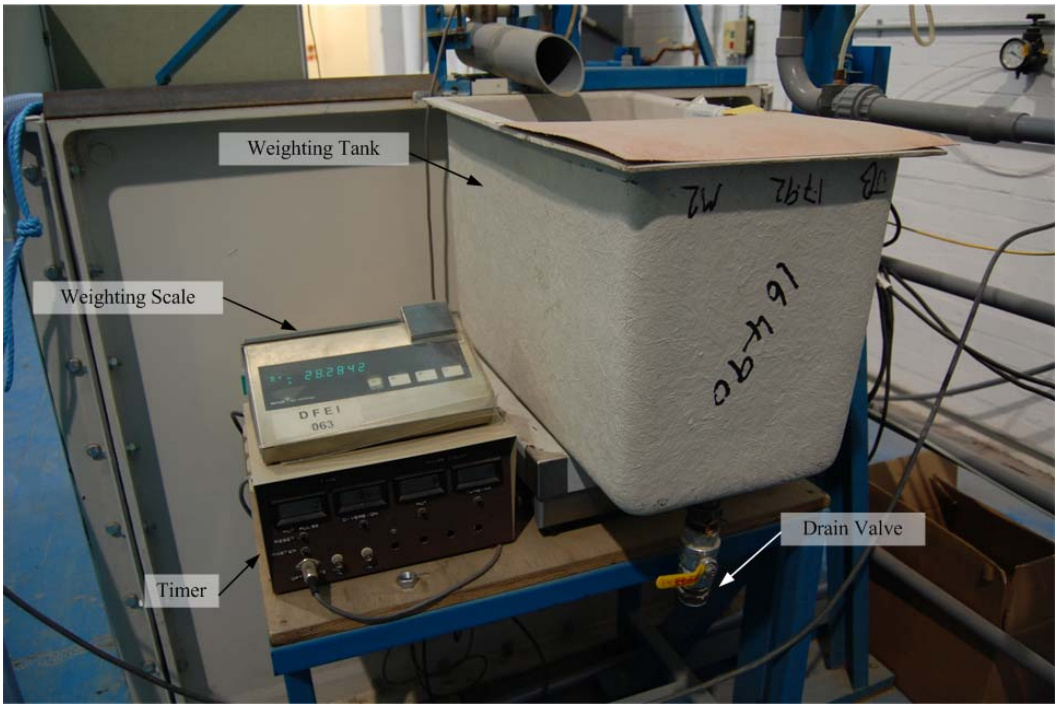

Figure 3-7 Weighing system

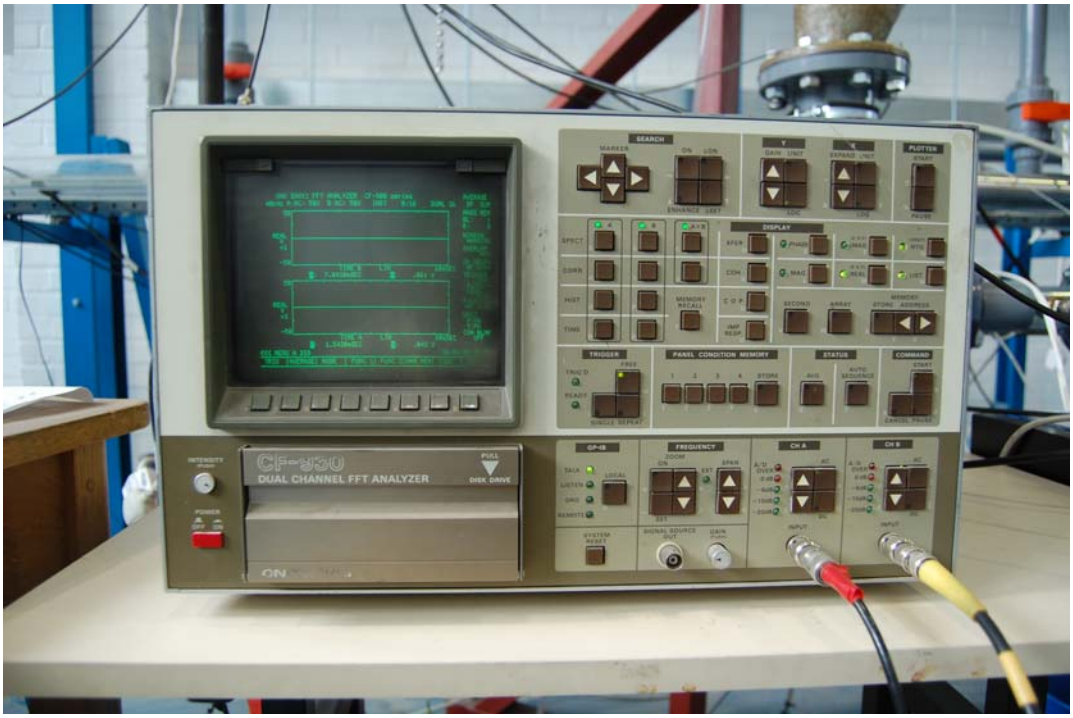

Figure 3-8 Ono Sokki FFT spectrum analyzer

Chapter 4. Conventional electromagnetic flowmeter

4.1 Introduction

In this chapter, the analysis of a conventional electromagnetic water meter having a rectangular flow channel is given and improvements are proposed. The design is modified to increase the flow signal at the same flowrate to enable the meter either to operate with improved signal to noise ratios or with lower power consumption by maintaining the flow signal but reducing the current to the coil.

4.2 Meter design

First of all, the given electromagnetic flowmeter design having a coil to generate the magnetic field is investigated and simulated. This flowmeter is designed as an ideal electromagnetic flowmeter as described in the previous chapter, in which it consists of a rectangular flow channel, line electrodes and a uniform magnetic field. Such a design is desirable for use in domestic water metering since the range of flows is such that the flow regime changes from laminar to turbulent and with the change there is also a change in velocity profile. The ideal flowmeter responds only to the mean flow and not to the velocity profile.

Figure 4-1 shows the outline diagram of the given electromagnetic flowmeter having a coil and a transformer core. This flowmeter has a rectangular flow channel, a C-shape transformer core which is made with soft iron, and coils which are located at the middle of the transformer core and opposite to the opened gap.

The rectangular flow channel has a 10mm width, 4.5mm height, a cross-sectional area of 45mm^2 and the length of the flow channel is assumed to be 40mm long. The rectangular flow channel is typically made with an engineering plastic with at least 1.0mm wall thickness to ensure that it will withstand the line pressure of the water distribution system so that the basic design of this meter has a 6.5mm gap between ends of transformer.

The coil is assumed to have 5,000 turns of copper wire having a gauge of 0.32mm (AWG 28). AWG stands for American Wire Gauge for copper wire and the copper resistance is 212.872 Ohm/1000m (Wire Gauge and Current Limits, www.powerstream.com). The coil dimensions are: height 45mm and outer diameter 32.8mm. The length of wire is calculated as 336.2m and resistance is 71.56 ohms.

A pair of line electrodes are placed in the middle of the rectangular flow channel vertically and facing each other. The length of line electrodes is the same as the height of the flow channel but with a thickness which is infinitely narrower in the axial direction giving an ideal concept electrode. A drawing of the rectangular flow channel and the line electrodes is shown in Figure 4-2.

For the mathematical model, the flow channel is converted to a series of cubes as elements of the flow signal, each of which has 0.1mm by 0.1mm by 0.1mm dimensions. This model can help in converting modelling results from COMSOL Multiphysics into a 3-dimensional matrix to be used in MATLAB software for further analysis. During the converting, the rectangular flow channel is converted into the numerical matrix having 401 by 101 by 46.

The flow signal calculation can be obtained by having a model for each component of the electromagnetic sensing technique which is obtained from the magnetic field, the virtual current and the flowrate. Before starting the simulation, the following assumptions are adopted to undertake modelling in this chapter:

1) The electrodes have high and uniform contact impedance.
2) Flow profile only has a rectilinear component in laminar or flat profile.

Assumption 1) means that the current from the fluid in and out of the electrode is neglected and an electrode potential then settles at the mean value of the potential over the electrode area. Assumption 2) means that these modelling results have compared the sensitivities for two velocity profiles which have no swirl and are not disturbed. The first assumption is valid for electrodes which are narrow in the axial direction. The second assumption is valid because the development length of the meter after the inlet contraction will be short for laminar flow and in turbulent flow will lead to a flat profile which will not be developing within the measuring section of the meter.

By using this approach, it is possible to employ an analytical expression for the velocity profile under laminar flow, compute the potential at any point of the side wall of the flow channel and then compute the average potential over an electrode shape which is symmetric to the vertical centre line of the flow channel, and to examine the ratio of the sensitivity of the flowmeter as the flow changes from laminar flow to a flow with a flat flow profile.

With assumption 2), the flow has only x-components therefore the z-component of the magnetic fied and the y-component of the virtual current only have been considered.

4.3 Modelling of conventional electromagnetic flowmeter

4.3.1 Magnetic field modelling

Figure 4-3 shows the geometry of the flowmeter design for the modelling which includes the coil and the transformer core with the rectangular flow channel in 2D. The 40mm long rectangular flow channel is located between two ends of the C-Shape transformer core which has been made with a piece of soft iron steel, the flow channel has a top and bottom wall as thick as 1mm but the thickness of the wall has varied from 0mm to 2mm in order to understand the distribution of the magnetic field in the flow channel.

The soft iron is almost pure iron, has a low carbon content and is easily magnetised and demagnetised with a small hysteresis loss. Normally soft iron has less than 10% of carbon and no other appreciable alloying element. Soft iron is the most common form of steel as its price is relatively low while it provides material properties that are acceptable for many applications. In this modelling, the electric conductivity of soft iron is set at 1.12×10^7 S/m and the relative permeability of mild steel, μ_r is set at 2000 (Gilmour, 1986).

The dimensions of the coil are: outer diameter 37.4mm and height 45mm when the coil has a 5,000 number of turns with 0.32mm gauge wire. The coil is wound on the vertical post of the C-shape transformer core and it is assumed that there is no space between the wires to form the coil when winds wire because the coil has been treated as a single conductor in the modelling software, which has a certain current density according to the number of turns, the supplying current and cross-sectional area.

Because of the complexity of the geometry of the meter, the modelling is undertaken in 2D geometry. In the modelling geometry, the coil is divided into two cross-sectional parts by

the transformer core and each cross-sectional area is set to a current density parameter from actual operational conditions.

The supply current to the coil is assumed to be controlled to 2mA. The coil has 5000 turns so its ampere turn is I_o x $N.T.$ = 0.002 x 5000 = 10A·Turn. The vertical cross-section area of one side of coil is 45 mm x 11.4mm = 513 mm^2 = 5.13 x 10^{-4} m^2. Therefore the current density at the one side of the cross-sections of coil in the modelling is 19493.2 A/m^2 and the opposite side is −19493.2 A/m^2. This current density values are assigned for the sub-domain parameter for the modelling.

Figure 4-4 shows the mesh structure of the modelling. The number of mesh points employed in the modelling is 10,900 and has 21,598 triangular elements generated automatically by the modelling software. In the gap area, a higher mesh density is assigned to improve the accuracy of the modelling. Hence the total number of meshes is not exactly the same for all the geometries having different gap sizes.

The modelling result for the geometry having the 4.5mm height flow chamber is shown in Figure 4-5. The area the author is concerned with is only the flow channel domain so the data have been taken into a 2D matrix using MATLAB. To adopt 2D results to the real flow channel with 3D geometry, a conversion program code in MATLAB has been devised. Because the shape of the transformer core is cylindrical, the magnetic field is axially symmetric and 3D results can be analysed by rotating a 2D matrix around the axis of the transformer core.

In the 3D model, the magnetic flux density B_{3D} at the each grid is calculated by

$$B_{3D}(x, y, z) = B_{2D}(\sqrt{x^2 + y^2}, z) \qquad (4\text{-}1)$$

where the centre of the transformer core is set as the origin. The algorithm of the rotating data is shown in Figure 4-6. Verification of the data rotation technique, simplified 3D cylindrical model which has a permanent magnet, has been undertaken and compared with the results from 2D modelling of the same geometry.

Figure 4-7 shows the vertical component of magnetic flux density, B_z along the centre line of the rectangular flow channel having 10mm width and 4.5mm height. The transformer core is located between 15mm and 25mm in the plot. The wall thickness of the model has been varied from 0mm to 1.5mm. The plane plots in the middle of the flowmeter with different wall thicknesses are shown in Figure 4-8. The magnetic flux density is quite uniform under the end of the transformer core but near the edge of core the magnetic flux density is reduced because the vertical component of the flux is decreased while the flux diverges. The line with square symbols in figure 4-7 shows the magnetic field when the wall thickness is set to 0 which means that no actual wall exists. The case is more likely to be that the real geometry is shown in the line with circle symbols in figure 4-7. The modelling is set to 1.5mm wall thickness at the top and bottom sides of the flow channel. The wall makes the length of air gap longer so the magnetic field level is lowered.

The maximum value of the B_z is 2.7×10^{-3} T without any wall and 1.4×10^{-3} T with 2.0mm thick wall at the top and down-side of the flow channel. To increase the level of signal with the same supply current to the coils, the air gap between the ends of the transformer core should be reduced. However the actual flow channel has to be made with a thickness to endure a line pressure of 16bar and thus a wall thickness of less than 1mm is not practical. Therefore a minimum air gap is proposed to be 6.5mm for a 10mm by 4.5mm rectangular flow channel and the maximum magnetic flux density is obtained as 1.75×10^{-3} T.

4.3.2 Virtual current modelling

As shown in the literature review in chapter two, the virtual current ***j*** represents flow signal contributions at unit space inside the flow channel and has dependency on the geometry of the flow channel and the shape of the electrodes.

For this virtual current modelling, the Conductivity Media DC Mode of AC/DC Module of COMSUL Multiphysics is used. The AC/DC module contains a set of application modes adapted to electromagnetic simulations and the Conductivity Media DC Mode simulates the current in a conductivity material under the influence of an electrical field.

In the model, the 40mm long rectangular flow channel is designed with line electrodes in the middle of the channel as shown in Figure 4-9. The positive line current source is applied at the red coloured electrode line in the figure and the negative line current source at the blue coloured electrode.

For the line electrodes, line current source Q_{jl} is applied to the edges shown in Figure 4-9. The unit of Q_{jl} is electric current per unit length. 1 A/m is set for the line current source for these boundary conditions and therefore the value for the edge parameter for the modelling is±≠ obtained by dividing 1 by the length of the line electrode. As a result, the edge parameters for the modelling of 4.5mm height flow channel are set at 222.22 A/m for the positive line electrode and −222.22 A/m for the opposite electrode.

Figure 4-10 shows the y-component of virtual current on the middle plane of the rectangular flow channel. The virtual current comes from the left hand side electrode to which the positive current source is applied and travels toward the right hand side electrode which has the negative current source. The boundary of the flow channel is set as the electric insulator which means that there is no loss or extra supply on the boundaries as described;

$$\mathbf{n} \cdot \mathbf{J} = \mathbf{0} \qquad (4\text{-}2)$$

The virtual current density near the electrodes is very much higher than at the centre of the flow channel. This means the contribution to the flow signal near the electrodes has a greater effect on the flow signal if the uniform magnetic field and the rectilinear flow are applied into the flow channel. In practice, however, this greater effect near the electrode is not always welcome because of the sensitivity issue which depends on flow profile. To reduce the unnecessarily large effect near the electrode in a point electrode circular cross-section electromagnetic flowmeter, the magnetic field will be modified to give more weight, not around the electrodes but towards the middle of the flow channel. The surface graph of virtual current in the middle of the flow channel is shown in Figure 4-11.

4.3.3 Weight function

The weight function models how the electromotive force generated at each point of the flow channel contributes to the total flow signal and is calculated using equation (2-13). Hence for a flow which is rectilinear and which has only x-component of flow, the weight function can be calculated using only y-component of the virtual current and the z-component of the magnetic field as

$$W_x = B_z \cdot j_y \qquad (4\text{-}3)$$

Where W_x is the x-component of weight function, B_z is the z-component of the magnetic field and j_y is the y-component of the virtual current. The weight function of modelling is calculated by multiplying together the two components of the vectors B and j.

The weight function is shown in Figure 4-11. The contributions to the flow signal near the electrodes are significantly higher than in any other area.

4.3.4 Flow signals

The flowmeter performance can be evaluated by the sensitivity to the flow profile. The sensitivity S which is described in chapter two, is a dimensionless quantity to evaluate the performance of the electromagnetic flowmeter. This quantity is important for water meters because the flow range to be measured covers laminar to turbulent flow profiles. The meter has to have less sensitivity against the flow profile change which means the sensitivity is close to 1.

By the definition, the sensitivity is defined as the ratio of the electric potential difference, U_{XY} induced between two electrodes X and Y as:

$$S = U_{XY} / LBv_m \tag{4-4}$$

where L is the distance between electrodes X and Y, B is the scalar of magnetic flux density and v_m is the mean velocity. In the case of a real electromagnetic flowmeter, the sensitivity can be written using the flow signals in the laminar flow profile and the flat flow profile as:

$$S = U_{\text{laminar}} / U_{\text{flat}} \tag{4-5}$$

In this chapter, the laminar flow profile is calculated by

$$\frac{v_x}{v_m} = k(1 - \frac{x^2}{d^2}) \tag{4-6}$$

where v_m is the mean velocity, and d is the width of the flow channel in 2-dimensions. To calculate the laminar flow profile in the whole rectangular flow channel, equation (4-6) is expanded for 3D as:

$$v(x,y) = kv_m(1-\frac{x^2}{w^2})(1-\frac{y^2}{h^2}) \tag{4-7}$$

where w is the width of the flow channel and h is the height. The coefficient k has been determined by inverse calculation. Firstly, k is set as unity then the average velocity is calculated after obtaining the velocity profile using equation (4-7). With the velocity field, the average velocity v_m is calculated. After this step, k can be calculated by dividing the average velocity v_m by the desired average velocity. In this modelling, k = 2.2589 is used for a 10mm by 4.5mm rectangular flow channel. Figure 4-12 shows the laminar flow profile used in this modelling for the 10mm by 4.5mm rectangular flow channel at the mean velocity of 0.049 m/s which is equivalent to 8 L/hr with 10mm by 4.5mm rectangular flow channel.

A flat flow profile also assumed and generated to be used to calculate the sensitivity, S of the flowmeter; the flat flow has uniform flow velocity over all the cross-section of the flow channel except that the flow velocity is zero at the wall.

The flow signal can be calculated by equation (2-12). In this model, the flow channel has been divided into 401 by 101 by 46 cells which represent the contribution of the flow signal at each cell and the unit volume of the cell is $(0.0001)^3$ m^3. Equation (2-12) can be rewritten as:

$$U = \left(\sum_{i=1}^{401} \sum_{j=1}^{101} \sum_{k=1}^{46} u_x(ijk) j_y(ijk) B_z(ijk) \cdot 0.0001^3 \right) \tag{4-8}$$

where $u_x(ijk)$ is the flow velocity, $j_y(ijk)$ is the virtual current and the $B_z(ijk)$ is the magnetic flux density. The index *i, j, k* refer to the position of the cell. The flow channel has been divided into the unit cell which has the 0.1mm x 0.1mm x 0.1mm dimension, the contribution at each cell can then be calculated by multiplying by $(0.0001)^3$.

The flow signal of the geometry having 1mm thick walls on the top and the bottom of the flow channel at average velocity v_m = 0.049 m/s is 0.757 μV when the flow profile is laminar and 0.793 μV with a flat profile. The ratio of these two signals is 0.9670 and Figure 4-14 shows the ratio R, when the wall thickness varies for the 10mm by 4.5mm flow channel..

4.4 Improved meter design

The flow signal can be increased by reducing the air gap between the ends of the transformer core by a factor of 1.5 from 6.5mm to 5mm which means the height of the flow channel is changed from 4.5mm to 3mm. The width of the flow channel also can be modified from 10mm to 15mm but the cross-section area is the same as the original geometry which will ensure that the pressure drop within the meter body will be comparable to the original design. Figure 4-15 shows the cross-section view of the flow channels. Figure 4-15 (a) is for the 10mm by 4.5mm rectangular flow channel and Figure 4-15 (b) the 15mm by 3mm.

The sensitivity of the flowmeter also has to be addressed. The ratio of the laminar and flat flow signal should be closer to unity to have better meter characteristics. Therefore a pair of soft iron plates are applied to this modification in order to improve the uniformity of the magnetic field over the whole flow channel. The thickness of the soft iron plate is assumed

to be 1mm and the length is changed from 10mm to 40mm. The drawings for the modifications are shown in Figure 4-13.

Modelling is taken from 2D geometry and extended in the same manner as in the previous section. The plots of the z-component of magnetic field, *Bz* are shown in Figure 4-16 for the models which have the length of plates set at 15mm, 30mm and 40mm. The magnetic field between the soft iron plates is more uniform then by not applying them to the magnetic field. The plots of the z-component of magnetic flux density on the centre line of flow channel are shown in Figure 4-17. The figure shows that the magnetic flux density is flatter when the longer soft iron plates are in place.

Figure 4-18 shows the weight function on the middle plane of the 15mm by 3mm rectangular flow channel with a pair of 30mm long soft iron plates. The highly contributed areas displayed in the dark red coloured region near the electrodes are five times greater.

Figure 4-20 shows the flow signals of the rectangular flow channel which is 15mm wide and 3mm high with a wall thickness of 1mm. The flow signal calculation of laminar and flat flow profiles for the 15mm by 3mm rectangular flow channel with this geometry is 1.485 μV at 8 L/hr when 15mm long soft iron plates are applied and gives a 1.93 times greater signal than the original design of the flowmeter. The flow signal is increased by inserting longer plates and the ratio *R* is 0.99573 or close to unity when the plates cover the whole flow channel which is 40mm long. The chart of the ratio R v the length of soft iron plates is shown in Figure 4-21.

This means the improved meter has less sensitivity to the flow profile change and this is an important improvement for the water meter application because the meter is required to operate in both laminar and turbulent regimes. At the minimum flow Q1 of 8L/hr the Reynolds number is 740 which corresponds to laminar flow and at the maximum flow Q3 of 1.6m3/hr the Reynolds number is 14800 which corresponds to turbulent flow. The lower

sensitivity to change within the velocity profile implies that no correction to the meter factor with flow is required.

These modifications which reduce the air gap of the transformer core by a factor of 0.66 and placed a pair of soft iron plates to cover the flow channel, can improve the level of flow signal at about twice the minimum flowrate and the performance is more like the ideal flowmeter which is independent on flow profile. Alternatively with the same flow signal the power required in the coil will be reduced by a factor of 4 with a consequent reduction in battery volume.

The other advantage of this modification is to reduce the supply current in the coil by half from 2 mA to 1 mA to obtain the same level of flow signal as in the 10mm by 4.5mm rectangular flow channel. In that case, the flowmeter operates twice as long under the same operating conditions.

According to these results, the flow signal will be increased by changing the height of the rectangular flow channel but keeping the cross-sectional area. From the equation (2-3), the relationship of the flow signal, the magnetic flux density and the height of the flow channel at the given flowrate can be derived. The magnetic flux density is inversely proportional to the height, so the flow signal is:

$$e \propto \frac{B}{h} \tag{4-9}$$

The magnetic flux density can be calculated as:

$$B = \frac{1}{\mu_0} \frac{N \cdot I}{h + 2h_w} \tag{4-10}$$

Table 4-1 The flow signals of laminar and flat flow profile for 15mm by 3mm rectangular flow channel with varying lengths of soft iron plates at 8*l*/hr

Length of Plate [mm]	*Flow Signal (Laminar) [μV]*	*Flow Signal (Flat) [μV]*	*Ratio S* $U_{Laminar} / U_{Flat}$
15	1.485	1.526	0.97302
20	1.568	1.595	0.98317
25	1.616	1.634	0.98909
30	1.643	1.656	0.99262
35	1.658	1.667	0.99475
40	1.662	1.669	0.99573

where N is number of turns of coil, I is current to the coil, h is the height of the rectangular flow channel and h_w is the height of the wall at the top and bottom of the channel.

The ratios of signal increase by reducing the height are listed in Table 4-2. The values are normalised to unity to the original height. The flow signal is increased by 95% when the channel height is reduced from 4.5mm to 3.0mm. The calculated flow signal with a 4.5mm height flow channel is 0.757 μV at 8 L/hr and increases to 1.485μV for the 3.0mm height flow channel. The ratio of signal increase from modelling is 1.96.

The flow signal can be further increased by reducing the channel height as shown in Table 4-2, but the reduction is limited by two factors. The first is that the minimum gap of the channel must be bigger than 2.0mm to avoid any clogging by particles in the water.

Table 4-2 The ratio of signal increase by changing the height of channel.

d	*h*	$h+h_w$	*Increase ratio of B*	*Increase ratio of h*	*Increase ratio*
10.0	4.5	6.5	1.00	1.00	1.00
15.0	3.0	5.0	1.30	1.50	1.95
18.0	2.5	4.5	1.44	1.80	2.60
22.5	2.0	4.0	1.63	2.25	3.66
30.0	1.5	3.5	1.86	3.00	5.57
45.0	1.0	3.0	2.17	4.50	9.75

The other limitation is the manufacturing difficulty. The flow channel is usually moulded in one piece but in the case of the larger width, the channel has to be moulded in two pieces and bonded in the middle. The bonding point of this case is where the electrodes are inserted so the bonding may be broken when high pressure is applied. For these reasons, the 15mm by 3mm is finally presented for the improved design of the conventional electromagnetic flowmeter.

4.4.1 Calculation of Power consumption

The conventional electromagnetic flowmeter is to be operated with a D type cell having 3.6V and 19Ah capacity. The power consumption can be estimated by calculating the resistance of coil and supplying current.

The resistance of coil is 77.56 ohms as estimated in the previous section and the supplying current is assumed to be 2mA for the original design. The power consumption is then 286 μW. This power consumption is independent of the operating frequency of the electromagnetic flowmeter but is proportional to the duty cycle so that the power consumption will be reduced by half when the duty cycle is reduced by half, as shown in Figure 4-22.

The improvements can increase the flow signal to a factor of 1.96 at least, then this gain will be used to reduce the power consumption by decreasing the supplying current but keeping the signal level the same as the original design. The supplying current can be lowered by 51.0% to 1.02 mA for the improved design. The power consumption is also calculated as 74.4 μW at 100% duty cycle.

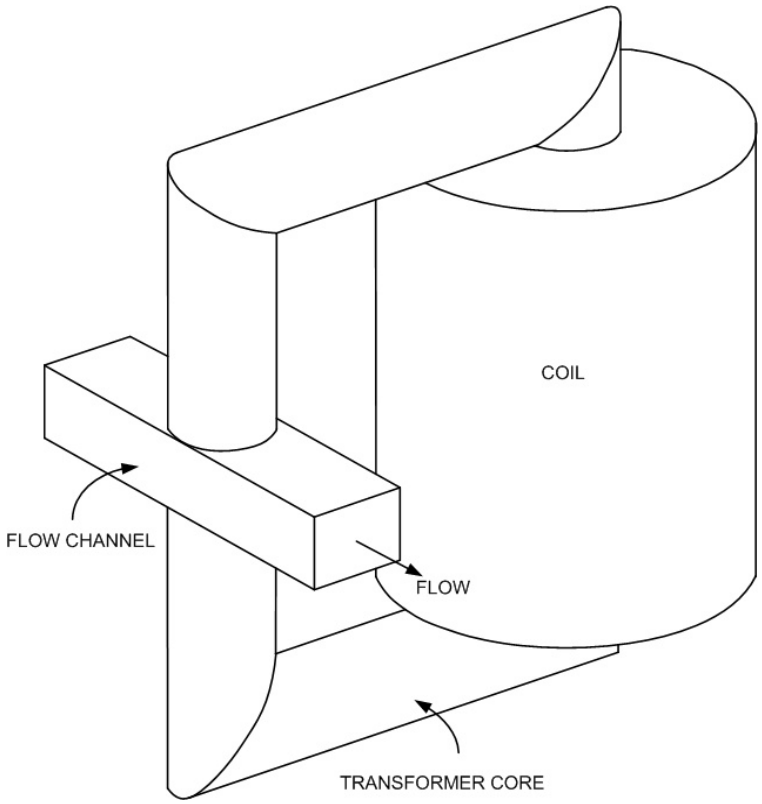

Figure 4-1 Conventional electromagnetic flowmeter

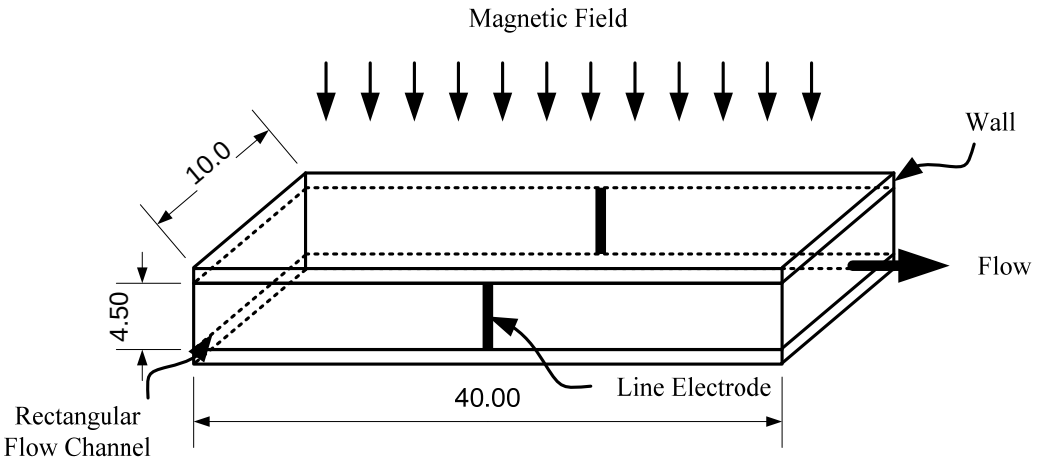

Figure 4-2 Dimension of the rectangular flow channel

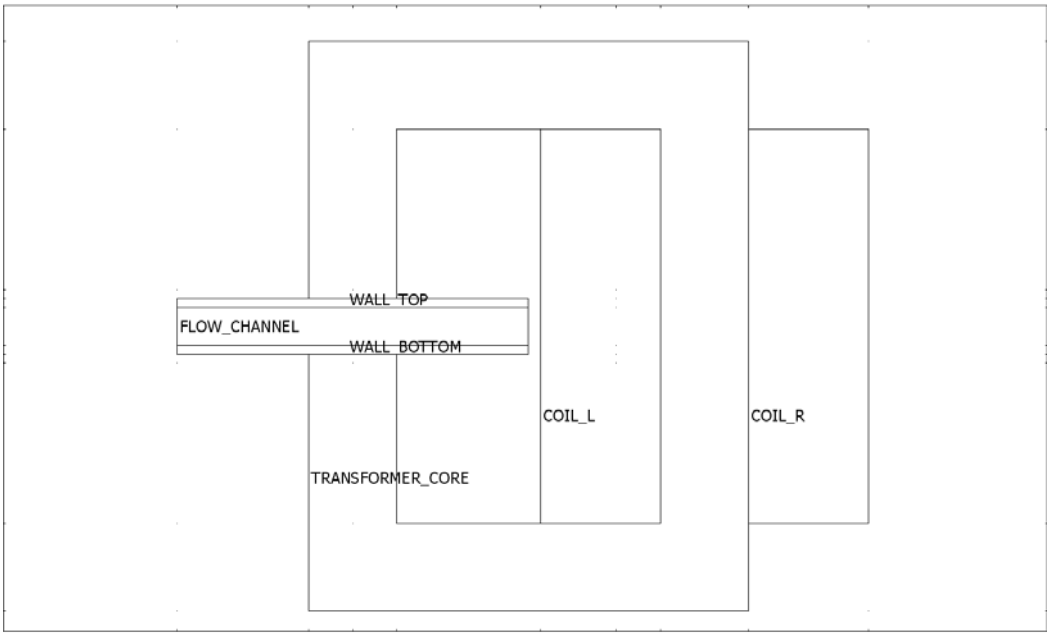

Figure 4-3 The 2D modelling geometry for the flowmeter using coils. The top and bottom wall of the flow channel is applied. The wall thickness is 1mm for both

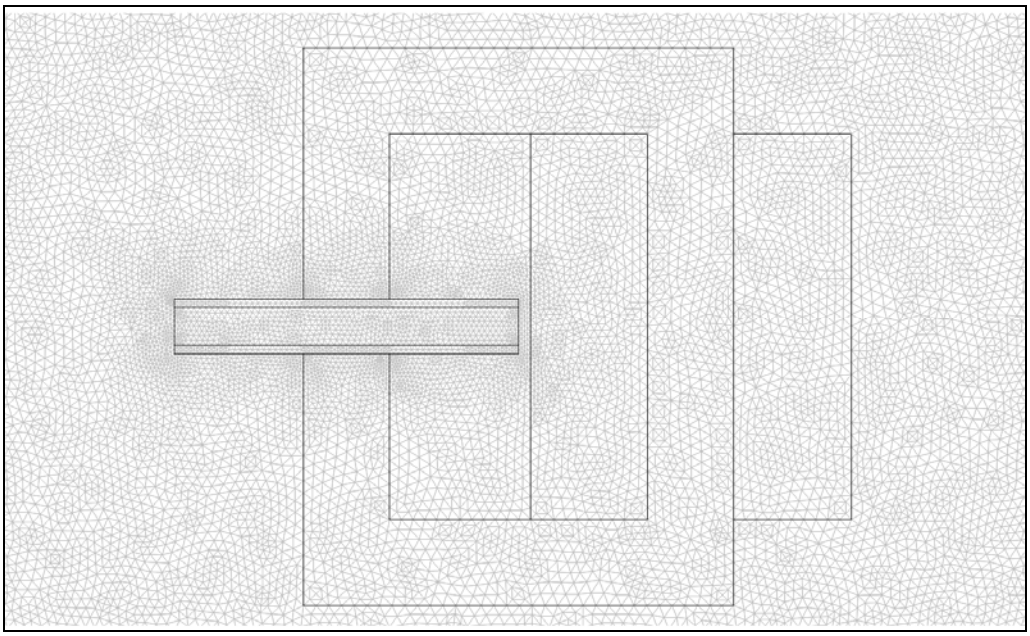

Figure 4-4 Mesh structure of the modelling. Much finer meshes are allocated in the flow channel and the walls

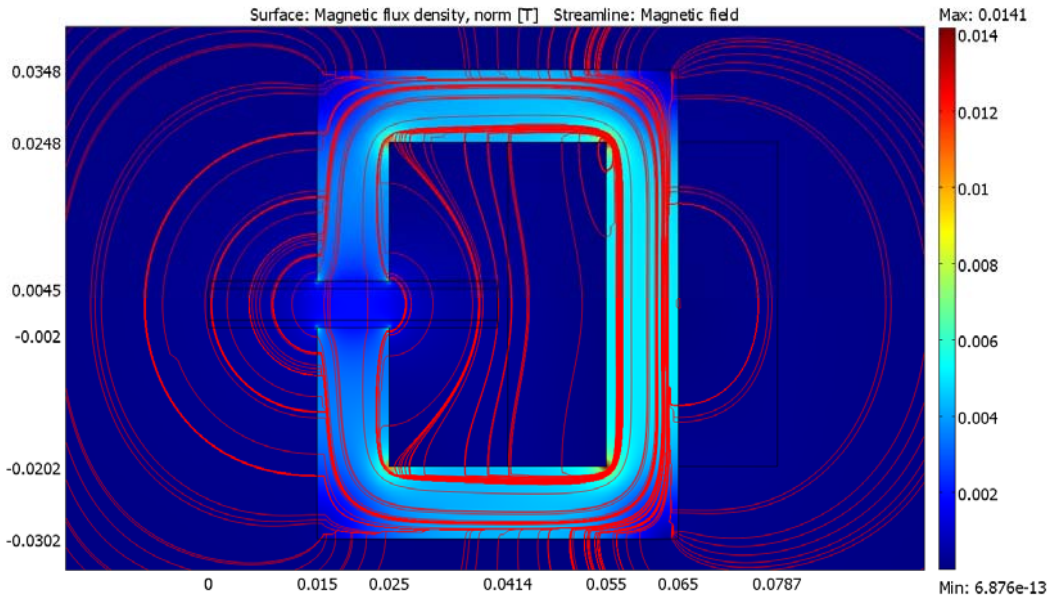

Figure 4-5 Surface and streamline plot for the modelling for the rectangular flow channel having 10mm by 4.5mm cross-section area

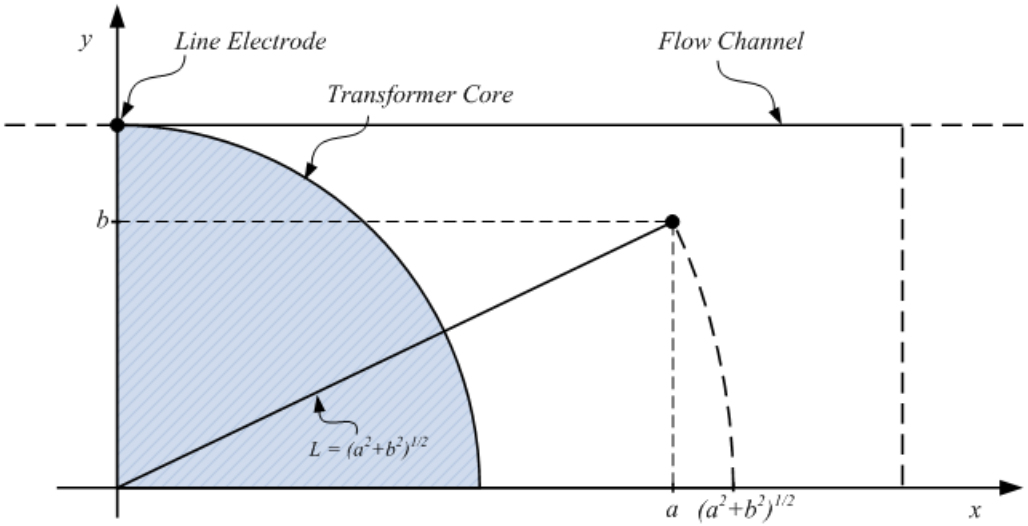

Figure 4-6 Diagram for the algorithm of data rotating technique. Data at (a, b) is taken from data at (a2+b2)1/2

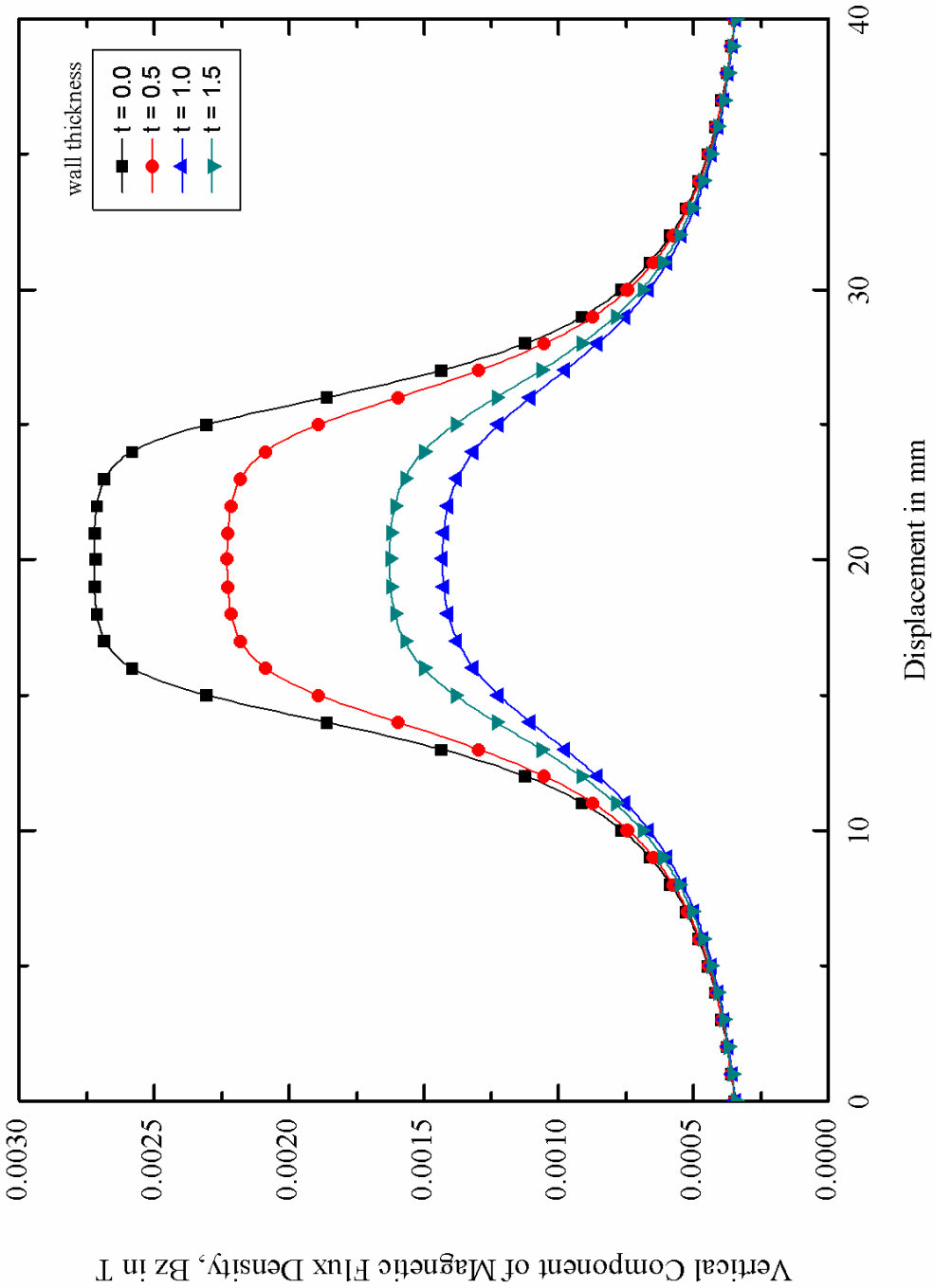

Figure 4-7 The vertical component of magnetic flux density, Bz along the flow direction of the 10 mm by 4.5 mm rectangular flow channel.

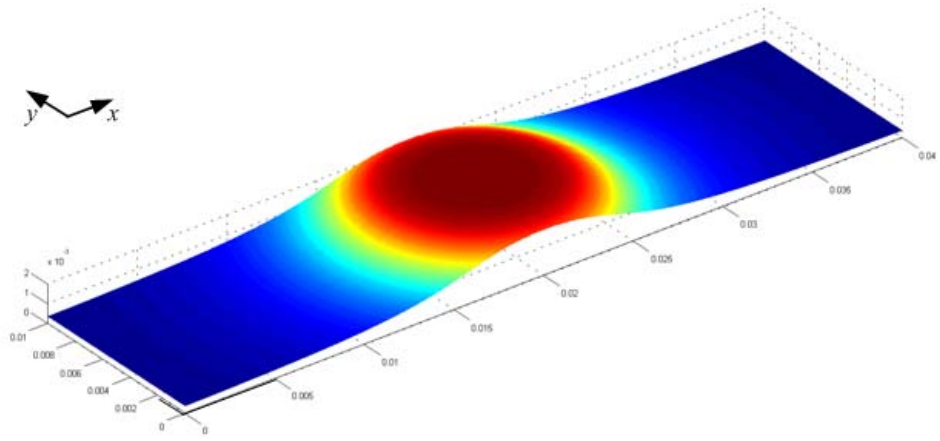

(a) wall tickness, t = 0.0 mm

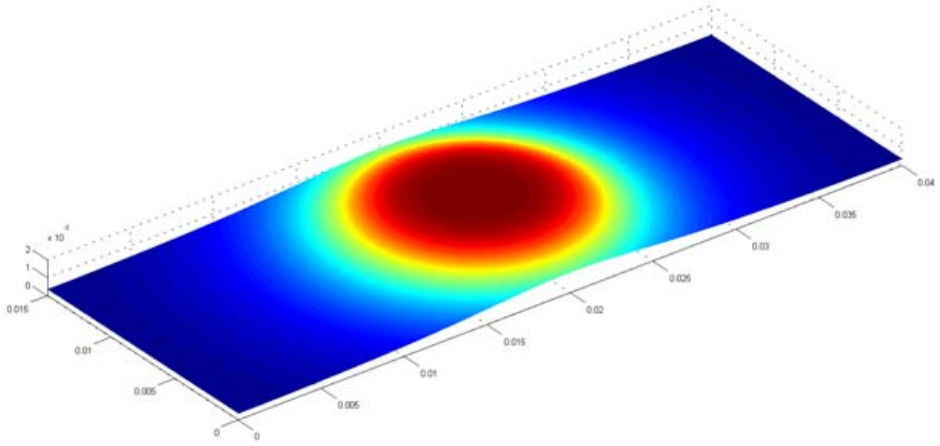

(b) wall tickness, t = 15.0 mm

Figure 4-8 The vertical component of magnetic flux density, Bz in the middle plan (z = 2.25mm) along the direction of the flow channel. Figure (a) and (b) shows the flux density at the different wall thickness.

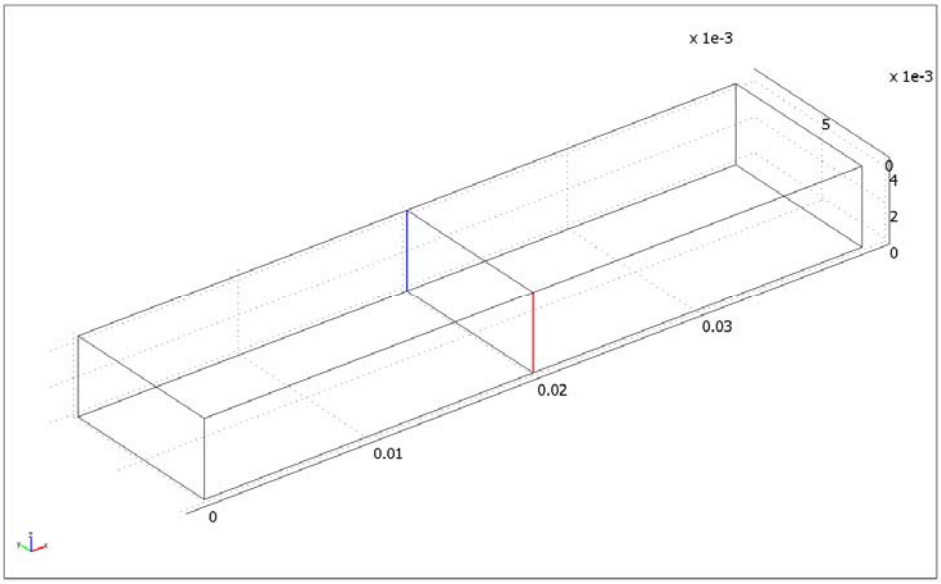

Figure 4-9 The geometry of the rectangular flow channel having line electrodes in the middle.

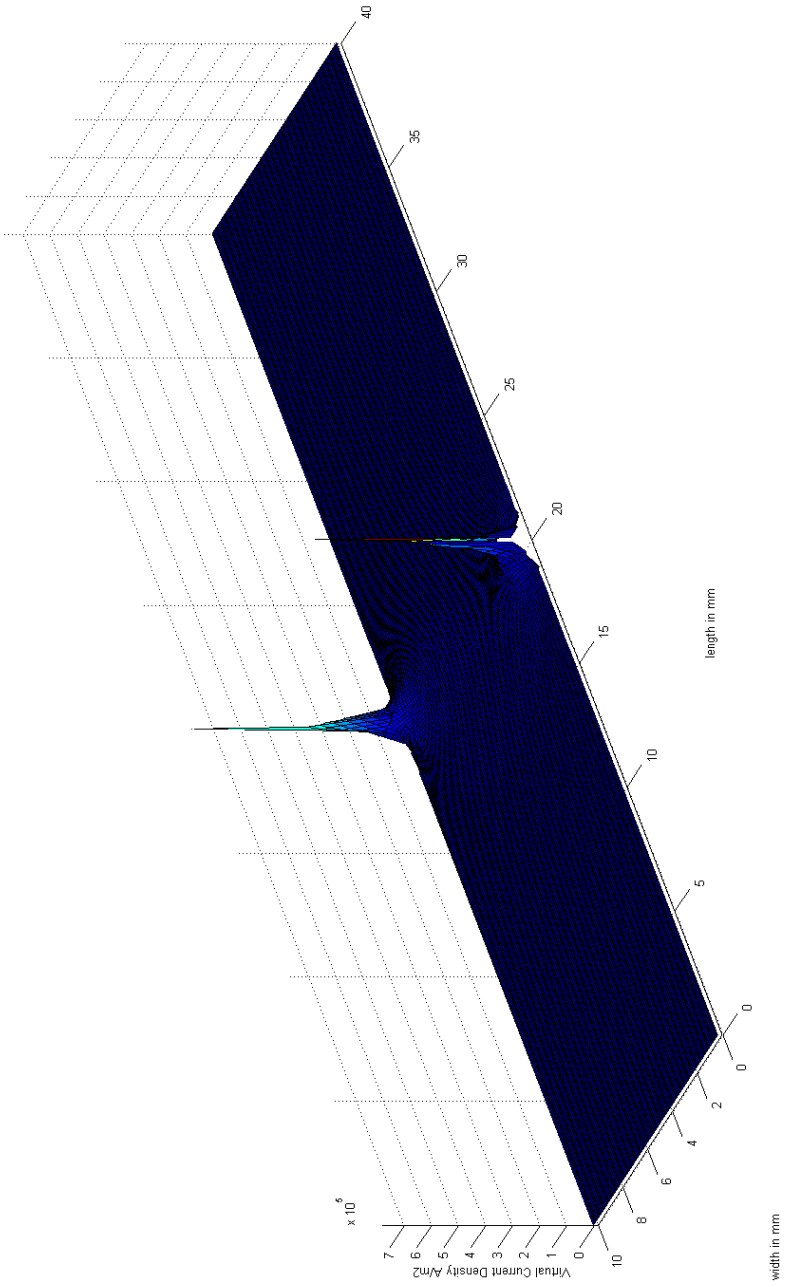

Figure 4-10 The y-component of virtual current on the middle plane of the rectangular flow channel.

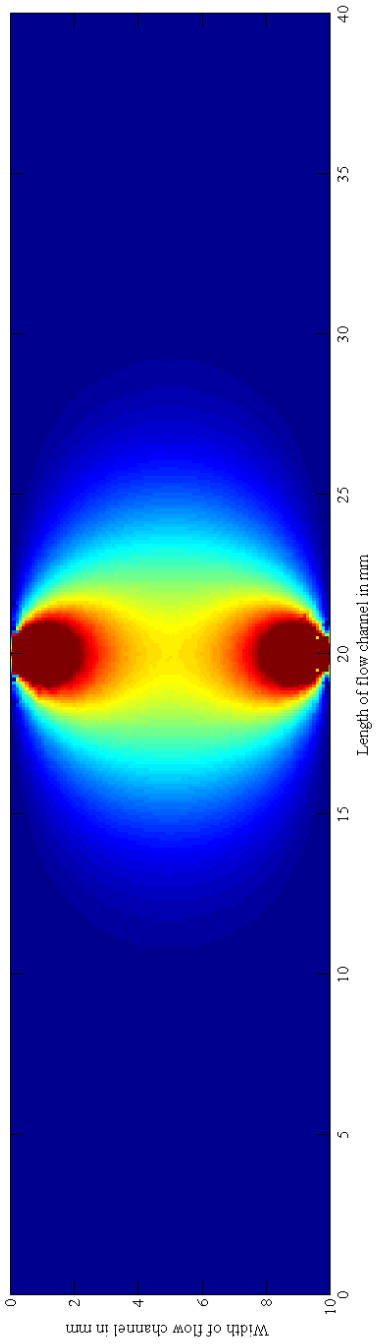

Figure 4-11 The weight function on the middle plane of the 10 mm by 4.5 mm flow channel with 1 mm walls.

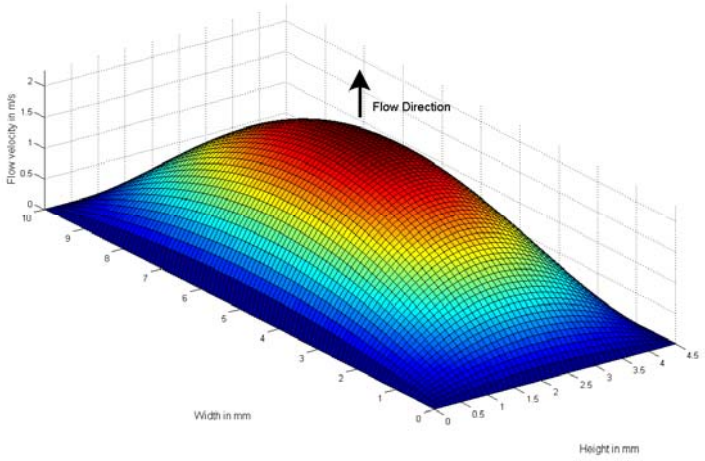

Figure 4-12 The laminar flow profile in the 10 mm by 4.5mm rectangular flow channel at the mean velocity is 1 m/s.

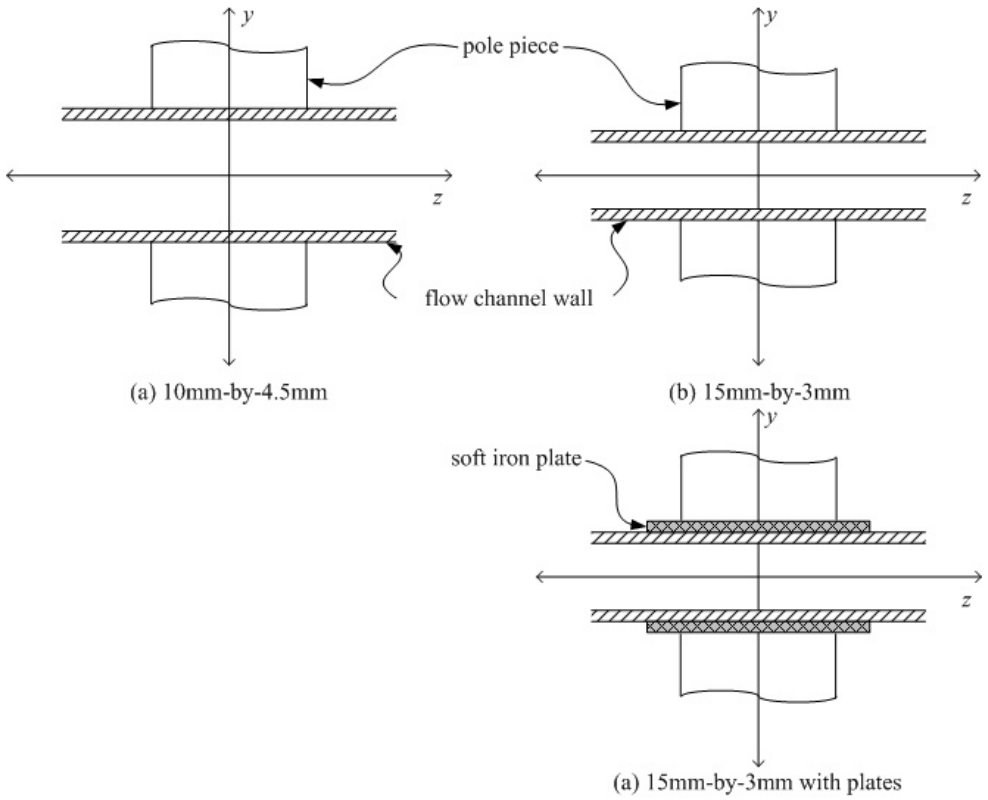

Figure 4-13 A pair of soft iron plates is applied to increase the uniformity of magnetic field.

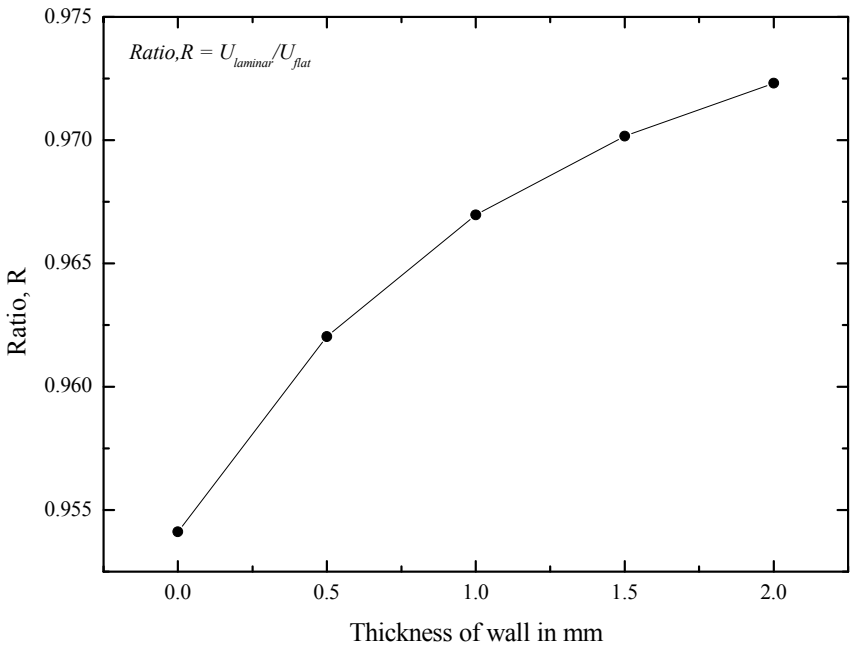

Figure 4-14 Changing of Ratio, R for 10mm by 4.5mm rectangular flow channel with different wall thickness.

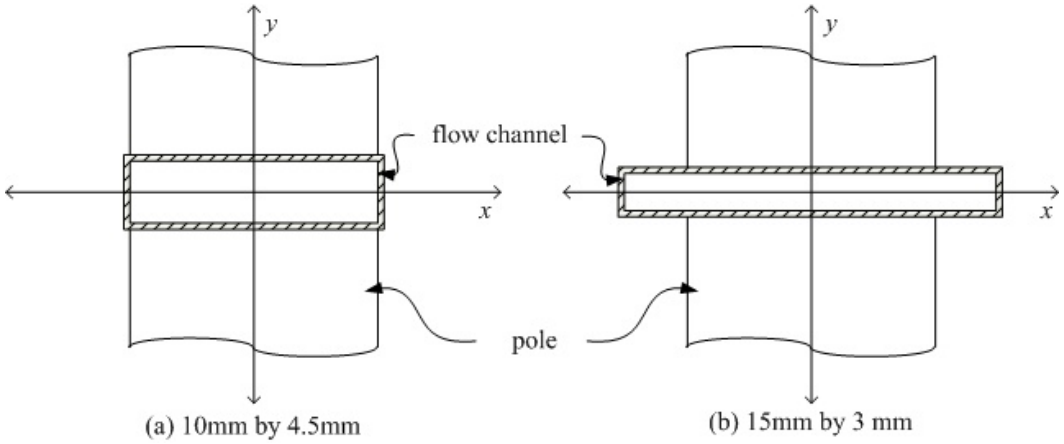

Figure 4-15 The modification of flow channel. The cross-section is changed from (a) 10 mm by 4.5mm to (b)15 mm by 3 mm.

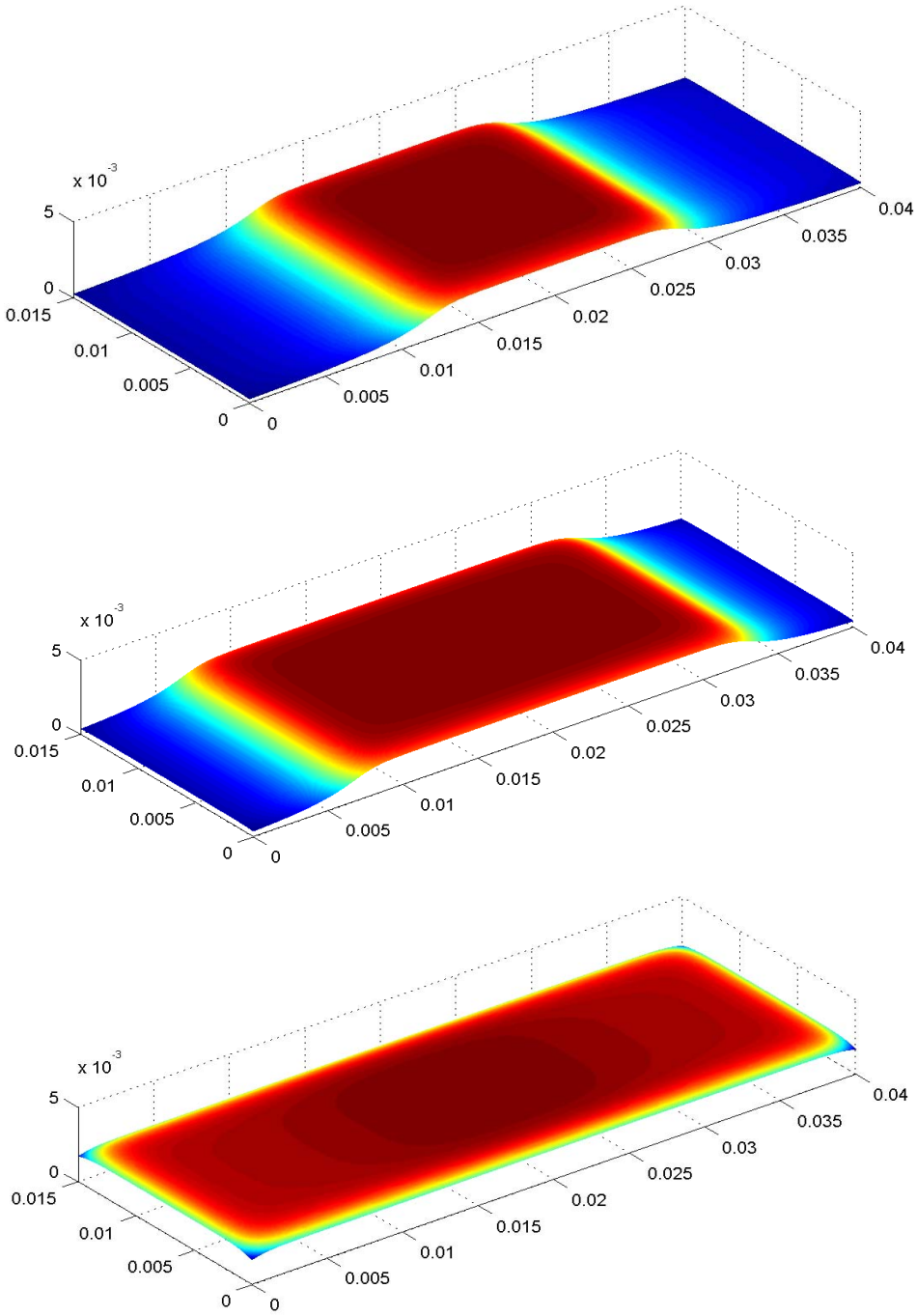

Figure 4-16 The z-component of magnetic flux density with soft iron plate having the length is 15 mm, 30mm and 40mm on the middle plane of flow channel.

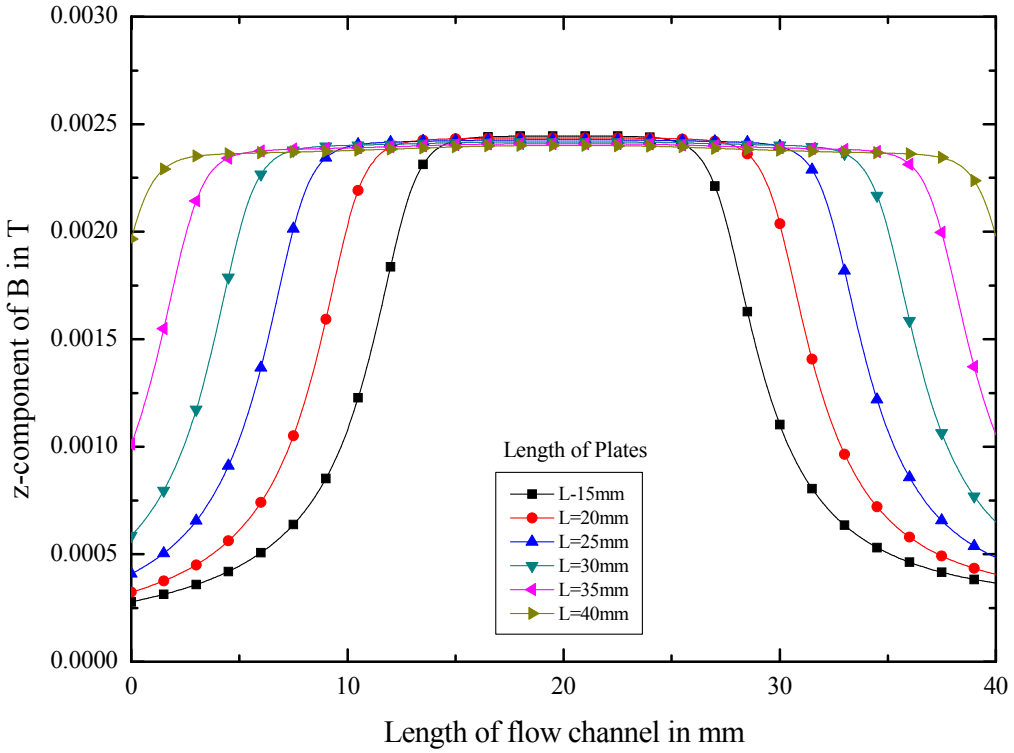

Figure 4-17 Magnetic flux density of 15mm by 3mm rectangular flow channel with the soft iron plate having length L is 15mm to 40mm

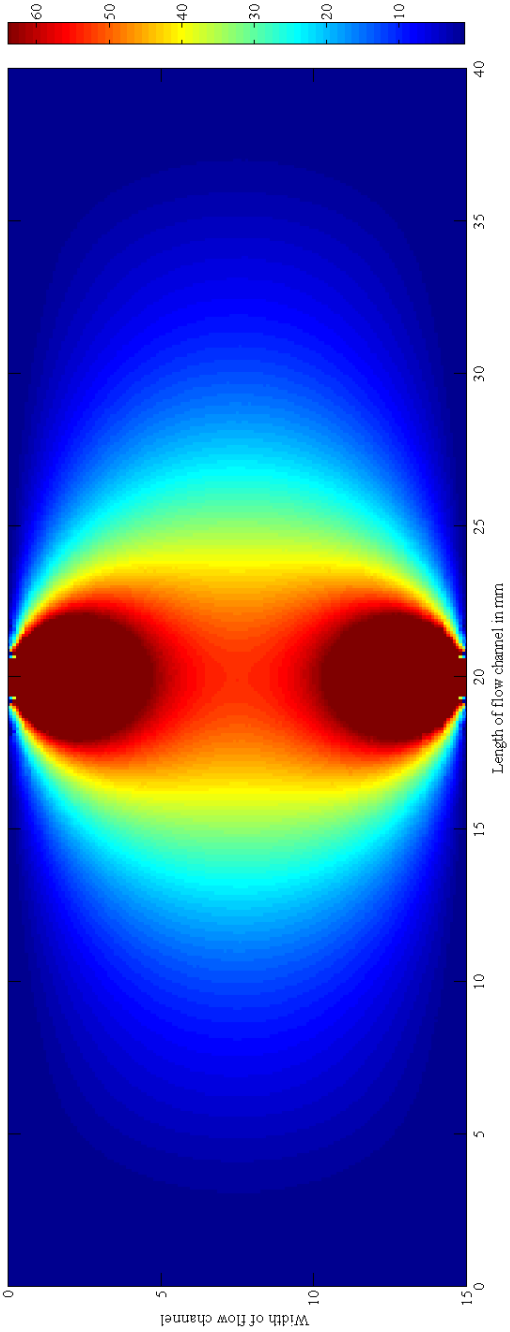

Figure 4-18 Weight function on the middle plane of 15mm by 3mm rectangular flow channel with 30mm long soft iron plates

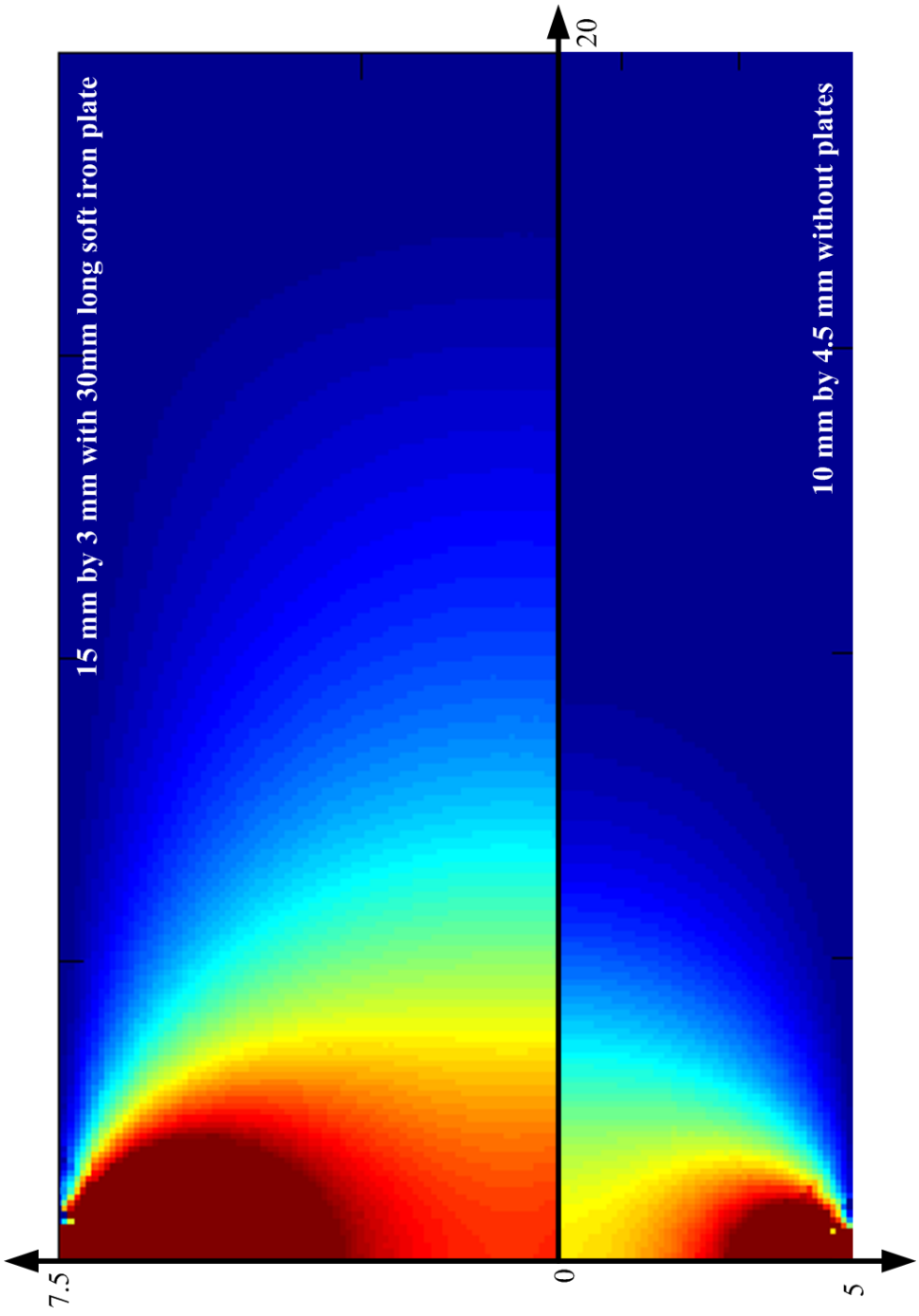

Figure 4-19 Comparison images of 15mm by 3mm flow channel with plate and 10mm by 4.5mm flow channel.

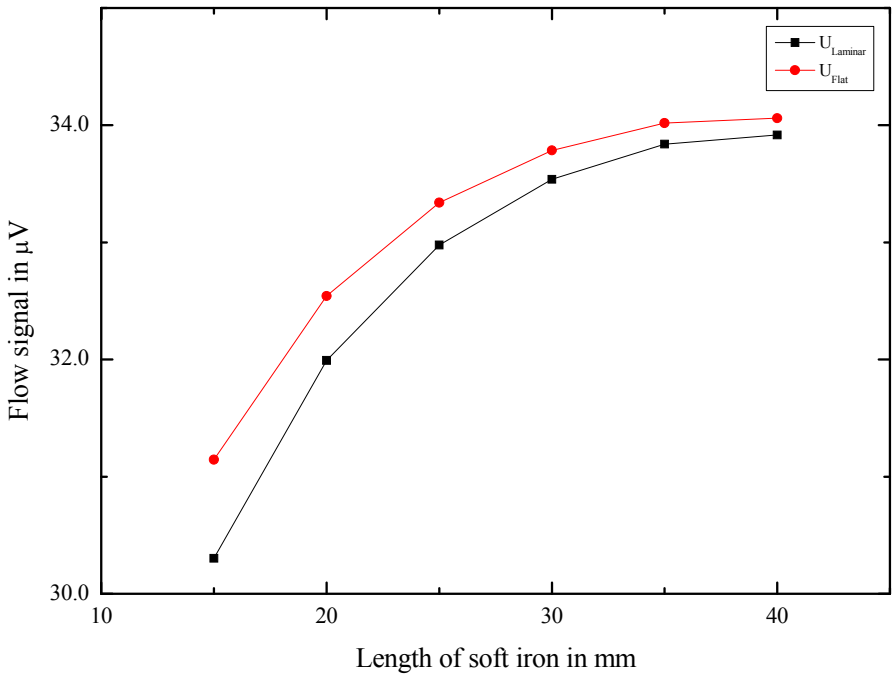

Figure 4-20 Comparison of flow signals with laminar and flat flow profiles

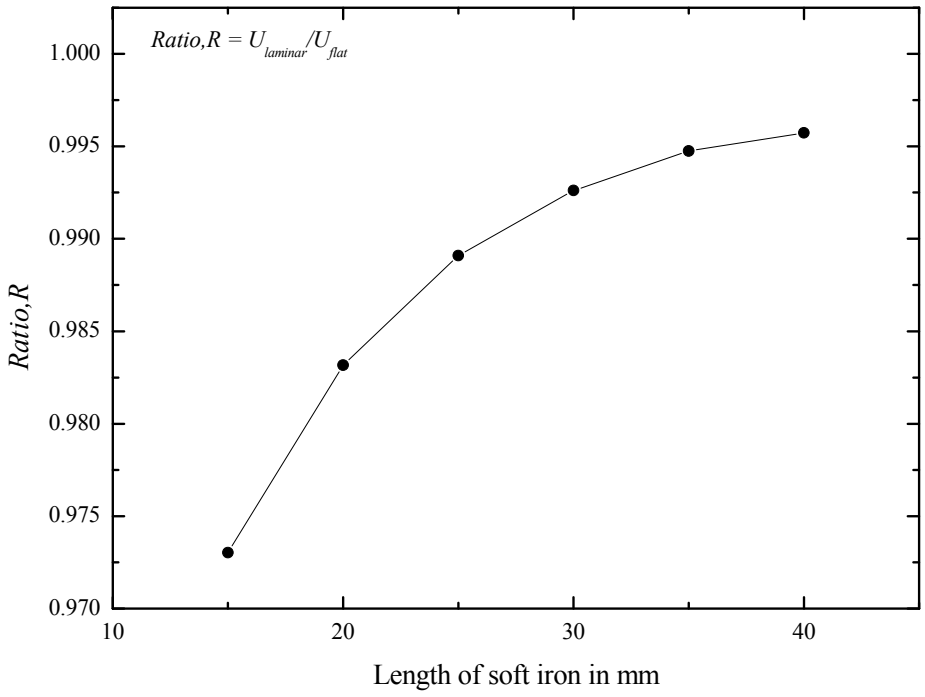

Figure 4-21 Sensitivity of flowmeter which is 15mm by 3mm rectangular flow

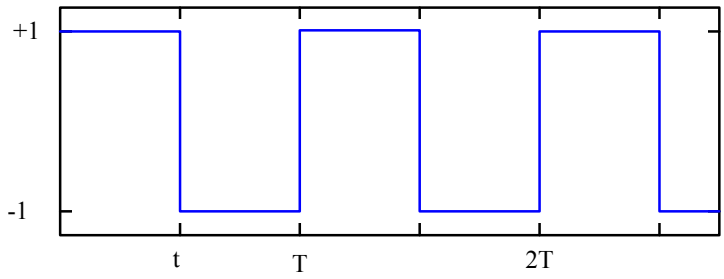

(a) 100% duty cycle

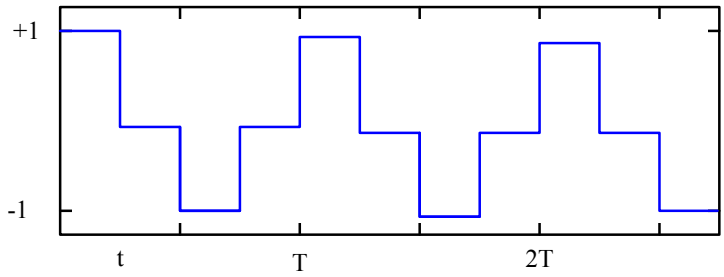

(b) 50% duty cycle

Figure 4-22 Duty cycles of electromagnetic flow meter

Chapter 5. Electromagnetic flowmeter without coil

5.1 Introduction

In the previous chapter, the conventional electromagnetic flowmeter which uses a coil as its magnetic field source has been studied. The power consumption can be lowered by a factor of 1.35 from the original design by reducing the height of the flow channel from 4.5mm to 3mm and enlarging the width from 10mm to 15mm.

Nevertheless, the coil is energy inefficient as well as being a volume wasting device. To overcome these problems an alternative electromagnetic flowmeter is proposed.

In this chapter, Terfenol-D, a magnetostrictive material is adapted as an alternative method for the coil-less electromagnetic flowmeter, which changes its magnetic property by stress on the material. As the source of magnetic fields, Neodymium permanent magnets are used and Terfenol-D controls the change of magnetic flux in the magnetic circuit.

Stress is applied to the Terfenol-D material by laminating the material with a piezoelectric layer and the magnetic field is simulated by COMSOL Multiphysics.

In the later section of this chapter, the magnetostrictive material is replaced with an extra air gap, changing the length to control the magnetic field as would happen with Terfenol-D. In this way modelling and experimental work of a permanent magnet flowmeter are undertaken.

5.2 Magnetostrictive material

The magnetostrictive material is considered as a part of the alternative magnetic field control device. The benefit of using this material is that the magnetic circuit can be controlled by the magnetic field without any mechanical action damaging the magnetic circuit. Additionally if the mechanical action cannot secure precisely the same movement every time it happens, then this will change the magnetic field in an unstable way, therefore the magnetostrictive material is a better alternative.

5.2.1 Meter design

The magnetic field control device using Terfenol-D magnetostrictive material is therefore considered as it has an air gap for the rectangular flow channel as explained earlier, and shown in Figure 5-1. In the drawing, the block of Neodymium (NdFeB) magnet which is 10mm by 10mm by 25mm, is used to generate a constant magnetic field and is located at the left end of the transformer core. The Terfenol-D magnetostrictive material is located at the middle of the bridge between the upper and lower transformer core pieces and has the air gap at the right end of the transformer core, having a length of 7mm for the rectangular flow channel.

In this magnetic circuit, the magnetic flux from the permanent magnet, Φ_p comes out from the top end of the permanent magnet, goes through the upper transformer core, and is then divided into the path of the Terfenol-D material and the air gap. The magnetic flux though Terfenol-D material, Φ_m can be simply described as a function of relative permeability changing by external stress, as described in the previous chapter. The relative permeability of Terfenol-D material is set at 3.0 to 10.0 according to table 2-4 taken from the manufacturer's specification. The relative permeability is to be changed by the application

of external stress. The other part of the magnetic flux travels toward the air gap, Φ_g. The leakage flux is also considered in the modelling but not described in the drawing.

5.2.2 Magnetic field modelling

For the modelling of the magnetic flux controller using Terfenol-D material, the 3D magneto-statics model in AC/DC module is used. For this modelling, the geometry consists of the transformer cores, the permanent magnet, Terfenol-D material and the air gap.

To allocate more meshes in the air gap, the finer mesh parameter is set only in the air gap sub domain and the unstructured mesh generated by the modelling software is used. The mesh statistics taken from the modelling software are given in Figure 5-2.

The transformer cores are assumed to be mild steel which has very high magnetic permeability. The relative permeability is set to 1,200 in the modelling parameter setting but the rest of the parameter of mild steel is used as a default setting of iron from the library of modelling software.

The results are shown in Figure 5-3, when the permeability of Terfenol-D material, μ_m is set to 3.0 (Figure 5-3 (a)) and 10.0 (Figure 5-3 (b)). The red arrows in these figures show the direction and magnitude of magnetic flux. When a certain external stress is applied to Terfenol-D magnetostrictive material so that the permeability of Terfenol-D is increased, more magnetic flux lines pass through the material and the magnetic flux in the air gap is reduced.

The maximum value of the magnetic flux density at the middle line of the air gap is 0.12349 T when μ_m is 3.0. This value is decreased to 0.08207 T when the Terfenol-D material has the greatest value of the permeability according to its specification. The comparison chart of the magnetic flux density at the middle line of the air gap is shown in

Figure 5-4. The magnetic field at the gap is 0.1134 T when the relative permeability is 3.0, and 0.07739 T when the permeability is 10.0.

Table 5-1 Mesh statics for the modelling of magnetic flux controller

Number of degrees of freedom	299,262
Number of mesh points	8,268
Number of elements – Tetrahedral	46,504
Number of boundary elements – triangular	5,788
Number of edge elements	508
Number of vertex elements	64

The permeability of Terfenol-D material varies when the length of the magnetostrictive material is changed by an external stress or strain, which is known as the reverse effect of the magnetostrictive effect. As reviewed in section 2.3.4, Ueno used the laminated piezoelectric material and Terfenol-D material to employ an external stress on Terfenol-D material.

In this section, the laminated piezoelectric and Terfenol material is taken into the modelling. The magnetic flux density at air gap can be calculated by equation (2-53) so that the modelling of Terfenol-D material with piezoelectric layers is accomplished in order to compute the total displacement of Terfenol-D material when an electric voltage is applied to piezoelectric layers.

A Terfenol-D material bar which has 10mm by 10mm by 10mm dimensions and piezoelectric material layers on either side having 1 mm thickness are studied initially. In

the model, the piezoelectric material and Terfenol-D material is assumed to be laminated without any adhesive material between them. The length of Terfenol-D material is varied, i.e. 10mm, 15mm and 20mm. The electric potential between the top and bottom piezoelectric layers is ±60V, ±100V and ±150V.

The model consists of a Terfenol block laminated by two 1mm thick PZT-5H piezoelectric layers, as shown in Figure 5-5. The boundary conditions at the centre of the Terfenol material are constrained and all other surfaces set free. The top and bottom boundary of the device is set as having the electrical potential from ± 60V to ±150V.

Table 5-2 lists the material property for Terfenol material. The matrices for the material properties for PZT-5H are listed as:

$$c_E = \begin{bmatrix} 126 & 79.5 & 84.1 & 0 & 0 & 0 \\ & 126 & 84.1 & 0 & 0 & 0 \\ & & 117 & 0 & 0 & 0 \\ & & & 23.0 & 0 & 0 \\ & sym & & & 23.0 & 0 \\ & & & & & 23.3 \end{bmatrix} GPa$$

$$e = \begin{bmatrix} 0 & 0 & 0 & 0 & 17 & 0 \\ 0 & 0 & 0 & 17 & 0 & 0 \\ -6.5 & -6.5 & 23.3 & 0 & 0 & 0 \end{bmatrix} C/m^2$$

$$\varepsilon = \begin{bmatrix} 1.503 & 0 & 0 \\ 0 & 1.503 & 0 \\ 0 & 0 & 1.3 \end{bmatrix} \times 10^{-8} F/m$$

where c_E is the elasticity matrix, e is the piezoelectric coupling matrix and ε is the absolute permittivity matrix. The matrices also imply that the polarisation direction of the materials is in the vertical direction as z-axis.

Table 5-2 Property table for Terfenol for modelling

Property	Terfenol
E(Young's modulus)	30 GPa
V(Poisson's ratio)	0.25
Rho(density)	9250 kg/m3

Figure 5-6 and Figure 5-7 show the modelling results of Terfenol-D/Piezoelectric devices which have 10mm by 10mm by 10mm dimensions of Terfenol with 1mm thickness of piezoelectric layers (Figure 5-6) and 20mm by 10mm by 10mm of Terfenol with 2mm thick piezoelectric layers (Figure 5-7). These figures show the deformation image of the devices. When the electric potential is applied between the top and bottom layers of piezoelectric material then the outer edges of this material begin to shrink. The bottom surface of the top layer and top surface of the bottom layer are all bonded to the Terfenol-D material so the Terfenol-D material also shrinks. This displacement is simulated and the integration of the x-component of displacement is measured for lengths of 10mm, 15mm and 20mm Terfenol-D material.

From equation (2-53), the magnetic flux change at the air gap is a function of the total strain of the magnetostrictive material, so modelling has been undertaken to obtain the

strain of the Terfenol material under the supply voltages. The modelling results of the integration of x-directional displacement are listed in

Table 5-3. The strain S_m is defined as the x-component of displacement over length of Terfenol-D material so the integration of S_m can be calculated, as listed in Table 5-4.

Table 5-3 Integration of x-directional displacement of Terfenol material

Terfenol material	*Supply voltage*		
	± 60 V	*± 100 V*	*± 150 V*
10 x 10 x 10	2.129×10^{-12}	3.549×10^{-12}	5.323×10^{-11}
15 x 10 x 10	1.329×10^{-11}	2.215×10^{-11}	3.322×10^{-10}
20 x 10 x 10	3.215×10^{-10}	5.357×10^{-11}	8.036×10^{-10}
30 x 10 x 10	8.764×10^{-10}	1.461×10^{-10}	2.108×10^{-9}

Table 5-4 Integration of strain of Terfenol material

Terfenol material	*Supply voltage*		
	± 60 V	*± 100 V*	*± 150 V*
10 x 10 x 10	2.129×10^{-10}	3.549×10^{-10}	5.323×10^{-9}
15 x 10 x 10	8.860×10^{-10}	1.477×10^{-9}	2.215×10^{-8}
20 x 10 x 10	1.608×10^{-9}	2.679×10^{-9}	4.018×10^{-8}
30 x 10 x 10	2.921×10^{-9}	4.870×10^{-9}	7.027×10^{-8}

The thickness of the PZT layer does not affect the change of the magnetic flux at the air gap (Ueno *et al.,* 2005) although the thickness of the PZT has been assumed as 1mm for top and bottom layers. The electric supply voltage between the top and bottom sides of the PZT layer is from ± 60V to ± 150V. Figure 5-8 shows the comparison chart of total stain of piezoelectric/Terfenol laminated device which has the different dimensions of 10mm, 15mm, 20mm and 30mm in length. The total strain of Terfenol is increased as the supply voltage is increased. The strain of longer Terfenol material shows a much greater change in its geometry.

The magnetic flux change at the air gap can be calculated by equation (2-53). First of all, the coefficient λ needs to be determined in advance, which is a function of permeance of the permanent magnet P_m, the air gap P_g, and the leakage P_l. The permeance of leakage is not easy to be determined but the value is roughly estimated by modelling as 0.5×10^{-7} then λ is calculated as 0.794. The piezomagnetic coefficient e_m is taken as 330 from Ueno's results (Ueno *et al.*, 2005).

The magnetic flux density change can be calculated from Table 5-4. From this table, the magnetic flux change at the gap is 1.394 x 10-4 T for 10mm by 10mm by 10mm Terfenol with ± 150V supply voltage.

With the obtained variation of the magnetic flux, the flow signal is calculated from equation (2-2) with the 10mm by 4.5mm rectangular flow channel placed at the gap. The calculated flow signal at 8 *l*/hr for 10mm by 10mm by 10mm Terfenol-D material is 0.068 μV, and 0.303 μV for 30mm by 10mm by 10mm Terfenol-D material under the same conditions.

Table 5-5 Magnetic flux change at the gap, $\Delta\Phi_g$

Terfenol material	Magnetic flux change at the gap, $\Delta\Phi_g$ T		
	± 60 V	*± 100 V*	*± 150 V*
10 x 10 x 10	5.576×10^{-6}	9.295×10^{-6}	1.394×10^{-4}
15 x 10 x 10	1.547×10^{-5}	2.578×10^{-5}	3.867×10^{-4}
20 x 10 x 10	2.105×10^{-5}	3.508×10^{-5}	5.262×10^{-4}
30 x 10 x 10	2.550×10^{-5}	4.252×10^{-5}	6.134×10^{-4}

The flow signal level of this flowmeter can be also improved by reducing the height of the channel, as proposed in chapter four, from 4.5mm to 3mm so that the flow signal improves from 0.069μV to 0.072μV for 10mm by 10mm by 10mm for the Terfenol device, and 0.303μV to 0.318μV at 8L/hr and ±150V supplying voltage for 30mm by 10mm by 10mm for the Terfenol device. The improvement on the flow channel will increase the flow signal to a factor of 1.05.

5.2.3 Power consumption

In the simulation, the supply voltage to the magnetostrictive device is higher than has been used in the conventional electromagnetic flowmeter. But the power consumption by the laminate magnetostrictive/PZT composite is much less than the coil because the static operation of the piezoelectric material consumes virtually no power. A piezoelectric layer behaves very much like an electrical capacitor, so a much longer lifetime with same power capacity is expected.

The energy stored to the capacitor is calculated by

$$W = \frac{1}{2} C V^2 \tag{5-1}$$

The capacitance of piezoelectric material can be calculated by

$$C = \varepsilon_T \frac{A}{d} \tag{5-2}$$

where A is a cross-section area of piezoelectric material and d is the height. ε_T is the permittivity of piezoelectric material. For the 10mm by 10mm by 1mm piezoelectric layer, the permittivity is 1.503×10^{-8} F/m so capacitance of the layer is 1.503 nF. The energy dissipating from this device per cycle is 33.82 μJ. At a frequency of 1Hz this device has a minimum dissipation of 33,82 μJ which implies a current of 9.39μA from a supply of 3.6V, assuming an ideal voltage transformation.

5.3 Mechanical Actuator

The mechanical actuator is considered to prove the alternative method for the coil-less electromagnetic flowmeter because the change of permeability of the Terfeno material can be assumed as changing the length of the air gap. In this section, mechanical actuators such as a piezoelectric actuator and a solenoid actuator are used to change the length of the air gap. The modelling of the magnetic field control device is simulated and compared with the experimental results.

5.3.1 Meter design

First of all, the magnetic equivalent circuit with the extra air gap, which has already been shown in the previous chapter, is used to design a prototype of the electromagnetic flowmeter. The first prototype flowmeter is shown in Figure 5-10 and Figure 5-11.

The prototype has the Neodymium magnet which is 10mm by 25mm by 20mm in size, one pair of mild steel plates as a transformer core and a mild steel movable yoke. The transformer core is a 90mm by 65mm mild steel plate and the movable yoke is 10mm by 25mm with 2mm thickness. The transformer core has three legs each to contact to the permanent magnets, the flow channel and the other transformer core. Tha gap in which to fit the flow channel is 6mm.

5.3.2 Magnetic field modelling

The modelling results without placing the movable yoke is shown in Figure 5-12. The magnetic field flows from the permanent magnet through the upper fixed yoke then it is divided into two paths, which flow to the air gap and to the end of the fixed yoke.

When the movable yoke is attached to the ends of the fixed yokes, as shown in Figure 5-13, the magnetic flux patterns change because the length of the air gap at the end of the fixed yoke is significantly reduced and the magnetic flux can flow through the air gap at the end of the fixed yoke through the movable yoke.

For the modelling, the permeability and other material properties of mild steel are taken from the material library of modelling software as relative permeability μr is 1200 and the remanence of magnet Br is set to 1.22 T. The N pole of the magnet is on upper side and contacted to the upper fixed yoke because the Neodymium permanent magnet has the value of 1.22 T of remanent flux density, B_r and the relative permeability is 1.02; these values are taken from the magnet manufacturer resources.

The magnetic field change is measured at the centre of the air gap, when the magnetic equivalent circuit is closed, which means the movable yoke which is placed to connect the two fixed yokes, is 0.04095 T. The magnetic field is increased to 0.10668 T when the movable yoke is placed at the end of the fixed yoke.

Modelling is also undertaken to investigate how the magnetic field will change at the gap when the movable yoke is placed at different locations, such as 0.5mm to 3mm; the results are shown in Table 5-6 and the chart in
Figure 5-14. The magnetic field measured at the centre of the air gap is 9.54 $x10^{-2}$ T when the movable yoke is placed 0.5mm from the fixed yokes. The magnetic field is increased to $1.03x10^{-1}$ T when the movable yoke is placed as far away as 3.0mm from the fixed yokes.

The magnetic field change per 0.5mm moving is $3.81x10^{-3}$ T when the movable yoke moves from 0.5mm to 1.0mm away from the fixed yokes. The magnetic field change for the same displacement is reduced to $7.50x10^{-4}$ T. The magnetic field change is 4 times greater when the movable yoke is moving near the end of the fixed yoke than moving the same distance but further away. Near the fixed yoke, the magnetic attraction force is greater than further away so the design of the movable yoke should take into account the amount of mechanical force required.

Based on the modelling results, a prototype of the electromagnetic flowmeter is designed, as shown in Figure 5-15. The magnetic circuit has the permanent magnets, two set of fixed yokes and the movable yoke.

The fixed yoke is E-shaped and two fixed yokes face each other. In the middle of the fixed yokes, the air gap for the flow channel is located. The spacer for the mechanical actuator to support the fixed yoke is placed between the fixed yokes at the end. The flow channel is located inside the magnetic circuit, which has a rectangular section within the air gap, but

the inlet and outlet are circular. For a stabilised flow profile, the reducer and diffuser section are placed between the inlet and outlet, and rectangular flow channel.

The total length of the meter is 110mm to satisfy the regulation of 15mm for a domestic water meter. Circle type electrodes of which the diameter is 2.5mm are screwed in from the outside of the flow channel body to contact to the water. These are used to improve the sealing of the meter and do not affect the sensitivity of the meter to velocity profile effects.

The prototype of the magnetic circuit is shown in Figure 5-17. The yokes are made with mild steel as described above. Permanent magnets are N38 grade Neodymium magnets which use seven magnet blocks. The dimension of each magnet block is 25mm x 10mm x 21mm. The magnetic field measured by a portable Gauss meter, as shown in Figure 5-16, at the centre of the top surface of the magnet block is 4.59×10^{-1} T. The magnetic field from the modelling with the same dimension gives 4.82×10^{-1} T.

The modelling result is 5% larger. This error can be considered to be the geometrical difference with one single block in modelling and seven blocks in practice which have small air gaps or particles between layers. Another possible source of the error is the difference of the remanence of magnet, B_r. The B_r is set as 1.22 T in the modelling parameter but the actual value can be between 1.20 to 1.22 T.

The magnetic field of the magnetic circuit is measured as the gap is changed from open to closed by using the portable Gauss meter as shown in Figure 5-16. The Gauss meter has a transverse probe which can measure the magnetic field in a 0.2mm by 0.2mm area using a Hall sensor at the tip. The measurements are shown Table 5-7.

The measured magnetic flux change at the air gap is 1.53×10^{-2} T and this change is smaller than the simulated result by a factor of 4.3. This difference is likely to have resulted from the different characteristics of the modelling parameters, actual properties of material and

the electromagnetic modules. In addition, the surface of the yokes are not clean and uniform as defined in the model; this roughness can enlarge the surface area so that the magnetic flux leakage will be significantly higher than ideal modelling results.

Table 5-6 The magnetic field changes at the gap from modelling

Displacement (mm)	*Magnetic field at the gap (T)*	*Magnetic field change (T)*
0.5	0.09536	-
1.0	0.09917	0.00381
1.5	0.10075	0.00158
2.0	0.10179	0.00104
2.5	0.10254	0.00075
3.0	0.10307	0.00053

Another possibility of error is the design of the yokes. The yokes are made in solid mild steel and the thickness between the air gap at the opposite end is thinner than the area between the magnets and the air gap. The thinner area is saturated when the magnetic circuit is closed in order not to divert more flux through the movable yoke. This may also be a reason why the magnetic field change is less than in the modelling results.

The prototype of the flow channel is shown in Figure 5-18. The length of the flow channel is 15mm and is shorter than the proposed drawing. The inner height of the channel is

4.5mm and the width is 10mm. To measure the magnetic field, a search coil is placed between the flow channel and the fixed yoke, as shown in Figure 5-20.

The search coil is made up of three turns of coils which have 22mm width and 12mm height and a cross-sectional area of 2.64 x 10-4 m^2. The magnetic field change can be calculated by

$$\frac{de}{dt} = B \cdot A \cdot N \tag{5-3}$$

where B is the magnetic field, A is the cross-sectional area of search coil and N is number of turns. From equation (5-3), the magnetic field can be obtained by

$$\Delta B = \frac{1}{A \cdot N} \int \frac{de}{dt} \tag{5-4}$$

Therefore, if $\int de/dt$ is 1μV then ΔB is 1.26 x 10^{-3} T

Table 5-7 The magnetic field changes at the gap from experiments

Magnetic circuit status	*Magnetic field at the gap (T)*	*Magnetic field change (T)*
Open	6.57 x 10^{-2}	-
Closed	5.04 x 10^{-2}	1.53 x 10^{-2}

5.3.3 Experiments

The assembled flowmeter in installed in the test rig as shown in Figure 5-21. The inlet and outlet are connected to the 22mm main pipe of the rig. The fixed yokes are secured by cable ties as seen. The movable yoke is placed behind the side of the flowmeter and bonded at the end of the copper rod. The copper rod is finally jointed to the electrical actuator. In this stage, the electrical actuator is used to generate the mechanical movement to the movable yoke. The actuator is operating at 12VDC. The schematic of experimental instruments is shown in Figure 5-23.

To operate the flowmeter at a variable frequency, a square wave from the function generator is supplied to the control circuit. The power relay controls the supply voltage on and off at the same frequency as the function generator. The copper rod is used for moving the electrical actuator away from the search coil and electrodes to avoid any noise signal from the actuator. The length of the copper rod is 20cm.

The electrodes are connected directly to the spectrum analyser. This analyser can calculate an integral of the signal from channel B so the search coil is connected to channel B and its output thus measures the flux and flux change rather than the rate of change of flux. The electrodes are connected to channel A. The screen capture of the spectrum analyser is shown in Figure 5-24 and Figure 5-25.

The waveforms on the screen are captured in 5Hz and 10Hz operation modes. The upper screen shows the voltage from the search coil and the lower screen the integral of the signal. When the movable yoke moves toward the fixed yoke, the magnetic field at the air gap for measurement is reduced. In reverse, when the movable yoke moves backward, the magnetic field at the air gap is increased. This effect is also shown in figure 5-24 and 5-25. The change of the magnetic field can be calculated by measuring the peak to peak voltage from the lower waveform on the analyser screen.

Initially, the magnetic field change is measured at zero flow using the search coil. To measure the peak to peak value of the integration of signal from the search coil at 5Hz operation the frequency is 210 μV which is equivalent to 2.10×10^{-2} T of magnetic field change at the air gap. This value is 37.3 % larger than the results measured by the Gauss meter in the previous section because the search coil is located much nearer to the surface of the fixed yoke and the Gauss meter measured at the centre of the air gap. The magnetic field changes at 5Hz and 10Hz are not significantly different as seen in figure 5-24 and 5-25 .

The operational frequency has been reduced, but at frequencies of less than 1Hz the movable yoke is attracted to the fixed yoke and was found to be difficult to move. Therefore a 1.5Hz operation frequency is chosen for the experiments.

The flow signal is measured using the spectrum analyser from 18.9 L/hr to 74.8 L/hr as shown in Figure 5-26. The flow signal at 18.9L/hr is 5.13 μV and 21.5 μV when the flowrate is 74.8 L/hr.

The flow signal shows linearity as the linear fitted line in Figure 5-26. The flow signal can be converted to magnetic field changes as

$$B = \frac{V \cdot Q}{h} \tag{5-5}$$

where Q is flowrate in m^3/sec, h is the height of the channel in m and V is the flow signal in V. The average magnetic field from the calculation above is 4.50×10^{-3} T.

The calculated magnetic field is shown in Figure 5-27. The error in the average value is +5% to −3.5%. The error comes from the displacement of the movable yoke which is not perfectly controlled. The maximum displacement is planned to have 3mm but it is not

possible to measure the error of the displacement when the actuator and movable yoke are operating.

The magnetic field level is less than the measured value with the portable Gauss meter. The major reason for the difference is the action of the movement. The movable plate is not perfectly contacting with the fixed yoke and the alignment of the fixed yoke is not secure because of the striking action. A further reason may be that the magnetic flux density is saturated at the moving yoke and the thinner area of the fixed yoke.

This can limit the effect of the magnetic field control. To avoid the defects of the first prototype, two prototypes are prepared, as shown in Figure 5-28. Figure 5-29 shows a picture of the assembled prototype. These prototypes are laminated to reduce the eddy current and the thicknesses are increased to 5mm and 15mm. Prototype 3 has a different configuration as the permanent magnets are in the middle of the yoke, the air gap for the flow channel is at the right hand side and the air gap for the movable yoke is at the left hand side.

The magnetic field is measured for prototypes 2 and 3 with a Gauss meter. When the same size of movable yoke is placed on the end of the yoke, the magnetic field at the centre of the air gap is 3.34×10^{-2} T and 6.82×10^{-2} T when the movable yoke is off. The magnetic field change at these two states is 3.84×10^{-2} T. This value is 2.5 times larger than for prototype 1. Table 5-8 shows the comparison of magnetic field strengths at the centre of air gap for the prototypes. Prototype 2 has the largest difference, i.e. as large as 3.48×10^{-2} T.

Table 5-8 The magnetic field change comparison prototypes from modelling

Prototype	*Measured magnetic field in T*		
	Open state	*Closed state*	*Difference*
Prototype 1	6.57×10^{-2}	5.04×10^{-2}	1.53×10^{-2}
Prototype 2	6.82×10^{-2}	3.34×10^{-2}	3.48×10^{-2}
Prototype 3	5.66×10^{-2}	3.52×10^{-2}	2.14×10^{-2}

5.3.4 Piezoelectric actuator

The mechanical actuator used in the previous section has a relatively large volume but the piezoelectric actuator is smaller than any other mechanical actuator as it can be fitted into the meter itself although the maximum deflection and blocking forces are very limited.

By the calculation of equation (2-36), the tip deflection has been obtained, which is a function of the length, width, and thickness of the cantilever. The theoretical results of the tip deflection and block force of the unimorph and bimorph cantilevers are calculated for which have 40mm length, 10mm width, 0.1mm thickness of metal, and 0.127mm of the thickness of the piezoelectric material (total thickness of the unimorph cantilever is 0.227mm).

From the calculation, the magnetic flux change is also capable of being calculated from the deflection of the unimorph cantilever. The concept drawing for the flowmeter having the piezoelectric cantilever actuator is shown in Figure 5-30.

The drawing is based on Figure 5-10 and modified to fit the piezoelectric cantilever in. The unimorph cantilever, which is located at the end of the fixed yokes and the movable yoke, is bonded on at the tip of the cantilever actuator so that the movable yoke's position can be changed by the deflection of the piezoelectric actuator.

As shown in Figure 5-31, the Thunder TH-8R piezoelectric actuator is to be employed for consideration. The actuator has piezoelectric layer on a stainless steel substrate. The piezoelectric layer is covered and protected by an aluminium top layer. These layers are bonded using high performance bonding material, LaRC-SI which has been developed by NASA (adapted from FACE International Corporation booklet). The specification of TH-8R is shown in Table 5-9.

The structural dimension of Thunder TH-8R is that the footprint is 63.6mm x 13.72mm, the thickness of the piezoelectric layer is 0.2mm and the total thickness is 0.43mm. The actuator is slightly bent so the height at the centre is 3.84mm.

The maximum deflection of the actuator is 1.98mm when ± 240V is supplied to the cantilever actuator. The deflection is proportional to the supply voltage so the 0.5mm deflection can be obtained by supplying ± 60V to the cantilever actuator.

Table 5-9 Specification of Thunder TH-8R

Capacitance	*Max Voltage*			*Typical Maximum Displacement*		*Block Force*
	+	-	*Peak to peck*	*Simply Supported*	*Cantilevered*	
166nF	480V	240V	± 240V	0.41mm	1.98mm	67N

5.3.5 Limitations of the coil-less design

Although the coil-less electromagnetic sensing techniques can replace the conventional measuring method, the techniques in terms of energy consumption have some limitations.

The magnetostrictive device studied in this chapter is still far away from commercialisation because of its cost. The simple Terfenol-D block for the model cost £400 when the simulation was undertaken.

In addition, the magnetic field change, by using the Terfenol/PZT device, is small compared to the conventional method, because the external strains from the piezoelectric layers were small. So the design of the device is needed to be optimised to produce more strain in the Terfenol material.

The mechanical actuator also has some limitations. The results show the movable yoke can change the magnetic field where the flow is measured but the prototype is not yet compact in terms of design for the flowmeter. The cantilever piezoelectric actuator is still not

suitable for this application. The maximum blocking force of Thunder TH-8R actuator is 67N but it is difficult to move the movable yoke from the fixed yoke.

For the further design using a piezoelectric actuator, the amplified piezoelectric actuator can be considered. The amplified piezoelectric actuator offers large deformation and large stroke because of a pre-stress applied to the piezoelectric material and an efficient mechanical amplifier (Claeyssen *et al.*, 2007).

The amplified piezoelectric actuator APA400M from Cedrat, France offers 400um of displacement with 40N of blocked force. This device is compact enough to be installed within the flowmeter body with a 1.4cm height. The different amplified piezoelectric actuators are shown in Figure 5-32.

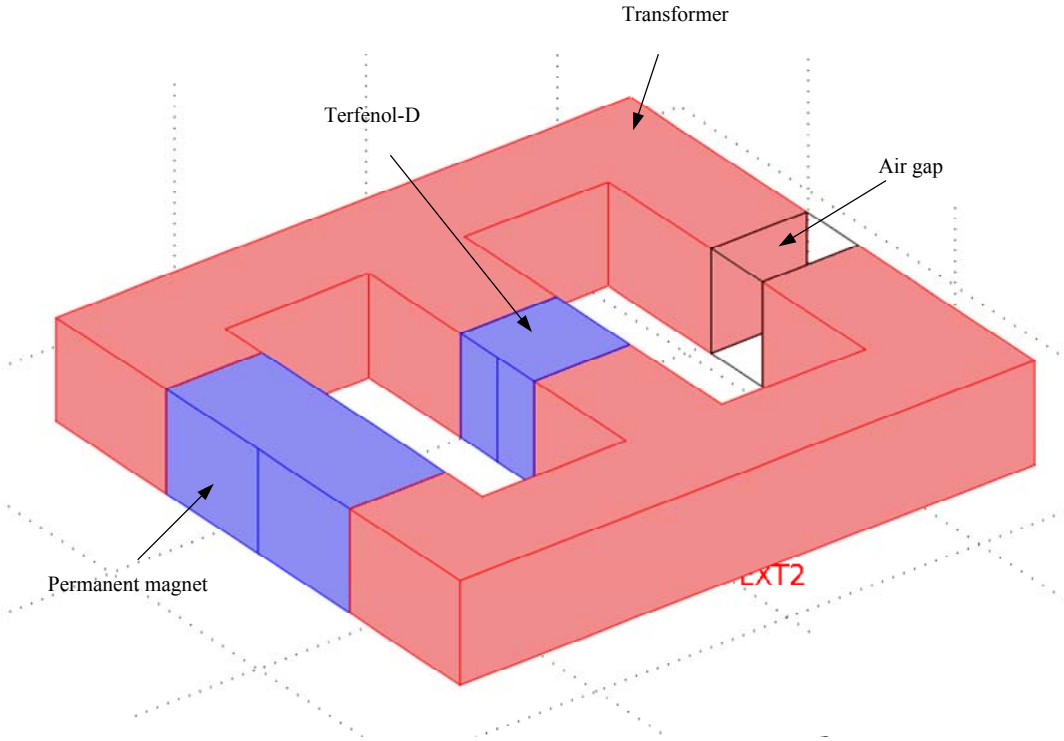

Figure 5-1 Model drawing for the magnetic circuit with Terfenol-D material

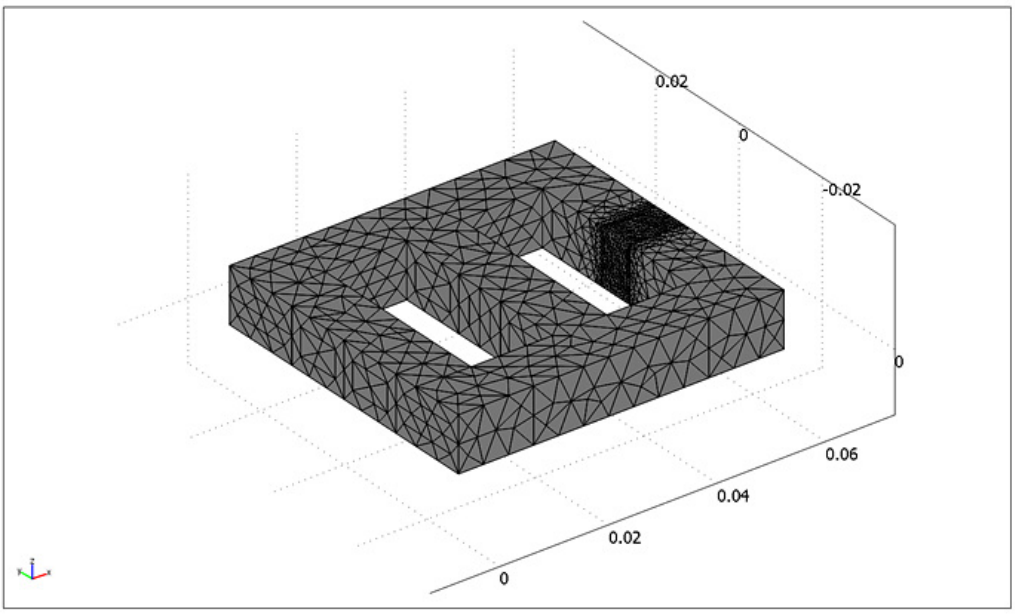

Figure 5-2 Meshes for the modelling

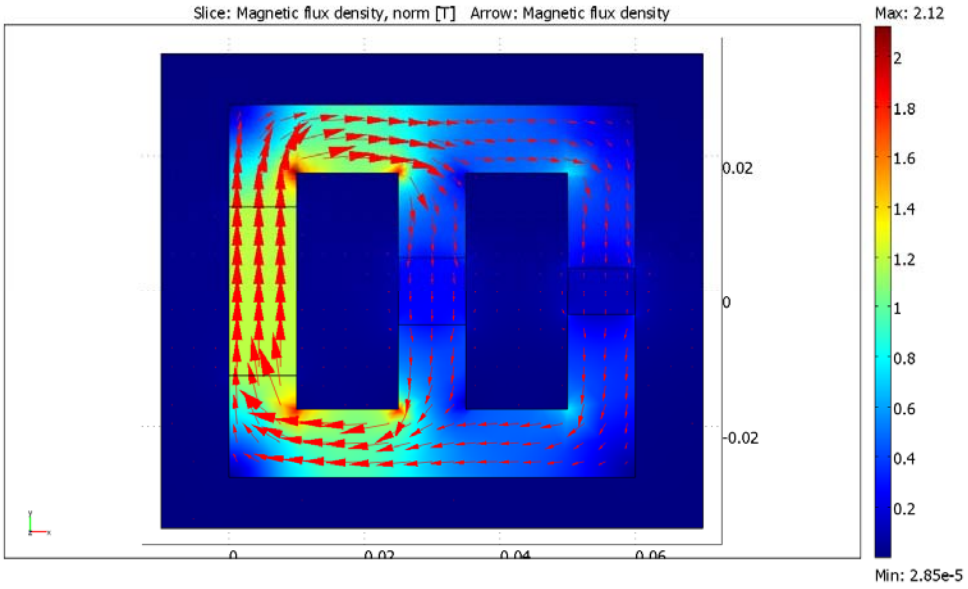

(a) Terfenol-D with low permeability

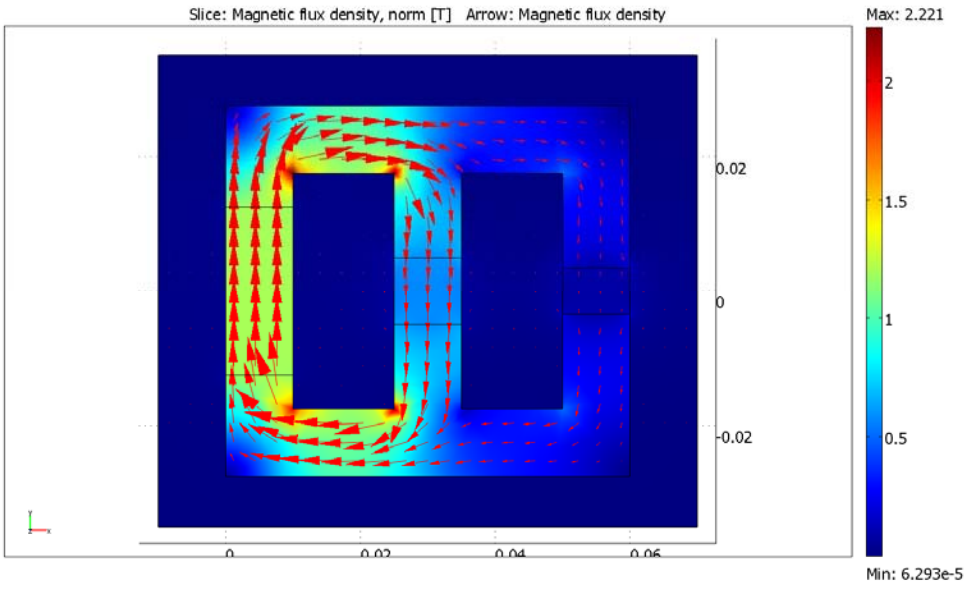

(b) Terfenol-D with high permeability

Figure 5-3 Magnetic flux changes for different magnetic permeability of Terfenol-D

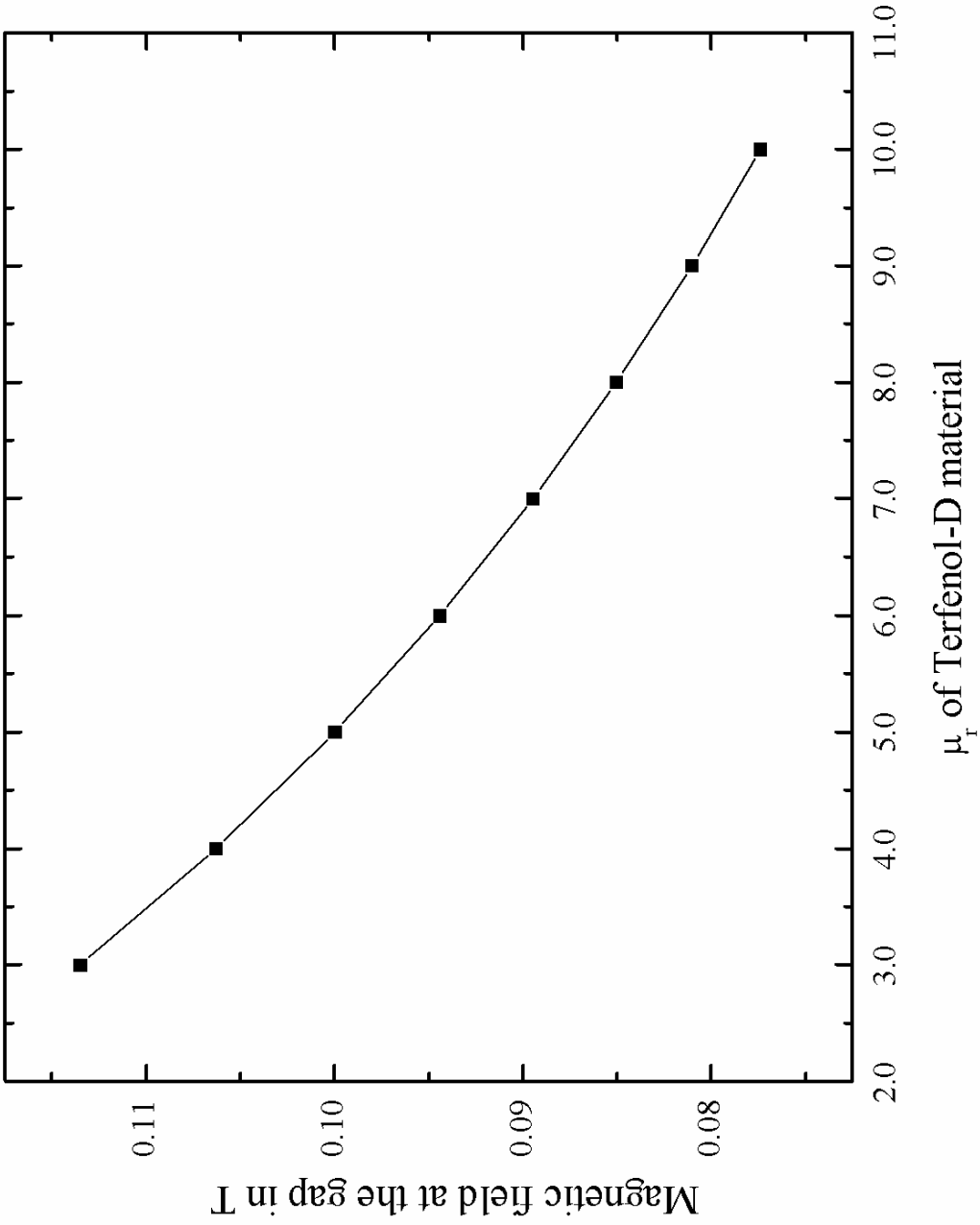

Figure 5-4 Magnetic field change against changing the magnetic property of Terfenol material

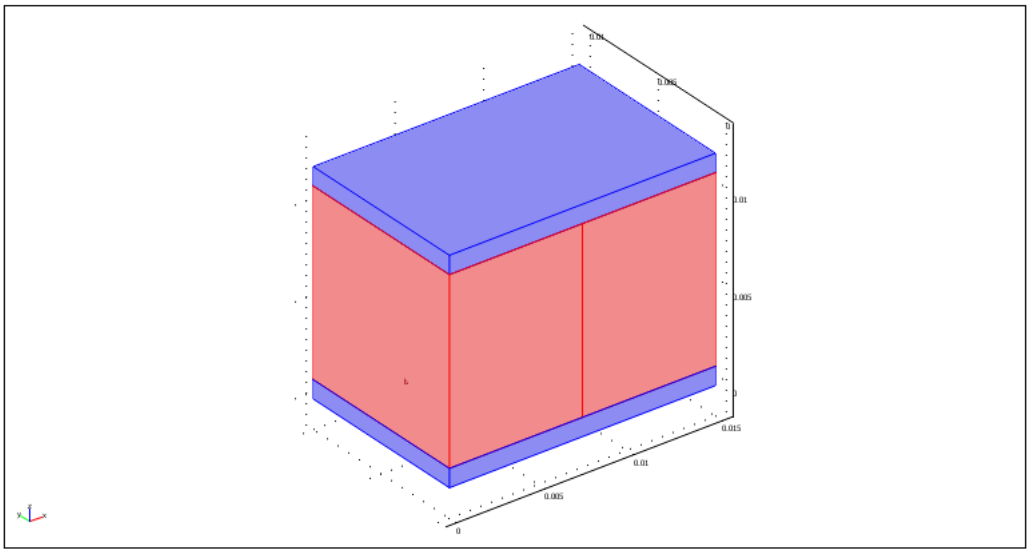

Figure 5-5 Geometry for the laminated piezoelectric/Terfenol material

Terfenol material is 15mm x 10mm x 10mm and the thickness of piezoelectric material is 1mm

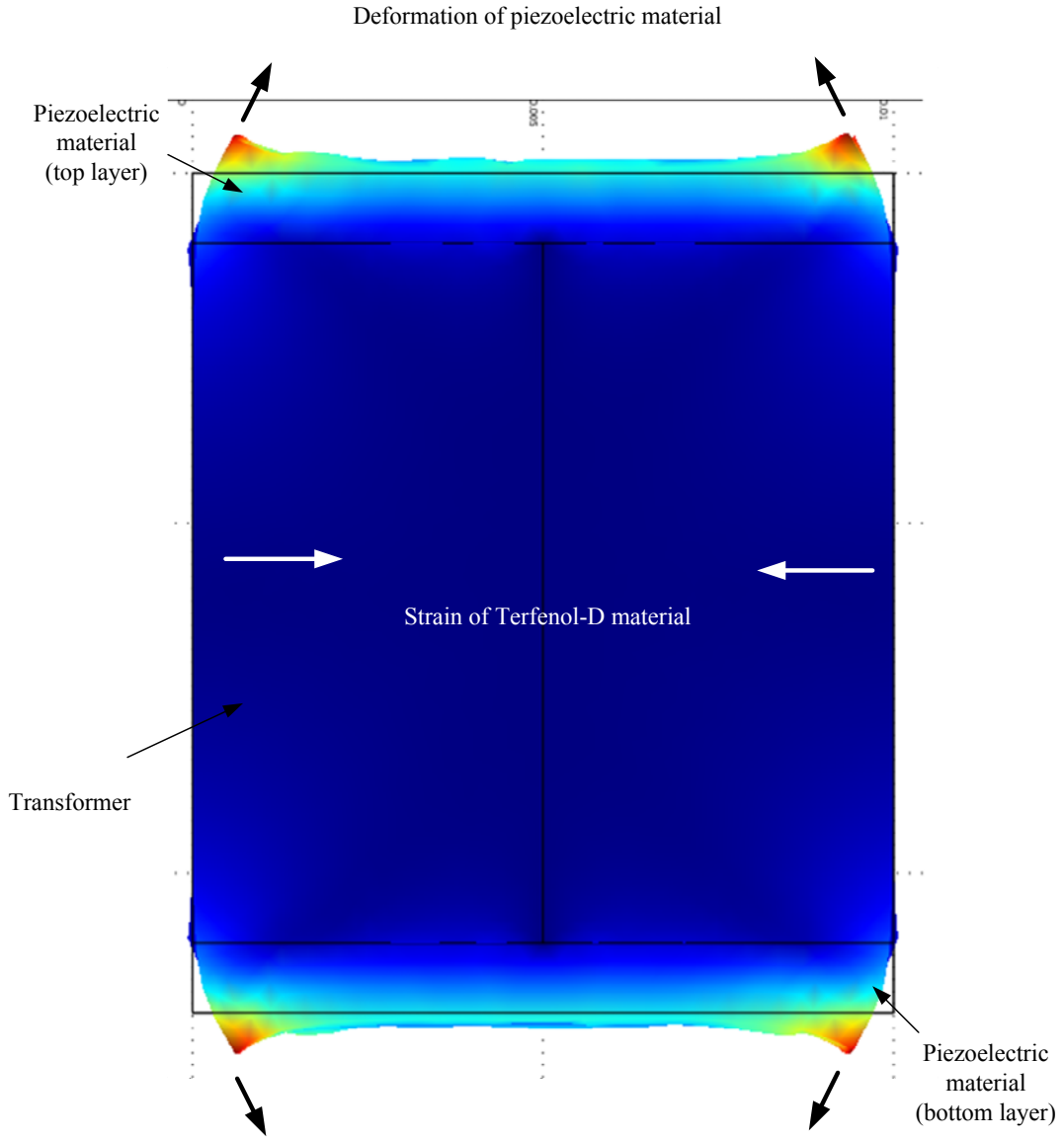

Figure 5-6 Deformation image of 10mm by 10mm by 10mm Terfenol-D material with 1mm thickness piezoelectric layers with ± 150V supplied

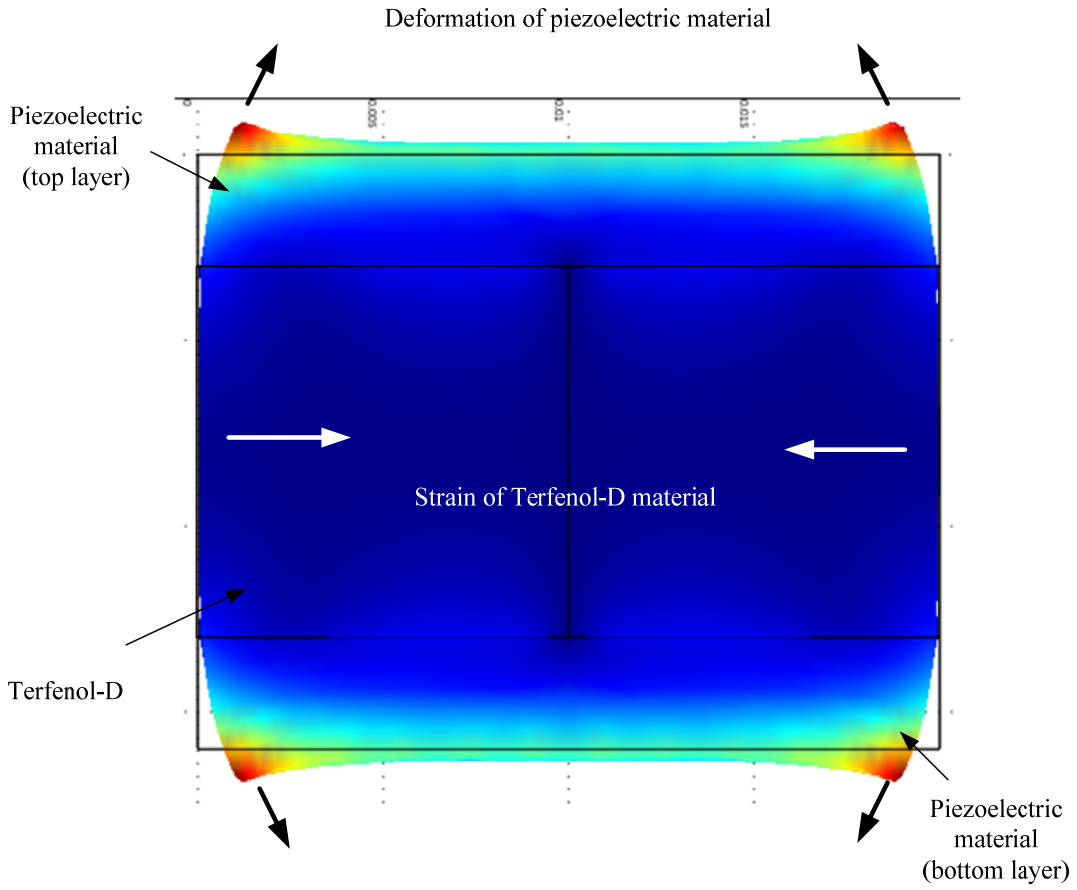

Figure 5-7 Deformation image of 10mm by 20mm by 10mm Terfenol-D material with 2mm thickness piezoelectric layers with ± 150V supplied

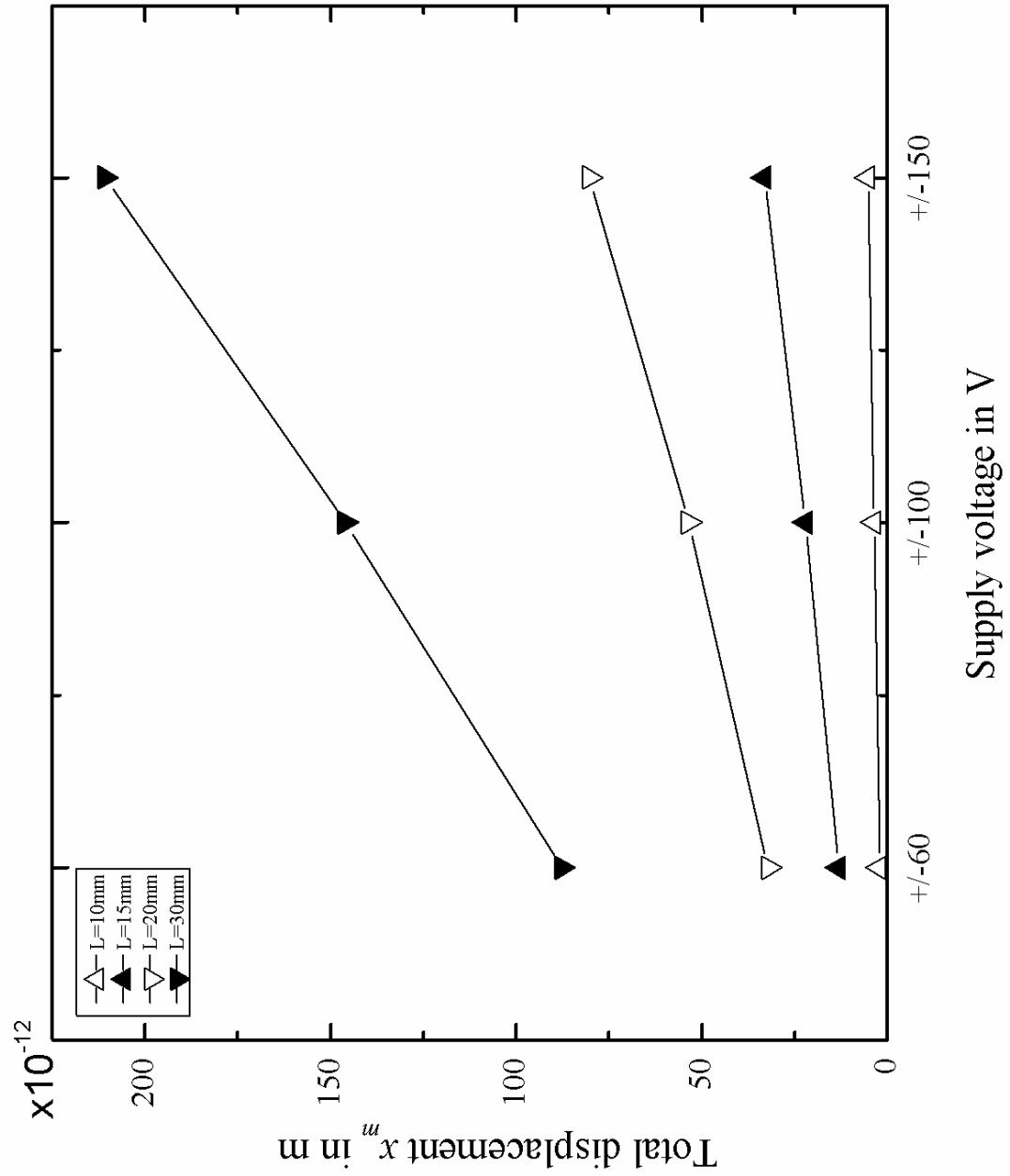

Figure 5-8 Total displacement x_m of Terfenol-D material at different supply voltages

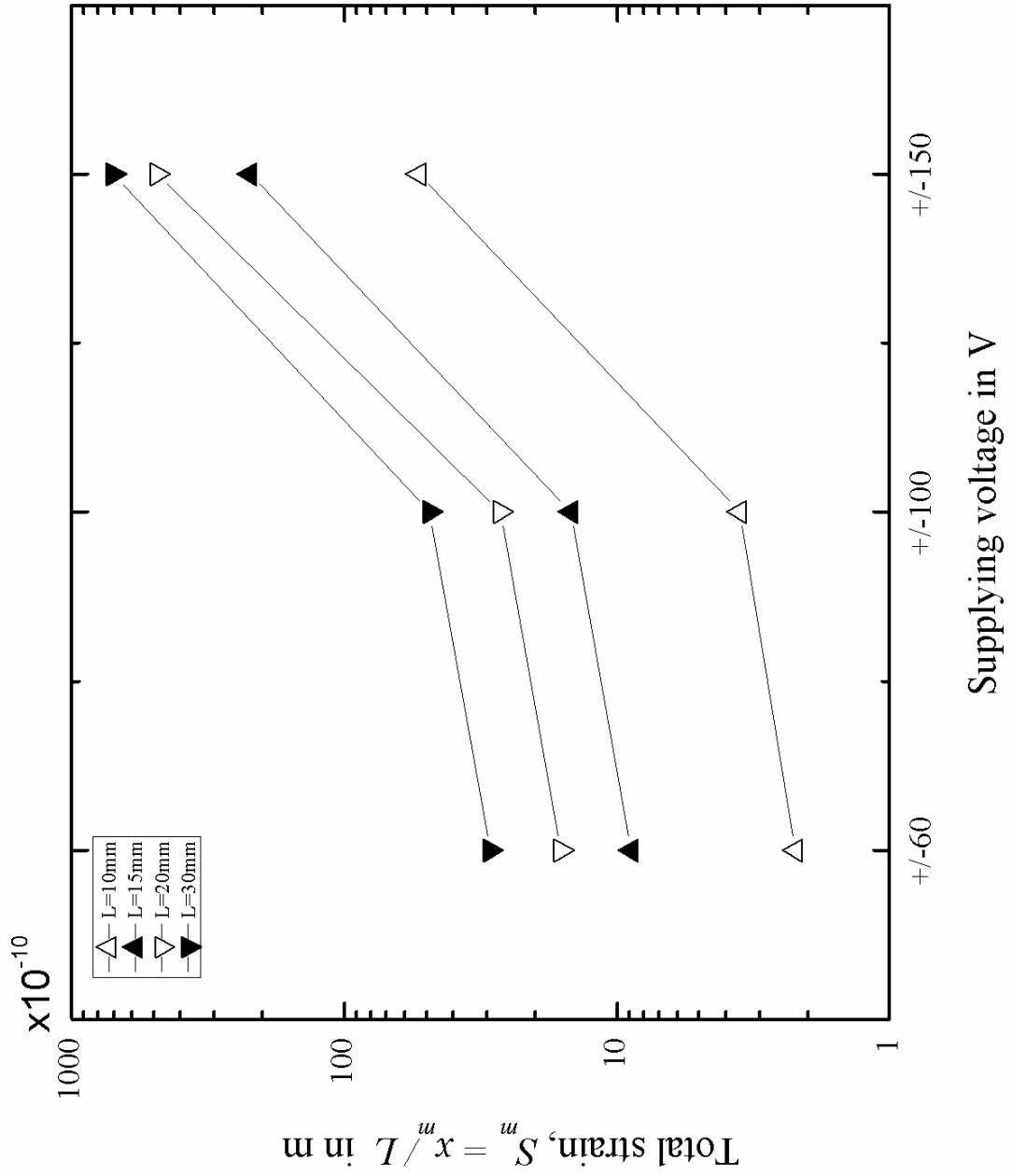

Figure 5-9 Total strain Sm = x_m / L of Terfenol-D material at different supply voltages

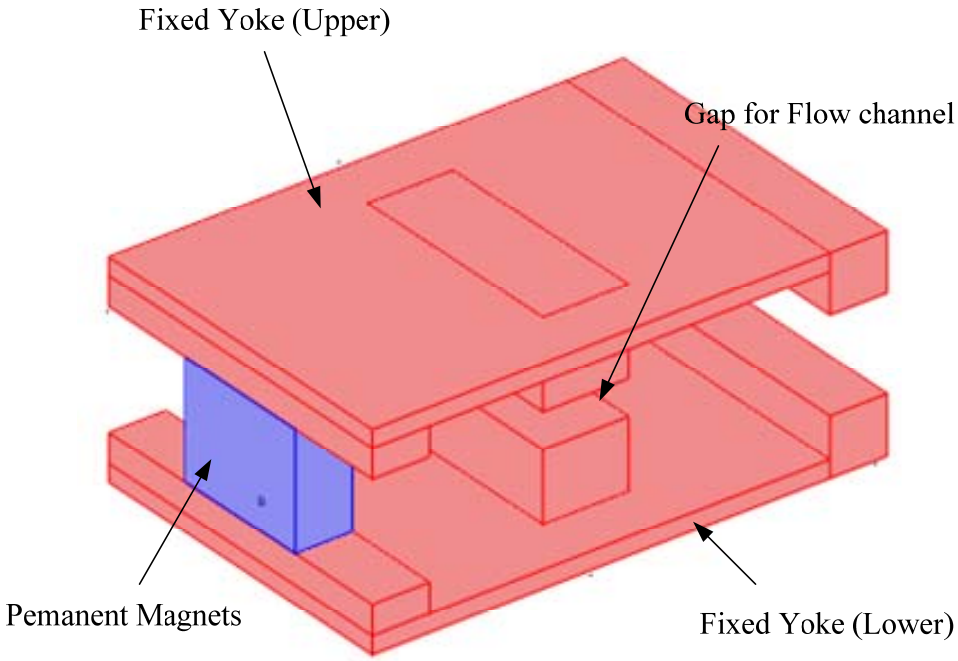

Figure 5-10 Proto type electromagnetic flowmeter using permanent magnets

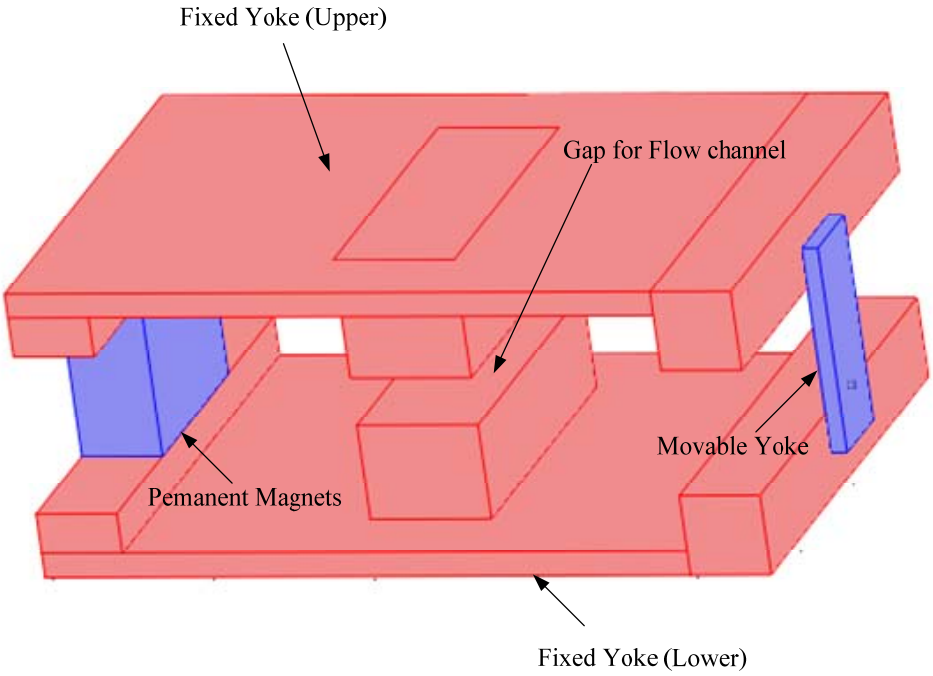

Figure 5-11 Reverse view of the proto type to show the movable yoke at the opposite end

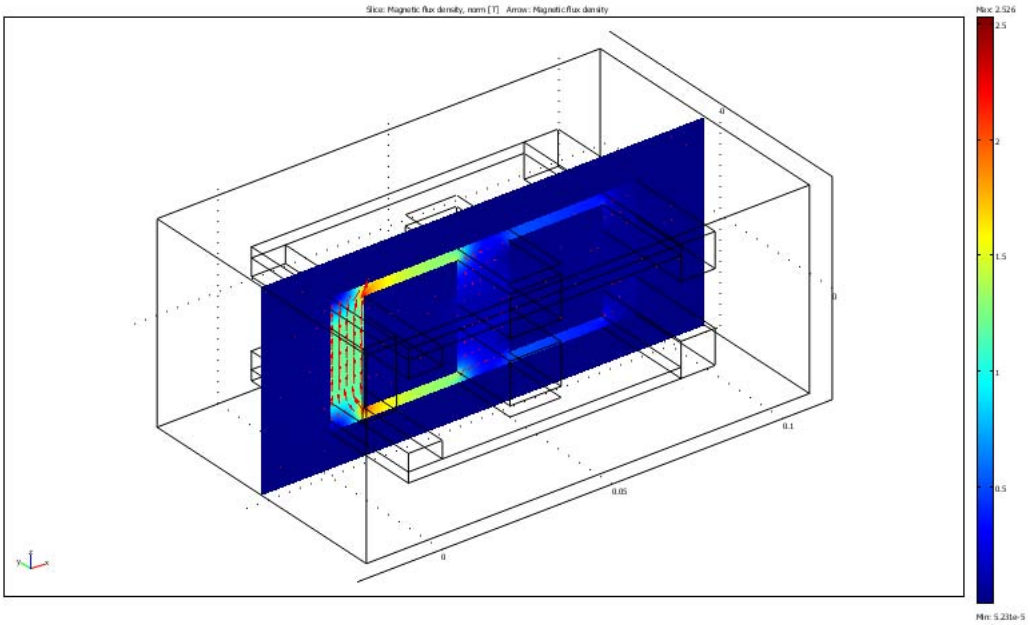

Figure 5-12 Magnetic field modelling result without the movable yoke (open state)

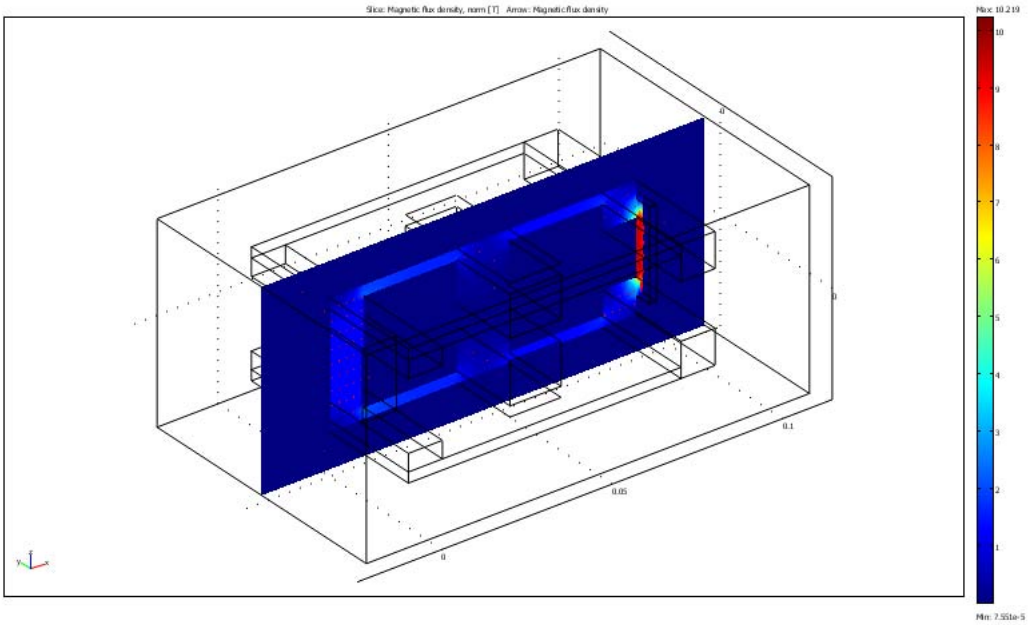

Figure 5-13 Magnetic field modelling result with the movable yoke at the closed state

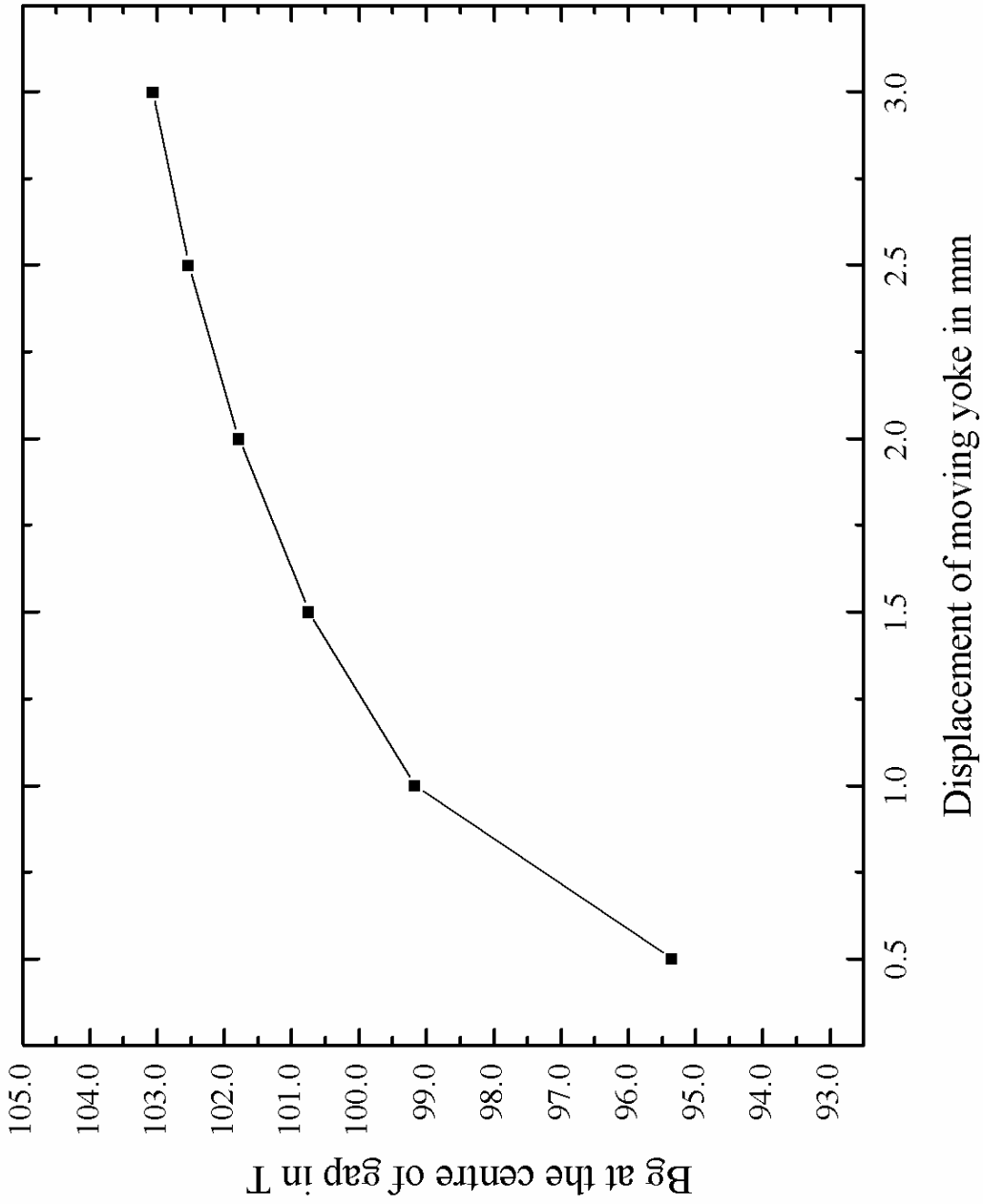

Figure 5-14 Magnetic field strength at the centre of the air gap in placing the movable yoke in different distance from the fixed yoke

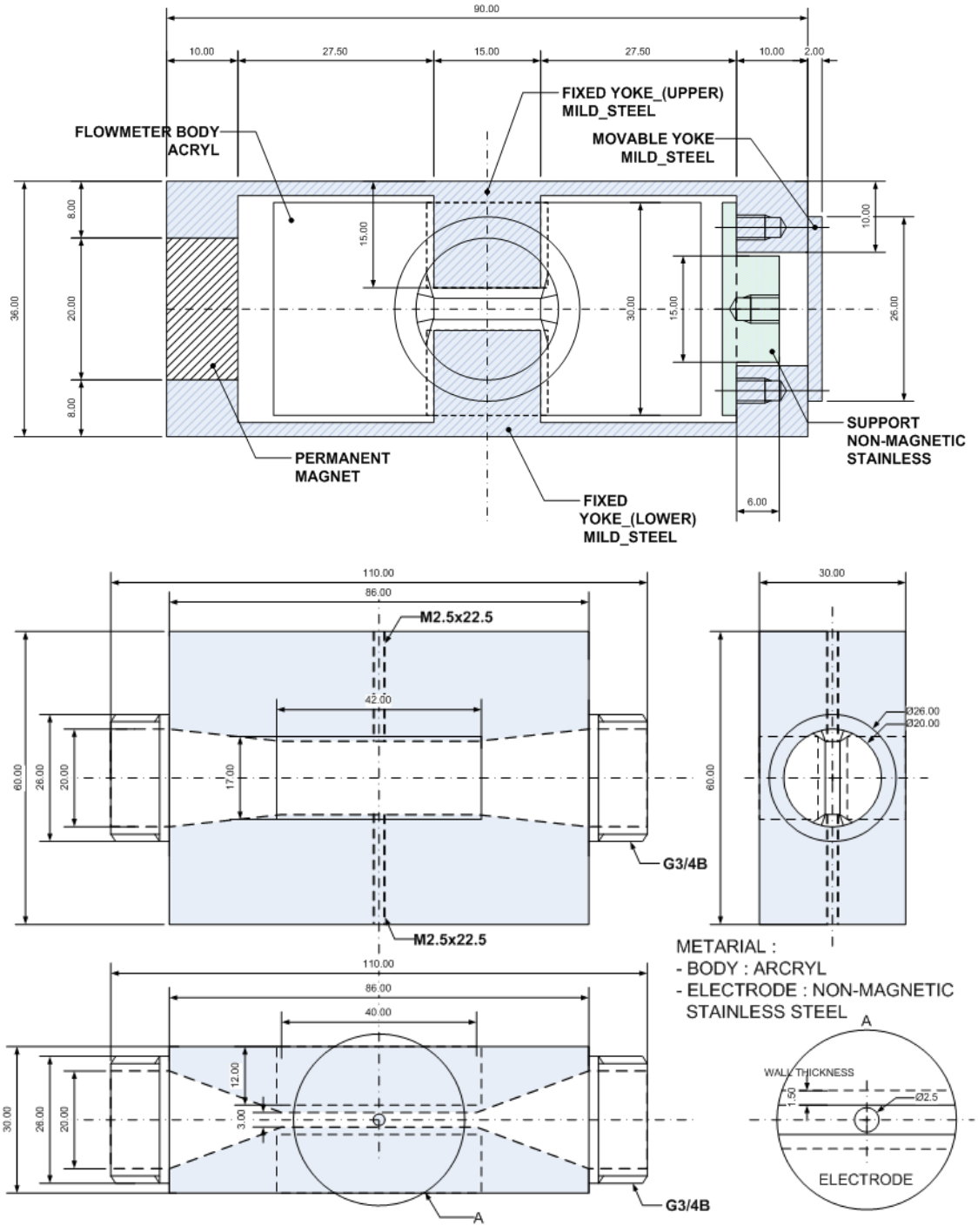

Figure 5-15 Drawings of the proto type of flowmeter using piezoelectric actuator device

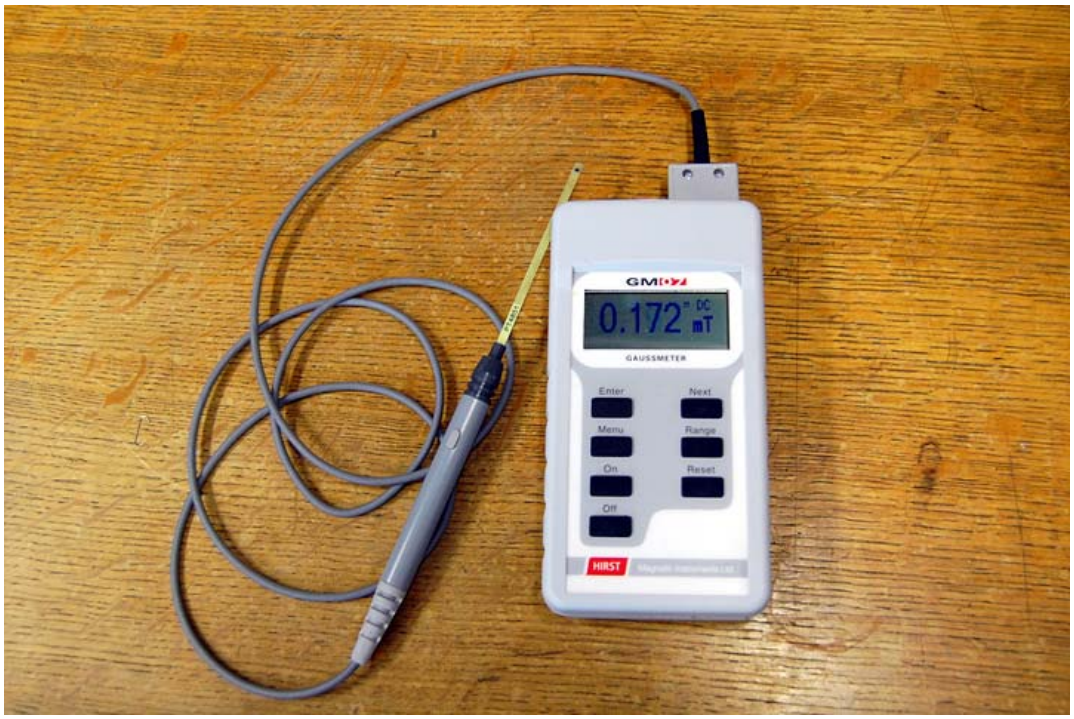

Figure 5-16 Portable Gauss meter GM07

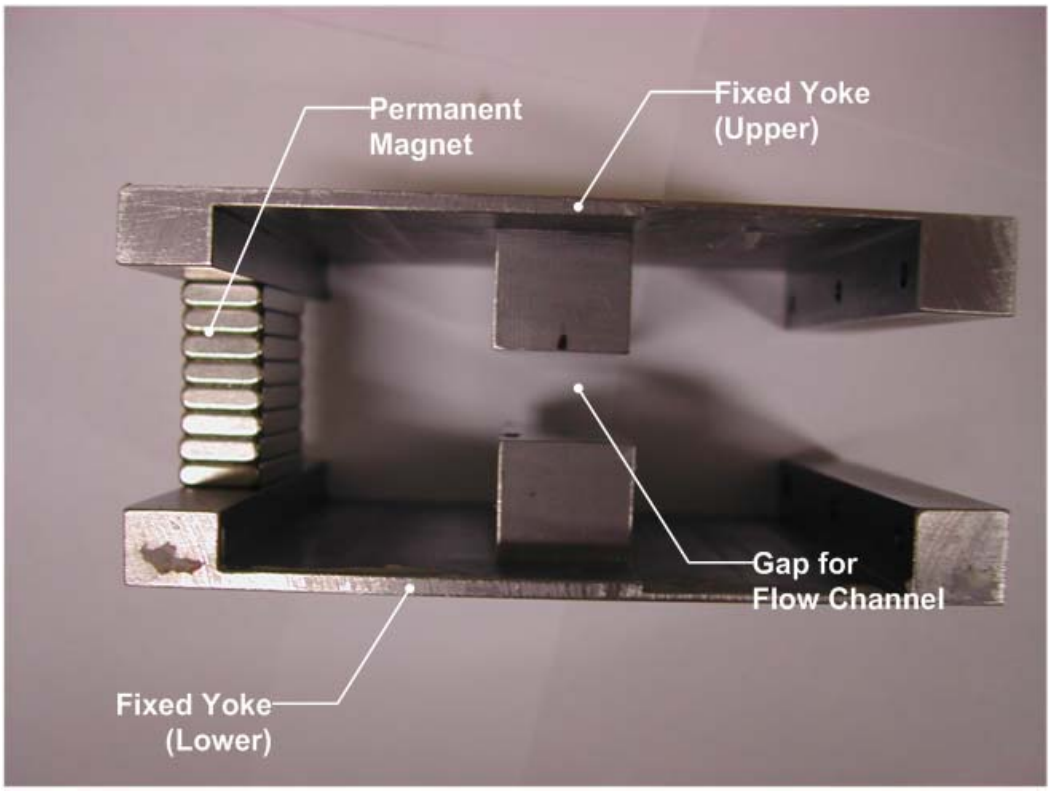

Figure 5-17 Fixed yokes and permanent magnets

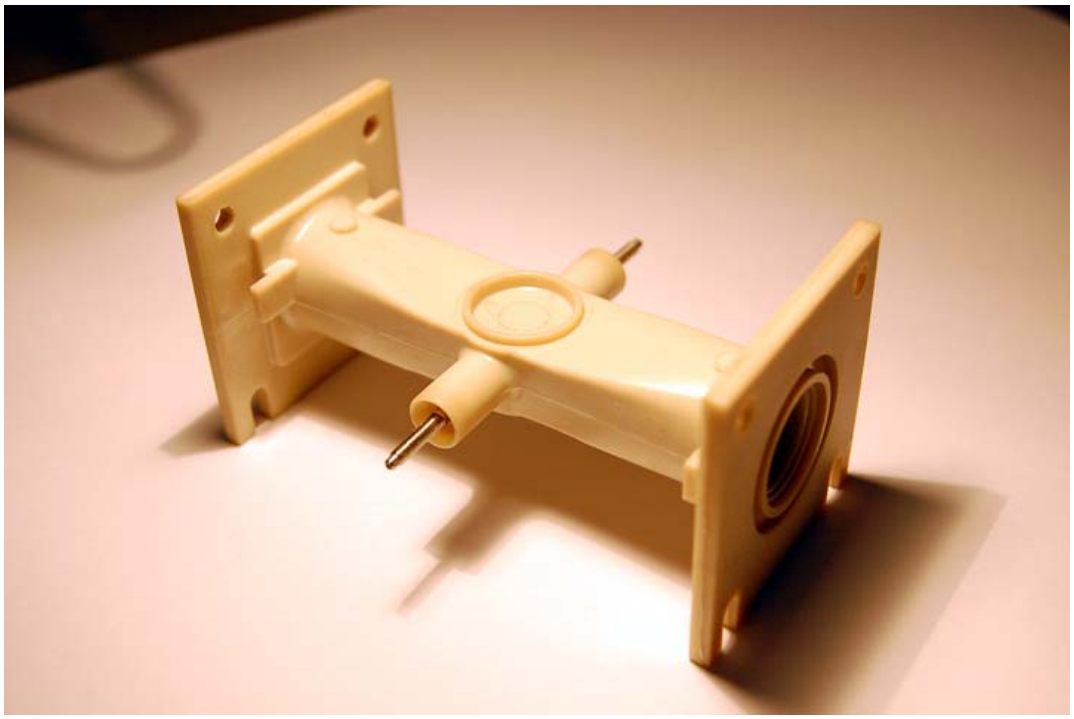

Figure 5-18 Picture of the flow channel

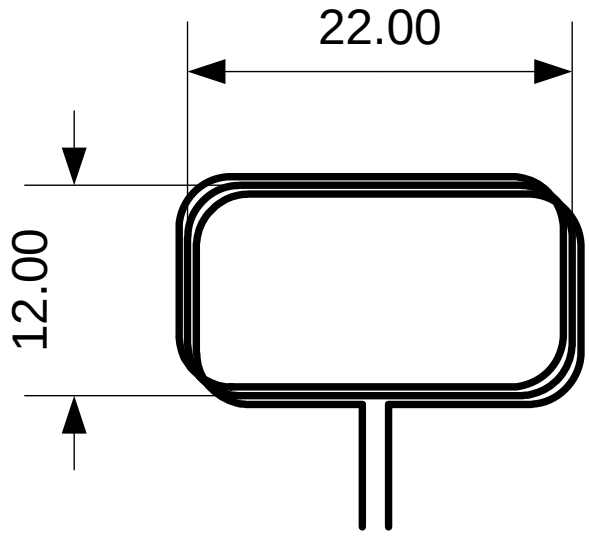

Figure 5-19 Drawing of the search coil

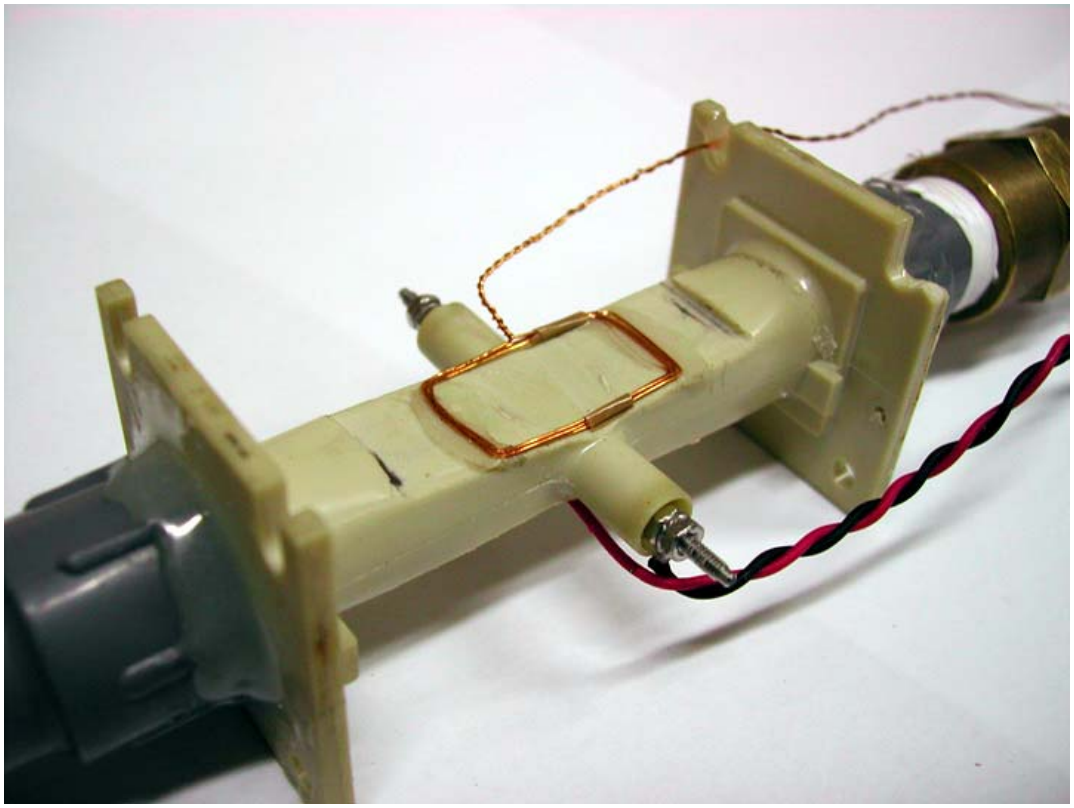

Figure 5-20 Flow tube with connection and search coil

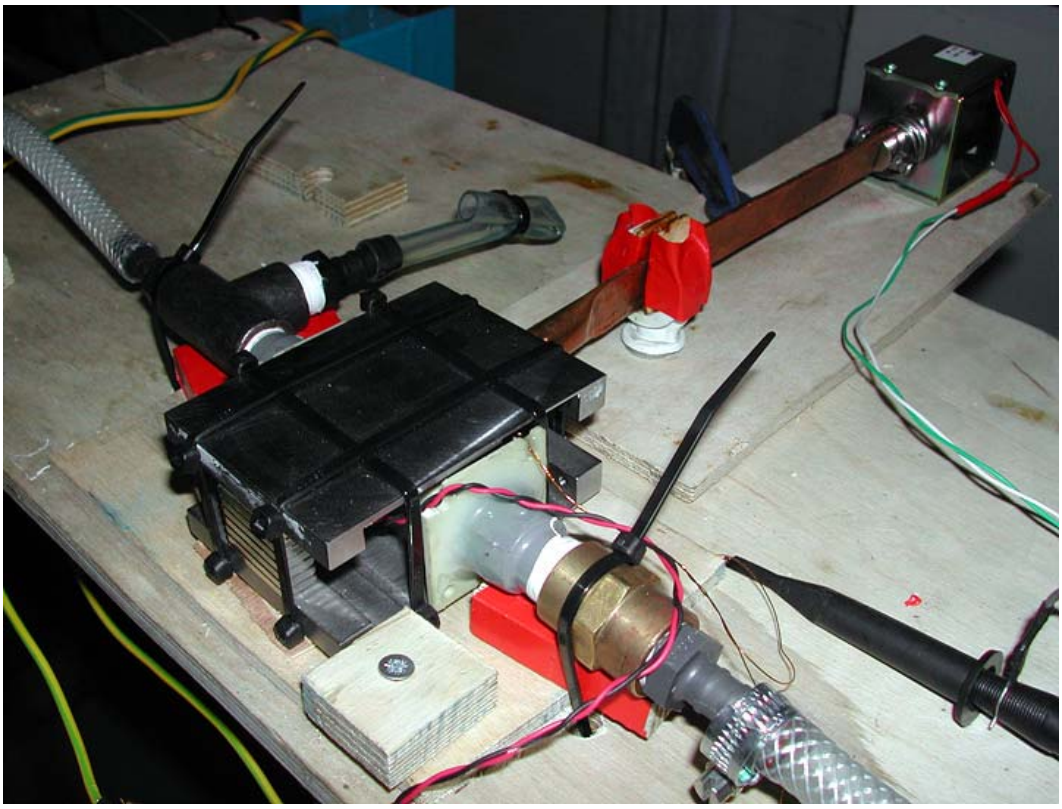

Figure 5-21 Assembled proto type flowmeter

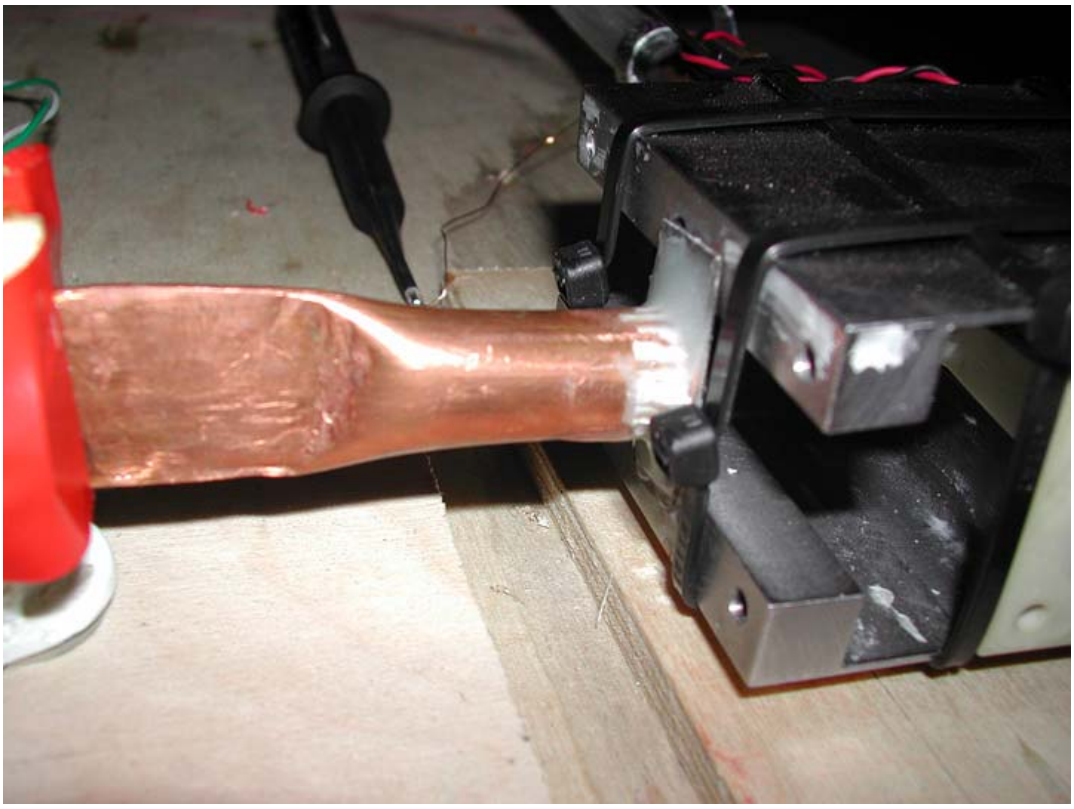

Figure 5-22 Picture of movable yoke at the end of fixed yoke

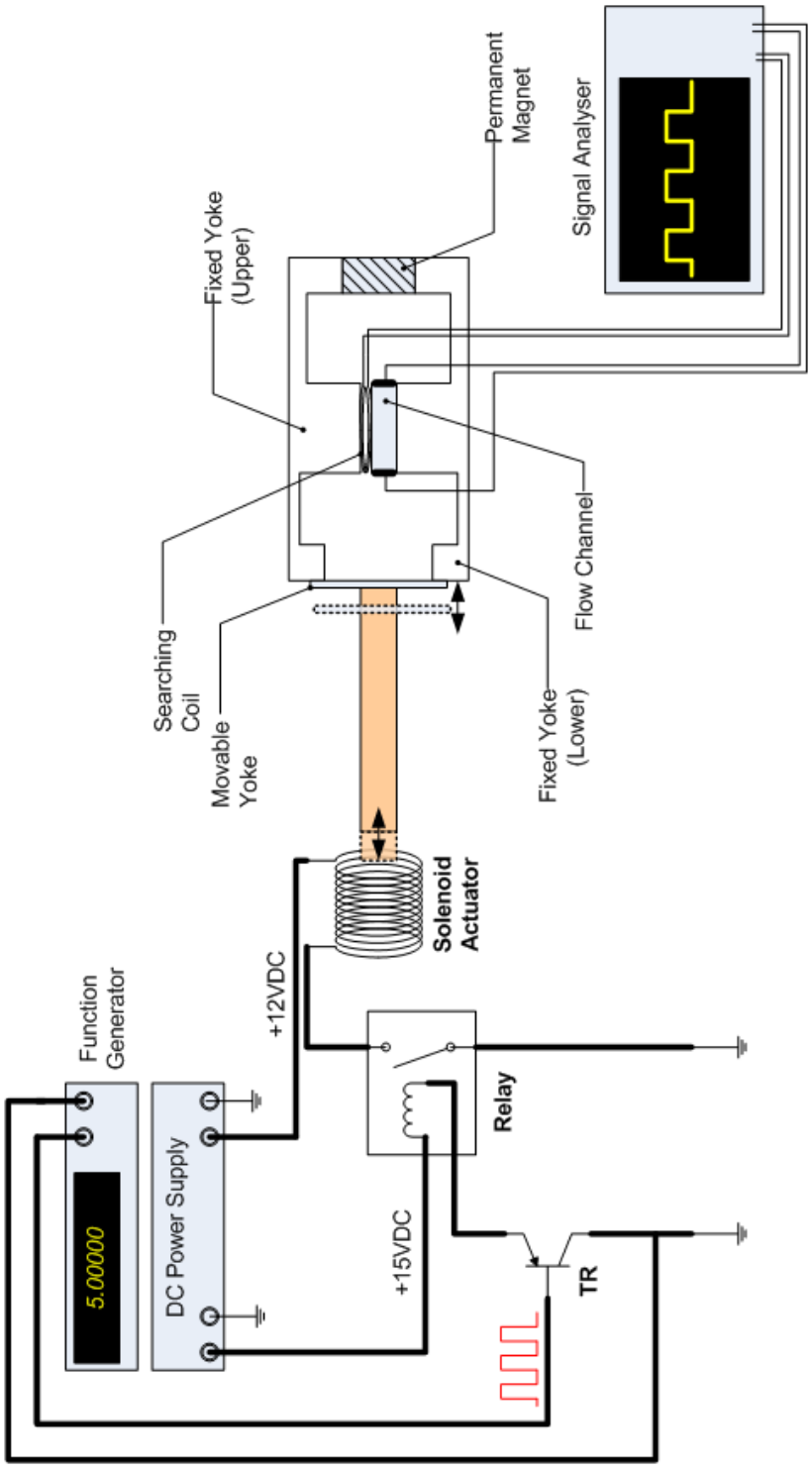

Figure 5-23 A diagram of instrumentation

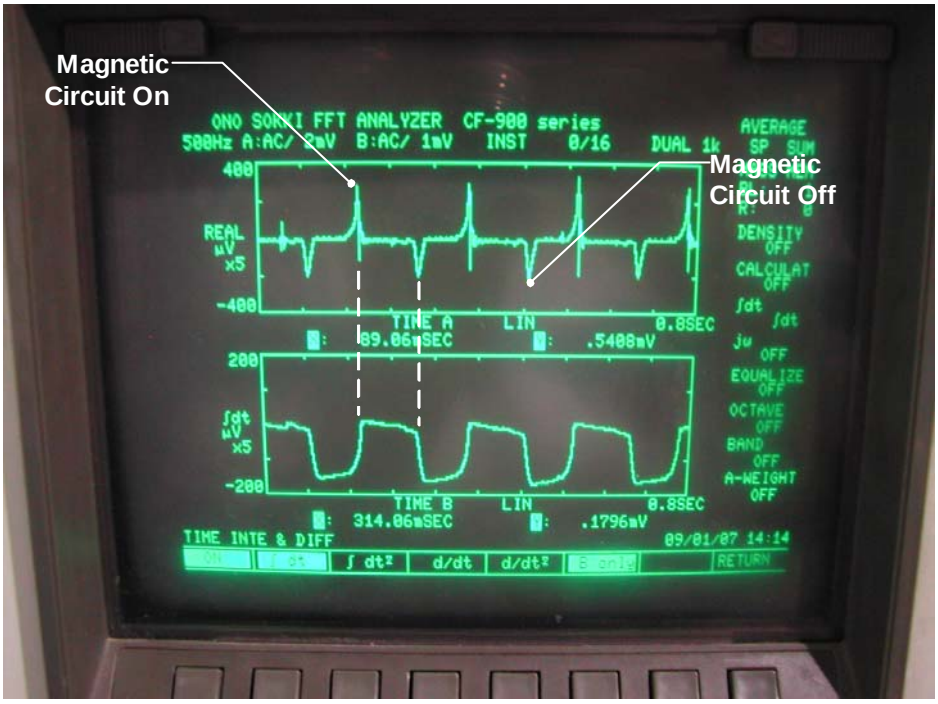

Figure 5-24 The change of magnetic flux at the air gap for flow channel at 5 Hz operation frequency

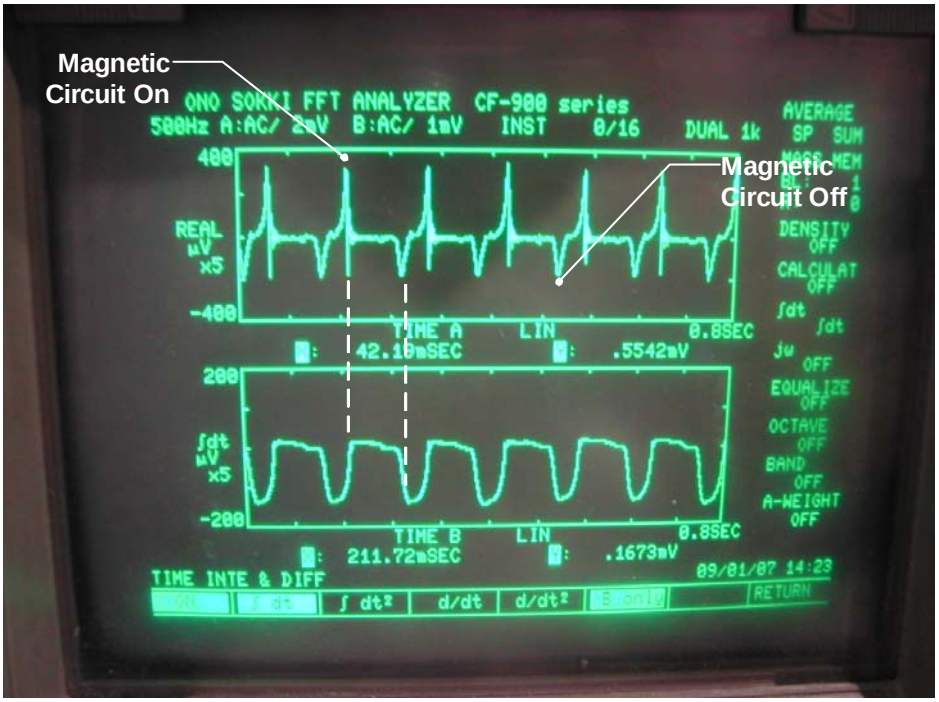

Figure 5-25 Magnetic Flux change at 10Hz operation mode

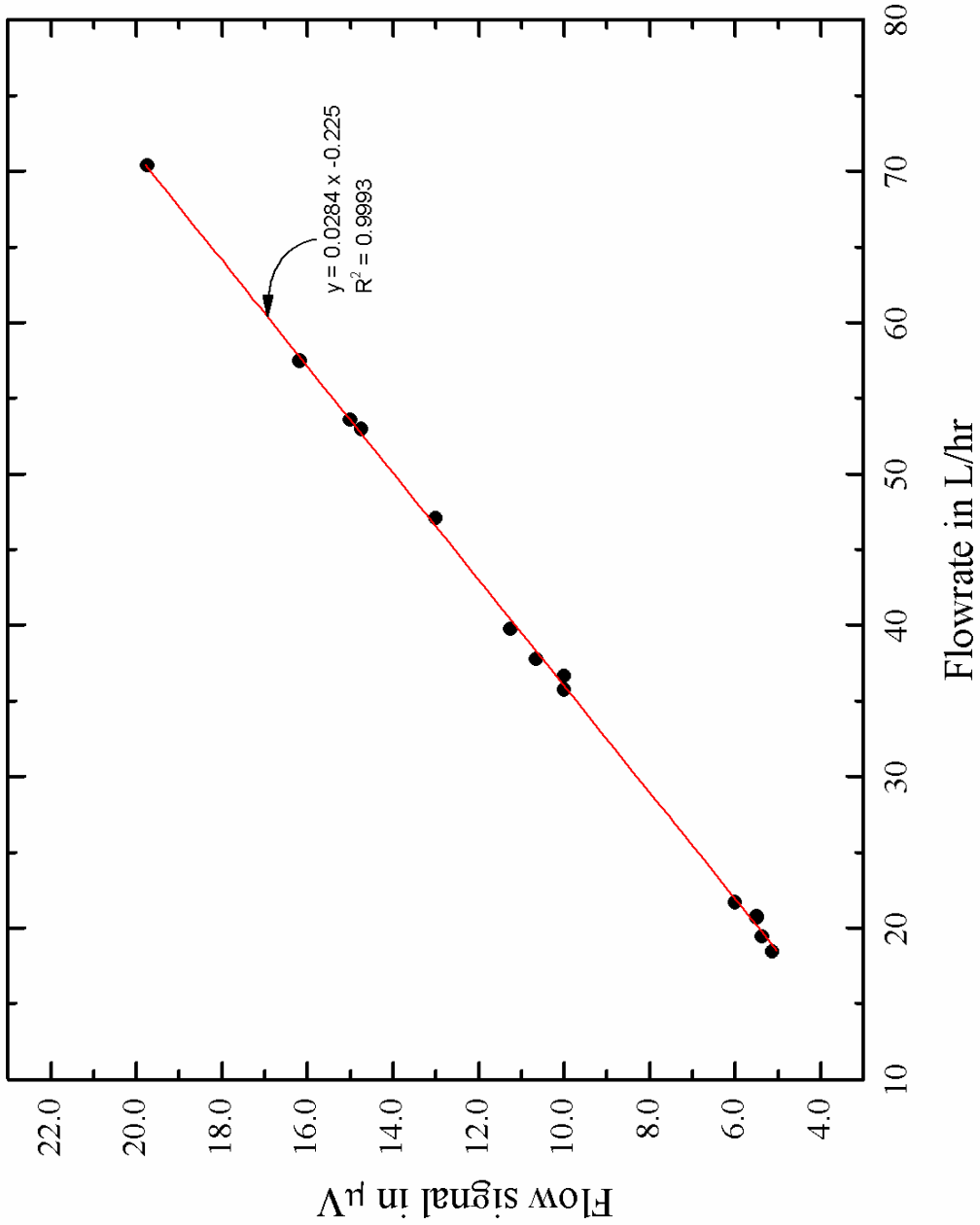

Figure 5-26 Flow signal at 1.5 Hz operation frequency

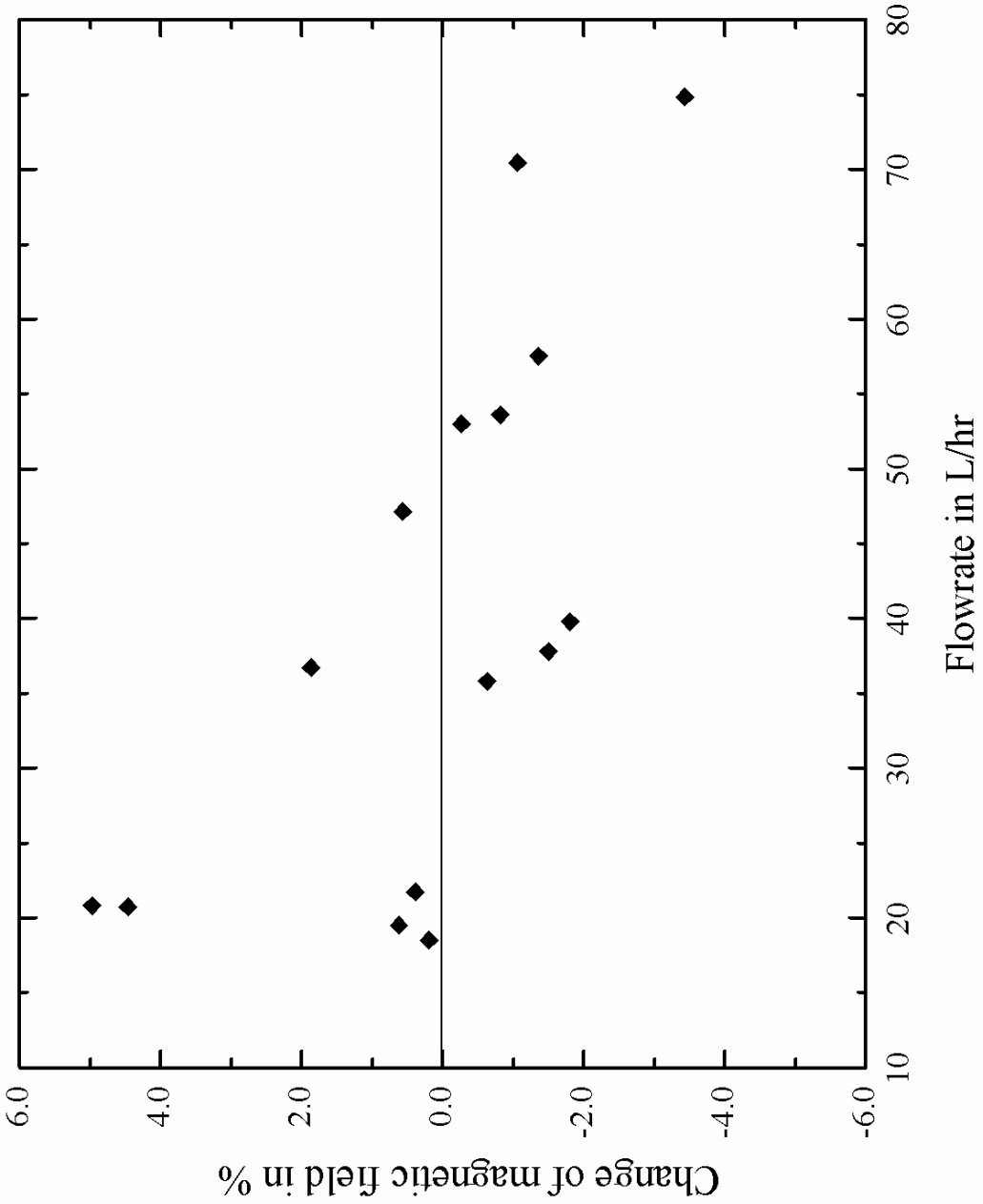

Figure 5-27 Error of magnetic field changes

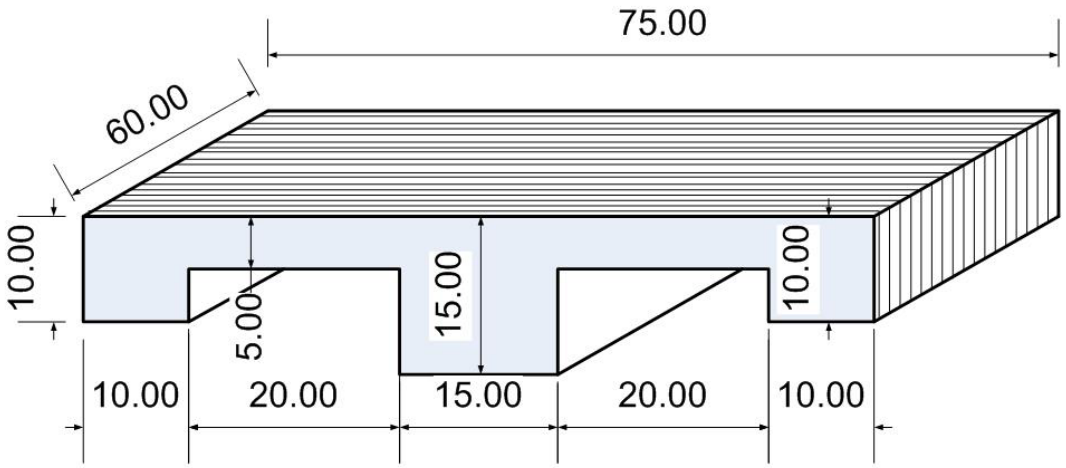

proto-type 2

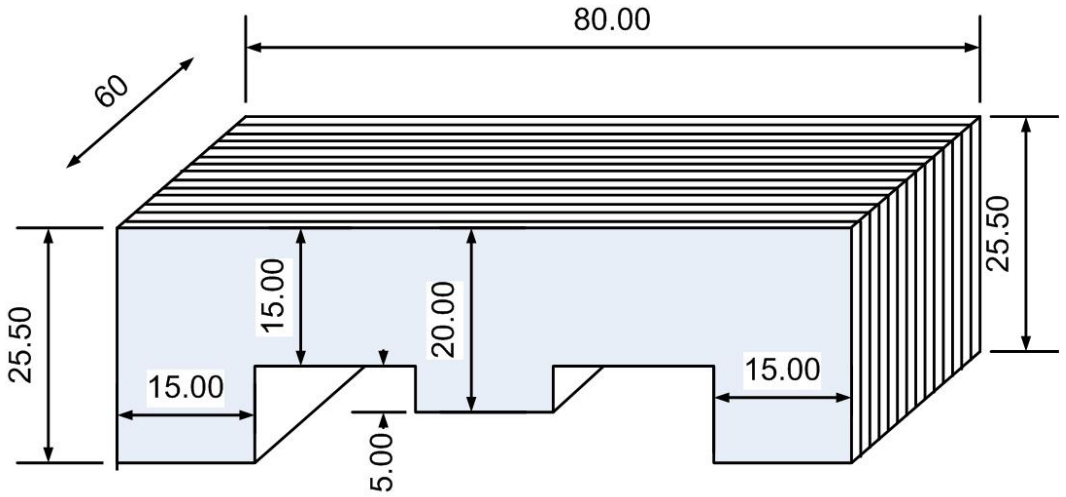

proto-type 3

Figure 5-28 Laminated yokes for proto-type 2 and proto-type 3

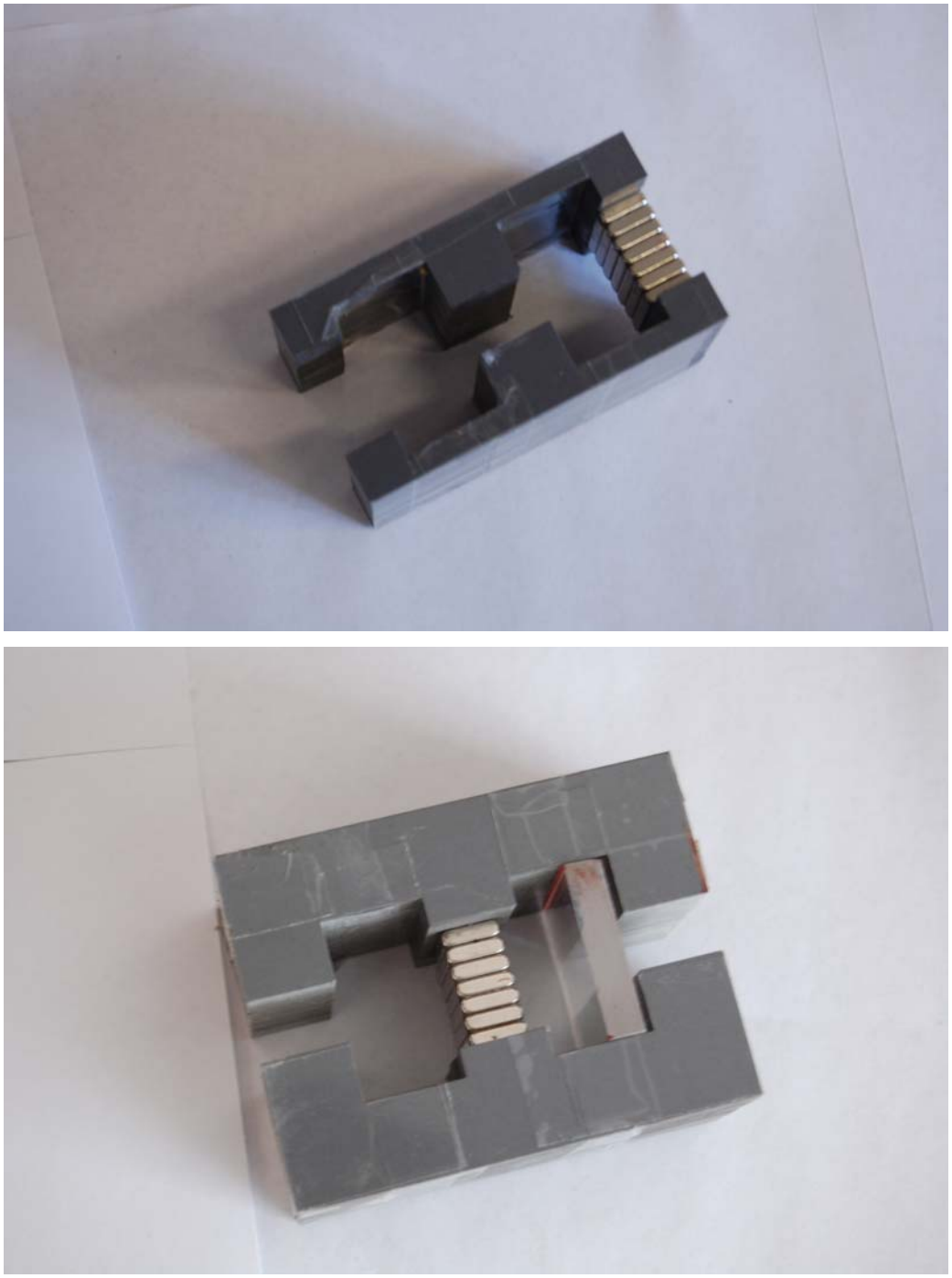

Figure 5-29 Assembled proto-type 2 (top) and proto-type 3 (bottom)

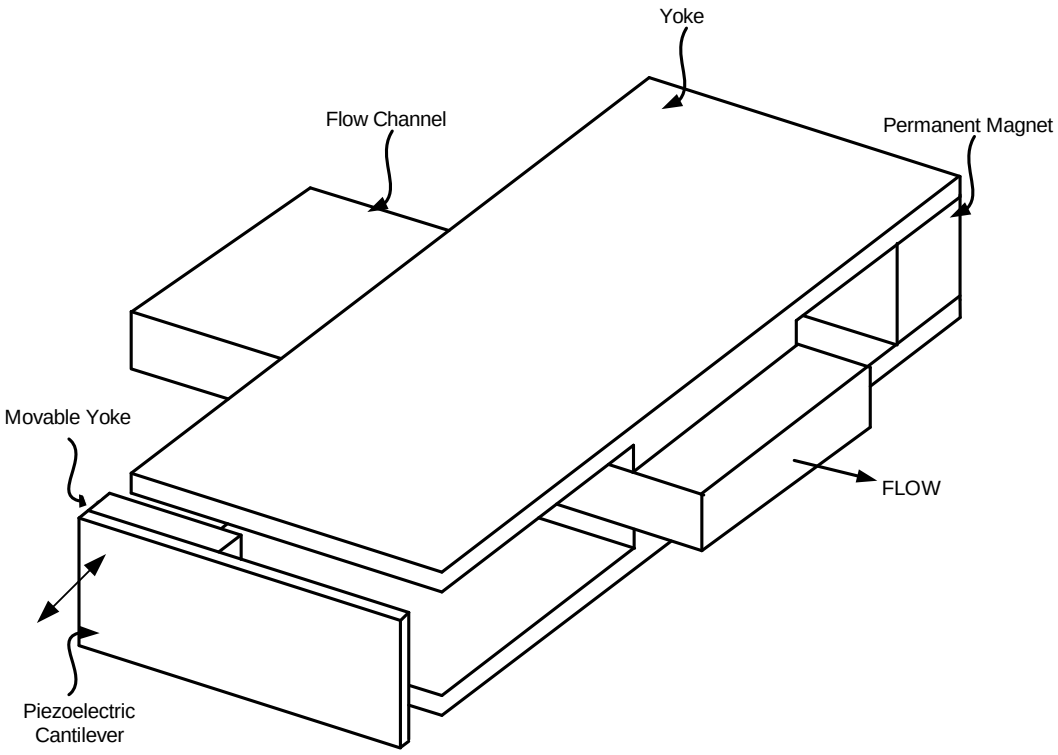

Figure 5-30 Flowmeter using a piezoelectric cantilever actuator

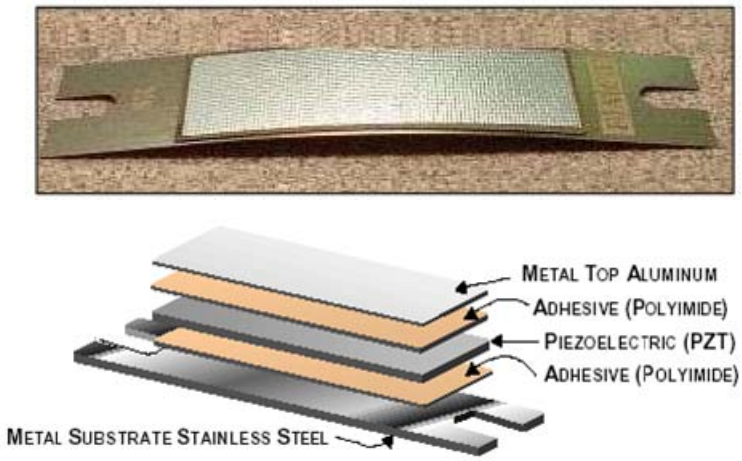

Figure 5-31 THUNDER TH-8R piezoelectric actuator
(from product catalogue from FACE International Corp.)

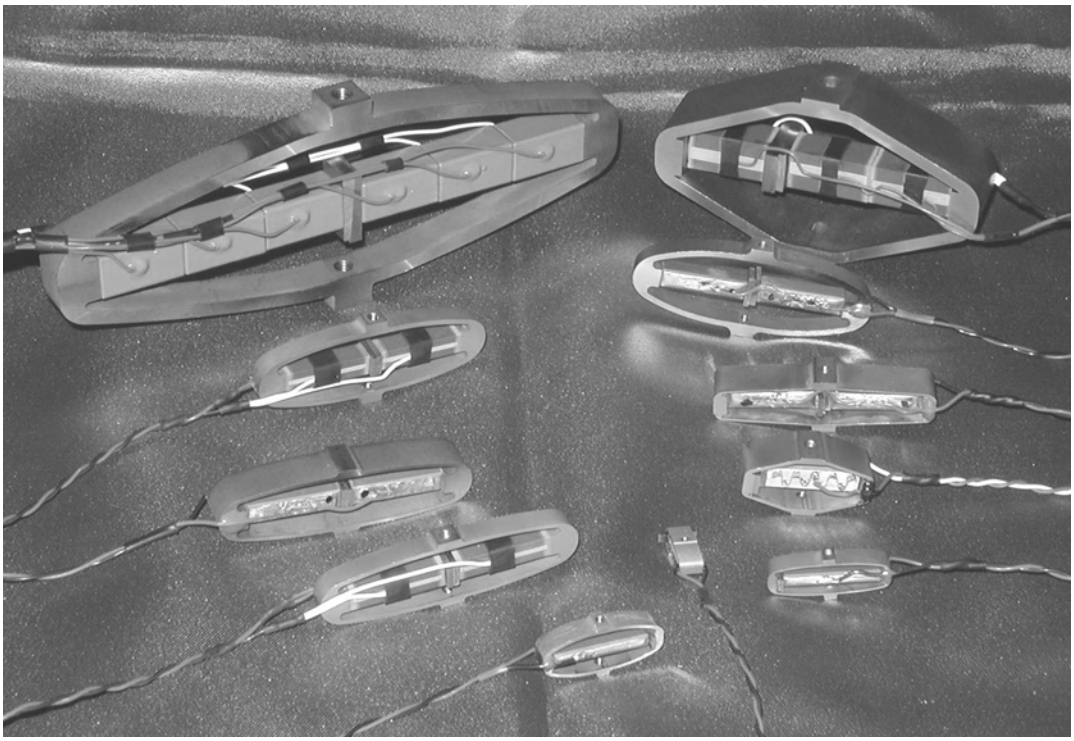

Figure 5-32 The different amplified piezoelectric actuators from Cedrat (Claeyssen *et al.*, 2007)

Chapter 6. Fluidic oscillator

6.1 Introduction

In this thesis, the work on the fluidic oscillator is also focused on investigating the meter performance and design review to improve the flow signal. The fluidic oscillator is converted to 2-dimensional geometry for fluid dynamics modelling. The flow signal and meter factor are also investigated to understand the effects of changing the fluidic oscillator geometry.

The location of electrodes and magnets are also considered in order to obtain any better flow signal strength, especially at low flowrates. The experiments have been performed in the test rig of the PASE Lab at Cranfield University.

6.2 Fluidic oscillator design

The fluidic oscillator referred to in this chapter is shown in Figure 6-1, has a jet, diffuser walls, a splitter post, feedback channels and an exit channel. The height of the fluidic oscillator channel is 19mm. The single magnet is located inside the splitter pocket and two electrodes are located at the top side of the fluidic oscillator. The single magnet is a 10mm x 3mm x 25mm block type Neodymium magnet. The configuration of this fluidic oscillator

is shown in Figure 6-2. The single magnet is taller than the height of the channel so the top of magnet juts out from the fluidic oscillator.

The diameter of the electrodes is 2mm and in the experimental work they are directly connected to the spectrum analyser in order to measure both the frequency and the amplitude of the generated signal.

The width of the jet is 3.62mm so the cross-sectional area of the jet is 6.88×10^{-5} m^2. The width of the feedback channel is 7mm, which provides a circular path towards the jet.

6.3 CFD modelling

In order to evaluate the meter performance, CFD modelling is undertaken using the Chemical Engineering Module of COMSOL Multiphysics. This module consists of a number of modelling interfaces, called application modes, which form the backbone of the module. They are based on the equations for momentum transport, energy transport, and mass transport.

For this modelling, the incompressible Navier-Stokes model for laminar flow is used. This model is the solution for the general momentum balance and continuity equations for fluids with constant density.

The maximum flowrate for modelling the fluidic oscillator is 2 m^3/hr and the Reynolds number is 2.9×10^4. This flowrate is in the turbulent flow region. The flow modelling for this flowrate had to be done for the turbulent model but it is extremely difficult to simulate for time-dependent behaviour. Due to the significantly different mixing-length scales, the

stable solution of the turbulent modelling needs a very fine mesh but the increasing number of mesh will make the computing time become unfeasible.

In this thesis, the flow modelling for the turbulent flow is simulated by the laminar model with the implication of a turbulent parameter for sub-domain settings by changing the artificial diffusion settings. The laminar Navier-Stokes model has to turn Streamline Diffusion option (GLS) on and set Crosswind diffusion factor, C_k as 0.1 as the default parameters. But for the turbulent modelling in the laminar model for this work, Streamline Diffusion option and Crosswind diffusion option have been turned off and the Isotropic diffusion, δ_{id} has been used and set to 0.1.

6.3.1 Flow modelling in 2D

The actual flow channel in practice has 3D geometry but in this section, the geometry is simplified to 2D geometry to reduce both the number of meshes required and the computing time. The mesh point for the 2D geometry is at least 50,000 points and is able to compute the fluid behaviour within 3 hours. However, for 3D geometry, the mesh points will be more than 5 million points but it is not possible to compute this number on a standard desktop computer which only has a 2GB memory and 32bit operating system.

This 2D modelling simplification is possible because the height to jet width aspect of the oscillator is 5.21. This is considered to be justified and also the comparison with actual results, both in terms of the frequencies and amplitudes observed, supports the decision to undertake the modelling in 2D. The middle plane of the actual fluidic oscillator is converted to a 2D geometry for the modelling. The 2D modelling results are expanded into 3D for the flow signal calculation later.

The initial flow which has only an x-component of velocity, is set from 20L/hr to $2m^3$/hr. In order to set the parabolic flow profile at the inlet, the inlet velocity is set as

$$inlet\ velocity = initail\ \ flow \times 1.16 \times 10^{-4} \times 4 \times s(s-1) \qquad (6\text{-}1)$$

where, initial velocity is the flowrate in l/hr, s is inlet distance factor from the modelling software.

The modelling is undertaken with a time domain solver which can model the oscillation of the fluid within the oscillator chamber. The time domain parameter is set to see at least 10 oscillations at the given flowrate. The inlet velocity and time stepping parameters are listed in Table 6-1.

The exit boundary is defined as the outlet condition with constant pressure. The remaining walls are set as walls with a no-slip condition. The density of water is defined as $1x10^3$ kg/m^3 and dynamic viscosity is to $1x10^{-3}$ Pa·s. To use this laminar Navier-Stokes model to 2000 l/hr flowrate, the isotropic diffusion parameter is modified to 0.025 but this value is set to 0.01 for a 20 l/hr flowrate. The geometry and mesh structure is shown in Figure 6-3. Finer meshes are generated near the walls and edges so that the total elements are 18290.

The CFD modelling at different times at 20 l/hr is shown in Figure 6-4. The jet is formed at the beginning of the simulation and developed in the first second until the tip of the jet reaches the splitter face. Once it hits the splitter face, the jet is diverted to one of the channels between the splitter body and the diffuser walls which is shown at 1.4 sec to 1.8 sec in the figure.

Therefore, the jet passes the channel slips out though the exit channel but some flow is caught at the edge of the exit and feedback channels as shown at 1.8sec. The feedback flow will reach the jet region then the feedback flow separates the jet from the diffuser wall. The separated jet is attracted to the opposite wall as shown in the picture at 2.8sec.

Table 6-1 Modelling parameters for the time dependent modelling

Flowrate	Inlet velocity (m/s)	Time	
		Step (sec)	Span (sec)
20 L/hr	2.326×10^{-2}	$3.6. \times 10^{-2}$	27.0
50 L/hr	5.814×10^{-2}	1.44×10^{-2}	10.8
100 L/hr	1.163×10^{-1}	7.20×10^{-3}	5.40
200 L/hr	2.326×10^{-1}	3.60×10^{-3}	2.70
500 L/hr	5.814×10^{-1}	1.44×10^{-4}	1.08
1000 L/hr	1.163	7.20×10^{-4}	0.54
2000 L/hr	2.326	3.60×10^{-4}	0.27

6.3.2 Meter factor

The meter performance is evaluated by the volume per pulse meter factor, K, over the whole flow range as defined as:

$$K = \frac{Q}{f} \tag{6-2}$$

where Q is the volumetric flowrate and f is the oscillation frequency. The meter factor means a flow volume per single oscillation. The oscillation frequency is measured at the location of one of electrodes and the volumetric flowrate is calculated using inlet velocity.

In the experiment, the oscillation frequency is measured by the spectrum analyser with FFT function and the flowrate is measured by the weighing system of the test rig.

The inlet of the geometry is still 2-dimensional but in this section, the 2D geometry will expand by extruding the geometry so the cross-sectional area at the inlet is 19 x 19mm^2. To obtain the mean oscillation frequency, three areas of waveform are chosen as tops, bottoms and middle. These areas are shown in Figure 6-5.

The meter factor from experiments and modelling is compared, as shown in Figure 6-6, to verify the modelling because it is undertaken in a simplified 2D geometry.

The meter factor from the experiments shows that the meter factor starts as high as 10.8445 at 15.6 L/hr and sharply drops to 9.7809 then gradually increases to 10.6737 at 150L/hr. The meter factor settles at around 10.6 afterwards. The meter factor calculated from the modelling starts with 11.0418 at 20L/hr then drops to 10.1429 at 60L/hr. The meter factor increases up to 10.9815 at 1m^3/hr but slightly decreases to 10.8497 at 2m^3/hr.

The meter factor from the modelling is 3.7% higher at a maximum of 600 L/hr than the experiments which would imply that the actual oscillation frequency at the same flow is slower. But between the 80L/hr to 200L/hr flowrate, the meter factor from the modelling fits with the experimental results. This can be agreed because the laminar model is used for the entire flow range and Reynold's number at 200L/hr is 2921 which means the flow profile is not entirely a turbulent regime.

The limitation of 2D geometry in the modelling is that the model has no top and bottom walls but there is the complication of the geometry at the outlet, especially where the top and bottom walls meet the exit in real geometry. The structure of the area of the exit and side walls is shown in Figure 6-7. The red painted areas show the difference of extended

3D modelling geometry and the actual geometry. This blocked area will increase the error by taking the laminar model in turbulent flow profile.

6.4 Flow signal calculation

The flow signal of the fluidic oscillator is calculated by taking the magnetic field modelling, the virtual current modelling and CFD modelling. Near the sensing area, the normal component to the magnet surface is mostly a contributed component of the magnetic field and the vertical component of the virtual current is also a dominated component. Therefore, only the rectilinear component which is the x-axis component of the flow velocity is useful to the modelling.

For the calculation, the magnetic field and virtual current results are converted into a matrix of small cube cells measuring 0.5mm by 0.5mm by 0.5mm. 2D CFD modelling results are converted into a 2D matrix and stacked up to the top layer.

6.4.1 Magnetic field

The fluidic oscillator has a single permanent magnet vertically inserted in the pocket inside the splitter body. The magnet has 10mm by 3mm by 25mm dimensions and an N38 grade Neodymium magnet is used.

The geometry of the single magnet and the modelling result is shown in Figure 6-8. The direction of the magnetic field is on the horizontal plane. The magnetic field strength at the centre line from the magnet surface is measured. The magnetic field at the surface is 0.229T but it decays to 0.093T at 5mm away from the surface. The magnetic flux density on the centre line is shown in Figure 6-9.

The magnetic field is simulated and obtained on the vertical line from the electrode to the bottom layer, and is shown in Figure 6-10. On the chart, the x-axis shows the displacement from the bottom layer to the electrode on the top layer. Near the top layer, the magnetic flux density is 0.102 T but near the bottom layer this is reduced to 0.058T as low as 45% of the magnetic flux density at the top layer. The magnetic field drops to 10% within a 16mm range from the top layer which means the flow signal contribution from the magnetic field distribution is weighted to the upper section of the fluidic oscillator.

6.4.2 Virtual current

For the virtual current modelling, Conductive Media DC in the AC/DC module of COMSOL Multiphysics is used for 3D. The 2D fluidic oscillator geometry is extruded as high as its height of 19mm. The electrodes are represented by points at the top layer at 25mm from the exit boundary and ± 5mm from the centre line of the fluidic oscillator. All the boundaries are set as electrical insulation. The electrode points are set to have a 1A and -1A point current source each. The streamline of virtual current of the fluidic oscillator is shown in Figure 6-11. The streamlines are coming from one electrode and travelling to the other electrode through the channel.

The virtual current density on the middle plane is shown in Figure 6-12.

Figure 6-13 shows the virtual current density on the vertical line from the electrode to the bottom line. The virtual current density is very high at the electrode surface at 7.24 x 10^4 A/m2 and drops significantly to 40% of its initial value within 2.3mm which means the flow signal contribution in terms of virtual current is concentrated near the electrodes.

6.4.3 Flows signal calculation

The flow signal is calculated from a simulated magnetic field, virtual current and velocity field using the same method described in the conventional electromagnetic flowmeter chapter except that in this case the result is computed at every time-step for the velocity distribution. The weight function is calculated from the magnetic field and the virtual current modelling results. The weight function can be written as a vector product of the magnetic field and virtual current as:

$$\mathbf{W} = \mathbf{B} \times \mathbf{j} = \begin{bmatrix} \mathbf{i} & \mathbf{j} & \mathbf{k} \\ B_x & B_y & B_z \\ j_x & j_y & j_z \end{bmatrix} = (B_y j_z - B_z j_y)\mathbf{i} + (B_x j_z - B_z j_x)\mathbf{j} + (B_x j_y - B_y j_x)\mathbf{k}$$

In this modelling, the z component of weight function is neglected because CFD modelling just has x- and y-components of velocity so the z-component of weight function can be eliminated. The y-component of velocity is also able to be neglected because the x-component of flow velocity dominates the flow element and the y-component of flow velocity is negligible so the weight function is

$$\mathbf{W} = \mathbf{B} \times \mathbf{j} = \begin{bmatrix} \mathbf{i} & 0 & 0 \\ B_x & B_y & B_z \\ j_x & j_y & j_z \end{bmatrix} = (B_y j_z - B_z j_y)\mathbf{i} \qquad (6\text{-}3)$$

The calculated weight function on the middle plane of the fluidic oscillator is shown in Figure 6-14. Most of the flow contributions are concentrated near the side walls of the splitter, where the centre of the single magnet is located.

The x- and y-components of flow velocity are taken by exporting the modelling result to MatLAB. The flow velocity components are then multiplied to weight function values.

The flow signal wave forms are shown in Figure 6-15 to Figure 6-18 at 40L/hr, 100L/hr, 200L/hr and 1000L/hr and each waveform is from simulation results. The oscillation frequency and peak to peak voltage are listed in Table 6-2. Meter factors are calculated from the results. The oscillation frequency is determined by taking an average from three different points on these waveforms. Until the flowrate reaches 100 l/hr, the waveforms are stable but between 100l/hr and 200l/hr which is the transit region between the laminar and turbulent flow profiles, the baseline of the waveform moves up and down. This baseline instability is shown clearly when the waveform is FFT converted and the spectral content of the waveform shown.

Table 6-2 Oscillation frequency, f_{osc} and flow signal from simulation

	40 l/hr	100 l/hr	200 l/hr	1000 /hr
f_{osc} (Hz)	1.02	2.70	4.65	25.0
$V_{p\text{-}p}$ (μV)	76.2	203.1	445.0	2177.2
Meter factor	10.8932	10.2881	11.9474	11.1111

The flow signal is also obtained by experiments for comparison. The flow signal is taken through a differential amplifier to the spectrum analyser. The spectrum analyser converts the input signal to a frequency domain by FFT function. The oscillation frequency and the amplitude of flow signal are taken from the FFT spectrum. The flow signal from the FFT is converted to peak to peak voltage by multiplying by √2.

The data from modelling results show that the flow signal increases linearly except at the lowest flowrate, 20L/hr. This signal loss can be observed in the experimental data at the same flow range which is from 15L/hr to 38L/hr. But the actual flow signal drops 80% between 38 L/hr to 100 L/hr then the signal gains upwards. At a higher flowrate, the actual flow signal shows some losses because of the gain characteristics of the differential amplifier.

The flow signal, dropping from experimental results of between 40 l/hr to 200 l/hr, shown in figure 6-19, is likely to be a consequence of the flowmeter operating at these flows in the transition region in which the jet Reynolds number changes from 584 to 2920. In this transition region, the signal quality became poor, as shown in Figure 6-17. Figure 6-17 shows clearly the poorer flow signal at 200L/hr compared to Figure 6-15 at 40L/hr. The peak to peak value at each wave is not changed too much at 40 l/hr, but it changes more than 25% compared with the next two peaks at 200L/hr. This disappeared at flowrates greater than 200L/hr.

The other concern is the loss of signal strength at the lower flowrate, i.e. under 40 L/hr. To boost the flow signal, the configuration of the permanent magnet and electrodes are changed as shown in Figure 6-20. The locations are listed in Table 6-3.

The locations E3, E3a and E4 are designed not to use the y-component of the magnetic field by placing them on the top layer of the fluidic oscillator. But the simulated flow signals with these configurations do not boost the signal because the magnetic field off the centre is significantly smaller when compared to the value at the centre. The magnet is moved towards the jet to place the electrode where the flow velocity may be higher. Locations E1a and E2a place the electrodes nearer to the magnet, as seen in Figure 6-20.

Figure 6-21 to Figure 6-23 show the flow signal spectrum at the different locations, E1, E1a, E2 and E2a. The modelling is undertaken at 20L/hr, 40L/hr and 60L/hr which are the

flowrates at which the signals are of poor quality. The spectrum is obtained by FFT conversion to the flow signal waveform. The biggest peak in the figure is the dominant oscillation frequency at the flowrate. A smaller peak appears at double the frequency of the oscillation frequency which is the second harmonic of the oscillation frequency.

The flow signal amplitudes from the different configurations are listed in Table 6-4. In Figure 6-23, the flow signal amplitude at 60L/hr is not increased because the low frequency noise reduces the flow signal amplitude in FFT analysis. The low frequency noise is also shown in Figure 6-23.

By moving the electrode closer to the splitter wall by 1mm increases the flow signal up to 23.6% which means that moving the electrodes closer to the permanent magnet effects more than by placing the electrodes on the jet stream.

Table 6-3 Locations of magnet and electrodes

Magnet		Electrodes	
Index	Magnet location (mm)	Index	Location (mm)
M1	28.0 ~ 38.0	E1	(23.0, 5.0)
M2	29.0 ~ 39.0	E1a	(23.0, 4.0)
		E2	(24.0, 5.0)
		E2a	(24.0, 4.0)
		E3	(27.0, 5,6)
		E3a	(27.0, 5.5)
		E4a	(29.0, 5.0)

Table 6-4 Flow signal amplitude at different configuration

Flowrate	Freq	E1M1	E1aM1	E2M2	E2aM2
20L/hr	0.5490	8.6 uV	9.3	9.8	11.4
			(8.1%)		(16.3%)
40L/hr	1.0980	26.8	31.1	29.4	35.9
			(16.0%)		(22.1%)
60L/hr	1.6471	32.6	40.3	34.7	42.2
			(23.6%)		(21.6%)

Figure 6-1 Fluidic oscillator

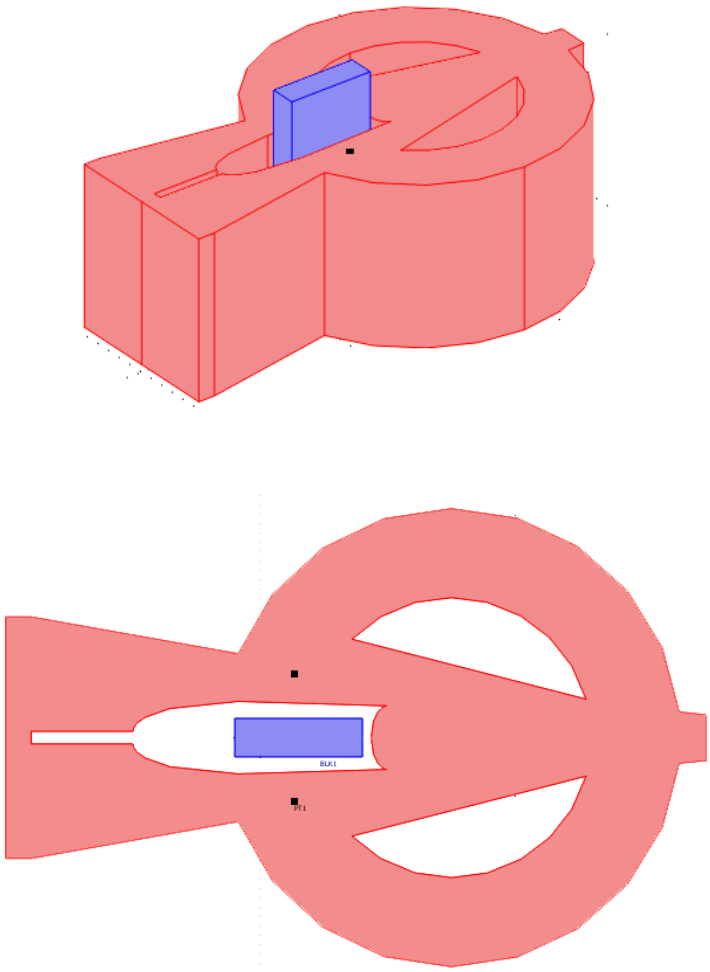

Figure 6-2 Modelling geometry and configuration of fluidic oscillator

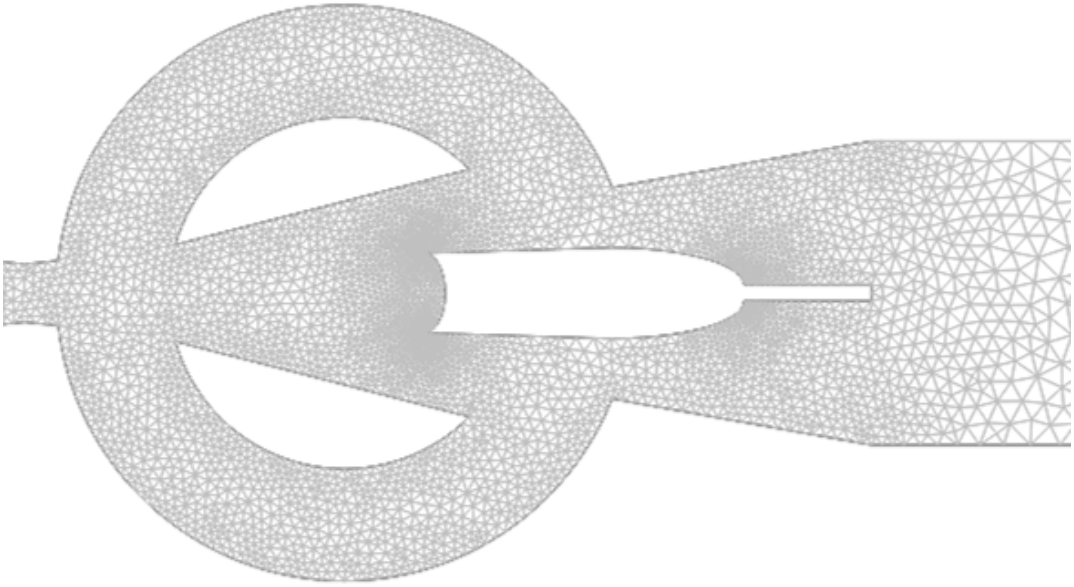

Figure 6-3 Geometry and mesh structure for 2D modelling

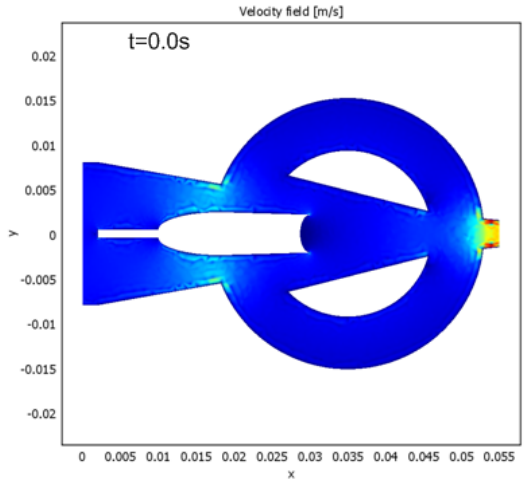
Velocity field [m/s]
t=0.0s
0.02
0.015
0.01
0.005
0
-0.005
-0.01
-0.015
-0.02
y
0 0.005 0.01 0.015 0.02 0.025 0.03 0.035 0.04 0.045 0.05 0.055
x

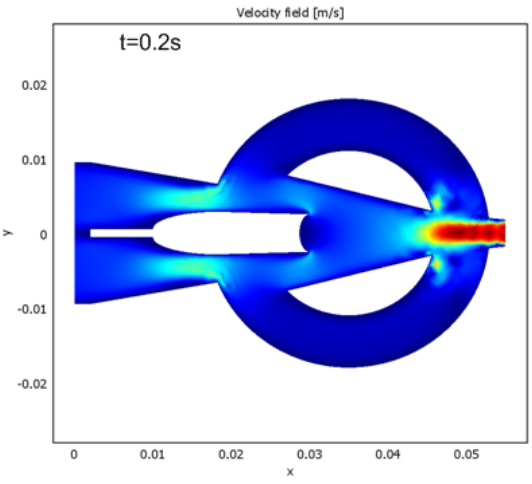
Velocity field [m/s]
t=0.2s
0.02
0.01
0
-0.01
-0.02
y
0 0.01 0.02 0.03 0.04 0.05
x

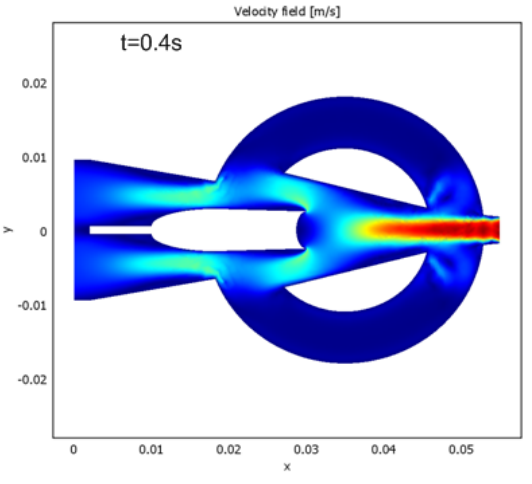
Velocity field [m/s]
t=0.4s
0.02
0.01
0
-0.01
-0.02
y
0 0.01 0.02 0.03 0.04 0.05
x

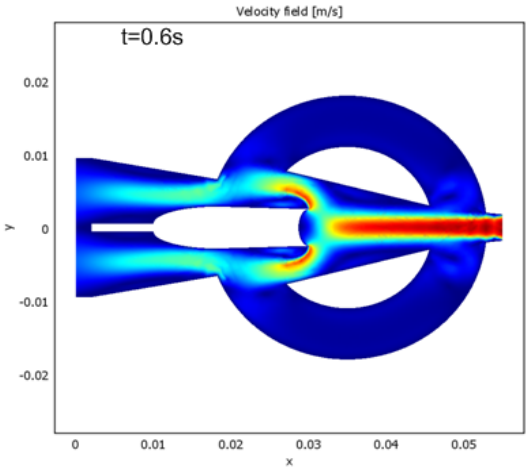
Velocity field [m/s]
t=0.6s
0.02
0.01
0
-0.01
-0.02
y
0
0.01
0.02
0.03
0.04
0.05
x

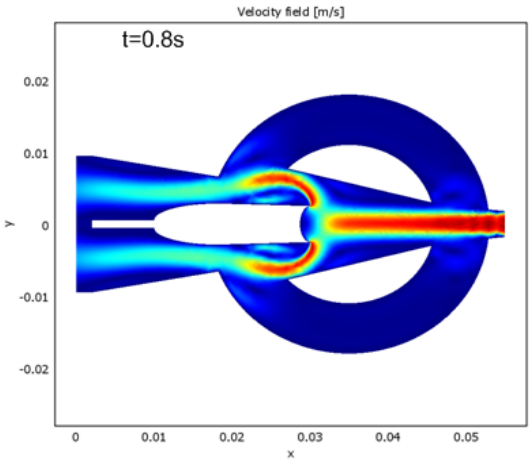
Velocity field [m/s]
t=0.8s
0.02
0.01
0
-0.01
-0.02
y
0
0.01
0.02
0.03
0.04
0.05
x

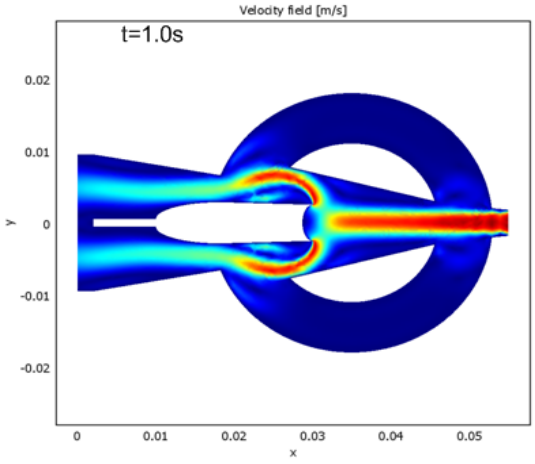
Velocity field [m/s]
t=1.0s
0.02
0.01
0
-0.01
-0.02
y
0
0.01
0.02
0.03
0.04
0.05
x

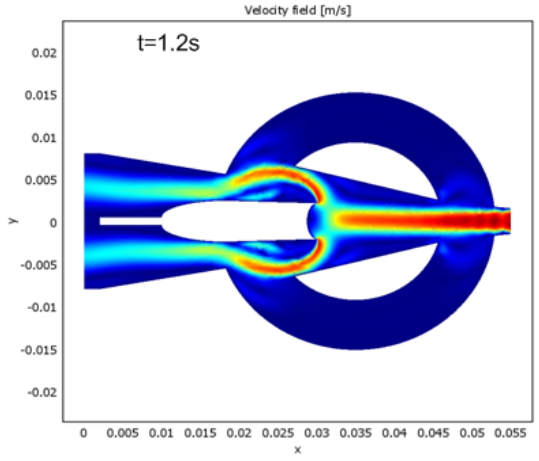
Velocity field [m/s]
t=1.2s
0.02
0.015
0.01
0.005
0
-0.005
-0.01
-0.015
-0.02
y
0 0.005 0.01 0.015 0.02 0.025 0.03 0.035 0.04 0.045 0.05 0.055
x

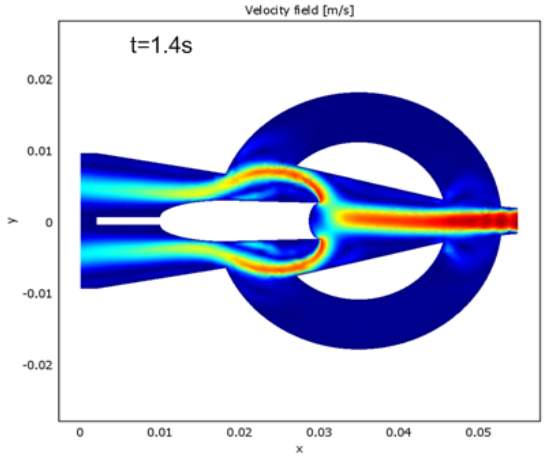
Velocity field [m/s]
t=1.4s
0.02
0.01
0
-0.01
-0.02
y
0 0.01 0.02 0.03 0.04 0.05
x

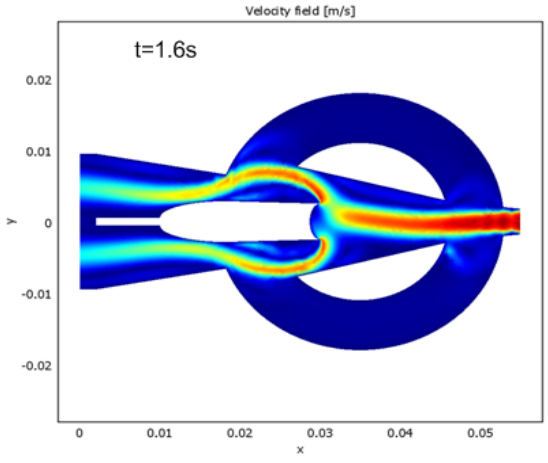
Velocity field [m/s]
t=1.6s
0.02
0.01
0
-0.01
-0.02
y
0 0.01 0.02 0.03 0.04 0.05
x

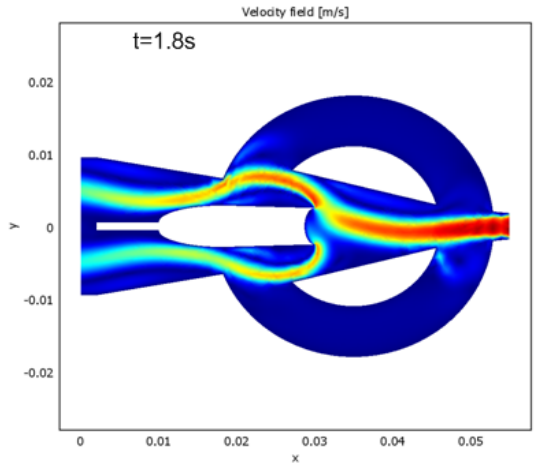
Velocity field [m/s]
t=1.8s
0.02
0.01
0
-0.01
-0.02
y
0
0.01
0.02
0.03
0.04
0.05
x

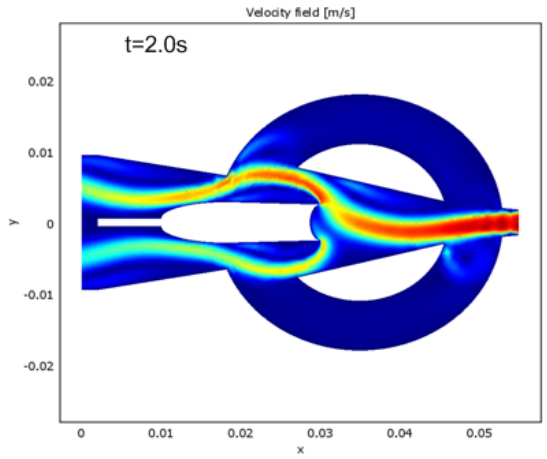
Velocity field [m/s]
t=2.0s
0.02
0.01
0
-0.01
-0.02
y
0
0.01
0.02
0.03
0.04
0.05
x

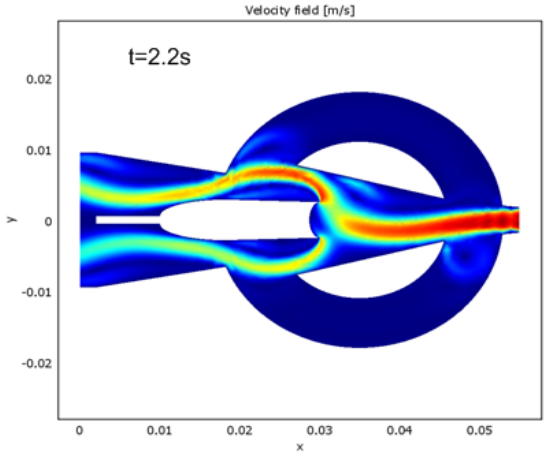
Velocity field [m/s]
t=2.2s
0.02
0.01
0
-0.01
-0.02
y
0
0.01
0.02
0.03
0.04
0.05
x

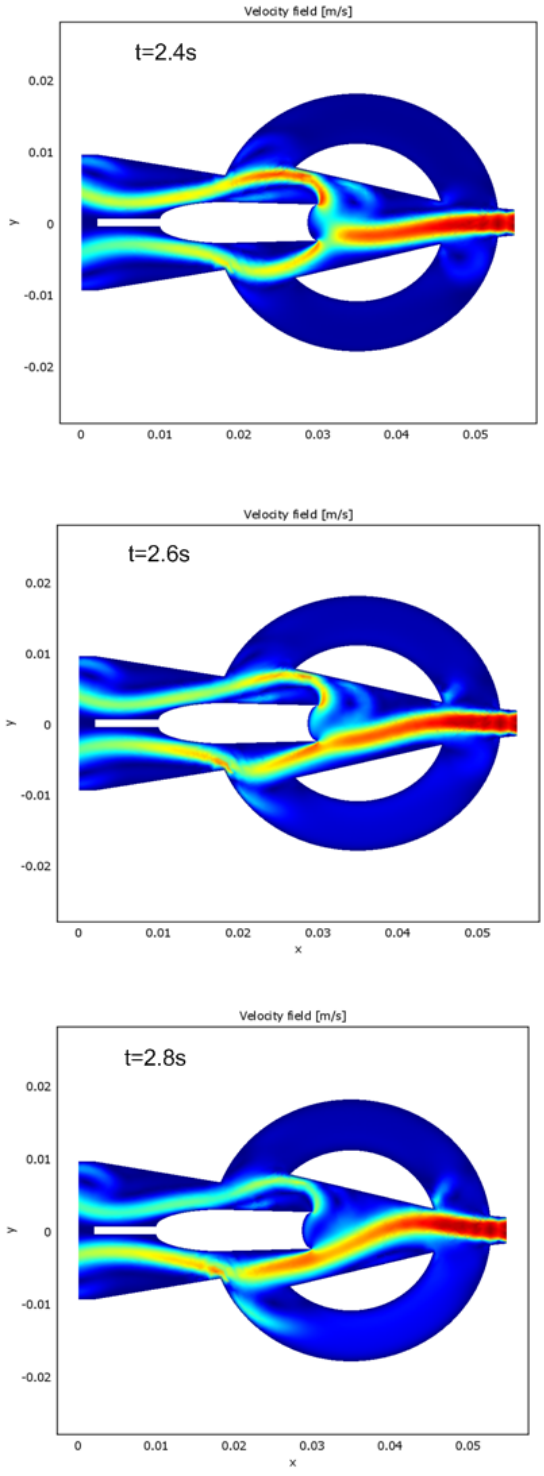

Figure 6-4 CFD modelling at 20L/hr

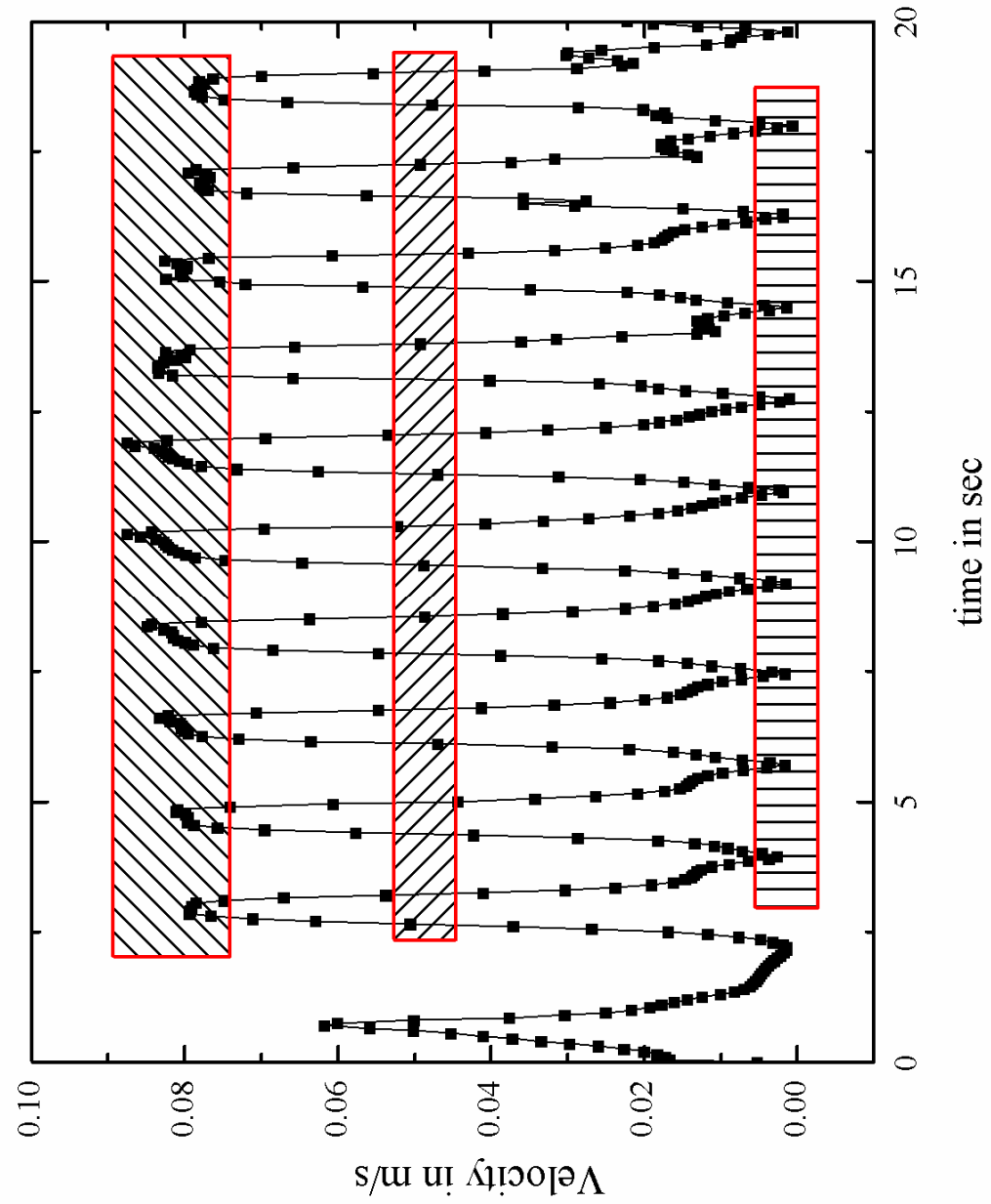

Figure 6-5 Flow velocity at one electrode with windows to pick up oscillation frequency at 20L/hr

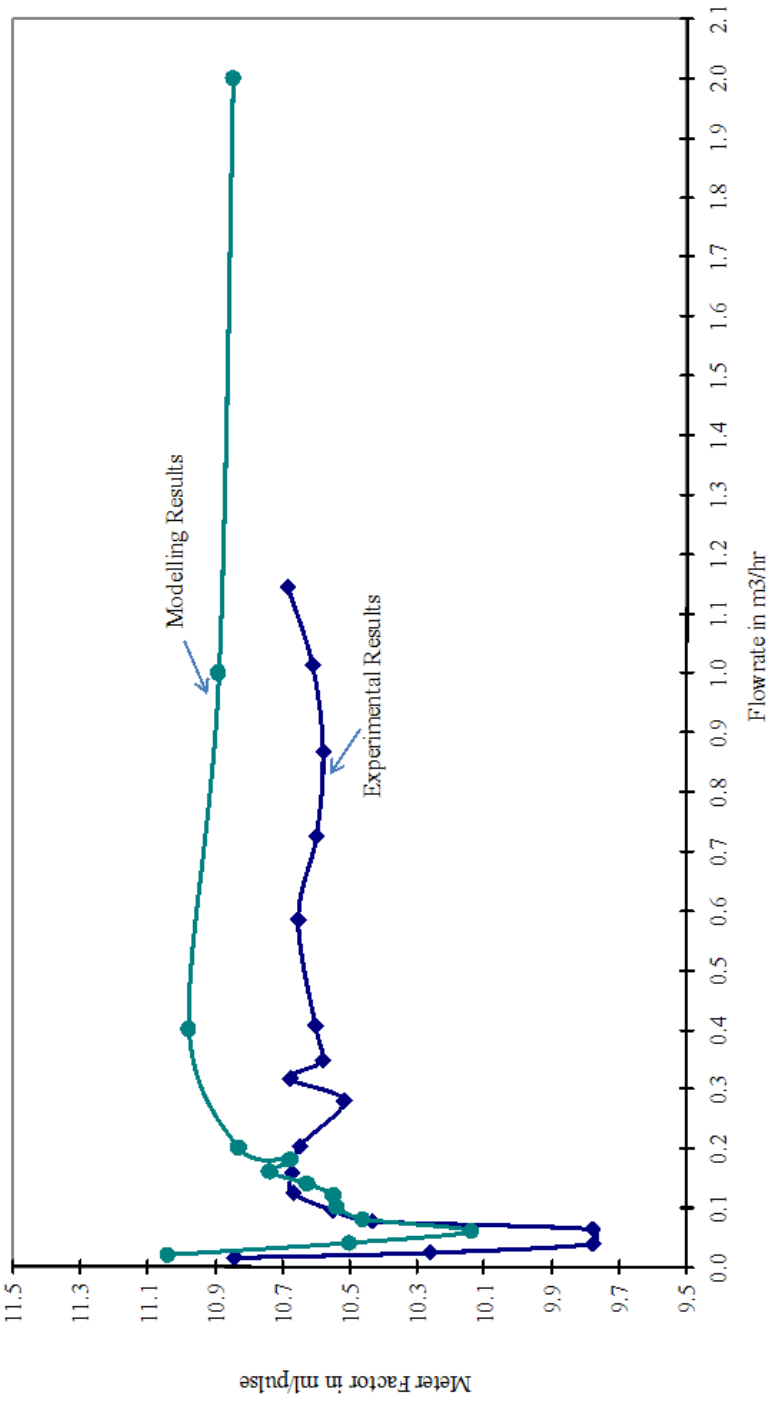

Figure 6-6 Meter factor comparison of fluidic oscillation

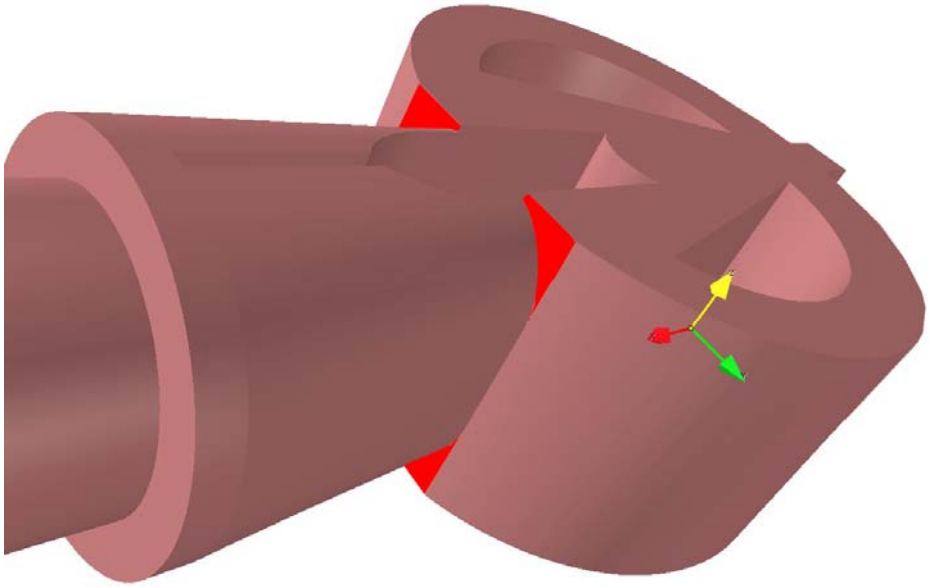

Figure 6-7 The actual geometry of the fluidic oscillator and structure at the exit channel and side walls

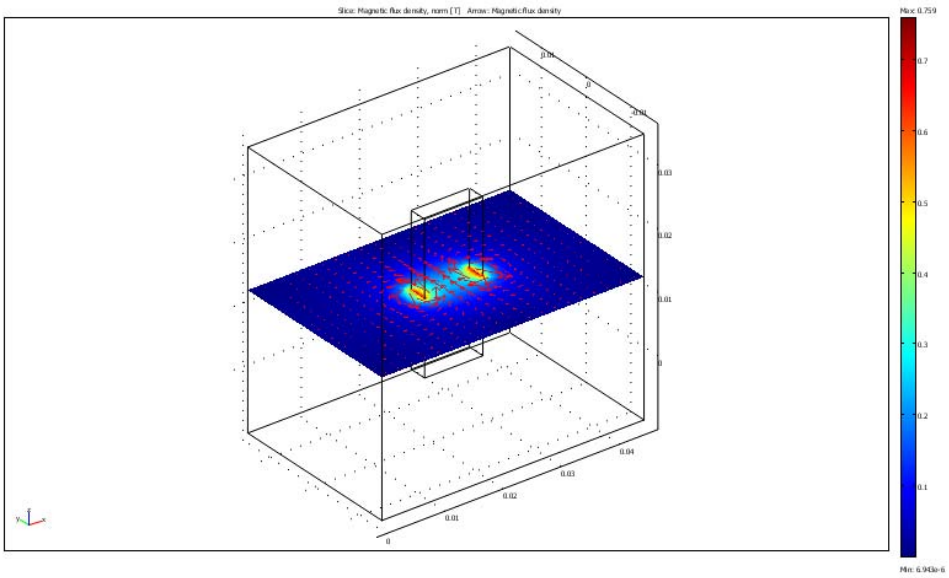

Figure 6-8 Modelling of single magnet

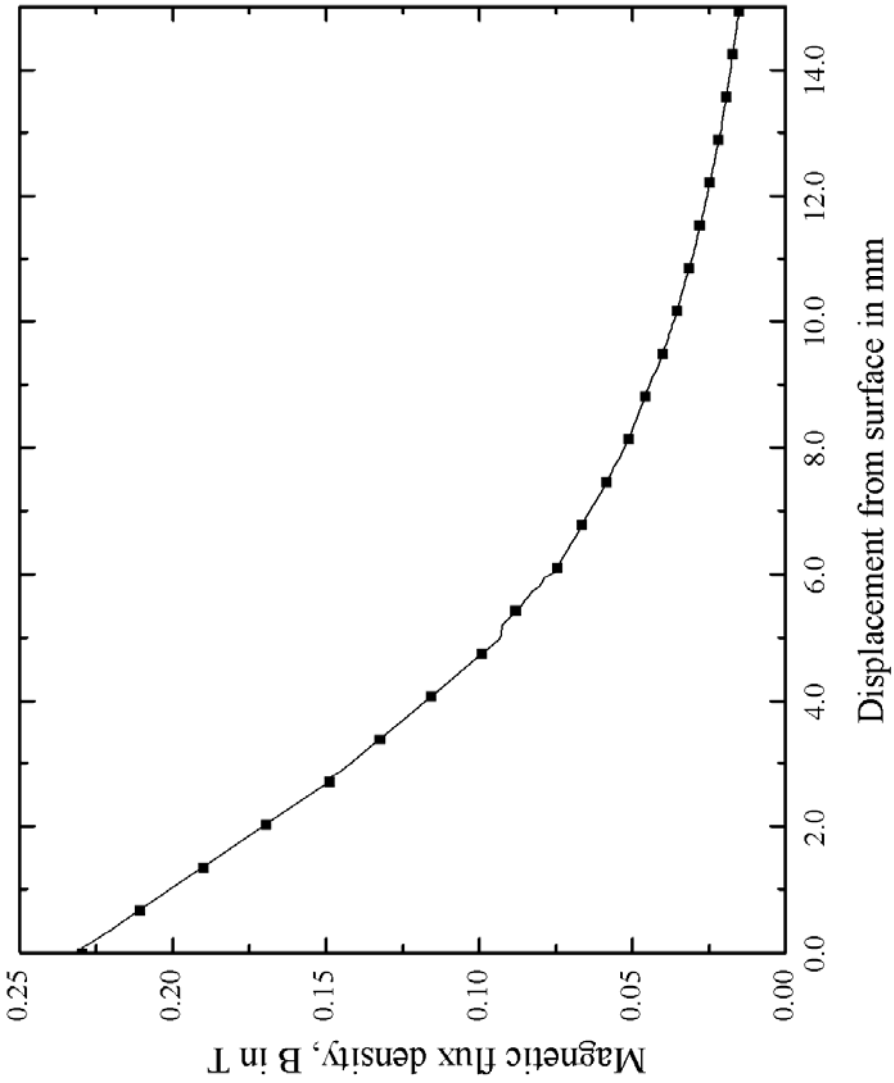

Figure 6-9 Magnetic flux density on the centre line of single magnet

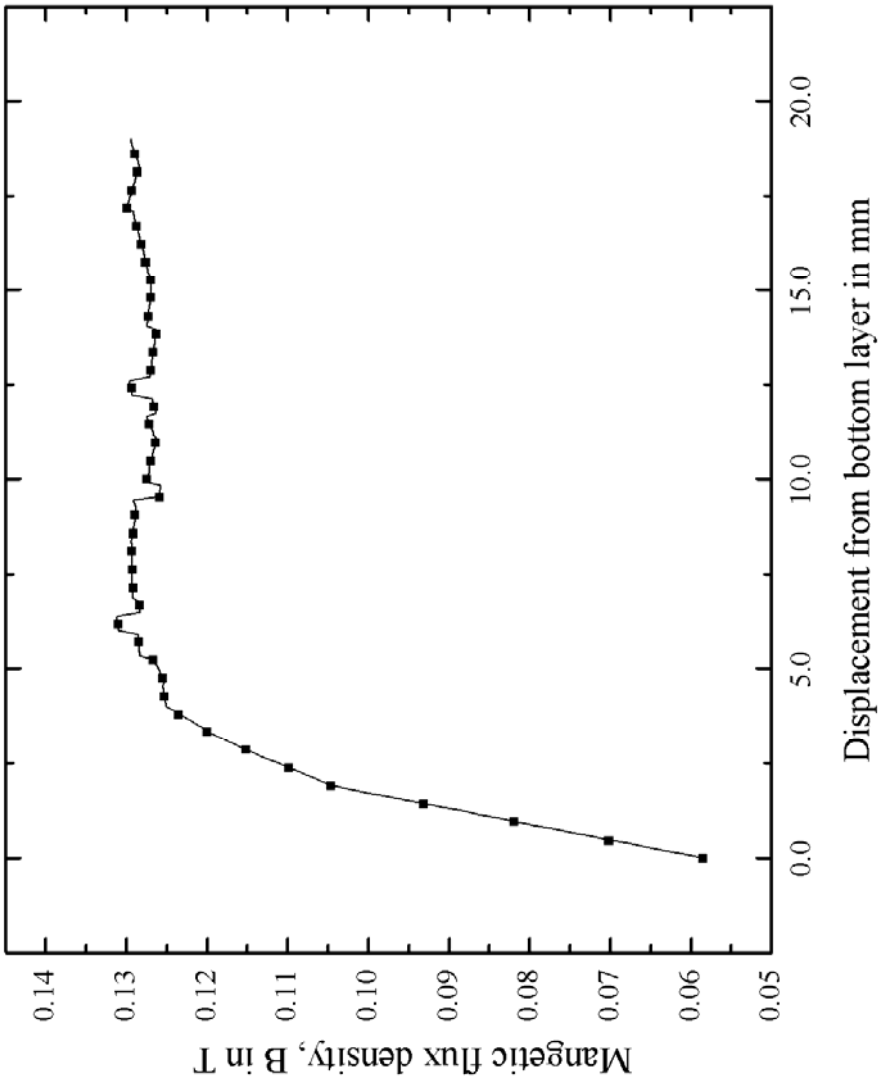

Figure 6-10 Magnetic flux density on the vertical line from electrode to bottom layer

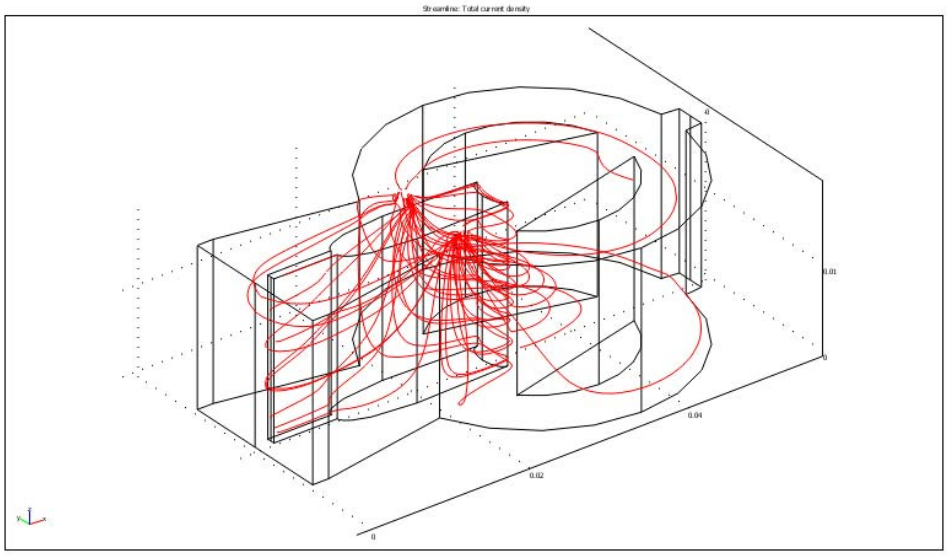

Figure 6-11 Modelling of virtual current of two electrodes on the top layer

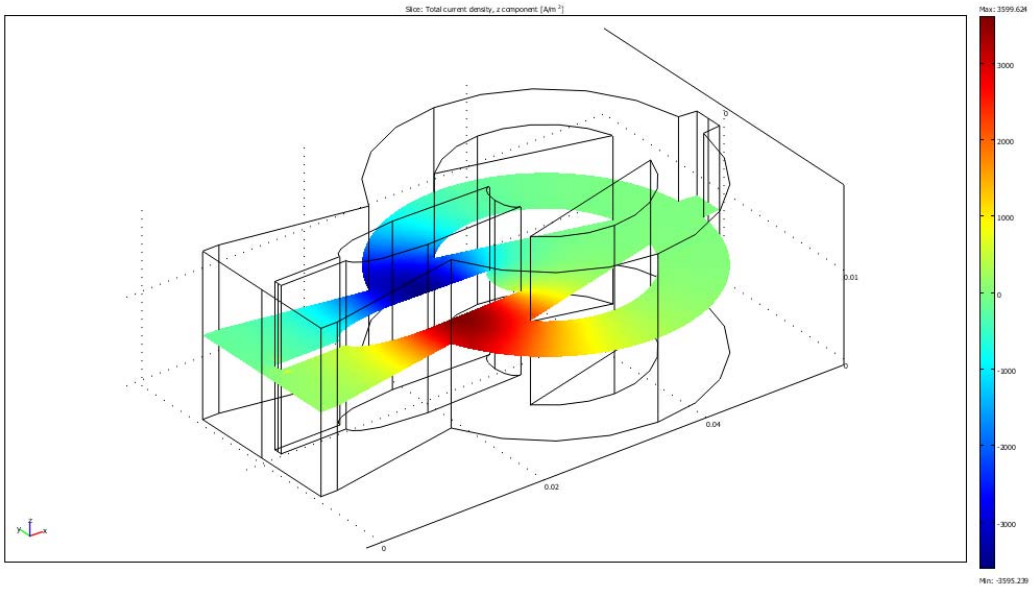

Figure 6-12 Virtual current distribution on the middle plane of fluidic oscillator

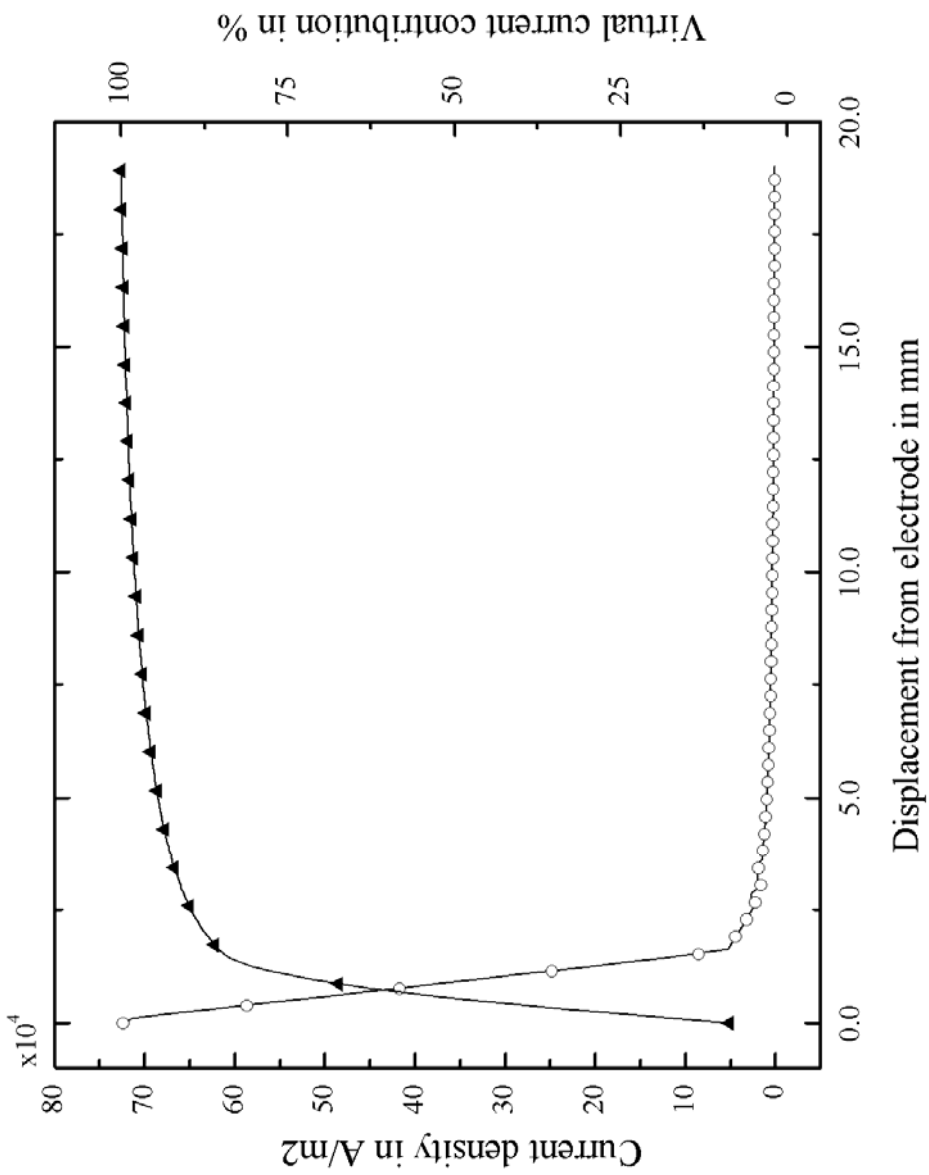

Figure 6-13 Virtual current and its contribution on vertical line from electrode

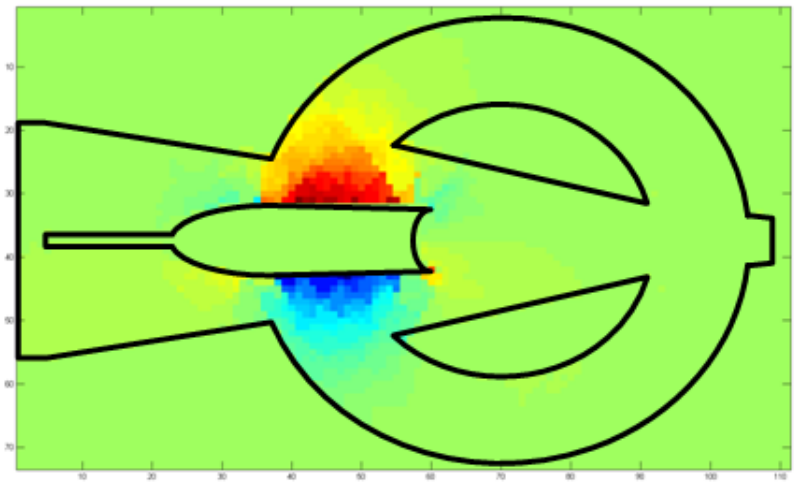

Figure 6-14 Weight function of fluidic oscillator on the middle plane

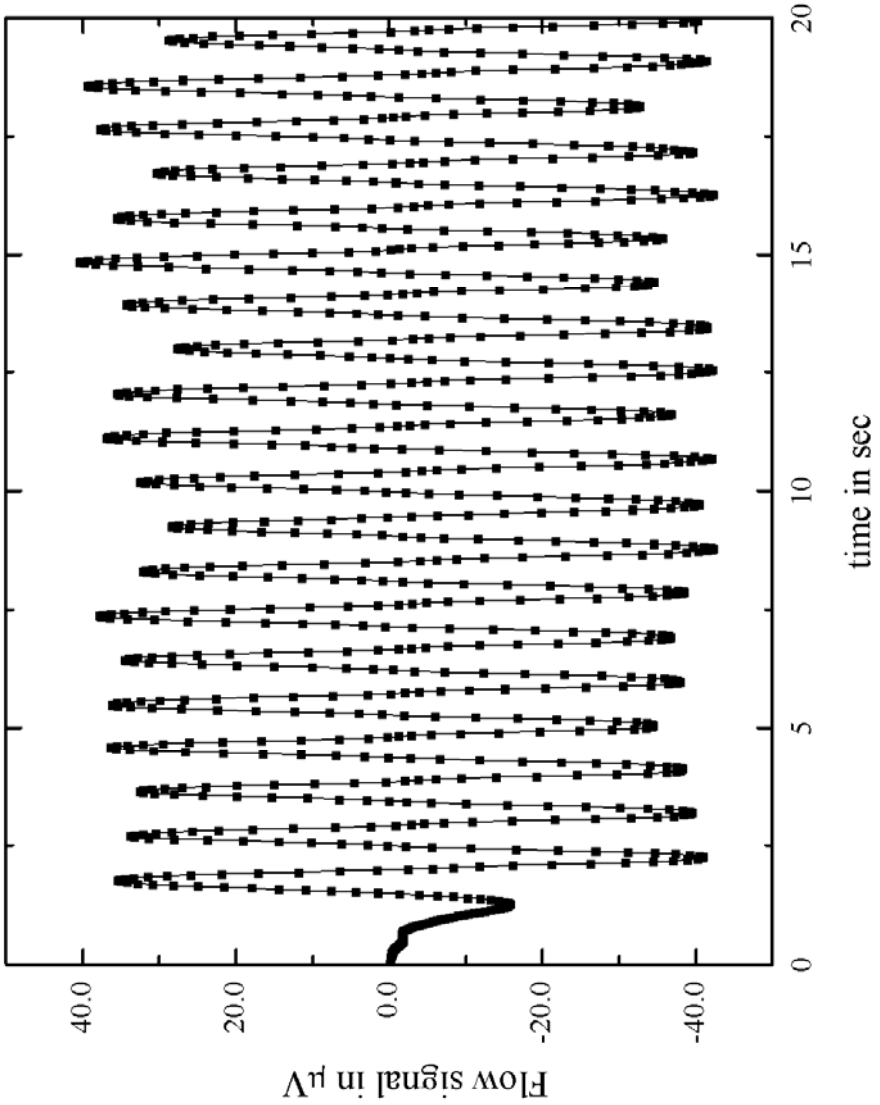

Figure 6-15 Flow signal at 40L/hr

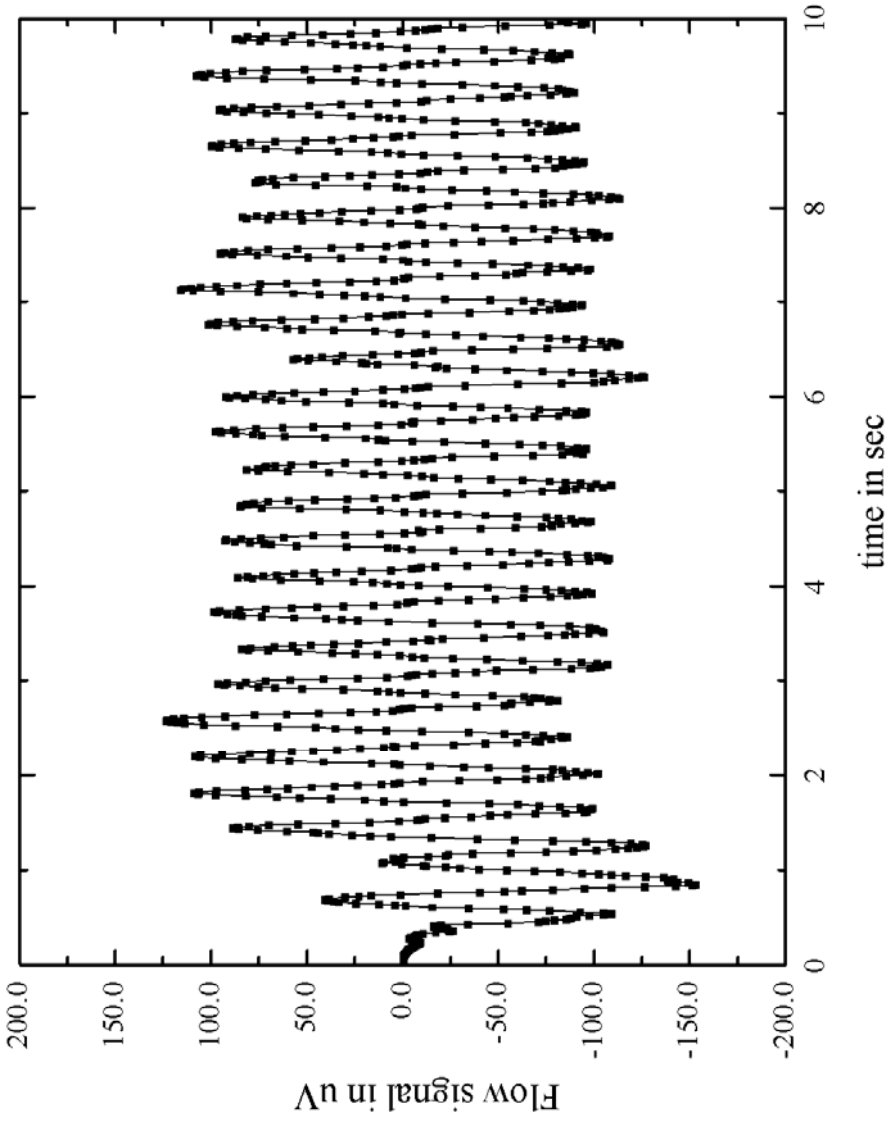

Figure 6-16 Flow signal at 100L/hr

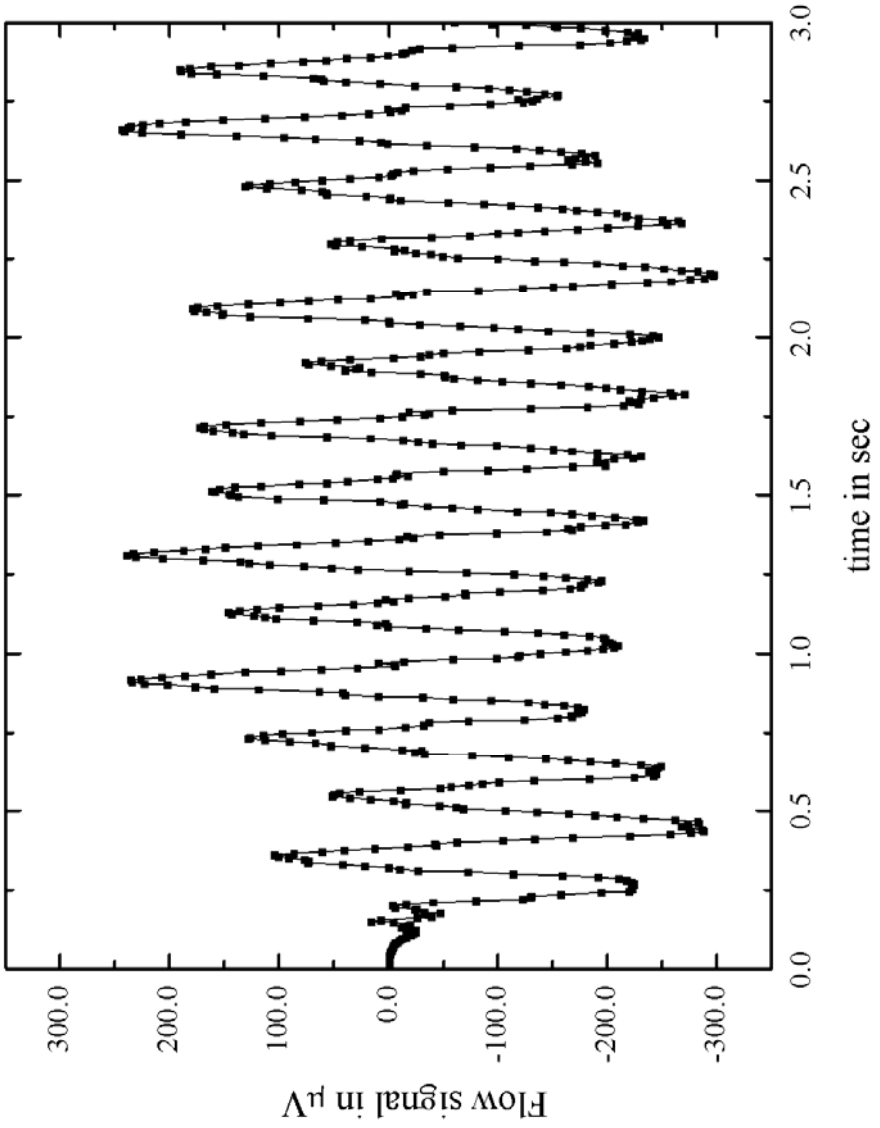

Figure 6-17 Flow signal at 200L/hr

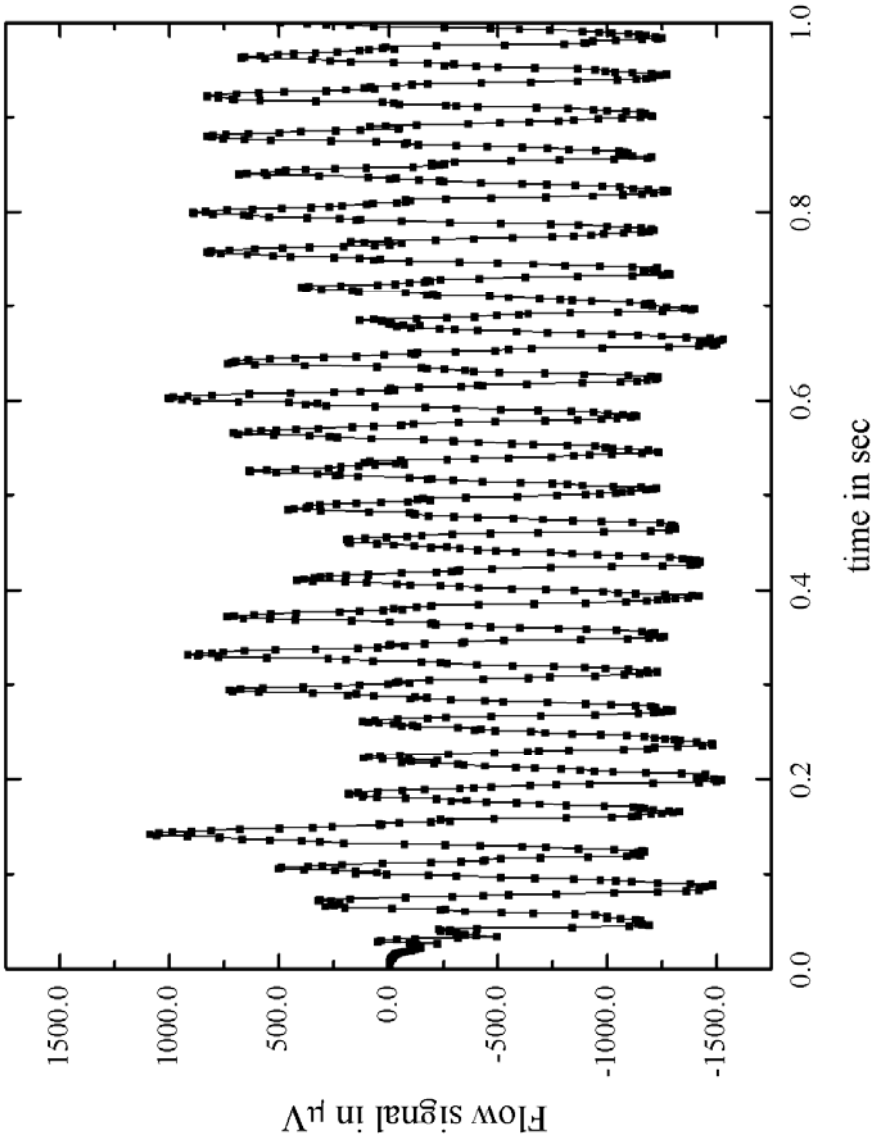

Figure 6-18 Flow signal at 1000L/hr

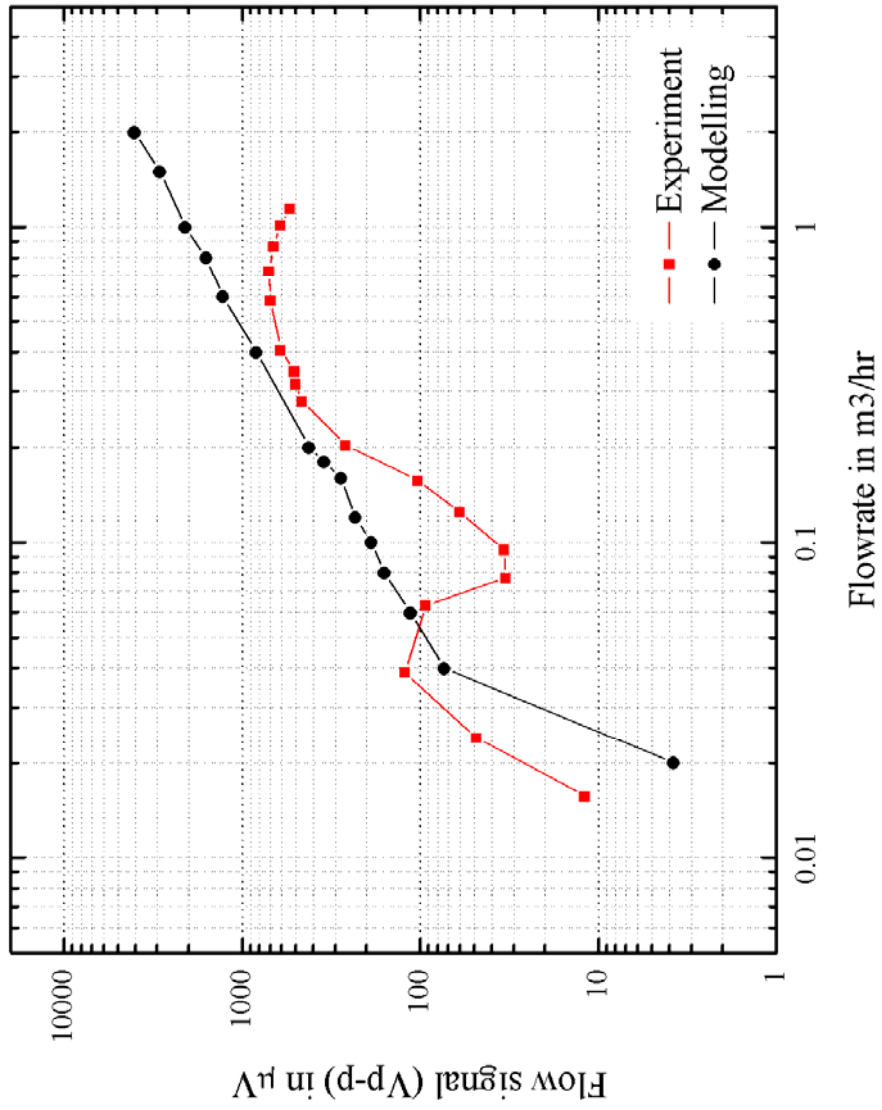

Figure 6-19 Comparison of flow signal from experiments and modelling

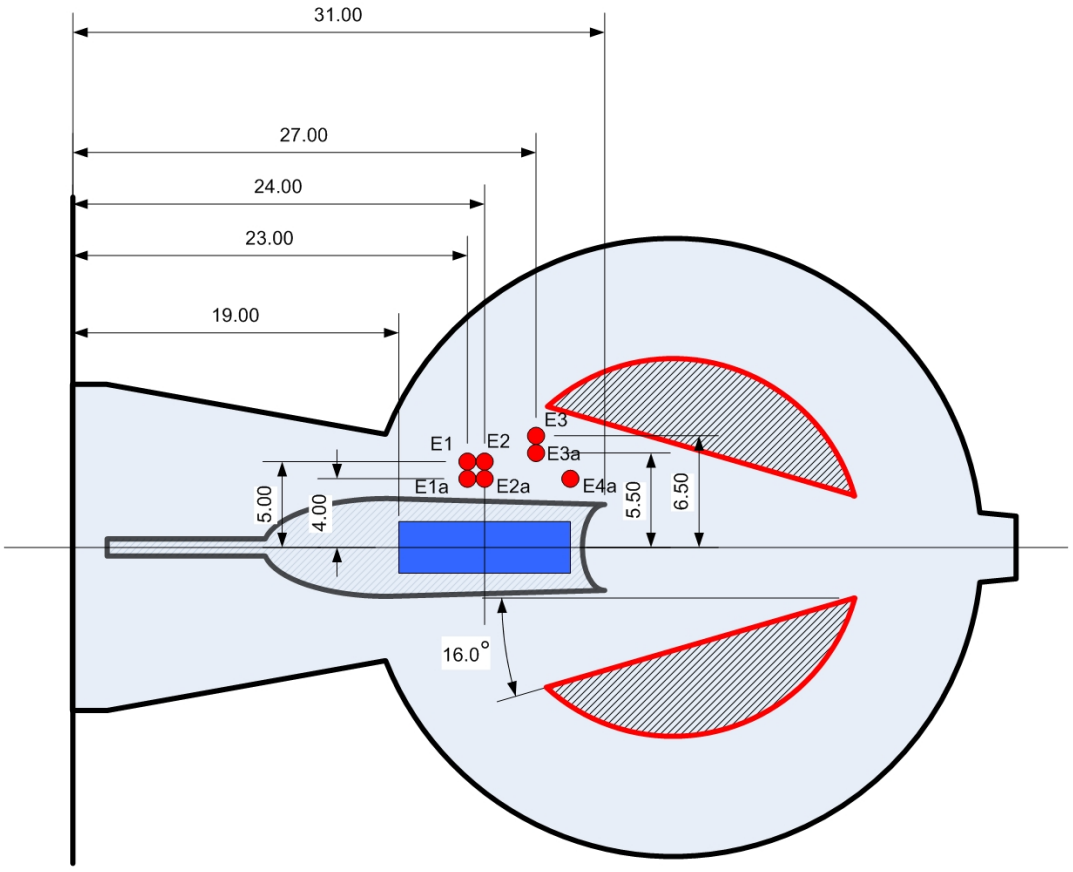

Figure 6-20 Electrodes locations

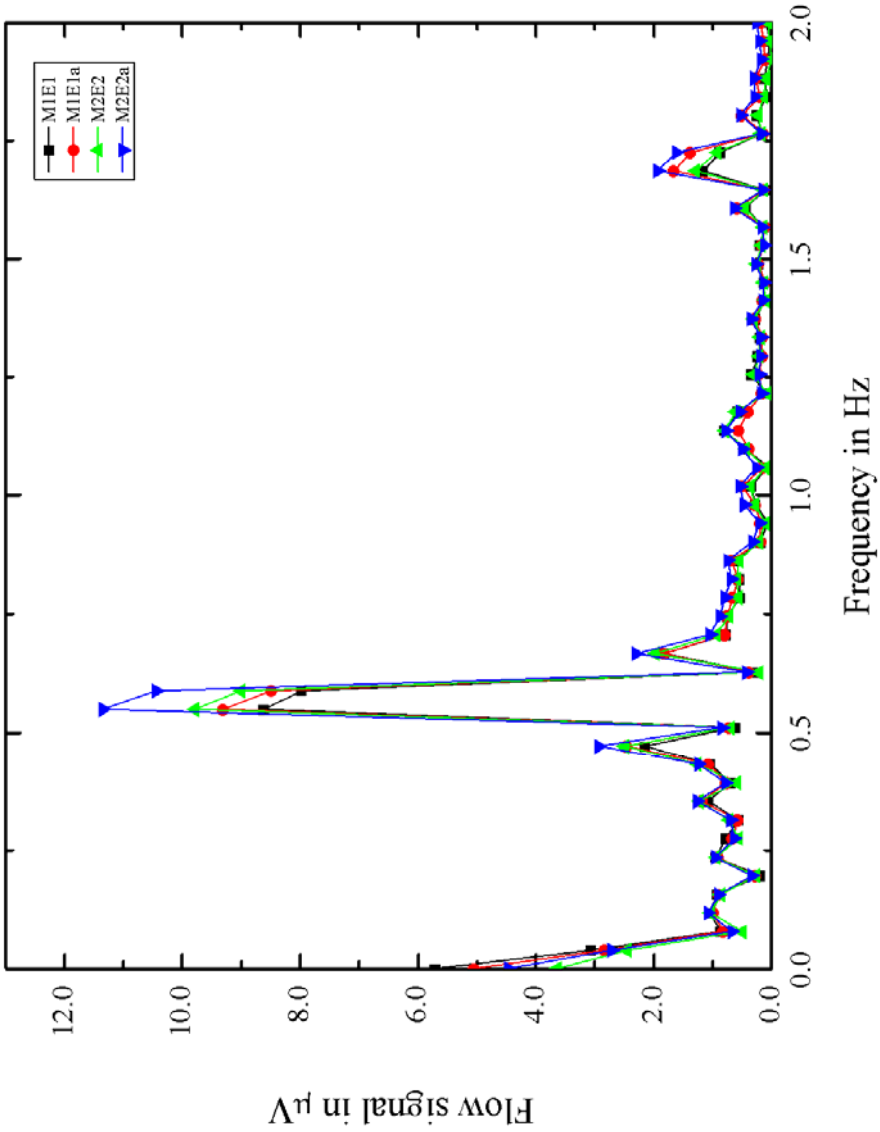

Figure 6-21 FFT spectrum at 20 L/hr

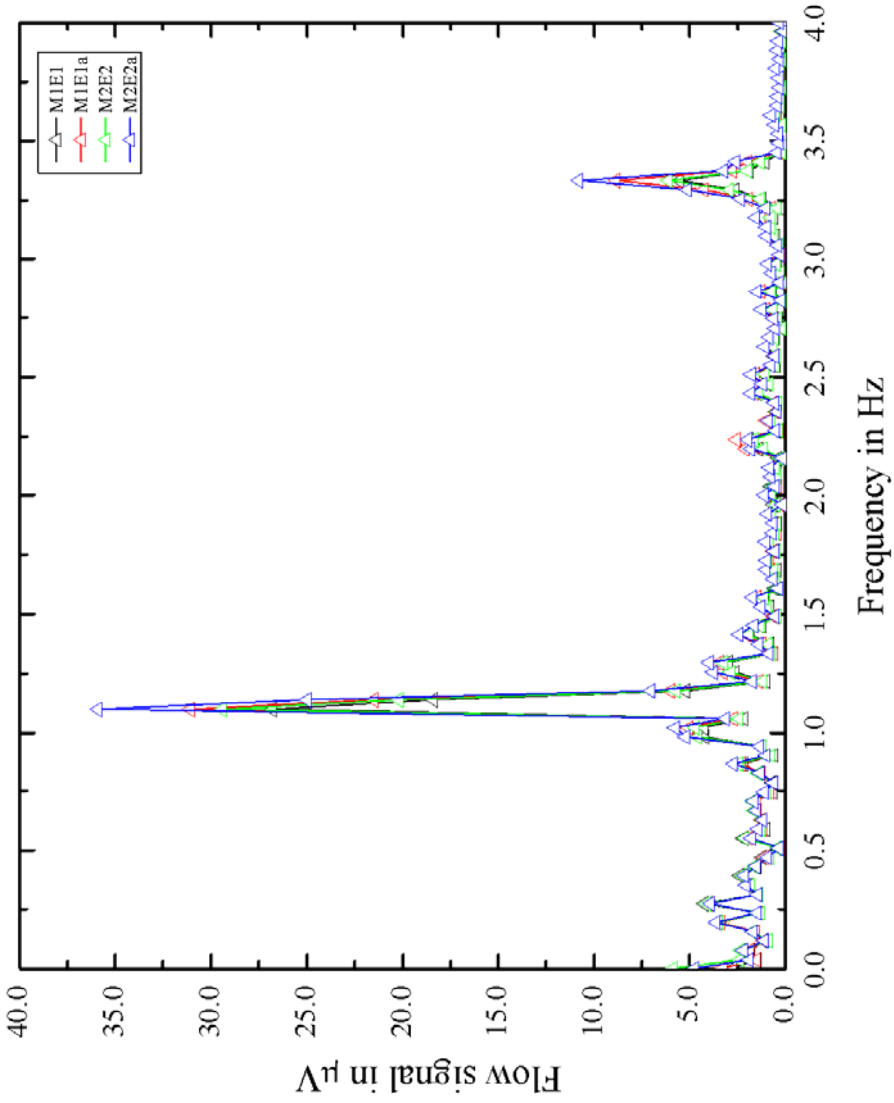

Figure 6-22 FFT spectrum at 40L/hr

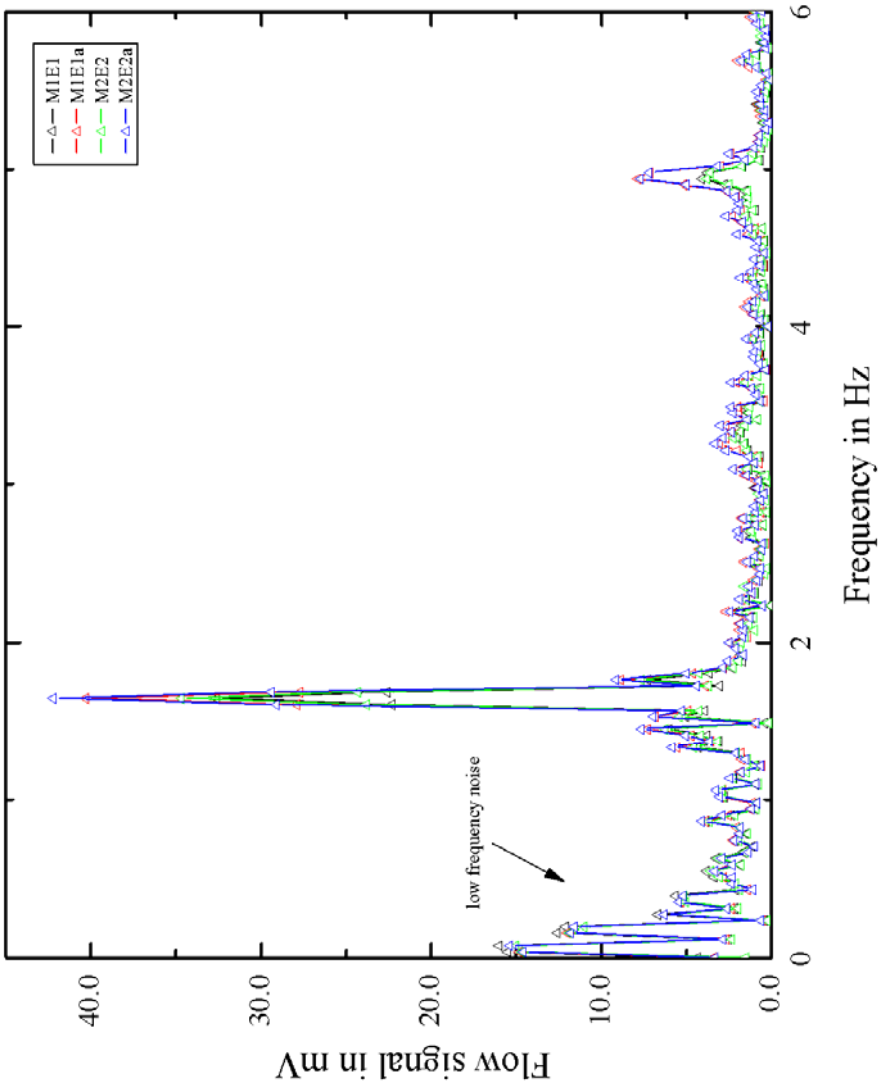

Figure 6-23 FFT spectrum at 60L/hr with low frequency noise

Chapter 7. Conclusions and Further Work

In this work, the electromagnetic sensing technique can be simulated to calculate the flow signal of the conventional flowmeter, the alternative electromagnetic flowmeter and the fluidic oscillator, which is calculated by taking a model of the magnetic field, the virtual current and the flow velocity. All these approaches demonstrate that it is possible to achieve good agreement between modelling and experimental data.

7.1 Conventional electromagnetic flowmeter

The flow signal of the conventional electromagnetic flowmeter is simulated to optimise the geometry of both the flow tube and the magnetic field. This has been undertaken to demonstrate that it possible to improve the sensitivity, velocity dependence and power requirements of such a flowmeter. By undertaking such modelling it is possible to optimise the geometry of the flow tube to increase both the magnetic field and the flow signal strength. A conventional 10mm by 4.5mm rectangular flow channel is modified to have a 10mm by 3mm cross-sectional dimension and with mild steel plates placed on the top and bottom layers to cover the flow channel. These modifications bring a much stronger magnetic field, then the flow signal is increased from 15.66 to 30.0~33.9 μV at a velocity of 1m/s depending upon the length of the mild steel plates. This optimisation implies that such a meter can be operated with an improved signal to noise ratio; having a flow signal of 1.485μV at the lowest flowrate for a Q3 is a 2 m3/hr meter against 0.758μV in the conventional design. This flow signal increase is also able to be used to reduce the power consumption and hence reduce the capacity of the battery by a factor of 1.96.

7.2 The alternative coil-less design

Results from the modelling of the alternative magnetic field control system show that if the piezoelectric actuator or Terfenol magnetostrictive material were to be used, the electromagnetic flowmeter will measure the flow without using coils. At this stage, the flow signal from the meter using the Terfenol-D/PZT device provides just a quarter of the flow signal of the conventional electromagnetic using coil. However, the power consumption is reduced by 54.7% from 74.7μJ to 33.85μJ.

The reason for the lower signal level is the total strain of Terfenol-D, i.e. when the external stress is applied it is still not large enough. To solve this problem, the design of the Terfenol-D device has to be revised when considering the thickness of the piezoelectric layers. This optimisation may replace Terfenol-D by the recently composited gigantic magnetostrictive material called Galfenol which is a much more robust material invented in 1998 (adapted from ETREMA products, INC homepage)

As the material cost of Terfenol-D is very high – about £400 per single block at the present time – so the experiments have necessarily been very limited. However, the possibility of using a coil-less electromagnetic flowmeter is revealed by this work providing more experiments with the material can be made.

7.3 The Fluidic Oscillator

The modelling results for the fluidic oscillator, which uses the electromagnetic sensing technique, are also studied to simulated the flow signal at the given geometry and

configuration of the electrodes and magnets. The modelling can now predict the flow signal level and its quality.

The flow signal of the fluidic oscillator has been improved by 23.6% by putting the electrodes closer to the magnet and locating them in the centre line of the magnet. This result shows the modelling can be used to optimise both the electrodes and magnets, and the geometry of the fluidic oscillator.

The modelling of the flow signal of the fluidic oscillator can also be used for other sensing technologies as the piezoelectric sensing technology combines piezoelectric modules with these results.

The modelling has been undertaken in 2D especially for the CFD model. This simplification reduces the computing time and resources but geometrical disagreements are raised near the top and bottom area of the inlet and outlet of the fluidic oscillator. Further research of CFD in 3D, i.e. more like actual geometry is needs to be accomplished.

7.4 Simulation tool for electromagnetic sensing technique

The simulation tool used in this thesis shows that the tool will be used to develop the water meter using the electromagnetic sensing technique as the conventional flowmeter and the fluidic oscillator. Using this tool will have several advantages in developing the meter. These include:

- Simulating any geometry even for complex structures
- Understanding the effect of each section of the flowmeter
- Reducing development time
- Saving development costs

The tool will reduce the development lead time because using a simulation tool is faster than manufacturing a prototype in practice. Before finalising the design, the simulation tool allows as many alternative designs as possible to be tried before producing the optimal design for testing.

7.5 Further work

Theoretical studies and further experiments are needed for further study. The coil-less electromagnetic flowmeter using Terfenol-D magnetostrictive material needs further detailed theoretical analysis and experiments with different sizes of Terfenol-D and to be evaluated and compared with the modelling results.

The design of the Terfenol-D/PZT laminated device is to be optimised to obtain a larger magnetomechanical effect for increasing magnetic flux change at the air gap using the same power. In the optimisation, changing the thickness of Terfenol-D material or using piezoceramic material will be considered. The length of the material also needs to be optimised. Then additional experiments using different dimensions of Terfenol-D material will be undertaken to obtain more experimental data.

The geometry of the fluidic oscillator should be extended to 3D as the real geometry to obtain the effects of top and bottom layers on CFD modelling. The shape difference at the exit should also be investigated to predict meter performance based on actual geometry.

The multiphysics modelling software can be used by combining two or more different solvers so that the flow signal from the fluidic oscillator has alternative sensing techniques such as piezoelectric sensors.

The theoretical analysis of the effect of changing geometry and relationship to pressure drop is also an area for further study.

References

Ahn, Y.C., Oh, B.D. and Kim, M.H. (2003) A current-sensing electromagnetic flowmeter for two-phase flow and numerical simulation of the three-dimensional virtual potential distribution: I. Fundamentals and annular flow. Measurement Science and Technology, vol. 14, pp. 239-250.

Amare, T. (1995) Electromagnetic flowmeter for dielectric liquids, in Department of Fluid Engineering and Instrumentation, PhD Thesis, Cranfield Univeristy, pp. 166.

Amare, T. (1999) Design of an electromagnetic flowmeter for insulating liquids. Measurement Science and Technology, vol. 10, pp. 755-758.

Arregui, F., Cabrera Jr., E. and Cobacho, R. (2006) Integrated Water Meter Management, IWA Publishing, London.

Arregui, F., Cabrera Jr., E., Cobacho, R. and Garcia-Serra, J. (2005) Key Factors Affecting Water Meter Accuracy, in Proceedings of IWA Leakage 2005 conference, Halifax, Canada.

Arregui, F.J., Cabrera Jr., E., Cobacho, R. and Garcia-Serra, J. (2006) Reducing Apparent Losses Caused By Meters Inaccuracies. Water Practice & Technology, vol. 4, pp.

AWWA (1999) Water Meters - Selection, Installation, Testing and Maintenance, American Water Works Association

Baker, R.C. (1991) Turbine and related flowmeters: I. Industrial practice Flow Measurement and Instrumentation, vol. 2, pp. 149-161.

Baker, R.C. (1993) Turbine flowmeters: II. Theoretical and experimental published information. Flow Measurement and Instrumentation, vol. 4, pp. 123-144.

Baker, R.C. (1993) Turbine flowmeters: II. Theoretical and experimental published information Flow Measurement and Instrumentation, vol. 4, pp. 123-144.

Baker, R.C. (2002) Flow Measurement Handbook, Cambridge University Press.

Ballato, A. (1995) Piezoelectricity: Old Effect, New Thrusts IEEE Transactions on Ultrasonics, Ferroelectrics, and Frequency Control, vol. 42, pp. 916-926.

Barrow, M. and Rogers, I.T. (1993) Rotary Piston Water Meter, ABB Kent Plc., GB.

Beale, R.B. and Lawler, M.T. (1974) Development of a Wall Attachment Fluidic Oscillator Applied To Volume Flow Metering. Flow - Its Measurement and Control in Science and Industry, vol. 1, pp.

Benbouzid, M.E.H. (1995) Finite Element Modelling of Magnetostrictive Devices: Investigations for the Design of the Magnetic Circuit IEEE Transactions on Magnetics, vol. 31, pp. 1813-1816.

Bentley, J.P. (2005) Princples of Measurement Systems, Prentice Hall.

Bevir, M.K. (1970) The theory of induced voltage electromagnetic flowmeter. Journal of Fluid Mechanics, vol. 43, pp. 577-590.

Bevir, M.K. (1970) Theory of Induced Voltage Electromagnetic Flowmeasurement. IEEE Tansactions on Magnetics, vol. MAG-6, pp. 315-320.

Bevir, M.K. (1971) Sensitivity of Electromagnetic Velocity Probes. Physics in Medicine and Biology, vol. 6, pp. 229-232.

Bevir, M.K., O'Sullivan, V.T. and Wyatt, D.G. (1981) Computation of electromagnetic flowmeter characteristics from magnetic field data. Journal of Physics D: Applied Physics, vol. 14, pp. 373-388.

Boucher, R.F. (1995) Minimum flow optimization of fluidic flowmeters. Measurement Science and Technology, vol. 6, pp. 872-879.

Boucher, R.F., Churchill, D., Mazharoglu, C. and Parkinson, G.J. (1991) A Fluidic By-Pass Venturimeter. Flocome '91, vol., pp. 565-569.

Boucher, R.F. and Mazharoglu, C. (1988) Low Reynolds Number Fluidic Flowmetering. Journal of Physics E: Scientific Instruments, vol. 21, pp. 977-989.

Buhl, T., Gaunaa, M., Bak, C., Hansen, P. and Clemmensen, K. (2005) Measurements on the Thunder TH-6R actuator, Riso National laboratory, pp. 20.

Butler, J.L. (1988) Application manual for the design of ETREMA Terfenol-D magnetostrictive transducers, EDGE Technologies, Inc., Ames, IA.

Calkins, F.T., Dapino, M.J. and Flatau, A.B. (1997) Effect of prestress on the dynamic performance of a Terfenol-D transducer, in Proceeding of SPIE 1997 Symposium on Smart Structures and Materials #3041-23, San Diego, CA, USA.

Calkins, F.T. and Flatau, A.B. (1996) Transducer based measurements of Terfenol-D material properties, in Proceeding of SPIE 1996 Symposium on Smart Structures and Smart Materials #2717-67, San Diego, CA, USA.

Carver, A. and Brunson, C. (2001) Fluidic Oscillation Measurement Proves a Cost Effective Solution. Pipelin and Gas Journal, vol. July 2001, pp.

Chakraborty, S. and Tomlinson, G.R. (2003) An initial experimental investigation into the change in magnetic induction of a Terfenol-D rod due to external stress. Smart Materials and Structures, vol. 12, pp. 763-768.

Claeyssen, F., Le Letty, R., Barillot, F. and Sosnicki, O. (2007) Amplified Piezoelectric Actuators: Static & Dynamic Applications. Ferroelectrics, vol. 351, pp. 3-14.

Cox, T.J. and Wyatt, D.G. (1984) An electromagnetic flowmeter with insulated electrodes of large surface area Journal of Physics E: Scientific Instruments, vol. 17, pp. 488-503.

Dapino, M.J. (1999) Nonlinear and hysteretic magnetomechanical model for magnetostrictive transducers, in Engineering Mechanics, PhD Thesis, Iowa State University, Ames, Iowa, pp. 273.

Dapino, M.J., Smith, R.C. and Flatau, A.B. (1999) A structural-magnetic strain model for magnetostrictive transducers, in Proceedings of SPIE, Smart Structures and Materials.

Durcan, L.P. (1998) Development of baseline stability in an electromagnetic flowmeter for dielectric liquids, PhD Thesis, Cranfield University, pp. 232.

Fletcher, S.I., Nicholson, I.G. and Smith, D.J.M. (2000) An investigation into the effects of installation on the performance of insertion flowmeters. Flow Measurement and Instrumentation, vol. 11, pp. 19-39.

Frey, M.P. The Developing role of helical turbine meters, Faure Herman Meter, Inc.

Fu, Y., Harvey, E.C., Ghantasala, M.K. and Spinks, G.M. (2006) Design, fabrication and testing of piezoelectric polymer PVDF microactuators. Smart Materials and Structures, vol. 15, pp. S141-S146.

Furmidge, N. (1996) Perfomance enhancement of a fluidic oscillator in Process and Systems Engineering, PhD Thesis, Cranfield University, Bedford, pp. 283.

Gebhard, U., Hein, H. and Schmidt, U. (1996) Numerical investigation of fluidic micro-oscillators. Journal of Micromechanics and Microengineering, vol. 6, pp. 115-117.

Groom, N.J. and Bloodgood, V.D.J. (2000) A comparion of Analytical and Experimental Data for a Magnetic Actuator, NASA.

Groom, N.J. and Dake Bloodgood, V. (2000) A Comparison of Analytical and Experimental Data for a Magnetic Actuator, NASA, Hampton, Virginia.

Gualtieri, J.G., Kosinski, J.A. and Ballato, A. (1994) Piezoelectric Materials for Acoustic Wave Applications IEEE Transactions on Ultrasonics, Ferroelectrics, and Frequency Control, vol. 41, pp. 53-59.

Guilbert, A.R. and Sanderson, M.L. (1996) A novel ultrasonic mass flowmeter for liquids, in IEE Colloquium on Advances in Sensors for Fluid Flow Measurement, pp. 8/1-8/4.

Harvey, P. (2004) Sensing Technologies for Fluidic Oscillator, in Power and Systems Engineering, EngD Thesis, Cranfield University, Bedford.

Hemp, J. (1975) Improved magnetic field for an electromagnetic flowmeter with

point electrodes. Journal of Physics D: Applied Physics, vol. 8, pp.

Hemp, J. (2001) A technique for low cost calibration of large electromagnetic flowmeters. Flow Measurement and Instrumentation, vol. 12, pp. 123-134.

Hemp, J., Sanderson, M.L., Koptioug, A.V., Liang, B., Sweetland, D.J. and Al Rabeh, R.H. (2002) Problems in the theory and design of electromagnetic flowmeters for dielectric liquids: Part 1: experimental assessment of static charge noise levels and signal-to-noise ratios. Flow Measurement and Instrumentation, vol. 13, pp. 143-153.

Hemp, J. and Versteeg, H.K. (1986) Prediction of electromagnetic flowmeter characteristics Journal of Physics D: Applied Physics, vol. 19, pp. 1459-1476.

Hemp, J. and Youngs, I. (2003) Problems in the theory and design of electromagnetic flowmeters for dielectric liquids. Part 3a. Modelling of zero drift due to flux linkage between coil and electrode cables. Flow Measurement and Instrumentation, vol. 14, pp. 65-78.

Hofmann, F. (2003) Fundamental priciples of Electromagnetic Flow measurement, KROHNE Messtechnik Gmbh & Co., pp. 71.

Hommena, J.A. (1997) MAGNETOMECHANICAL BEHAVIOR OF TERFENOL-D PARTICULATE COMPOSITES, in Theoretical and Applied Mechanics, MSc Thesis, University of Illinois, pp. 156.

Honda, S. (2000) On the Role of a Target and Side Walls to Fluidic Oscillation, in FLUCOME 2000, 6th International Symposium on Fluid Control, its Measurement and Visualisation, Sherbrooke, Canada.

Honda, S. and Yamasaki, H. (1985) A New Hydrodynamic Oscillator Type Flowmeter, in Proceedings of the FLUCOME 1985, International Symposium on Fluidic Control, its Measurement and Visualisation, City.

Honda, S. and Yamasaki, H. (1988) Fluidic Oscillator Type Flowmeter Without Control Ports, in Proceedings of the International Symposium on Fluid-Control, Measurement, Mechanics and Flow Visualisation, City.

Hussein, M. and David, R.W. (1989) Flow meter based on the trapped vortex pair fluidic oscillator. Review of Scientific Instruments, vol. 60, pp. 935-938.

James, R. (1994) Numerical Simulation of Flow through Fluidic Flowmeters, PhD Thesis, Cranfield University, Cranfield.

Jeans, S.J. (1946) The Mathematical Theory of Electricity and Magnetism, Cambridge University Press, London, UK.

Jiles, D.C. (1995) Theory of the magnetomechanical effect. Journal of Physics D: Applied Physics, vol. 28, pp. 1537-1546.

Jones, B. and Liang, C. (1996) Magnetostriction: Revealing the Unknown IEEE AES Systems Magazine, vol., pp. 3-6.

Jordan, T.L. and Ounaies, Z. (2001) Piezoelectric Ceramics Characterization, NASA.

Kalsi, H.S., Markland, E., Samuel, N.P. and Tofield, G.M. (1988) Factors Affecting Choice of Fluidic Flowmeters, in 2nd International Symposium on Fluid - Control, Measurement, Mechanics and Flow Visualisation.

Kawano, A., Honda, S., Hasegawa, T., Okavayashi, M. and Tanaka, H. (1985) Fluidic Flowmeters with Wide Measuring Range, in Proceedings of the FLUCOME 1985, International Symposium on Fluid Control, its Measurement and Visualisation, City.

Kim, J. and Jung, E. (2005) Finite element analysis for acoustic characteristics of a magnetostrictive transducer. Smart Materials and Structures, vol. 14, pp. 1273-1280.

Kroon, D.J. (1968) Laboratory Magnets, N.V.Philips' Cloeilampenfarieken, Eindhoven,Netherands.

Langman, R. (1990) Magnetic Properties of Mild Steel under Conditions of Biaxial Stress. IEEE Transactions on Magnetics, vol. 26, pp. 1246-1251.

Lanotte, L., Iannotti, V., Maritato, L., Attanasio, C. and Mercaldo, L.V. (1998) Effects of the internal strain on the magnetic differential permeability and the stress sensitivity in Co/Cu multilayers. Journal of Physics D: Applied Physics, vol. 31, pp. 287-290.

Law, M. (1994) The development and modelling of a novel clamp-on ultrasonic-thermal and ultrasonic multiple reflection flowmeter for liquid applications, in Department of Fluid Engineering and Instrumentation, PhD Thesis, Cranfield University, pp. 427.

Lee, E.W. (1955) MAGNETOSTRICTION AND MAGNETOMECHANICAL EFFECTS Reports on Progress in Physics, pp. 184-229.

Lee, K.S., Choi, J., S., Ahn, J.C., Kim, S.J. and Park, T.J. (2001) Research on under reading of water meters, Seoul Waterworks Laboratory, Seoul.

Lee, K.S., Choi, J., S., Shin, J.H. and Kim, E., I. (2001) Performance test on 13mm Class D watermeter, Seoul Waterworks Laboratory, Seoul.

Lim, K.W. and Chung, M.K. (1998) Relative errors in evaluating the electromagnetic flowmeter signal using the weight function method and the finite volume method. Flow Measurement and Instrumentation, vol. 9, pp. 229-235.

Liu, Y.X., Wan, J.G., Liu, J.-M. and Nan, C.W. (2003) Numerical modeling of magnetoelectric effect in a composite structure. Journal of Applied Physics, vol. 94, pp. 5111-5117.

Mark, B.M., Arthur, E.C., Marilyn, W.-F., Jan, L., Joseph, P.T. and Elizabeth, A.M. (1991) Characterization of Terfenol-D for magnetostrictive transducers. Journal of the Acoustical Society of America, vol. 89, pp. 1448-1455.

Michalski, A., Starzynski, J. and Wincenciak, S. (2001) 3D Approach to Designing the Excitation Coil of an Electromagnetic Flowmeter in Proceeding of IEEE Instrumentation and Measurement Technology Conference, Budapest, Hungary.

Mochizuki, T. (1989) Electromagnetic flowmeter capable of simultaneous measurement of flow rate and conductivity of fluid, Aichi Tokei Denki Co., Ltd., Japan.

Moffett, M.B., Clark, A.E., Wun-Fogle, M., Linberg, J., Teter, J.P. and McLaughlin, E.A. (1990) Characterization of Terfenol-D for magnetostrictive transducers. Journal of the Acoustical Society of America, vol. 89, pp. 1448-1455.

Moffett, M.B., Powers, M. and Clark, A.E. (1991) Comparison of Terfenol-D and PZT-4 power limitations Journal of Acoustic Society of America, vol. 90, pp. 1184-1185.

Niezrecki, C., Brei, D., Balakrishnan, S. and Moskalik, A. (2001) Piezoelectric Actuation: State of the Art. The shock and Vibration Digest, vol. 33, pp. 269-280.

Ogden, D.M. (1985) Calibration and testing of an electromagnetic flowmeter of novel design in Department of Fluid Engineering and Instrumentation, PhD Thesis, Cranfield University, pp. 346.

OIML (1985) Hot water neters, in OIML R 72 Edition 1985 (E).

OIML (2002) Heat meters Part 1: General requirements, in OIML R 75-1 Edition 2002 (E).

OIML (2006) Water meters intended for the metering of cold potable water Part 1: Metrological and technical requirements, in OIML R 49-1 Edition 2006(E).

Okabaysashi, M. and Haruta, M. (1985) Fluidic flowmeter, Osaka Gas Company Limited, Japan.

O'Sullivan, V.T. (1983) Computation of electromagnetic flowmeter characteristics from magnetic field data: III. Rectilinear weight functions Journal of Physics D: Applied Physics, vol. 16, pp. 1461-1476.

Ounaies, Z., Mossi, K., Smith, R. and Bernd, J. (2001) Low-field and High-field Characterization of THUNDER actuators, NASA, Hampton, Virginia.

Piefort, V. (2001) Finite Element Modelling of Piezoelectric Active Structure, in Applied Science, PhD Thesis, Universite Libre de Bruxelles, pp. 154.

Rosales, C. (2003) Modelling Noise in Electromagnetic Flowmeters, in Process and Systems Engineering, PhD Thesis, Cranfield University, Bedford.

Rosales, C., Sanderson, M.L. and Hemp, J. (2002) Problems in the theory and design of electromagnetic flowmeters for dielectric liquids. Part 2a: Theory of noise generation by

turbulence modulation of the diffuse ionic charge layer near the pipe wall. Flow Measurement and Instrumentation, vol. 13, pp. 155-163.

Rosales, C., Sanderson, M.L. and Hemp, J. (2002) Problems in the theory and design of electromagnetic flowmeters for dielectric liquids. Part 2b: theory of noise generation by charged particles. Flow Measurement and Instrumentation, vol. 13, pp. 165-171.

Ryu, J., Priya, S., Carazo, A.V., Uchino, K. and Kim, H. (2001) Effect of the Magnetostrictive Layer on Magnetoelectric Properties in Lead Zirconate Titanate/Terfenol-D Laminate Composites. Journal of the American Ceramic Society, vol. 84, pp. 2905-2908.

Salmasi, Z.S., Jin, W., Gregg, R.D., MacManus, G. and Howarth, C.T. (2001) Electromagnetic Flowmeter Having Low Power Consumption, ABB Metering Limited, GB.

Sanderson, M.L. (1994) Domestic water metering technology Flow Measurement and Instrumentation, vol. 5, pp. 107-113.

Sanderson, M.L. and Yeung, H. (2002) Guidelines for the use of ultrasonic non-invasive metering techniques. Flow Measurement and Instrumentation, vol. 13, pp. 125-142.

Schmoock, R.F. (1988) Electromagnetic Flowmeter with Alternating permanent magnet field, Fisher & Porter Co.

Shercliff, J.A. (1962) The Theory of Electromagnetic Flow Measurement, Cambridge University Press.

Sitti, M., Campolo, D., Yan, J. and Fearing, R.S. (2001) Development of PZT and PZN-PT based unimorph actuators for micromechanical flapping mechanisms, in Proceedings of the Proceeding of 2001 ICRA IEEE International Conference on Robotics and Automation, City.

Stoltenkamp, P.W. (2007) Dynamics of turbine flow meters, PhD Thesis, Technishe Universiteit Eindhoven, Eindhoven, pp. 155.

Sumitro, S., Kurokawa, S., Shimano, K. and Wang, M.L. (2005) Monitoring based maintenance utilizing actual stress sensory technology. Smart Materials and Structures, vol. 14, pp. 568-578.

Szebeszczyk (1994) Application of clamp-on ultrasonic flowmeter for industrial flow measurements Flow Measurement and Instrumentation, vol. 5, pp. 127-131.

Thunder White Paper(2001), Face International Corporation, pp. 10.

Ueno, T. and Higuchi, T. (2005) Design of Magnetostrictive/Piezoelectric Laminate Composite for Coil-Less Magnetic Force Control. IEEE Transactions on Magnetics, vol. 41, pp. 1233-1237.

Ueno, T. and Higuchi, T. (2005) Dynamic Response in Magnetic Force Control Using a Laminate Composite of Magnetostrictive and Piezoelectric Materials. IEEE Transactions on Magnetics, vol. 41, pp. 1082-1085.

Ueno, T., Qiu, J. and Tani, J. (2002) Magnetic Circuit Design Method for Magnetic Force Control Systems Using Inverse Magnetostrictive Effect: Examination of Energy Conversion Efficiency Depending on *E* Effect. Electrical Engineering in Japan, vol. 140, pp. 771-777.

Ueno, T., Qiu, J. and Tani, J. (2003) Magnetic Force Control With Composite of Giant Magnetostrictive and Piezoelectric Materials. IEEE Transactions on Magnetics, vol. 39, pp. 3534-3540.

Ueno, T., Qui, J. and Tani, J. (2004) Magnetic Force Control Based on the Inverse Magnetostrictive Effect. IEEE Transactions on Magnetics, vol. 40, pp. 1601-1605.

Upp, E.L. and LaNasa, P.J. (2002) Fluid Flow Measurement : A Practical Guide to Accurate Flow Measurement, Gulf Professional Pub., Boston.

Varga, I.K. (1981) Voltage generation through flow of liquid in dielectric tubes. Journal of Physics D: Applied Physics, vol., pp. 1395.

Webster, J.G. (1999) The Measurement, Instrumentation and Sensors Handbook, Springer.

Wilson, M.P., Coogan, C.H. and Southall, K. (1970) An Experimental Investigation of Fluidic Volume Floemeter. Journal of Basic Engineering, vol. 92, pp. 139.

Wright, P. (1980) The Coanda meter -a fluidic digital gas flowmeter Journal of Physics E: Scientific Instruments, vol. 13, pp. 433-436.

Wyatt, D.G. (1968) The electromagnetic blood flowmeter. Journal of Physics E: Scientific Instruments, vol. 1, pp. 1146-1152.

Wyatt, D.G. (1983) Computation of electromagnetic flowmeter characteristics from magnetic field data: II. Errors Journal of Physics D: Applied Physics, vol. 16, pp. 465-478.

Wyatt, D.G. and Phil, M.A. (1961) Problems in the Measurement of Blood Flow by Magnetic Induction. Physics in Medicine and Biology, vol. 5, pp. 369-399.

Wyatt, D.G. and Phil, M.A. (1961) Zero Error in Induction Flowmeters Employing a Permanent Magnet. Physics in Medicine and Biology, vol. 5, pp. 449-452.

Yamasaki, H., Takahashi, A. and Honda, S. (1988) A New Fluidic Oscillator For Flow Measurement, in 2nd International Symposium on Fluid - Control, Measurement, Mechanics and Flow Visualisation.

Yang, J., Chen, C., Tsai, K., Lin, W. and Sheen, H. (2007) A novel fluidic oscillator incorporating step-shaped attachment walls. Sensors and Actuators A: Physical, vol. 135, pp. 476-483.

Yang, J., Lin, W., Tsai, K. and Huang, K. (2005) Fluidic Oscillator, National Tsing Hua University, Taiwan.

Yi, J.H., Park, K.H., Kim, S.H., Kwak, Y.K., Abdelfatah, M. and Busch-Vishniac, I. (1995) Force Control for Magnetic Levitation System Using Flux Density Measurement, in Proceedings of the 34th Conference on Decision & Control, New Orleans, LA, USA.

Zhang, X.Z. (1998) 2D analysis for the virtual current distribution in an electromagnetic flow meter with a bubble at various axis positions. Measurement Science and Technology, vol. 9, pp. 1501-1505.

Zhang, X.Z. (1998) The virtual current of an electromagnetic flow meter in partially filled pipe. Measurement Science and Technology, vol. 9, pp. 1852-1855.